AD-A220 261

FLIGHT MODEL DISCHARGE SYSTEM

R.R. Robson and W.S. Williamson

Hughes Research Laboratories
3011 Malibu Canyon Road
Malibu, California 90265

September 1989

Final Report
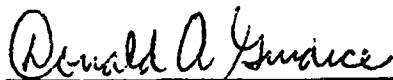September 1983 through May 1989

DTIC
S ELECTE
APR 10 1990
B D

90 04 09 273

This technical report has been reviewed and is approved for publication.

DONALD A. GUIDICE
Contract Manager

DAVID A. HARDY
Branch Chief

FOR THE COMMANDER

RITA C. SAGALYN
Division Director

This report has been reviewed by the ESD Public Affairs Office (PA) and is releasable to the National Technical Information Service (NTIS).

Qualified requestors may obtain additional copies from the Defense Technical Information Center. All others should apply to the National Technical Information Service.

If you address has changed, or if you wish to be removed from the mailing list, or if the addressee is no longer employed by your organization, please notify GL/IMA, Hanscom AFB, MA 01731. This will assist us in maintaining a current mailing list.

Do not return copies of this report unless contractual obligations or notices on a specific document requires that it be returned.

SECURITY CLASSIFICATION OF THIS PAGE

REPORT DOCUMENTATION PAGE

Form Approved
OMB No. 0704-0188

1a. REPORT SECURITY CLASSIFICATION	1b. RESTRICTIVE MARKINGS		
Unclassified			
2a. SECURITY CLASSIFICATION AUTHORITY	3. DISTRIBUTION / AVAILABILITY OF REPORT		
	Approved for public release;		
2b. DECLASSIFICATION / DOWNGRADING SCHEDULE	distribution unlimited		
4. PERFORMING ORGANIZATION REPORT NUMBER(S)	5. MONITORING ORGANIZATION REPORT NUMBER(S)		
HAC REF F4890	GL-TR-89-0270		

6a. NAME OF PERFORMING ORGANIZATION	6b. OFFICE SYMBOL (If applicable)	7a. NAME OF MONITORING ORGANIZATION
Hughes Research Laboratories		Geophysics Laboratory
6c. ADDRESS (City, State, and ZIP Code)		7b. ADDRESS (City, State, and ZIP Code)
3011 Malibu Canyon Road Malibu, CA 90245		Hanscom AFB Massachusetts 01731-5000

8a. NAME OF FUNDING / SPONSORING ORGANIZATION	8b. OFFICE SYMBOL (If applicable)	9. PROCUREMENT INSTRUMENT IDENTIFICATION NUMBER		
Geophysics Laboratory	GL/PHE	F19628-83-C-0143		
8c. ADDRESS (City, State, and ZIP Code)		10. SOURCE OF FUNDING NUMBERS		

8c. ADDRESS (City, State, and ZIP Code)	PROGRAM ELEMENT NO.	PROJECT NO.	TASK NO.	WORK UNIT ACCESSION NO.
Hanscom AFB Massachusetts 01731	63410F	2823	01	AA

11. TITLE (Include Security Classification)

FLIGHT MODEL DISCHARGE SYSTEM (U)

12. PERSONAL AUTHOR(S)
R.R. Robson and W.S. Williamson

13a. TYPE OF REPORT	13b. TIME COVERED	14. DATE OF REPORT (Year, Month, Day)	15. PAGE COUNT
FINAL REPORT	FROM 9/83 TO 5/89	1989, September	266

16. SUPPLEMENTARY NOTATION

17. COSATI CODES			18. SUBJECT TERMS (Continue on reverse if necessary and identify by block number)
FIELD	GROUP	SUB-GROUP	Spacecraft charging, charge control system, autonomous discharge system, xenon plasma source, geosynchronous charge control.

19. ABSTRACT (Continue on reverse if necessary and identify by block number)

The Flight Model Discharge System (FMDS) Program has been completed for the Geophysics Laboratory under Contract F19628-83-C-0143. The FMDS is an autonomous system that detects both absolute and differential charging of high-altitude satellites and actively discharges the associated potentials before hazardous arcing levels are reached by emitting a low-energy inert-gas plasma. FMDS operating principles are based on empirical results from the Air Force SCATHA (P78-2) and NASA ATS-6 satellites, both of which successfully demonstrated the principle of safely reducing spacecraft charging levels by the emission of a low-energy space-charge-neutral plasma — effectively "grounding" the spacecraft frame and dielectric surfaces to the potential of the ambient space plasma. FMDS uses a xenon plasma source capable of igniting within one second and of emitting a flow of space-charge-neutral plasma containing more than 1 mA of Xe^{++} ions. The spacecraft charging level is detected by sensors similar to those that operated aboard SCATHA (i.e., ion and electron electrostatic energy analyzers and surface-potential monitors).

20. DISTRIBUTION / AVAILABILITY OF ABSTRACT	21. ABSTRACT SECURITY CLASSIFICATION	
☐ UNCLASSIFIED / UNLIMITED ☒ SAME AS RPT. ☐ DTIC USERS	Unclassified	
22a. NAME OF RESPONSIBLE INDIVIDUAL	22b. TELEPHONE (Include Area Code)	22c. OFFICE SYMBOL
Donald A. Guidice	(617) 377-3989	GL/PHE

DD Form 1473, JUN 86   Previous editions are obsolete   SECURITY CLASSIFICATION OF THIS PAGE

This report describes the development details for the breadboard and flight models of the FMDS instrument. Operational characteristics of the electrostatic analyzers, surface-potential monitors, transient-pulse monitor, plasma source, microprocessor-based controller, and software architecture are described. Results of vacuum-chamber testing under simulated geosynchronous environmental conditions are also presented.

Keywords: → to field 18

Accession For

NTIS GRA&I	☑
DTIC TAB	☐
Unannounced	☐
Justification	

By_____
Distribution/
Availability Codes

| Dist | Avail and/or Special |

A-1

TABLE OF CONTENTS

TABLE OF CONTENTS

LIST OF ILLUSTRATIONS

LIST OF ILLUSTRATIONS (Continued)

LIST OF ILLUSTRATIONS (Continued)

LIST OF ILLUSTRATIONS (Continued)

LIST OF ILLUSTRATIONS (Continued)

LIST OF ILLUSTRATIONS (Continued)

LIST OF ILLUSTRATIONS (Continued)

LIST OF TABLES

LIST OF TABLES

SECTION 1
INTRODUCTION

The objectives of the FMDS program were to design, develop, fabricate, test, and deliver two flight units (later changed, by contract modification, to one flight unit) of a satellite Flight Model Discharge System (FMDS). The FMDS is a stand-alone system capable of autonomous operation (except for power) that monitors spacecraft potential, determines when spacecraft charging is present, and operates a discharge device to eliminate potentials and maintain the spacecraft in a neutral charge state. The FMDS is designed to be incorporated into the "housekeeping" function of any spacecraft subject to spacecraft charging. While full ground-command capability is retained for redundancy, only a "power on" command is required to activate the system. In addition to the capability for remote command override of its autonomous operation, the FMDS provides telemetry signals to monitor such functions as sensor outputs, controller "commands," plasma source operation, gas supply in the reservoir tank, and system state-of-health diagnostics (e.g., temperatures, voltages, and currents).

The technical effort under the FMDS program covered a roughly 5.5 year time span. It started in September of 1983 and the flight hardware was delivered in May of 1989. The major phases of the program were:

- Conceptual Design Review
- Preliminary Design Review
- Breadboard Demonstration
- Critical Design Review
- Flight Fabrication and Assembly
- Flight Testing.

In the following technical discussion, we present the results of the effort on the FMDS contractual program, which was carried out at Hughes Research Laboratories in Malibu, California. An overview of the FMDS is presented, followed by an in-depth treatment of the design, operation, and testing of the FMDS hardware and software.

SECTION 2
FLIGHT MODEL DISCHARGE SYSTEM TOTAL SYSTEM

The FMDS is a stand-alone system capable of autonomous operation (except for power) that monitors space-vehicle potential, determines when charging is present, and operates a discharge device to eliminate charge buildup and maintain the vehicle in a neutral charge state. The FMDS is designed to be incorporated into the "housekeeping" functions of any vehicle subject to spacecraft charging. While full ground-command capability is retained for redundancy, only a "power on" command is required to activate the system. It detects charging, operates to neutralize the charging, and returns to the passive mode when the charging hazard is no longer present.

The FMDS consists of three types of components:

(1)   Charging sensors:

•   Electrostatic Analyzers (ESAs). These sensors detect absolute charging relative to the ambient plasma in space.

•   Surface Potential Monitors (SPMs). These sensors determine differential charging relative to spacecraft ground.

•   Transient Pulse Monitor (TPM). This sensor detects the electromagnetic pulses generated by the onset of arcing.

(2)   An active discharge device (plasma source).

(3)   A control unit to interpret the sensor outputs, determine when and if charging is occurring, and control the discharge device.

A block diagram of the system is shown in Figure 2-1.

The controller incorporates comprehensive charging-detection algorithms that contain ground-alterable parameters to allow in-space refinement of FMDS operation. The controller incorporates redundant and fault-tolerant software to permit the FMDS to continue operation in the face of specific faults or failures. In addition, it has the capability for ground- or remote-command override of its autonomous operation, and also provides telemetry signals to monitor such functions as sensor outputs, controller status flags, plasma source operation, gas supply pressure in the reservoir tank, temperatures, voltages, and currents.

The FMDS is ultimately intended for extended satellite operation at geosynchronous orbit; however, it is designed to withstand the launch and operating environments of both geosynchronous and Shuttle orbits. While the primary emphases are safety and reliability, low

2

SATELLITE INTERFACES
(POWER, COMMANDS, AND TELEMETRY)

POWER

FEED
SYSTEM

GAS FEED

ESA

SPM

CONTROLLER

TPM

PLASMA
SOURCE
ELECTRONICS

PLASMA
GENERATOR

INTERNAL
ANTENNA

EXTERNAL
ANTENNA
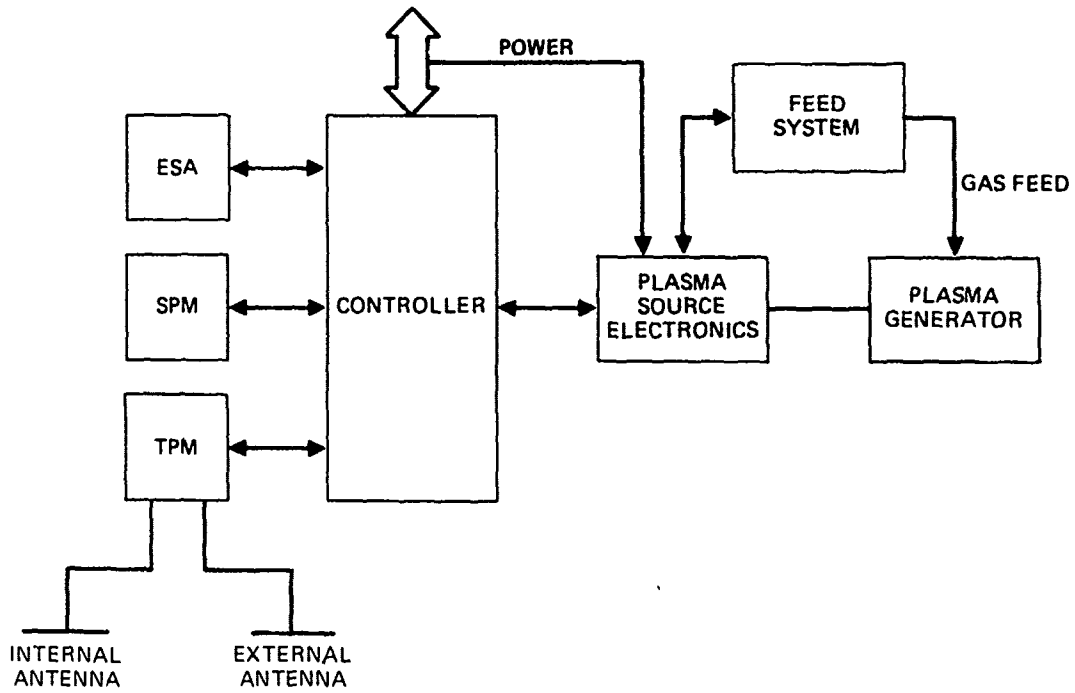
Figure 2-1. Block diagram of the FMDS.

operating and transient voltages are also considered to prevent Paschen breakdown and to minimize EMI.

2.1 OVERALL SYSTEM

Figure 2-2 is a photograph of the FMDS flight hardware as it was delivered (TPM not installed), with the flight components mounted on the system base plate. The base plate is an aluminum honeycomb-structure mounting plate to provide a simple, lightweight, and structurally sturdy interface with the host spacecraft. No attempt is made in this photograph to indicate the exact mechanical interface of the FMDS with the host spacecraft since at this time a specific ride has not been determined. The structurally integrated design approach also facilitates system testing in both laboratory vacuum chambers and environmental test fixtures (vibration, thermal/vacuum, etc.).

Because of the diversity of functions required of the various FMDS components, each element is packaged separately and attached separately to the common mounting plate. Maintaining separation between each of the components has the added advantage of facilitating substitution of upgraded component designs if such upgrades become available in the future.

The two SPMs and the ESAs are mounted on one end of the FMDS mounting plate to provide both maximal and similar exposure of the sensors to incoming particle flux while avoiding (as much as possible) any local distortions of electrostatic equipotentials that might be caused by other devices, such as the plasma source.

The plasma source is located at the other end of the FMDS where it is farthest from the charged-particle entrance aperatures of the ESAs; this minimizes the introduction of plasma-source-generated particles. In this location, the source is reasonably remote from both the ESAs and the SPMs.

The electronics packages for the plasma-generator, TPM, and controller; the SPMs; the ESAs; and the plasma generator are all at the same height. This uniformity allows adding a cover to FMDS to form a ground plane and to provide a mounting surface for the TPM external antenna if the FMDS is mounted to the exterior of a spacecraft.

Inasmuch as the FMDS is intended for satellite use, minimizing weight, volume, and power was of utmost concern. The overall FMDS, without the TPM installed, has a mass of 19.4 kg (42.8 lbs.) which is a 1.6 kg increase from the CDR estimate, and consumes less than 5.6 W (a decrease of 4.1 W from the CDR estimate) when the plasma source is not activated, and less than 21 W when it is activated. With the TPM installed, it is estimated that the FMDS would have a mass of 21.2 kg, and consume 13.2 W when the plasma source was not activated and 27.8 W when it was. FMDS weights and power consumption are summarized in Tables 2-1 and 2-2 respectively. The overall dimensions are 16.5 x 38.1 x 61 cm (6.5 x 15 x 24 in.).
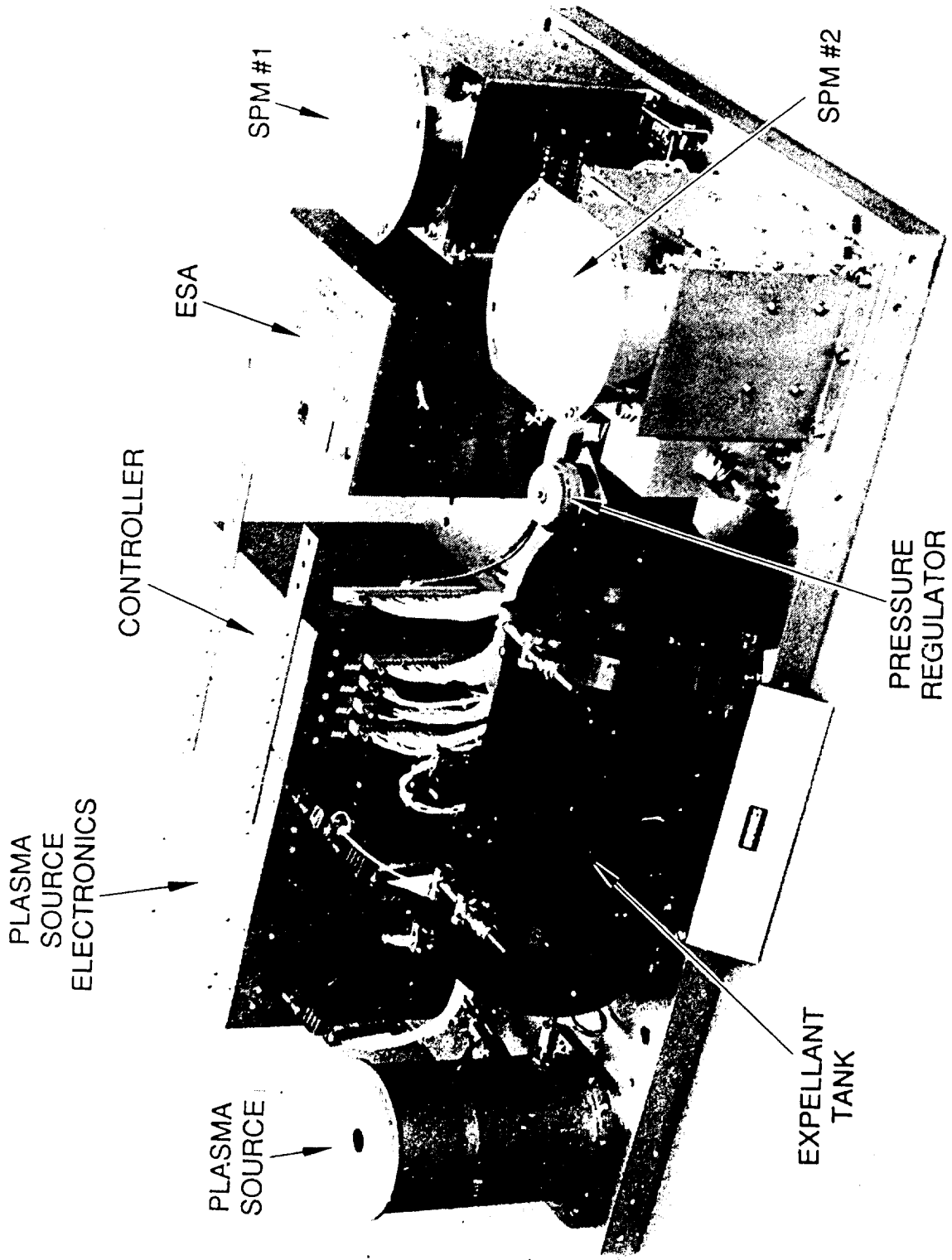
Figure 2-2. FMDS flight hardware as it was delivered, mounted on the 1-in-thick aluminum honeycomb plate.

PLASMA SOURCE ELECTRONICS

PLASMA SOURCE

CONTROLLER

ESA

SPM #1

SPM #2

PRESSURE REGULATOR

EXPELLANT TANK

TABLE 2-1. Summary of FMDS Weights.

Unit	CDR Estimate		Delivered Values		Original Contract Spec, lbs
	Mass, kg	Weight, lbs	Mass, kg	Weight, lbs	
ESA	2.7	6.0	1.873	4.13	6.0
SPM (2 Units)	1.4	3.0	2.544	5.61	3.0
Controller	1.7	3.7	1.415	3.12	—
Plasma Source	1.4	3.0	1.720	3.79	⎫
Source Electronics	2.0	4.4	3.461	7.63	⎬ 15.0
Feed System	4.2	9.2	4.067	8.97	⎭
Harness	0.7	1.5	0.595	1.31	—
Thermal Control	0.9	2.0	0.000	0.00	—
Mounting Plate	2.2	4.8	3.006	6.63	—
Miscellaneous Hardware	—	—	0.240	0.52	—
FMDS Dry Mass Without TPM	17.2	37.6	18.921	41.71	—
Xenon/Hydrogen	0.6	1.3	0.496	1.10	—
FMDS at Launch Without TPM	17.8	38.9	19.417	42.81	32.0
TPM	1.6	3.5	1.80*	3.97*	3.0
TOTAL	19.4	42.4	21.22	46.78	35.0

*Estimated

6

TABLE 2-2. Summary of FMDS Power Consumption.

Unit	CDR Estimate		Measured Values Worst Case		Original Contract Spec, W
	Source Off, W	Source On, W	Source Off, W	Source On, W	
ESA (S/N 002)	1.25	1.25	1.44	1.44	1.25
SPM (2 Units)	1.0	1.0	0.36	0.36	2.00
Controller	4.0	4.0	0.86	0.86	(4.0)
Plasma Source	0.0	13.7	0.00	14.67	(25.0)
Housekeeping Inverter	3.4	4.1	2.89	2.90	—
FMDS Without TPM	3.7	24.1	5.55	20.23	32.00
TPM	4.0·	4.0	7.6*	7.6*	3.00
TOTAL	13.7	28.1	13.15	27.83	35.00
FMDS Contract Spec	10.0	35.0	10.00	35.00	35.00

( ) = Inferred
*Estimated

7

2.2 COMPONENTS

The ESAs measure the energy distribution (from 50 eV to 20 keV) of electrons and ions incident upon the satellite. These energy distributions will shift when environmental conditions become conducive to spacecraft charging. A shift in the electron spectrum to higher temperatures is indicative that charging is likely to occur. There is a second shift in the energy distributions which is directly related to the potential of the satellite frame relative to the space potential. Because the ESAs are referenced to the satellite frame, and the particles originate with energies relative to space potential, any change in the potential of the satellite frame appears as shifts of the zero references in the particle-energy distributions. Algorithms in the controller detect these shifts (Figure 2-3) in order to (1) provide an early warning that threatening substorm conditions are developing (by detecting elevated electron temperature), and (2) detect that charging of the satellite frame has exceeded a threshold level (by detecting a zero shift in the ion spectrum). These algorithms provide a signal to turn ON the plasma source.

The SPMs detect the onset of differential charging of the satellite dielectric surfaces. When the satellite is in sunlight and charging conditions exist, the isolated dielectric surfaces that are shaded charge much faster than the satellite frame because of the absence of the neutralizing effect of photo-emission from these shaded surfaces (Figure 2-4). Therefore, through measurement of the potential on the surface of a shaded dielectric sensor, differential charging is detected quickly and prior to the detection of satellite-frame charging by the ESA. When the satellite is in eclipse, however, satellite-frame charging occurs faster than differential charging (Figure 2-4). In this circumstance the ESA is the prime detector.

The TPM detects electrical discharges that occur on the surface of the satellite as a result of differential charging. A floating-plate sensor is employed to pick up radiated electric fields caused by these discharges. If electrical discharges are occurring, the implication is that the satellite is charged up, that the plasma generator should be turned on, and that the other sensors have failed to detect the charging. The TPM has ground-adjustable parameters and can be commanded to ignore transients occurring within 1 s following receipt of a command by the spacecraft. The TPM is designed to avoid false arc-discharging alarms.

The controller provides for autonomous control of the FMDS relative to the remainder of the satellite. This device also ties together the other units of the FMDS. The brain of the controller is a microprocessor that contains the algorithms necessary to interpret the data from the sensors and command the plasma generator to turn ON when spacecraft charging is occurring and then turn OFF when it is no longer required. The plasma generator is turned OFF after a programmable time-out (when the emission current from the plasma generator has been less than a threshold value for a specified period of time) and when the ambient electron environment

8
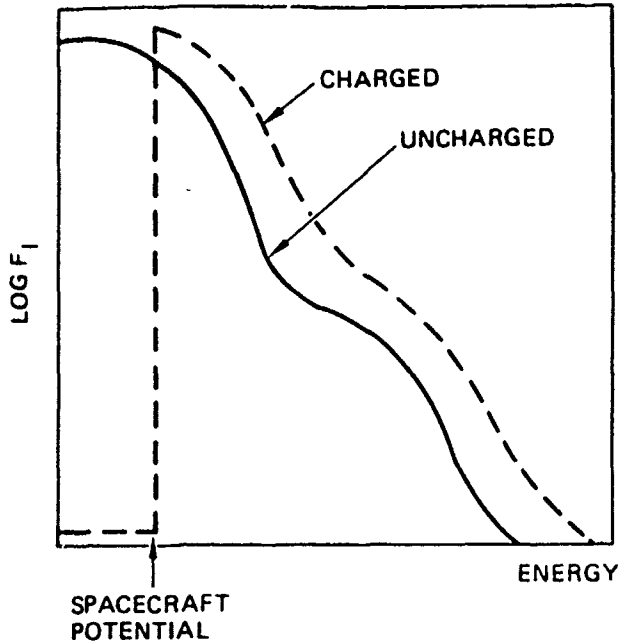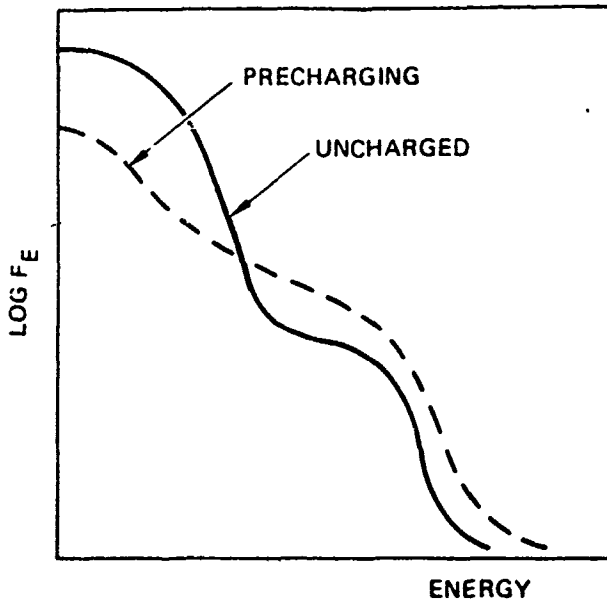
Figure 2-3. Shift in the observed ion and electron spectra caused by environmental conditions conducive to charging and by actual charging of the spacecraft.

SUNLIGHT CHARGING

ECLIPSE CHARGING
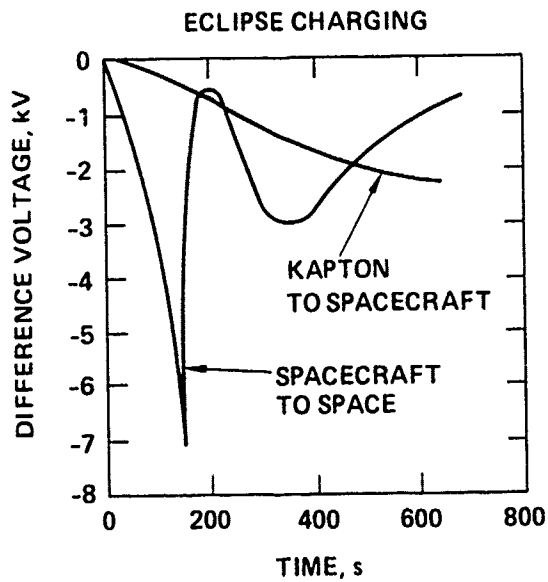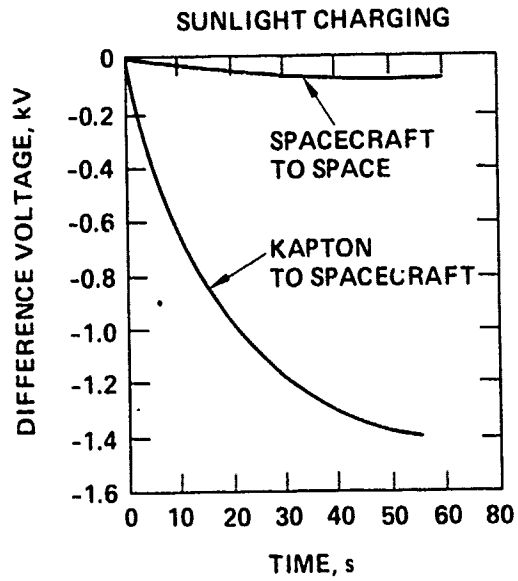
Figure 2-4. Charging characteristics of a shaded dielectric sensor.

returns to a quiescent condition. The controller also provides the command and telemetry interface with the satellite.

The plasma generator emits xenon and hydrogen ions and electrons in sufficient quantity (>1 ma) to bathe the satellite in a conductive low-energy (<50 eV) plasma. This conductive plasma drains the charge from dielectric surfaces and also forms a "plasma bridge" to the surrounding natural space-plasma environment. The plasma generator is capable of igniting in <1 s, operating for 1200 h, and executing 1000 ON/OFF cycles. It requires three power supplies and a gas-feed system consisting of a xenon/hydrogen (90%/10%) storage tank, a pressure regulator, valves, and a flow regulator.

Tables 2-3 through 2-8 list the major contractual specifications for the ESAs, SPMs, TPM, controller, plasma source, and system, respectively. The respective parameters of the final design are also listed in these tables.

Table. 2-3. Electrostatic Analyzer Original Contractual Specifications and Respective Final Design Parameters.

14881-17R6

ORIGINAL CONTRACTUAL SPECS	DELIVERED SPECS
ION AND ELECTRON SPECTRA $<$ 100 eV TO 20 keV	50 eV TO 20 keV
GEOMETRIC FACTOR $\approx 10^{-5}$ TO 10^{-4} cm^2 - SR	6×10^{-4} cm^2 - SR
$\geqslant$ 8 ENERGY CHANNELS	16 CHANNELS
$\leqslant$ 2% OVERLAP AT FWHM	$\leqslant$ 2% OVERLAP—NO GAPS
SWEEPS OF 2, 5, AND 10 s	SWEEPS OF 4, 8, 16, AND 32 s
VOLTAGES SETTLED TO 95% BEFORE COUNTING	VOLTAGES SETTLED TO $\geqslant$ 95% BEFORE COUNTING
GRID TO REPEL PLASMA SOURCE IONS AND ELECTRONS ($<$ 50 eV)	GRID BIASED AT 50 V
SUN SENSOR TO PROTECT CEM.	SUN SENSOR
CMD OVERRIDE OF SUN SENSOR	CMD OVERRIDE
REDUCE UV SCATTERING	SANDBLASTED PLATES
COMMANDABLE CEM BIAS	COMMANDABLE BIAS (8 LEVELS)
THREE-YEAR ON ORBIT LIFE	DESIGNED FOR THREE-YEAR OPERATIONAL LIFE
TELEMETRY	ACCUMULATED COUNTS, ENERGY CHANNEL, STATUS, AND DIAGNOSTICS
$<$ 1.25 W	$<$1.50 W
$<$ 6 lb	$<$4.2 lb

Table 2-4. Surface Potential Monitor Original Contractual Specifications and Respective
Final Design Parameters.

14881–18R4

ORIGINAL CONTRACTUAL SPECS	DELIVERED SPECS
DIELECTRIC SURFACE POTENTIAL MEASURED WITH ELECTRIC FIELD SENSOR	VIBRATING ELECTRODE ELECTROSTATIC VOLTMETER
POTENTIAL AND POLARITY FROM 100 V TO 20 kV	DUAL RANGE: $\pm$ 2 kV $\pm$ 20 kV
TWO DIFFERENT DIELECTRICS IN FLIGHT	TWO INSTRUMENTS WITH DIFFERENT DIELECTRICS
CHOICE OF SIX DIFFERENT DIELECTRICS	CHANGE SENSING PLATE TO CHANGE DIELECTRICS
TELEMETRY	SURFACE POTENTIAL, RANGE, DIAGNOSTICS
< 2 W	<0.4 W (2 UNITS)
< 3 lb	<5.7 lb (2 UNITS)

13

Table 2-5. Transient Pulse Monitor Original Contractual Specifications and Respective Final Design Parameters.

ORIGINAL CONTRACTUAL SPECS	DELIVERED SPECS
DIPOLE SENSOR	MONOPOLE (123 cm^2 PLATE)
MEASURE RADIATED ELECTROMAGNETIC PULSES	**MEASURE RADIATED ELECTROMAGNETIC PULSES**
MULTIPLE THRESHOLD LEVELS	8-BIT DAC
PARAMETERS MEASURED/1s	PARAMETERS MEASURED/4s
– MAX POSITIVE PEAK AMPLITUDE	– POSITIVE PEAK AMPLITUDE/PULSE
– MAX NEGATIVE PEAK AMPLITUDE	– NEGATIVE PEAK AMPLITUDE/PULSE
– POSITIVE INTEGRAL	– INTEGRALS NOT MEASURED
– NEGATIVE INTEGRAL	
– PULSE WIDTH	– PULSE WIDTH/PULSE
– NUMBER OF PULSES	– PULSES/4s
10 V/M TO 10 kV/m FIELD STRENGTH	10 V/m TO 10 kV/m
10 ns TO 10 μs PULSE WIDTHS	20 ns TO 10 μs
1 COUNT/ms MAX	1 COUNT/5ms
TELEMETRY	PARAMETERS MEASURED AND DIAGNOSTICS
< 3 W	<7.6 W*
< 3 lb	<4.0 lb

*ESTIMATED

14

TABLE 2-6. Controller Original Contractual Specifications and Respective Final Design Parameters.

T9234-6

Original Contract Specs	Delivered Specs
Provide autonomous operation of FMDS	Autonomous operation
Determine if threshold levels of charging have been exceeded	Charging above threshold will be detected
Turn on plasma source and operate for 5, 10, 30, or 60 min	Turn on and control plasma source. Turn off based on time (30, 60, 90, 120 min) and/or environmental conditions
Detect with 98% reliability — 95% of cases for charging ≥500 V — 100% of cases for charging ≥1000 V	Designed to meet based on SC9 data
Commandable threshold charging levels of 200, 500, 1000, and 2000 V	Same
Spacecraft arcing to activate plasma source	Arcing will activate plasma source
EMI pulses within 1 s of spacecraft command to be ignored	Ability to blank TPM for 1 s (requires signal from spacecraft)
External command adjustment of TPM algorithm	All algorithms will be adjustable via external command
External commanding of plasma source	Manual operation of complete FMDS
Telemetry	Status and diagnostics
Design to include considerations of radiation hardening	Hardened to 5×10^5 rads (flight)
Redundancy	Critical parameters stored in three locations (majority voting)
Excess capacity	Excess memory and I/O

15

Table 2-7.   Plasma Source Original Contractual Specifications and Respective Final
Design Parameters.

ORIGINAL CONTRACTUAL SPECS	DELIVERED SPECS
< 50 eV NEUTRAL PLASMA	< 40 eV
IONS FROM A NOBLE GAS	90% XENON–10% HYDROGEN
10 μA, 100 μA, AND 1 mA ION CURRENT LEVELS (SELECTABLE)	< 600 μA TO > 1 mA, 4 SELECTABLE SETPOINTS FOR DISCHARGE AND KEEPER
≤ 10s IGNITION	< 1s
1200 HOURS OPERATION	> 1200 hr
1000 ON-OFF CYCLES	> 1000 CYCLES
< 25 W	≤ 10 W OPERATING ≤ 20 W CONDITIONING
< 15 lb	< 20.5 lb DRY
BLOW-OFF COVER (IF COVER USED)	REMOVE-BEFORE-LAUNCH COVER
TELEMETRY OF EMISSION CURRENT AND DIAGNOSTICS	TELEMETRY OF EMISSION CURRENT AND DIAGNOSTICS

Table 2-8.   FMDS System Original Contractual Specifications and Respective Final Design Parameters.

Original Contractual Specs	Delivered Spects
Low-energy plasma within 30s of exceeding a charging threshold	Same except for ESA 16-s and 32-s weep which requires 38s
Analog telemetry outputs between 0.00 and 5.10 V	No analog signals to satellite
Digital commands and telemetry TTL compatible	TTL compatible and optically isolated
All ground returns self contain and isolated by ≥ megohm	Designed to meet - single ground point philosophy
Permanent magnetic fields ≥100 nT at 1 meter in any direction	Designed to meet
Mating connectors to be furnished	Mating connectors furnished
No cadmium-plated connectors or other hardware	No cadmium anywhere
<35 lbs.	<43 lbs. without TPM <47 lbs. with TPM
<10 W with plasma source off	<5.6 W without TPM <14 W with TPM
Power profile to be provided	Power profile measured and provided
High-rel parts for >3 yr life in deep space orbit	Rad-hard Class-B parts
Thermal models to be provided	Analytical thermal models provided
Ground support equipment to be provided - command/ telemetry and power source	Ground support equipment will be provided - command/telemetry, power source, and vacuum pump
EMI: designed to meet MIL-STD-461B and MIL-STD 1541	Designed to meet
Shall meet shuttle safety requirements - NASA handbook 1700.7A, JSE 11123 and JSC 13830	Designed to meet
Acceptance tests to be performed in accordance with MIL-STD-1540A	Designed to meet

17

Table 2-8. Continued.

T9234-8

Contractual Specs	Design

Random Vibration:
  Frequency (Hz)　　　　PSD (g^2/Hz)
  20　　　　　　　　　　0.004
  20-37.5　　　　　　　+12 dB/octave
  37.5-90　　　　　　　0.050
  90-200　　　　　　　+4 dB/octave
  200-700　　　　　　 0.150
  700-2000　　　　　　-4 db/octave
  Composite　　　　　　13.7 g rms
  Duration of 2 min along each of 3 orthogonal axis
	Designed to meet

Sine survey:
  0.5 to 1.0 g
  15 to 100 Hz
  One sweep up and down in each axis at 2 octaves/min
	Designed to meet

Transient shock: 25 g, 11 ms, half-sine pulse along each axis	Designed to meet

Thermal vacuum:
  $\geq 10^{-5}$ Torr
  -24°C to +61°C
  12 h at the low and high temperature levels
	Designed to meet

Thermal cycling:
  Ambient pressure
  -24°C to +61°C
  ≥ 8 cycles with 2 h dwell at low and high temperature,
  transitions at ≥ 3°C/min
	Designed to meet

Burn-in:
  Ambient pressure
  -24°C to +61°C
  ≥ 18 total cycles including those above
	Designed to meet

Depressurization/repressurization:
  Shuttle profile
  JSC 07700 Vol. XIV
  Attachment 1, Rev. G
	Designed to meet

SECTION 3
ELECTROSTATIC ANALYZERS

The FMDS incorporates ESAs to measure the distribution of ion and electron energies which are incident on the spacecraft. The ESAs are important to the FMDS charging-detection function because of the instruments specified for the FMDS, they alone can detect the onset of eclipse charging. (The SPMs respond too slowly when the spacecraft is in darkness.) The data can be analyzed to determine the actual vehicle potential (i.e., frame potential relative to space potential) rather than the dielectric-surface potentials monitored by the SPMs. In addition to these important charging-detection attributes, the ESAs provide valuable scientific information.

The ESAs employed on the FMDS are configured with short-cylindrical-section sensors. Instruments of this type have been used in physics experiments since the turn of the century, and similar devices have been flown on many spacecraft. However, the short-cylindrical-section sensors do present a problem with the ability of the proton (ion) detectors to discriminate against high-energy electrons as discussed in Section 10.2.6. The FMDS instrument incorporates 16 channels and fast sweep-times (4, 8, 16, or 32 s) in order to provide the rapid reaction time that is required in the FMDS mission.

3.1 ESA DESIGN

The ESA design is for 15 energy channels covering the range of 50 eV to 20 keV plus a background channel, making a total of 16 channels. The background channel is included to allow for subtraction of the scattered electron background in the lower energy channels. Table 3-1 lists the energy detection characteristics of the ESA. The following sections describe the design in more detail.

3.1.1 Detection Assembly Design

The basic design of the ESA detection assembly is shown in Figure 3-1. The assembly is similar to several that have been constructed by Panametrics, so it is a proven design with well-known detection characteristics. The unit has been designed for satellite use, and so can withstand the shock, vibration, and other environmental aspects of launch and orbital operations. The major characteristics of the detection assembly are described below.

- The analyzer plates have a narrow seperation, and the surfaces are treated to reduce particle and light scattering. This is important to reduce electron background from the scattering of the intense high-energy (tens of keV) electron fluxes present during spacecraft charging events. The plate design also strongly reduces the intensity of scattered solar UV reaching the CEM detector.

Table 3-1. Energy Detection Characteristics of the ESAs.

CHANNEL NUMBER	ENERGIES IN eV		
	E (LOW)	E (HIGH)	E (AVERAGE)
0	BACKGROUND CHANNEL		
1	50	75	62
2	75	111	93
3	111	166	138
4	166	247	206
5	247	368	308
6	368	549	459
7	549	819	684
8	819	1221	1020
9	1221	1821	1521
10	1821	2714	2267
11	2714	4047	3381
12	4047	6034	5041
13	6034	8997	7516
14	8997	13414	11205
15	13414	20000	16707

GEOMETRIC FACTOR 6×10^{-4} cm^2 – sr (CAN BE MADE SMALLER)

INTRINSIC ENERGY RESOLUTION Δ E (FWHM)/E (AVERAGE) = 39%

14881-12R1

CHANNELTRON
COLLIMATOR
AND 50 V BIAS

CYLINDRICAL PLATE
ANALYZER SECTION

INCIDENT
PARTICLES

CURVED CHANNELTRON
DETECTOR (CEM)

ESA HOUSING AND
ELECTROSTATIC SHIELD
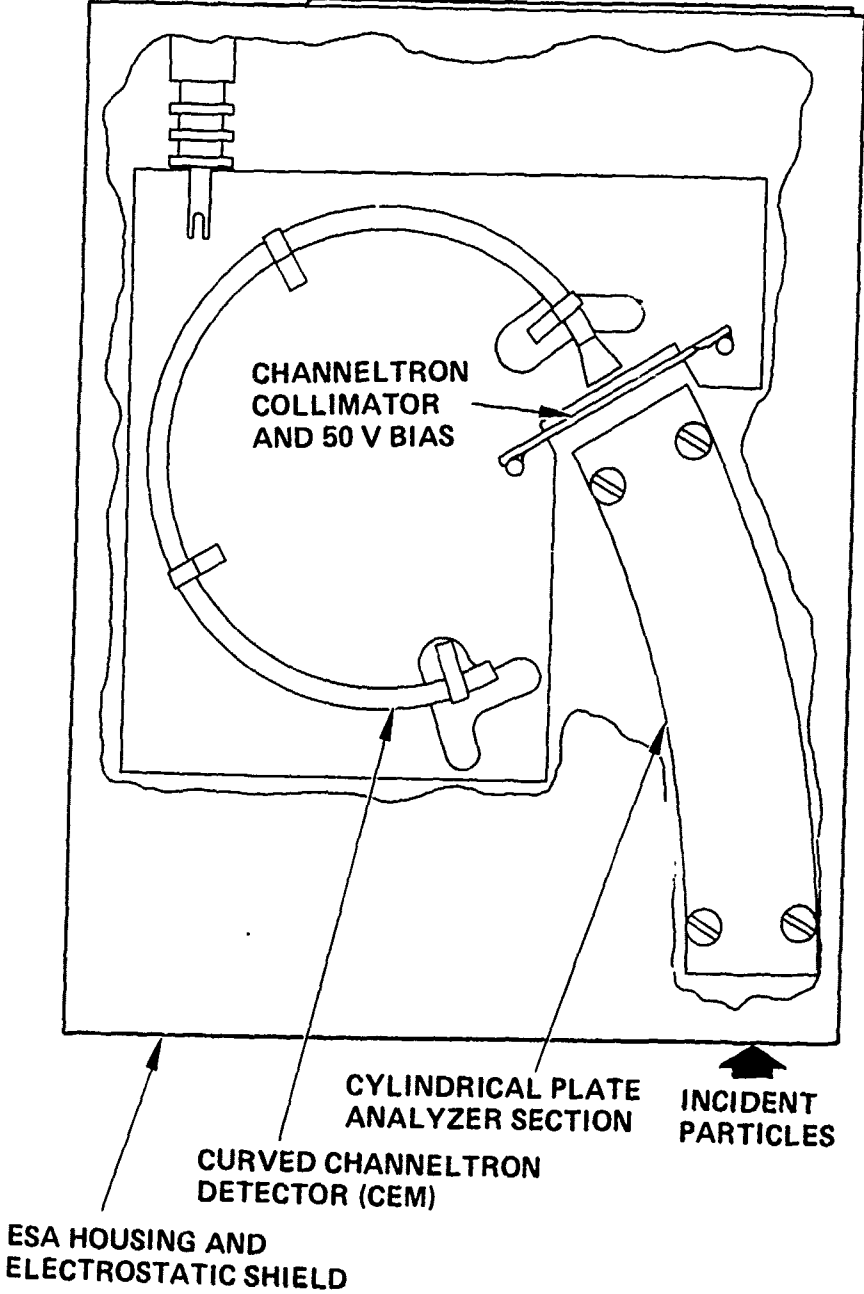
Figure 3-1. Basic design of the electrostatic analyzer detection assembly.

21

- The CEM and associated electronics are mounted on a ceramic circuit board. This reduces the level of organic vapors near the CEM which helps to prolong its life. Since the CEM is the component most likely to degrade, considerable care must be used to minimize organic contamination, which tends to hasten CEM gain degradation.

- The CEM ceramic board is easily replaced so that a CEM that has been degraded during prelaunch testing can be easily replaced.

- The ESA has a geometric factor of approximately 6×10^{-4} cm^2-sr, which is appropriate for geosynchronous orbit applications. The geometry of the detection head is shown in Figure 3-2 where:

$$a_1 = 0.318 \text{ cm}$$
$$b_1 = 2.032 \text{ cm}$$
$$d_1 = 1 \text{ cm}$$
$$a_2 = 0.318 \text{ cm}$$
$$b_2 = 1.016 \text{ cm}$$
$$d_2 = 1 \text{ cm}$$
$$R_1 = 11.008 \text{ cm}$$
$$R_2 = 11.404 \text{ cm}$$
$$s = 0.132 \text{ cm}$$
$$alpha = 28°$$
$$V/2 = 200 \text{ V maximum}$$
$$\text{Geometric Factor} = 6 \times 10^{-4} \text{ cm}^2\text{-sr}$$
$$\text{Energy Resolution} = 39\%.$$

A normalized curve for the detection characteristics of this design is shown in Figure 3-3. Adjacent energy bins are spaced such that their curves overlap from 0 to 2% at FWHM.

The physical design of the complete ESA unit is shown in Figure 3-4. The ESA detection assembly, photodiode, and electronics are all contained in a 4.5 x 6 x 5.5-in. housing. The housing also contains connectors for power and information flow to/from the controller and for access to test points.

3.1.2 Electronics Design

The basic electronics design for the ESA is shown in Figure 3-5, which indicates how the basic required operational characteristics are met. Significant features of the design for ions (electrons) include:

- A +50 V (-50 V) grid in front of the CEM to eliminate ions (electrons) below 50 eV, thus protecting the CEM from the plasma source ions (electrons).

- A CEM aperature biasing of -500 V (+500 V) to increase the detection efficiency for low energy ions (electrons). This voltage is held fixed to avoid efficiency changes with CEM gain-voltage changes.

22
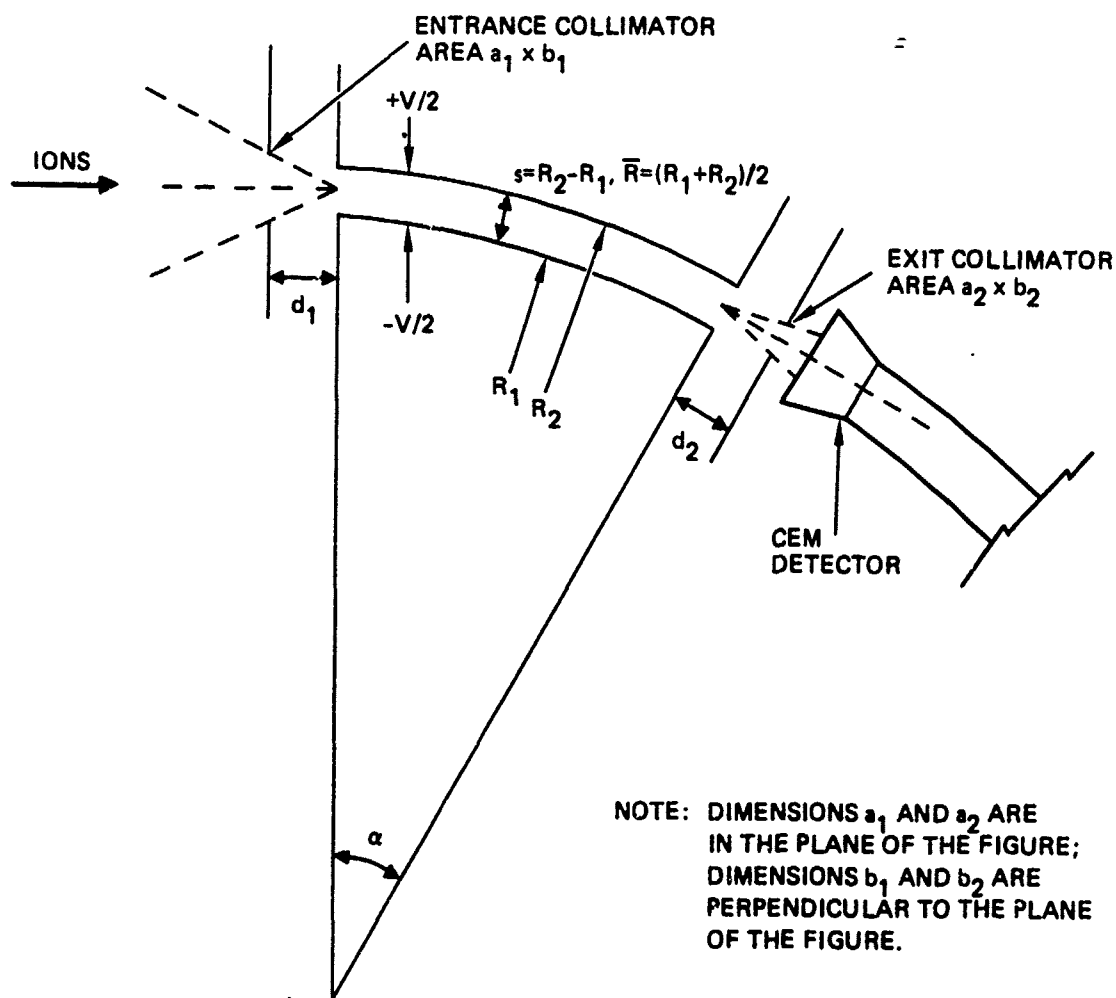
Figure 3-2. Basic geometry of the cylindrical plate electrostatic analyzer.

ENTRANCE COLLIMATOR
AREA $a_1 \times b_1$

IONS

+V/2

$s = R_2 - R_1$, $\bar{R} = (R_1 + R_2)/2$

EXIT COLLIMATOR
AREA $a_2 \times b_2$

d_1

-V/2

R_1 R_2

d_2

CEM
DETECTOR

α

NOTE: DIMENSIONS a_1 AND a_2 ARE
IN THE PLANE OF THE FIGURE;
DIMENSIONS b_1 AND b_2 ARE
PERPENDICULAR TO THE PLANE
OF THE FIGURE.

15816-4
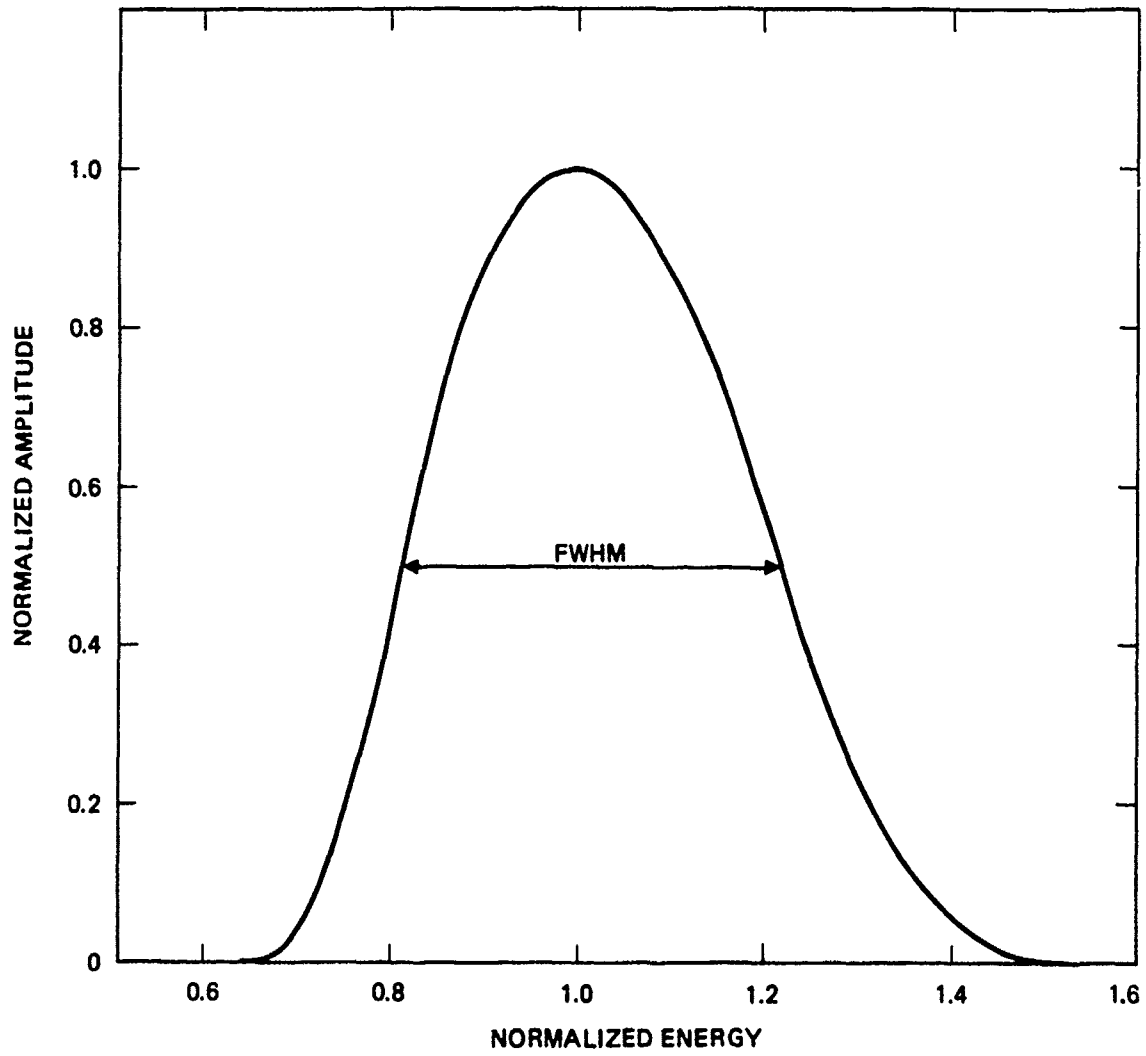
Figure 3-3. Normalized detection characteristic of a single energy bin.

24

Figure 3-4. Physical design of the ESA.
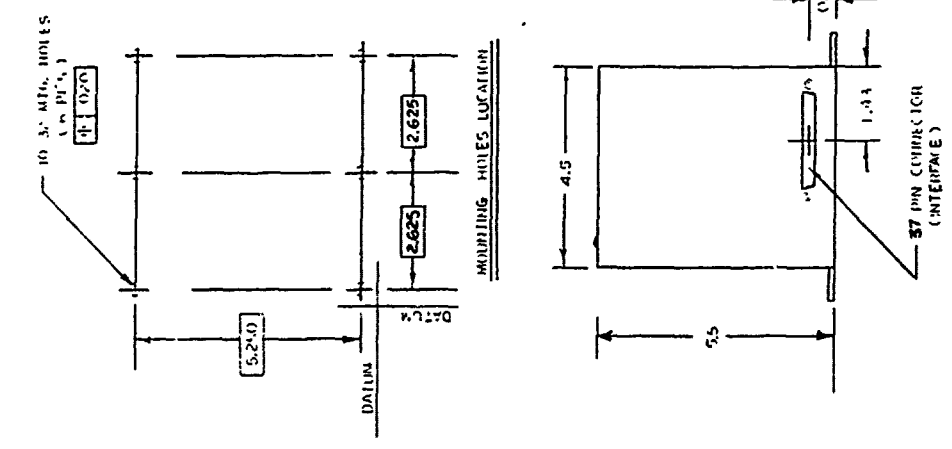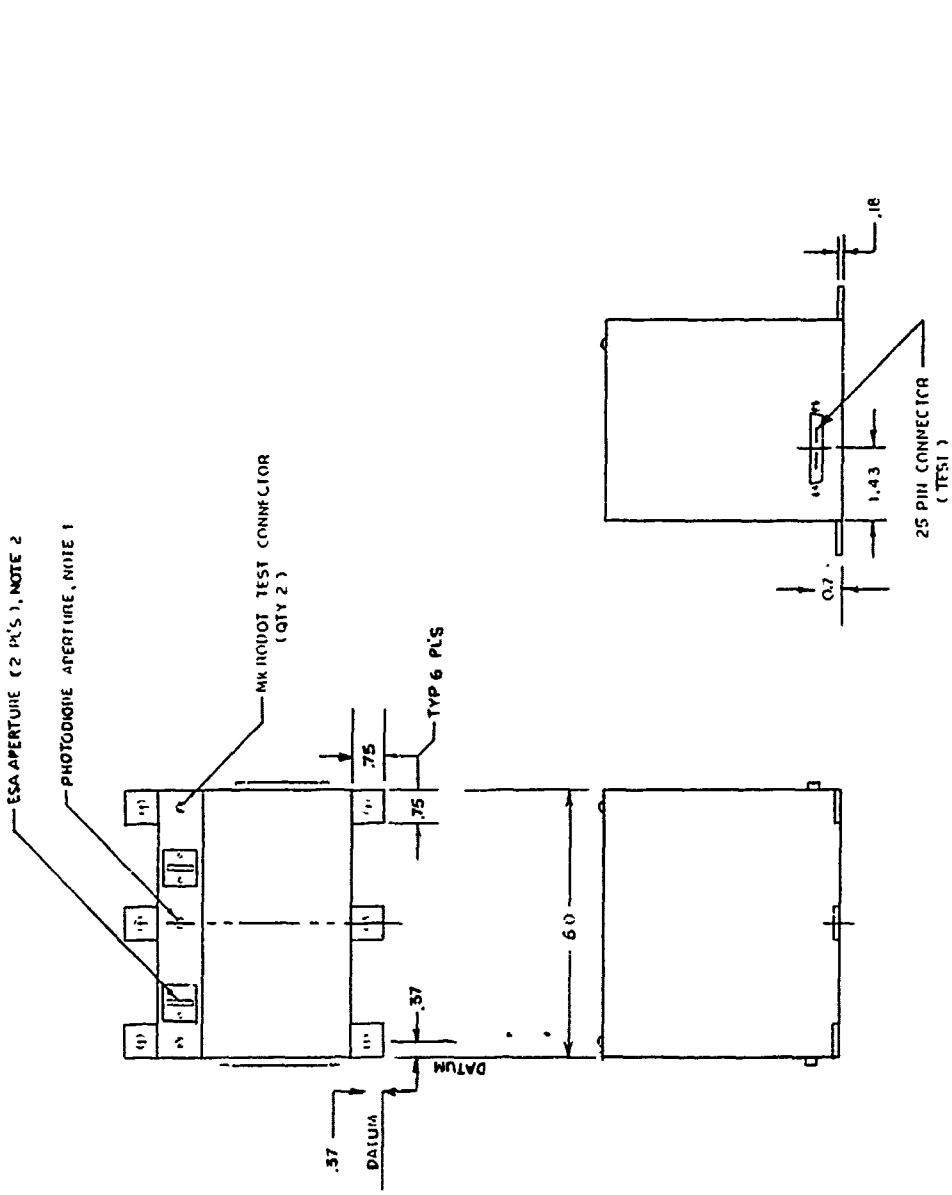
NOTES:
1. PHOTODIODE F.O.V. IS 60° FULL CONE.
2. ESA FOV'S ARE 30° FULL CONE

25

14881–10R1
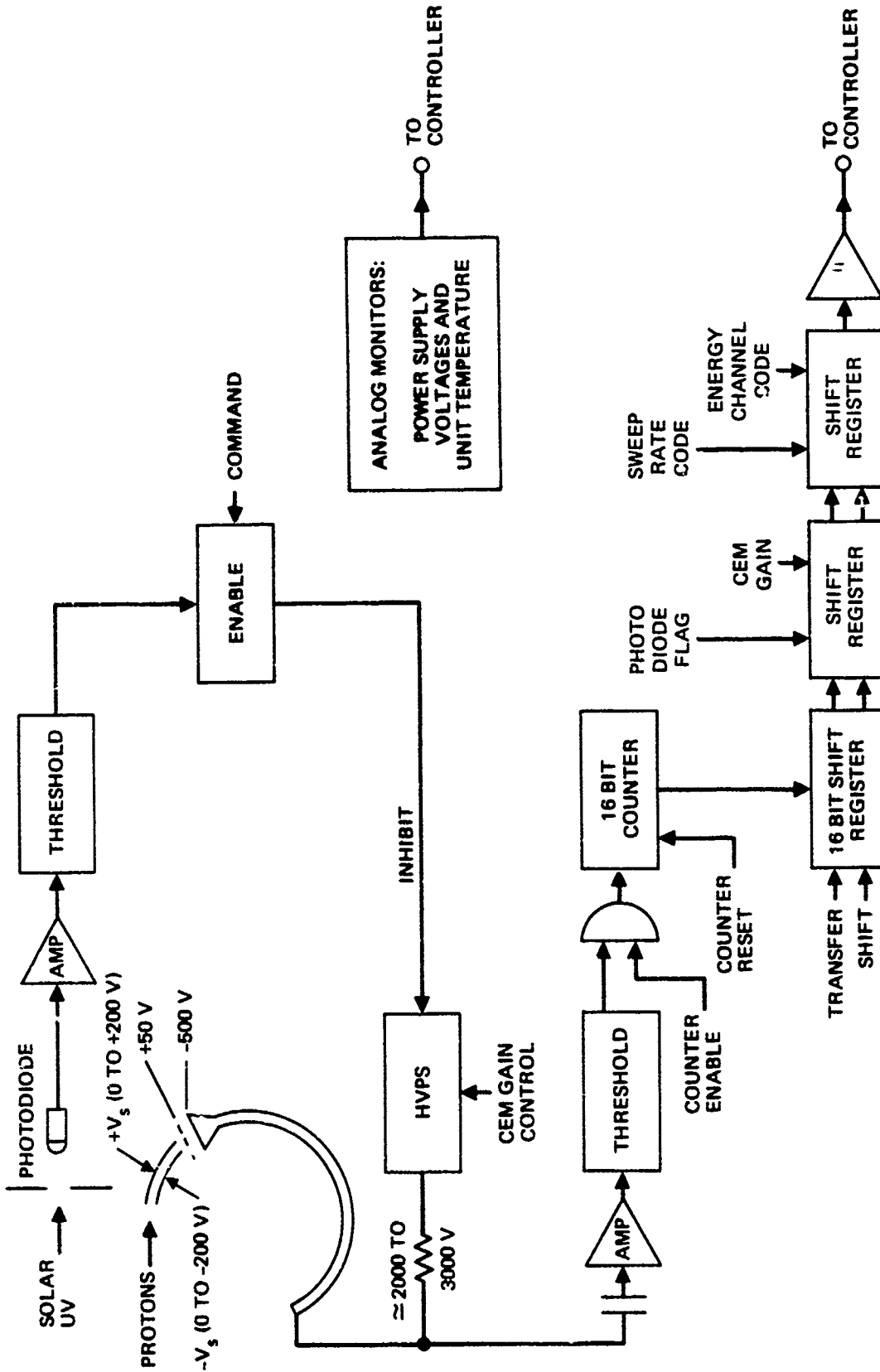
Figure 3-5. Block diagram of the ESA electronics for the ion detection head. Electron
detection of electronics are similar except for the polarity of some voltages.

26

- Adjustable CEM gain by command using a controlled high voltage power supply (HVPS).

- Reducible CEM gain when the unit is turned toward the sun, by means of the photodiode. This operation can be enabled or disabled by command.

- CEM counts which are accumulated in a 16-bit counter (65,535 maximum, after which the counter rolls over). This allows the CEM to operate at 262 kHz for the 4-s accumulation time, and at 32 kHz for the 32-s accumulation time, based on 16 channels.

- The ESA-plate voltage-sweep-control block diagram is shown in Figure 3-6. The control voltage drives a bipolar supply to provide the $+V/2$ and $-V/2$ in Figure 3-2. The ESA design is such that for 20-keV ions or electrons, $\pm V/2 = \pm 200$ V. The sequencing in Figure 3-6 is such that R_1 through R_{16} set up the central energy of each energy channel. The value of R_1 is set so that Channel 0 measures background, with no direct ion (electron) response. The circuitry can be readily set to provide the energy channels of Table 3-1.

The remainder of the electronics design is straightforward digital control circuitry, timing circuitry, power supplies, and interface buffers. The schematics for all of the electronics are presented in Figures 3-7 through 3-12.

3.1.3 CEM Lifetime

Channel Electron Multipliers (CEMs) are typically quoted as having a lifetime in excess of 10^{11} total counts before their gain starts to decrease. However, their lifetime is a strong function of the contaminants they are exposed to, particularly complex hydrocarbons like vacuum pump oil. A typical lifetime curve for a CEM is shown in Figure 3-13. The initial high gain is attributed to the sputtering of contaminants from the CEM surface. Electron avalanches produce ions from the contaminants; these ions produce additional electron avalanches which account for the high gain. As the surface is cleaned by the sputtering process, the gain falls to a minimum value and then increases slighty. This increase in gain is attributed to a further cleaning of the CEM surface. The gain then levels off and remains at this level to greater than 10^{11} counts, provided the CEM environment is and has been free from heavy hydrocarbons. Tests have been performed that show the gain is flat to at least 2×10^{11} counts[1], one test showed 7×10^{12} counts[2].

Assuming a conservative lifetime estimate of 10^{11} counts for the CEM, and a counting rate for ions of about 60 counts/s at GEO with our geometric factor of 6×10^{-4} cm^2-sr; the lifetime of a CEM should be at least 53 years. The estimated electron counting rate is expected to be about 13,300 counts/s, yielding a lifetime of only 0.25 years. Therefore, the entrance aperature of the electron ESA was reduced a factor of approximately 40 using a plate with three small holes to provide a 10 year lifetime.

27
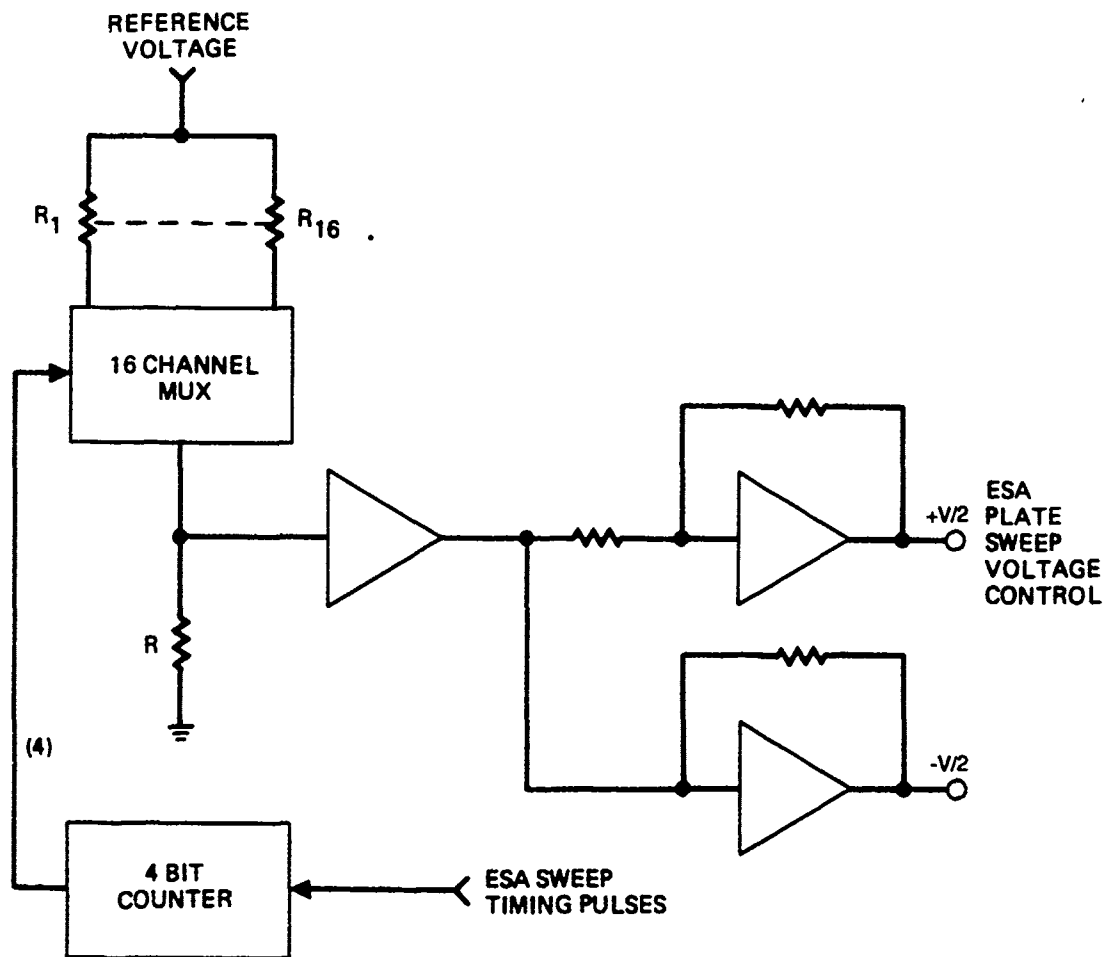
Figure 3-6. Block diagram of the ESA-plate voltage-sweep control.

Figure 3-7. Schematic of the ESA digital control electronics.

Figure 3-8. Schematic of the ESA voltage-sweep generator and ± 500 V dc-to-dc converter.

30
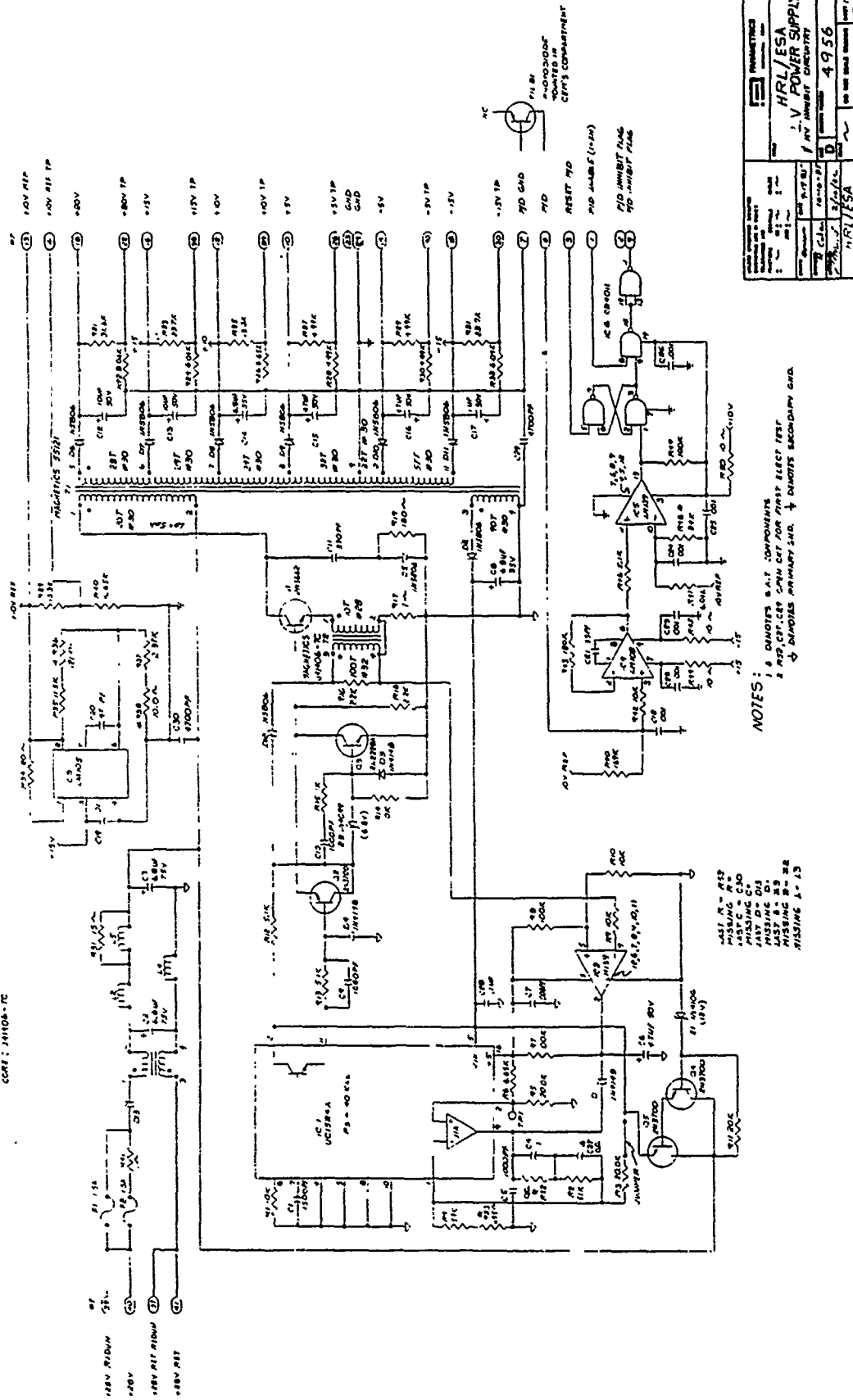
Figure 3.9. Schematic of the ESA low voltage power supply and high voltage inhibit circuitry.
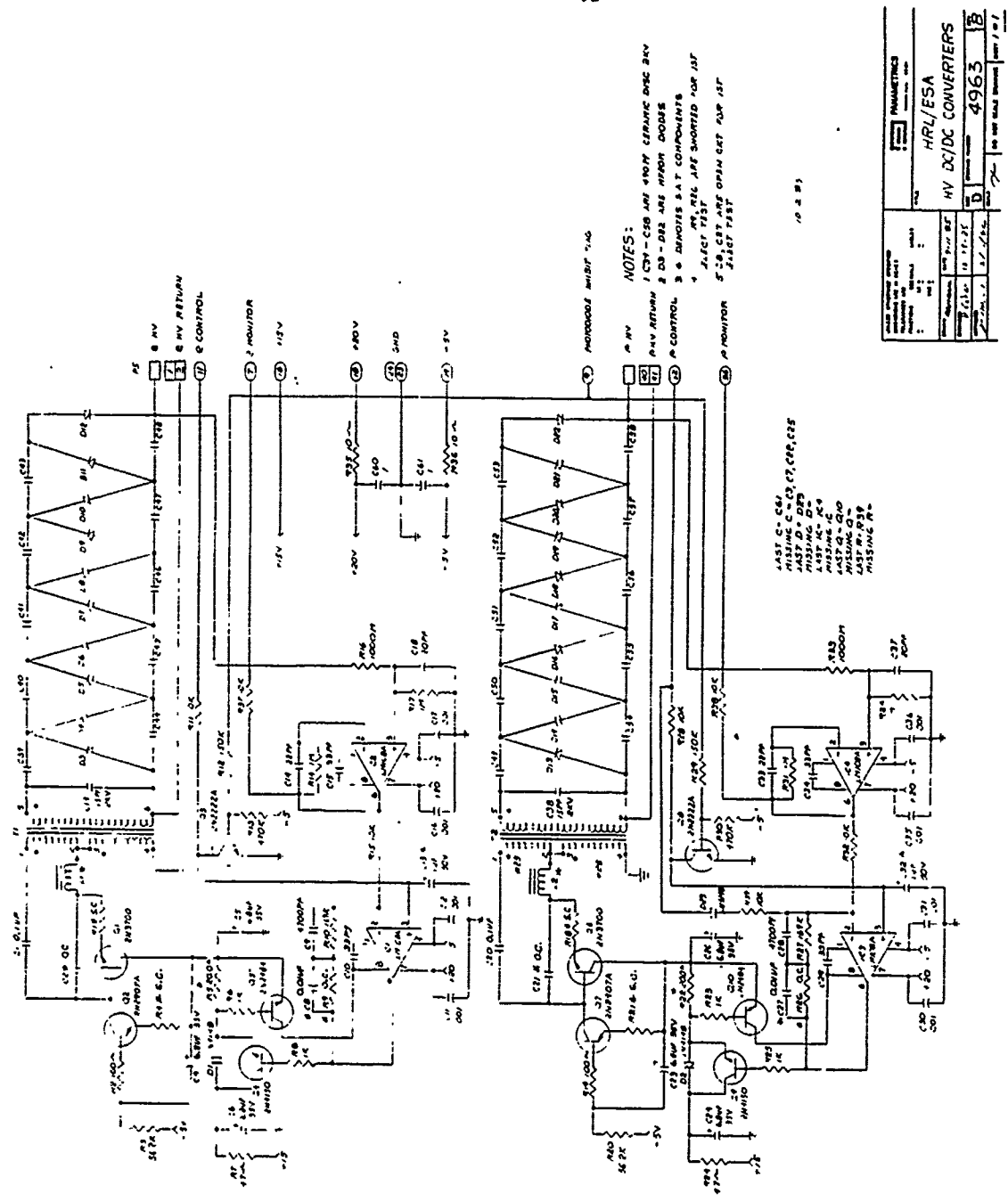
31

Figure 3-10. Schematic of the ESA high voltage dc-to-dc converter.

Figure 3-11. Schematic of the ESA detection circuitry.

Figure 3-12. Interconnection wiring diagram for the ESA.

34
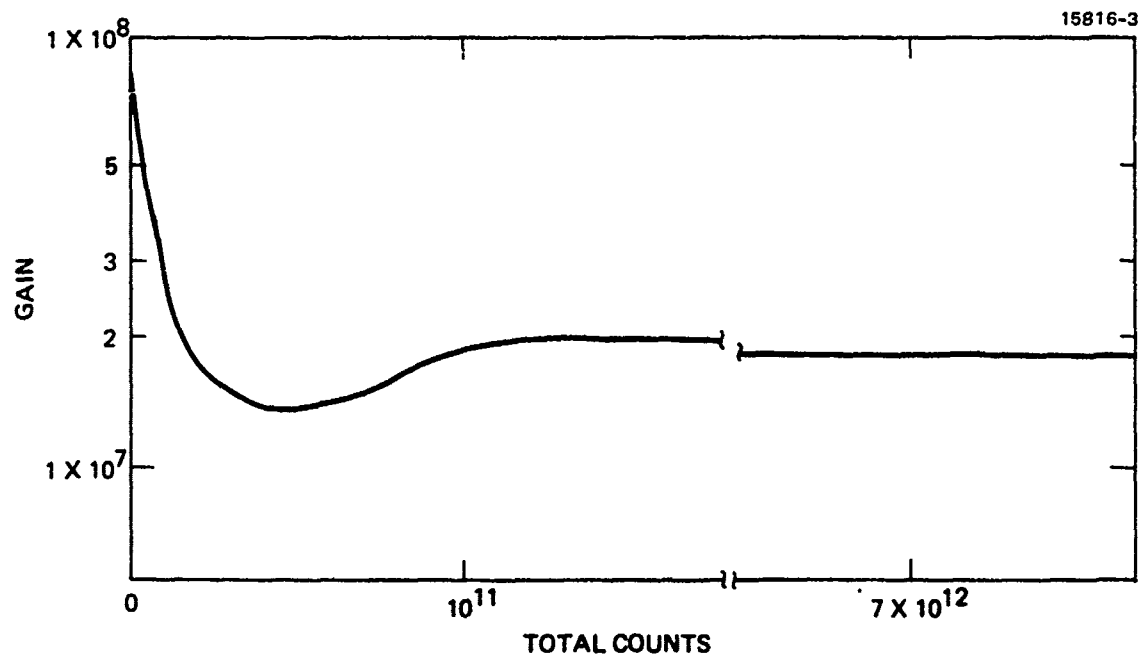
Figure 3-13. Typical gain versus total count curve for a CEM.

A counting rate of 60 counts/s or an average of 15 counts/channel for the minimum sweep time of 4 s is marginal from a statistical standpoint. The ESA 16-s and 32-s sweeps will give an average of 60 and 120 counts/channel/sweep respectively, which are statistically significant.

3.1.4 Commands and Telemetry

The ESA accepts a parallel digital command to set the ion detector CEM bias, the electron detector CEM bias, the sweep time, and to enable or disable the sun sensor. The digital bit patterns for these commands are listed in Table 3-2 and the digital interface is defined in Figure 3-14. The signals are LSTTL and 5-V CMOS compatible.

The ESA provides serial digital telemetry data for the energy channel, the sweep time, the ion detector CEM bias, the electron detector CEM bias, the sun sensor status, the sweep time reset flag, the sun sensor inhibit flag, the data overrun flag, the ion detector count, and the electron detector count. The digital bit patterns associated with this data are shown in Table 3-3 and the serial digital interface is defined in Figure 3-15. The signals are LSTTL and 5-V CMOS compatible.

3.2 BREADBOARD TEST RESULTS

The breadboard instrument fabricated by Panametrics was part of the breadboard demonstration and exhibited its ability to detect both ions and electrons and provide suitable data to the ion-ESA and electron-ESA algorithms. Operation of the ESA was not effected by the presence of the plasma emitted by the plasma source.
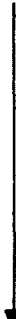
The ion ESA was calibrated at Hughes using a monoenergetic proton beam and a gimbal to vary the direction of the beam relative to the ESA entrance aperature. A typical calibration curve is shown in Figure 3-16. The response curves for several angles are shown, along with the envelope of these response curves, and the theoretical envelope for the instrument. The ratio of the high and low energies at FWHM (1.504) is very close to the theoretical value of 1.491. The center energy of 4.35 kV, however, is approximately 12% lower than the theoretical value of 4.94 kV. This can be corrected by slightly increasing the voltage on the detection plates. All of the energy bins exhibited similar responses except for the low energies (50 eV to 200 eV) where the Earth's magnetic field was effecting the trajectory of the proton beam.

The electron ESA could not be calibrated at Hughes because of the effect of the Earth's magnetic field on the electron beam.

36

Table 3-2. Digitial Bit Patterns for the ESA Commands.

ESA COMMANDS

ION OR ELECTRON CEM BIAS	MSB BIT 2	BIT 1	LSB BIT 0
LOWEST BIAS	0	0	0
	0	0	1
	0	1	0
MONOTONICALLY INCREASING	0	1	1
	1	0	0
	1	0	1
	1	1	0
HIGHEST BIAS	1	1	1

SWEEP TIME (s)	MSB BIT 1	LSB BIT 0
2	0	0
4	0	1
8	1	0
16	1	1

PHOTO DIODE	1 BIT
ENABLED	0
DISABLED	1

NOTE: ALL SIGNALS ARE POSITIVE TRUE ("1").
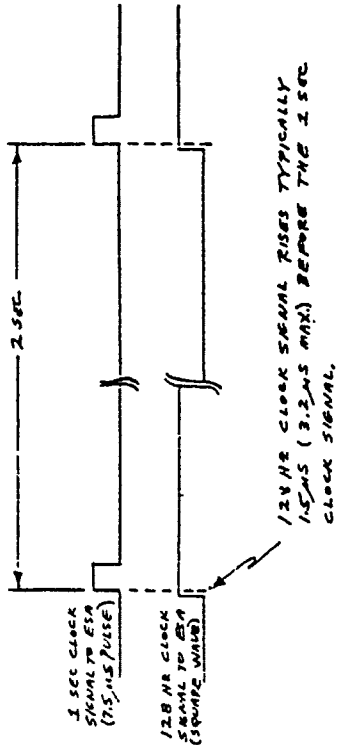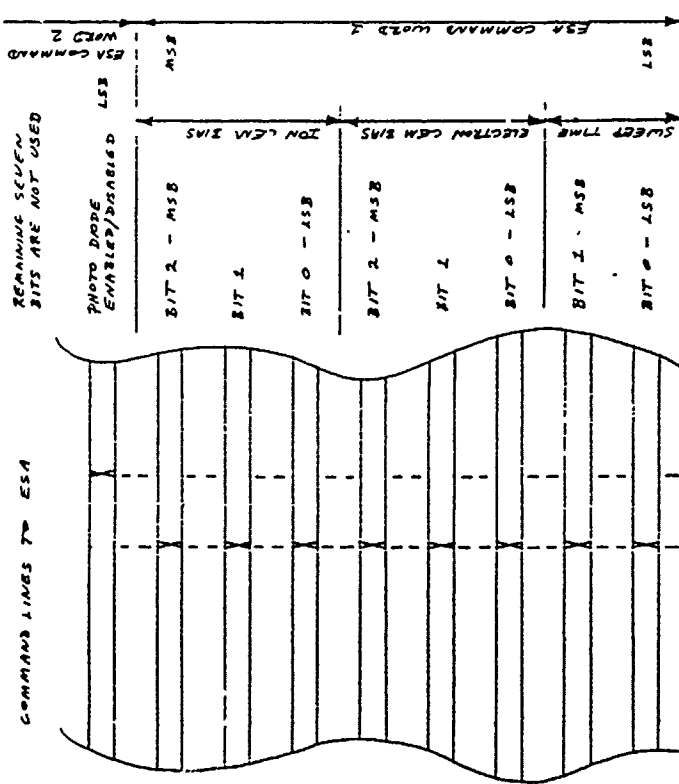
Figure 3-14. ESA digital command interface.

NOTES: (UNLESS OTHERWISE SPECIFIED)

1. COMMANDS ARE LATCHED ON THE CONTROLLER END.
2. ALL SIGNALS ARE POSITIVE TRUE ("1").
3. ALL SIGNALS ARE +5V CMOS COMPATIBLE

HUGHES AIRCRAFT COMPANY
RESEARCH LABORATORIES
MALIBU, CALIFORNIA

ESA COMMAND AND CLOCK SIGNAL INTERFACE

SIZE C   FSCM NO 82577   DWG NO 1099443

SHEET 1 of 1

Table 3-3. ESA Digital Telemetry Bit Patterns.

ESA DATA

ENERGY CHANNEL	MSB BIT 3	BIT 2	BIT 1	LSB BIT 0
0 – LOWEST ENERGY	0	0	0	0
1	0	0	0	1
2	0	0	1	0
3	0	0	1	1
4	0	1	0	0
5	0	1	0	1
6	0	1	1	0
7	0	1	1	1
8	1	0	0	0
9	1	0	0	1
10	1	0	1	0
11	1	0	1	1
12	1	1	0	0
13	1	1	0	1
14	1	1	1	0
15 – HIGHEST ENERGY	1	1	1	1

SWEEP TIME (s)	MSB BIT 1	LSB BIT 0
2	0	0
4	0	1
8	1	0
16	1	1

Table 3-3. Continued.

ESA DATA - CONTINUED

14881—28

ION OR ELECTRON CEM BIAS	MSB BIT 2	BIT 1	LSB BIT 0
LOWEST BIAS	0	0	0
	0	0	.
	0	1	0
	0	1	1
MONOTONICALLY INCREASING	1	0	0
	1	0	1
	1	1	0
HIGHEST BIAS	1	1	1

PHOTO DIODE STATUS	1 BIT
ENABLED	0
DISABLED	1

SWEEP TIME RESET FLAG	1 BIT
NORMAL	0
RESET OCCURRED	1

PHOTO DIODE INHIBIT FLAG	1 BIT
NORMAL	0
INHIBIT OCCURRED	1

Table 3-3. Continued.

ESA DATA — CONT'D

DATA OVERRUN FLAG	1 BIT
NORMAL	0
OVERRUN OCCURRED	1

ION OR ELECTRON COUNT HIGH BYTE	
BIT WEIGHT	BIT
256	0 - LSB
512	1
1,024	2
2,048	3
4,096	4
8,192	5
16,384	6
32,768	7 - MSB

ION OR ELECTRON COUNT LOW BYTE	
BIT WEIGHT	BIT
1	0 - LSB
2	1
4	2
8	3
16	4
32	5
64	6
128	7 - MSB

NOTE: ALL SIGNALS ARE POSITIVE TRUE ("1").

Figure 3-15. ESA digital data interface.

42
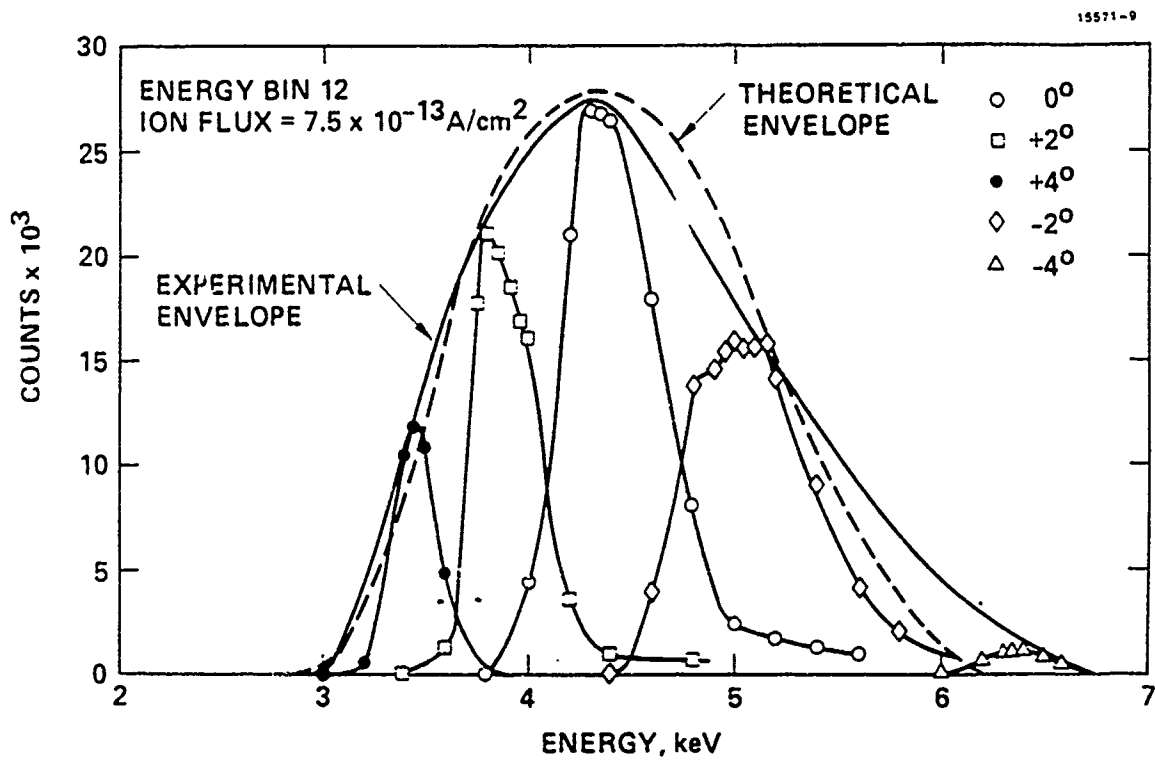
Figure 3-16. Calibration curve for energy bin 12 of the ion ESA.

3.3 FLIGHT INSTRUMENT TESTING (at Panametrics)

The flight units successfully completed their acceptance and environmental qualification tests at Panametrics and were delivered to Hughes. Figure 3-17 is a photograph of unit S/N 001. Figure 3-18 shows the preliminary test sequence and Figure 3-19 the environmental test sequence that was performed on each unit. The second unit (S/N 002) experienced an anomaly early in its testing, where the bias to the CEMs did not turn ON when it should have. Some resistor and capacitor values in the HV dc/dc Converter were changed and the problem did not occur again. These resistor and capacitor values were not changed in S/N 001. With the exception of this one anomaly, both units performed as expected and within predetermined tolerance limits throughout the environmental testing.

A summary of the energy channel nominal counts versus CEM bias (Channel Electron Multiplier bias) for the ion channel of S/N 001 using a H-3 beta source are presented in Table 3-4 and for the electron channel using a Ni-63 beta source are presented in Table 3-5. Nominal count was calculated as the midpoint between the minimum and maximum counts for each energy channel for all of the data taken during testing. Table 3-6 shows the nominal counts normalized to the CEM bias level 0 for the ion channel of S/N 001. The first eight energy channels (0 through 7) have relatively high counts (Table 3-4) and therefore good statistics. The averages of the normalized counts for energy channels 0 through 7 at each CEM bias level are also listed in Table 3-6. These averages are approximately linear with a slowly increasing slope as the bias level increases. These data represent operation within the plateau region of the CEM efficiency curve and below the noise region, which is the criteria for proper operation of the CEM. Similar data showing operation in the plateau region exist for the other three CEMs in the flight units.

Flight unit S/N 001 drew between 1.15 W and 1.49 W and unit S/N 002 between 1.09 W and 1.36 W over the full range of input voltage, temperature, and operating conditions. The measured masses of S/N 001 and S/N 002 are 1.88 kg (4.14 lbs) and 1.87 kg (4.12 lbs) respectively.

3.4 FLIGHT INSTRUMENT TESTING (at Hughes)

The flight instruments were first tested at Hughes under ambient conditions using a pulse generator to inject pulses of known amplitude and repetition rate into the test inputs. The flight controller, software, and harness were used to control the ESA under test. This configuration was used to confirm proper operation of the ESAs (except for the CEMs which do not operate properly under ambient pressure conditions) and to integrate them with the other FMDS hardware and software.
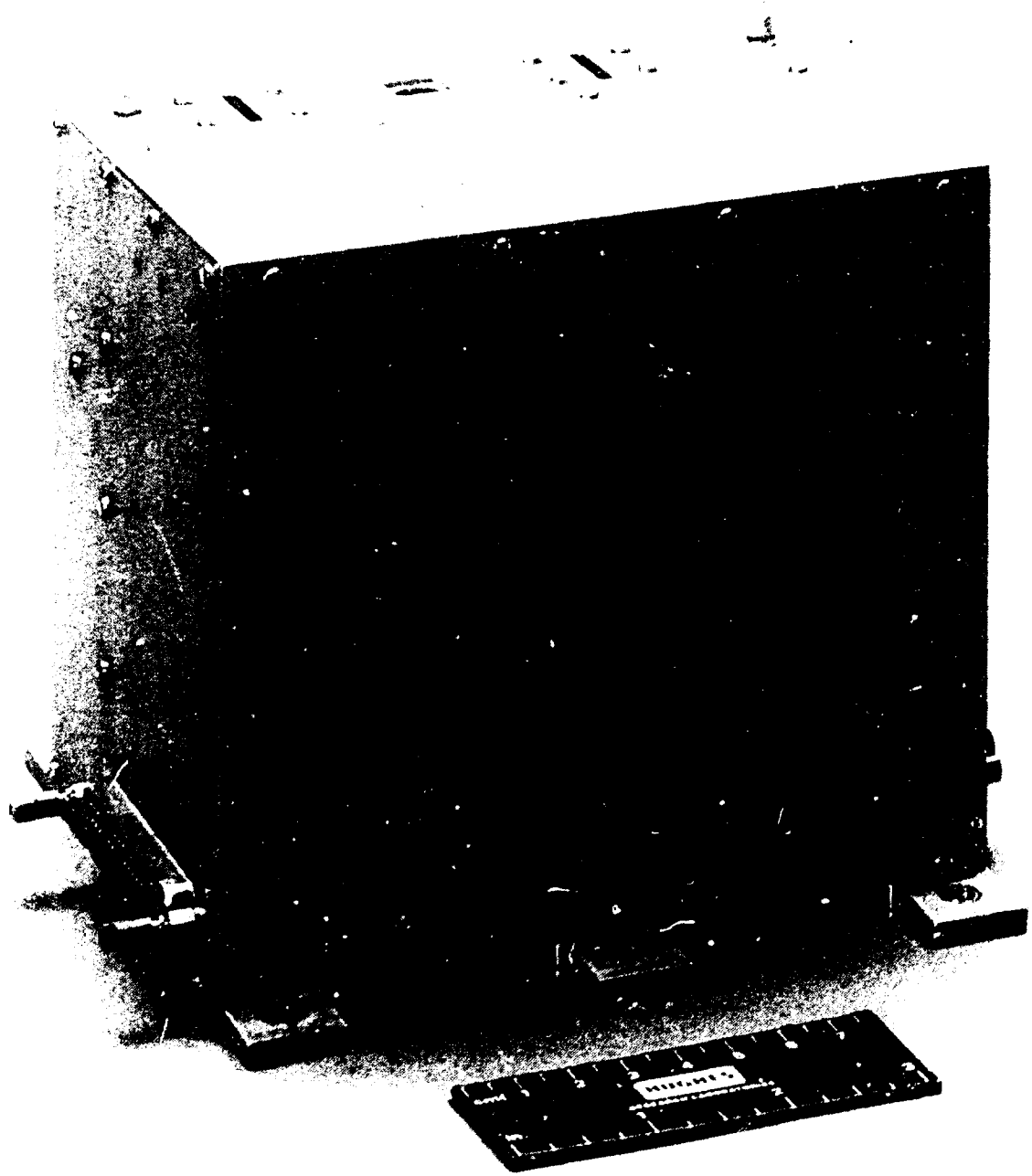
Figure 3-17. Flight ESA S/N 001.
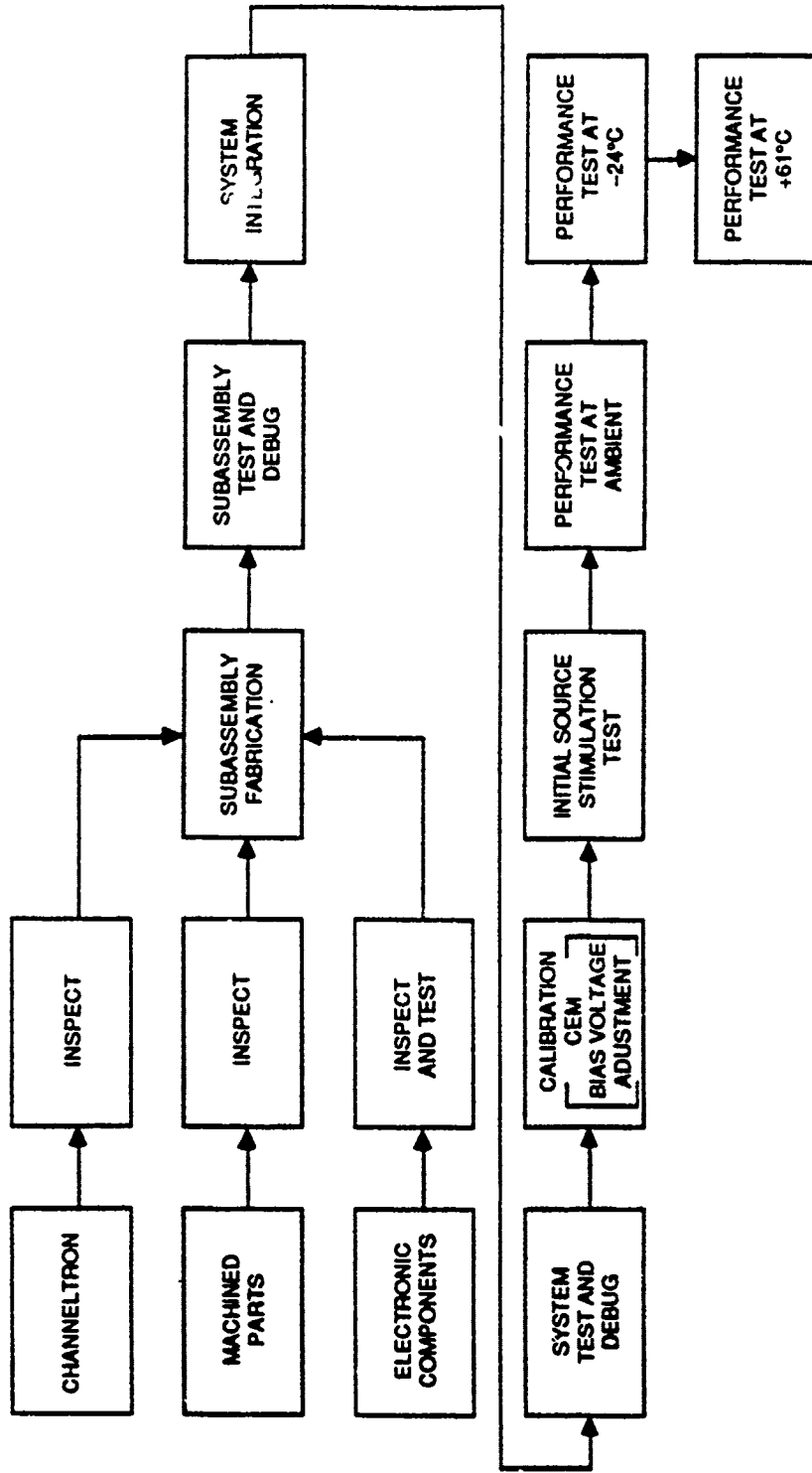
Figure 3-18. Preliminary test sequence.

46

C18296-2

```
┌─────────────────┐
│    BASELINE     │
│  PERFORMANCE    │                              ┌──────────────────────┐
│      TEST       │                         ┌───▶│  PERFORMANCE TEST    │
└─────────────────┘                         │    └──────────────────────┘
         │                                  │               │
         ▼                                  │               ▼
┌─────────────────┐                         │    ┌──────────────────────┐
│    BASELINE     │                         │    │   THERMAL CYCLING    │
│ SOURCE STIMULATION│                       │    │        TEST          │
│      TEST       │                         │    └──────────────────────┘
└─────────────────┘                         │               │
         │                                  │               ▼
         ▼                                  │    ┌──────────────────────┐
┌─────────────────┐                         │    │  PERFORMANCE TEST    │
│   SINE SURVEY   │                         │    └──────────────────────┘
└─────────────────┘                         │               │
         │                                  │               ▼
         ▼                                  │    ┌──────────────────────┐
┌─────────────────┐                         │    │      BURN IN         │
│     RANDOM      │                         │    └──────────────────────┘
│   VIBRATION     │                         │               │
└─────────────────┘                         │               ▼
         │                                  │    ┌──────────────────────┐
         ▼                                  │    │       FINAL          │
┌─────────────────┐                         │    │  PERFORMANCE TEST    │
│   PYRO SHOCK    │                         │    └──────────────────────┘
└─────────────────┘                         │               │
         │                                  │               ▼
         ▼                                  │    ┌──────────────────────┐
┌─────────────────┐                         │    │       FINAL          │
│ POST EXCITATION │                         │    │ SOURCE STIMULATION   │
│  PERFORMANCE    │                         │    │        TEST          │
│      TEST       │                         │    └──────────────────────┘
└─────────────────┘                         │
         │                                  │
         ▼                                  │
┌─────────────────┐                         │
│ THERMAL VACUUM  │─────────────────────────┘
│      TEST       │
└─────────────────┘
```
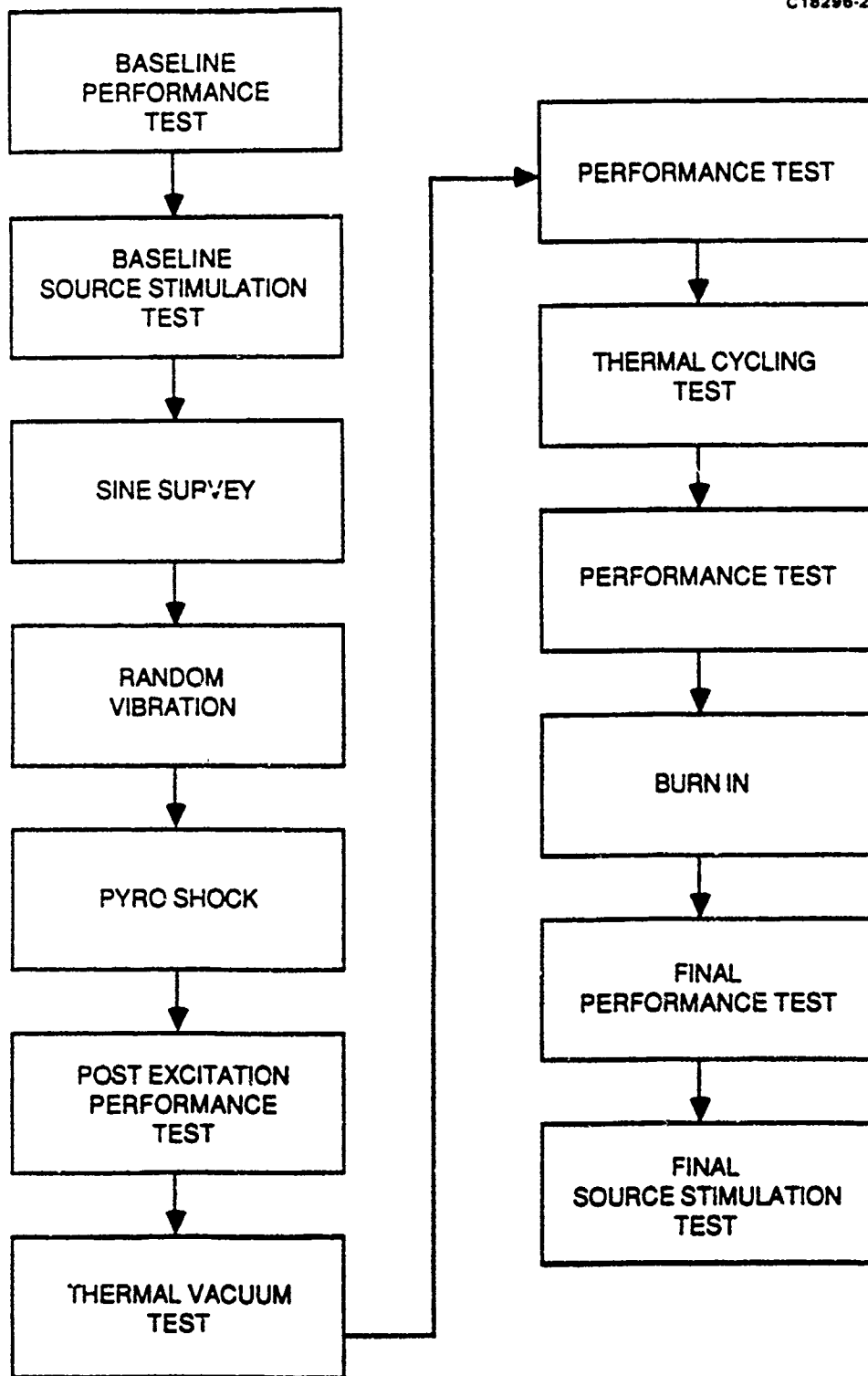
Figure 3-19. Environmental test sequence.

47

Table 3-4. Summary of Bias Voltage vs Energy Channel Nominal Counts for Ion
CEM (S/N001).

Energy Channel	i CEM Bias = 0	i CEM Bias = 1	i CEM Bias = 2	i CEM Bias = 3	i CEM Bias = 4	i CEM Bias = 5	i CEM Bias = 6	i CEM Bias = 7
0	64	78	83	77	95	107	110	125
1	56	66	79	71	88	95	120	135
2	69	62	86	89	95	91	125	132
3	63	72	69	86	86	111	108	119
4	65	63	77	86	77	112	101	117
5	59	62	66	80	79	96	105	130
6	56	66	73	83	74	83	97	101
7	59	62	69	68	77	57	99	105
8	42	55	60	64	78	75	84	106
9	44	47	53	57	63	67	79	89
10	36	39	43	42	57	54	76	75
11	31	34	43	43	45	49	62	56
12	17	18	26	23	34	31	41	37
13	10	14	22	13	24	17	23	28
14	7	7	9	8	6	6	10	12
15	3	4	3	4	2	4	6	5

Table 3-5. Summary of Bias Voltage vs Energy Channel Nominal Counts for Electron CEM (S/N001).

Energy Channel	e CEM Bias = 0	e CEM Bias = 1	e CEM Bias = 2	e CEM Bias = 3	e CEM Bias = 4	e CEM Bias = 5	e CEM Bias = 6	e CEM Bias = 7
0	76	88	94	86	112	125	144	135
1	84	90	92	96	117	133	139	135
2	73	91	87	101	107	103	140	135
3	92	89	94	107	109	122	144	156
4	87	95	96	114	115	145	142	137
5	92	90	101	103	119	130	148	142
6	87	91	99	99	125	126	156	147
7	95	103	119	110	131	128	156	165
8	96	106	119	115	126	149	167	179
9	108	124	121	133	144	151	180	208
10	143	136	155	162	172	183	204	228
11	159	172	176	201	216	254	242	288
12	231	212	252	256	274	308	348	360
13	290	313	318	371	386	391	462	495
14	337	394	395	456	478	534	571	599
15	402	436	497	529	574	614	659	750

Table 3-6. Nominal Counts Normalized to Ion CEM Bias = 0 (S/N001).

Energy Channel	i CEM Bias = 0	i CEM Bias = 1	i CEM Bias = 2	i CEM Bias = 3	i CEM Bias = 4	i CEM Bias = 5	i CEM Bias = 6	i CEM Bias = 7
0	1.00	1.22	1.30	1.20	1.48	1.67	1.71	1.95
1	1.00	1.18	1.42	1.28	1.58	1.701	2.15	2.42
2	1.00	0.91	1.25	1.29	1.39	1.32	1.82	1.93
3	1.00	1.13	1.10	1.36	1.37	1.75	1.71	1.89
4	1.00	0.97	1.18	1.32	1.18	1.72	1.55	1.79
5	1.00	1.05	1.11	1.36	1.33	1.62	1.78	2.19
6	1.00	1.19	1.31	1.50	1.33	1.49	1.74	1.82
7	1.00	1.04	1.17	1.14	1.30	1.47	1.67	1.77
8	1.00	1.30	1.42	1.51	1.85	1.77	2.00	2.52
9	1.00	1.07	1.19	1.28	1.43	1.52	1.78	2.01
10	1.00	1.07	1.18	1.15	1.57	1.50	2.11	2.07
11	1.00	1.11	1.41	1.41	1.46	1.61	2.02	1.82
12	1.00	1.06	1.55	1.36	2.06	1.85	2.45	2.24
13	1.00	1.40	2.20	1.30	2.35	1.70	2.25	2.75
14	1.00	1.00	1.29	1.14	0.86	0.86	1.36	1.64
15	1.00	1.40	1.20	1.60	0.80	1.40	2.20	2.00
Sum 0 - 7	1.00	1.08	1.23	1.30	1.37	1.59	1.76	2.02

50

The ESAs operated as expected and required only a couple of minor modifications to the software to correct a timing problem. However, when the plasma source power supplies were turned ON, large numbers of counts appeared in the output telemetry for the ion and/or electron channel that were not related to the pulse generator connected to the test input. These extra counts would go away if the ESA chassis was isolated (capacitively as well as resistively) from the system mounting plate. The problem was identified as conducted EMI on the cable and/or signal wires in the system harness causing the capacitance between the ESA chassis and the ESA electronic circuitry to introduce the extra counts at some point in the electronic circuitry. When the ESA chassis was isolated from the system mounting plate, the chassis would float up and down with the electronic circitry and not introduce the extra counts. The easiest way (and the only one found to be effective over a wide range of operating conditions) to eliminate the problem was to bypass (with a capacitor) to the ESA chassis each wire connected to the ESA. This was accomplished at the mating connector of the harness with the ESA.

The ability of the ESA to detect ions and electrons could only be performed under vacuum conditions and was performed as part of the system testing discussed in Section 10.

SECTION 4
SURFACE POTENTIAL MONITORS (SPMs)

Two Surface Potential Monitors (SPMs) are included as part of the FMDS to detect the charging of dielectric surfaces on the satellite. Because two different dielectric materials are to be used in flight, and because it is desirable to have them physically seperated (to minimize their effect on each other), the best approach was to use two instruments, with the only difference being the dielectric material (see Figure 2-2).

4.1 BASIC SPM DESIGN

In designing the SPMs, one of the main factors is that the charge buildup on the dielectric material is not altered because of the measurement. This dictates the use of some type of essentially infinite-impedance electric-field-sensing device.

Most electrostatic voltmeters with sufficient accuracy and resolution use a field-sensing probe that is closed-loop controlled to the same potential as the surface being measured. In this way, the field sensor has only to detect a null. To use this approach in this application, a "servo-amplifier" with an output of ±20 kV would be required; this is not practical within the weight and power limitations for this instrument. We have chosen, therefore, to use the approach that was adopted by NASA's Lewis Research Center for their surface-voltage sensor (SVS).[3] NASA's approach retains most of the advantages of a feedback sensing system, yet does not require high voltage. This system uses a combination of electrodes that attenuate the field produced by the sensing surface, and allows it to be nulled with a low-voltage (<±10-V) feedback signal.

We have slightly modified the specifications for the SPMs from those called out in the original RFQ issued by AFGL. The RFQ called for measurement over a range of 100 V to 20 kV and determination of polarity. If 8-bit digital data are used, then the resolution for a 20-kV full scale range is 78 V, which is rather course when looking for surface potentials of 200 V. Therefore, we are using a dual range instrument with nominal ranges of 0 to ±2 kV and 0 to ±20 kV. These ranges provide a resolution of 16 V and measure potentials to ±20 kV.

4.2 SPM SENSOR HEAD DESIGN

Since the SPMs will be required to survive vibration and shock experienced during launch, an ideal design would be all solid state; i.e., no moving parts as are present in a tuning fork. Therefore, several potentially feasible design principles were investigated such as modulation of a light beam within a fiber-optic bundle by the E-field and semiconductor-conductivity modulation by the E-field similar to the operation of field effect transistors. However, these ideas would have required considerable development and testing to achieve the level of flight readiness required by

52

the FMDS program. We therefore decided to utilize the most mature technology available at this time: the NASA LeRC vibrating electrode approach.

The functional operation of this approach is best understood with reference to Figure 4-1. If the dielectric surface is covered by a surface charge (represented in Figure 4-1(a) as negative), then the dielectric surface will assume some voltage, V_S, as indicated in Figure 4-1(b). The electric field associated with voltage V_S penetrates the entrance aperture of the electrically grounded sensor head such that the value of the field drops off precipitously within the sensor head. If we assume (for the sake of explanation) that the feedback-aperture plate is grounded (i.e., $V_A = 0$), the electric potential along the centerline of the sensor head would vary according to the curve marked "feedback aperture grounded."

In actual operation, however, the feedback-aperture plate is not grounded, but is set at a chosen potential, V_A. If we instead imagine that the dielectric surface is grounded (i.e., $V_S = 0$), the electric potential along the centerline of the sensor head would vary according to the curve marked "dielectric surface grounded." In practice the potential varies as the net potential curve which is influenced both by the potential on the dielectric surface and by the potential on the aperture plate. The associated electronics varies V_A in a manner that maintains the potential and the electric field at the signal sensor plate location equal to zero.

A cross section of the breadboard sensing head is shown in Figure 4-2. The input electrode with the dielectric material on its surface (a and b) is insulated from the rest of the instrument by a ring of G-10 glass epoxy. No electrical connection is made to this electrode. The potential of the front surface of the dielectric is transferred to the input electrode by capacitive coupling. Therefore, if the input electrode is to closely track the dielectric front surface, the capacitance from the input electrode to ground must be much smaller than the capacitance between the dielectric front surface and the input electrode. Creepage paths must also be kept long to support the 20 kV that may appear on the input electrode without bleeding the charge from it.

Sensing of the field is done using a vibrating electrode (g) driven by a tuning fork. Above the sensing electrode are two compensating electrodes (d and e) with holes of appropriate size for controlled penetration of the electrostatic field created by the charge on the collector plate. As it vibrates, the sensing electrode generates a displacement current that is proportional to the net field and at the vibration frequency. The phase of this signal is determined by the polarity of the net field. The field at the sensing electrode is nulled to zero by driving the first compensating electrode (d) for the low range or both compensating electrodes (d and e) for the high range to a voltage inversely proportional to that producing the field. By proper selection of the geometry, particularly the hole sizes in the compensating electrodes, the electrostatic field created by the charge on the collector plate can be tailored to permit nulling the maximum field with a maximum of 10 V applied to the compensating electrode(s).

13006—41R3

DIELECTRIC

PIEZOELECTRIC FORK-
DRIVE ELEMENT

NEGATIVE
SURFACE
CHARGE

V_A

FORK-
DRIVE
OSCILLATOR

₵

CENTERLINE
POTENTIAL,
V(X)
(cf. b, BELOW)

SIGNAL
SENSOR
PLATE

TUNING
FORK

FEEDBACK
APERTURE
PLATE

GROUNDED
ENCLOSURE

CENTERLINE POTENTIAL, V(X), V

DIELECTRIC SURFACE GROUNDED

O

X

FEEDBACK APERTURE
GROUNDED

NET
POTENTIAL

V_S
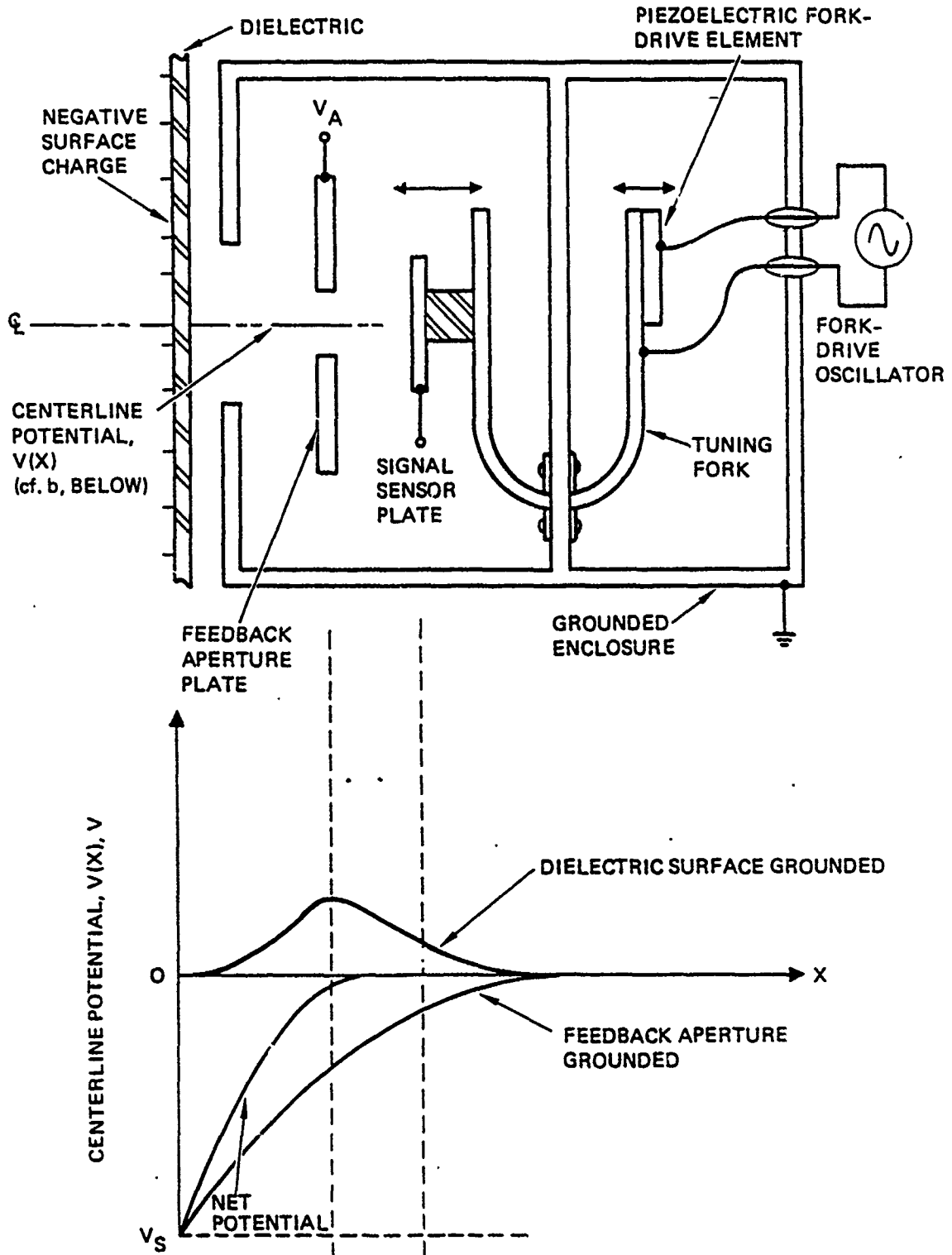
Figure 4-1. Functional operation of the vibrating electrode surface potential monitor.

54

14881-8
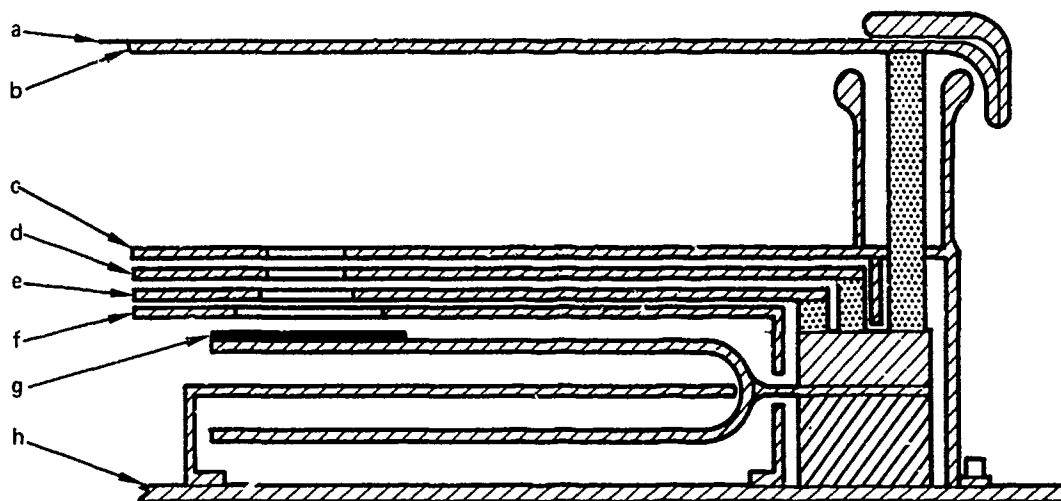
a = DIELECTRIC SAMPLE
b = INPUT ELECTRODE
c = GROUNDED SHIELD
d = 1ST COMPENSATING ELECTRODE
e = 2ND COMPENSATING ELECTRODE
    (GROUND FOR LOW RANGE)
f = GROUNDED SHIELD
g = SENSING ELECTRODE (BONDED TO TUNING FORK)
h = GROUNDED MOUNTING PLATE

Figure 4-2. Schematic cross section of the breadboard SPM sensor head design (not to scale).

To provide compensating-voltage multiplication factors of 200 in the low range and 2,000 in the high range, typical values of the crucial parameters (aperture/electrode diameter d and separation s) for this design are as follows (see Figure 4-2 for notation): d(c) = 8.4 mm, d(d) = 8.7 mm, d(e) = 11.9 mm, d(f) = 20 mm, d(g) = 22 mm, and s(b-d) = 27.6 mm.

4.3 BREADBOARD TEST RESULTS

The initial design of the breadboard SPM hardware was an open type of construction where the tuning fork and compensating electrodes were open to the environment. Vacuum chamber tests of this design showed a large and rapid zero shift whenever the electron gun, proton gun, or plasma source was operated. This zero shift would then gradually disappear over a period of hours provided that none of the charged particle sources were operated. This zero drift was attributed to the buildup of charged particles within the sensing head.

The sensing head was redesigned such that the tuning fork and attenuation plates are completely enclosed. Any openings in the sensing head are smaller than the Debye length of the highest density plasma environment expected. This design did not experience the zero drift described above. However, when it was operated in the configuration shown in Figure 4-3a, the output of the SPM reached a plateau above which it would not go as shown in Figure 4-4. This was attributed to scattered or secondary particles impinging on the input electrode, causing secondary emission, and preventing the electrode potential from increasing above the plateau value (even though the Kapton dielectric front surface was above the plateau value). The configuration in Figure 4-3b did not experience this problem since scattered or secondary particles or local plasma cannot get to the input electrode.

On separate occasions, the SPM was exposed to a monoenergetic electron beam with two types of material on its input electrode; gold and Kapton. As is typical, the gold did not start to charge until the energy of the electron beam was between -9 and -10 keV (Figure 4-4); it linearly increased with increasing energy thereafter. The Kapton started to charge when the electron energy reached -1.1 keV and then linearly increased with increasing energy. Activation of the plasma source returned the Kapton surface to near zero potential with the electron beam ON or OFF. The plasma source was not available at the time the gold surface was tested; however, other tests have shown that a plasma source will discharge a gold surface.

4.4 FLIGHT SPM SENSING HEAD DESIGN

The flight SPM has been designed to simulate the configuration of Figure 4-3b since this is the only configuration that responded properly under all of the conditions tested. Figure 4-5 shows the flight design where the input electrode is now supported by an annular insulating ring from the side rather than from below as in the breadboard design. This allows the dielectric sample

56

15816-2
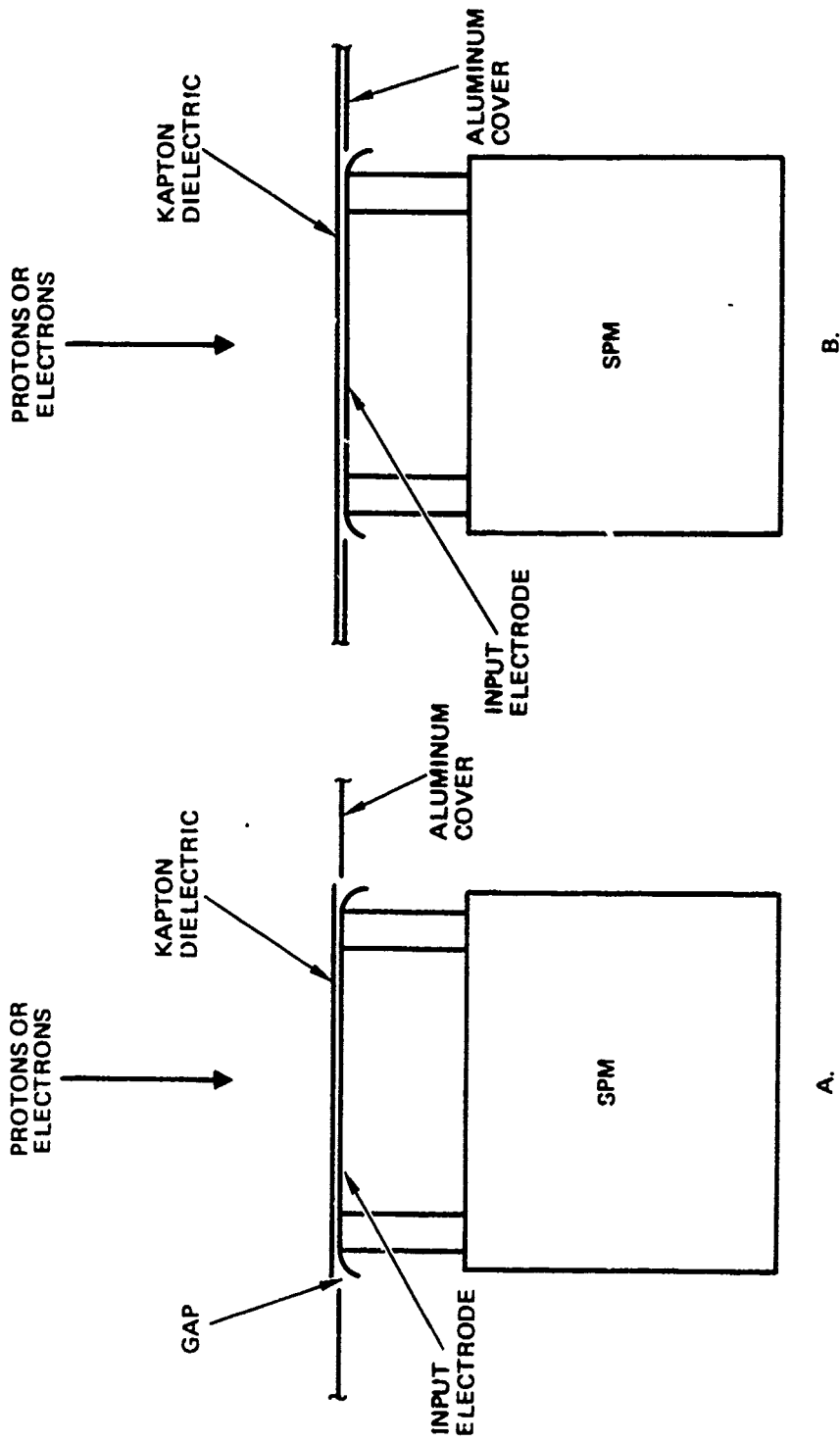
Figure 4-3. Test configurations for the breadboard SPM.

57
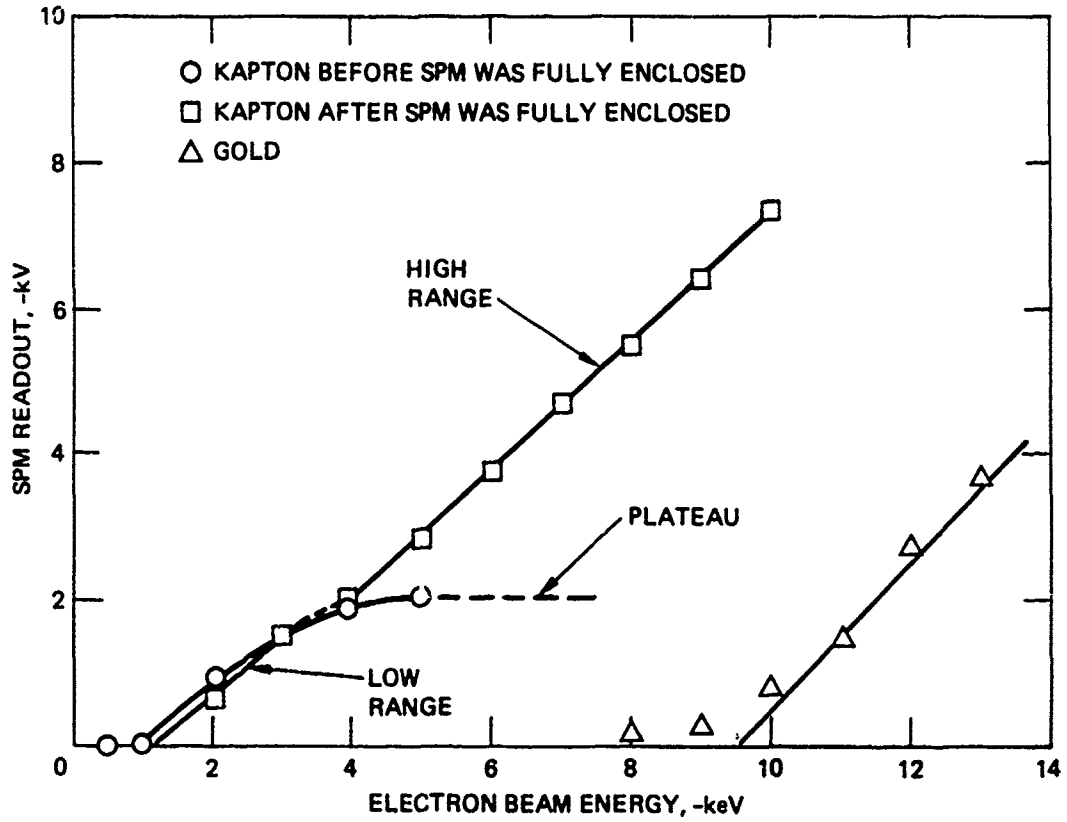
Figure 4-4. Calibration data for the breadboard SPM.
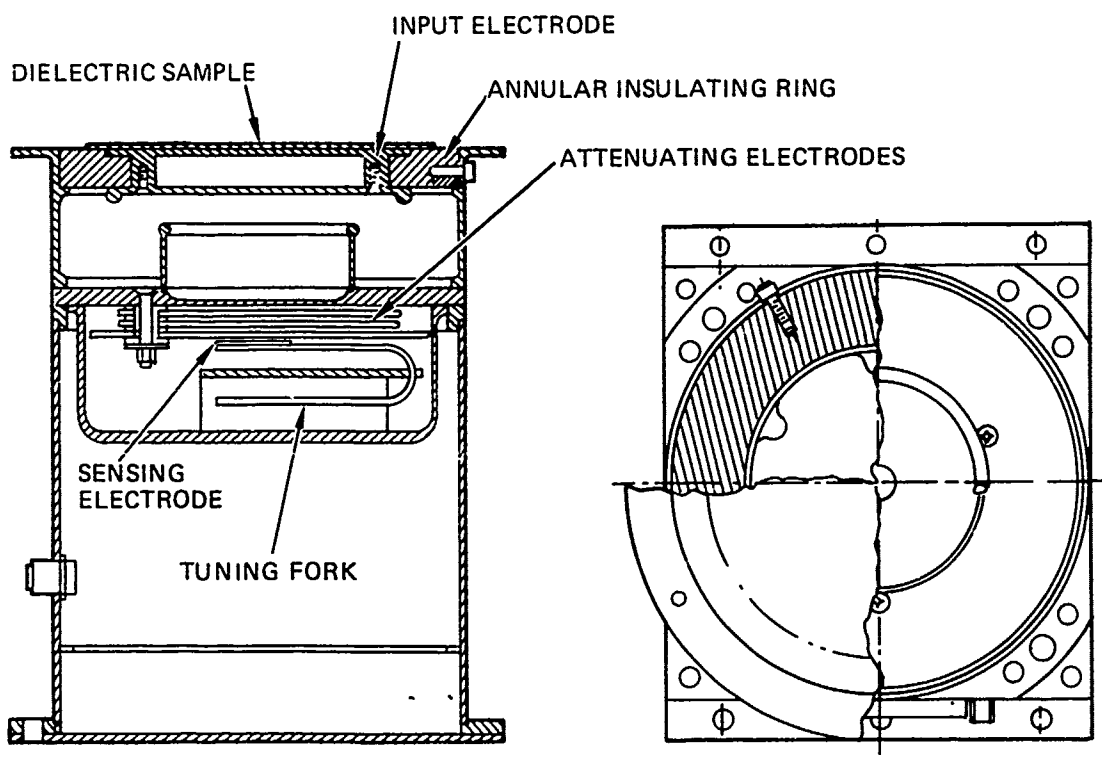
Figure 4-5. Flight package design for the SPM.

to extend past the input electrode onto the annular insulating ring, thereby shielding it from any particles or plasma in the immediate area. The compensating electrodes and tuning fork are mounted in a manner similar to the breadboard and the electronics are contained on two printed circuit cards mounted in the lower portion of the housing.

The SPMs are designed in a manner that allows the front-surface material to be changed. This change is accomplished by replacing the annular insulating ring, input electrode, and front surface material as an assembly. The selection of front surface materials includes but is not limited to VDA backed Kapton, Kapton with conductive black paint, Kapton with white paint, solar cells, second-surfac_ radiator mirrors, and a floating conductor (e.g., germanium).

A possible problem with the SPM is the input electrode gathering some charge not related to the potential of the dielectric front surface. This charge would then introduce a zero offset into the SPM. The breadboard design called for a shorting relay and software routine that would connect the input electrode to ground when the SPM was in full sunlight. Under full sunlight conditions the dielectric front surface should be within 100 V of ground, and therefore, the SPM would be zeroed to within 100 V. This scheme required that the spacecraft periodically rotate the SPMs into full sunlight. This requirement and the need for a small lightweight 20-kV relay turned out to be significant engineering problems.

The flight design deletes the relay and uses a 2-h time constant (RC network) to discharge the input electrode. A 2-h time constant requires approximately 10^{13} ohms from the input electrode to ground; this could conceivably be provided by the leakage of the annular insulating ring. A normal operating scenario has differential charging, which will immediately charge the front surface of the dielectric, and the input electrode will go to the same potential. The 2-h time constant will start to bleed the charge from the input electrode; however, differential charging normally occurs in minutes, and if it is of any significant level, the plasma source will be turned ON. The plasma source will immediately remove the charge from the front surface of the dielectric and return it to ground. The 2-h time constant will then reset the input electrode to ground. The problem with this approach is that very slow (compared to 2-h) differential charging will not be detected by the SPMs.

We tried using Vespel for the annular insulating ring and tested it in a vacuum chamber under simulated operating conditions. Vespel demonstrated an acceptable initial time constant; however, the input electrode decayed toward a voltage level that was in the range of 25 to 90% of the voltage originally applied to the input electrode -- the level depending on the length of time the voltage was applied before allowing the input electrode to start decaying. The input electrode appeared to decay with a much longer time constant (> factor 10) after the initial time constant. Fused silica and G-10 glass epoxy exhibited characteristics similar to Vespel.

These decay characteristics are not fully understood; however, we believe that the characteristics observed are due to charge migration on the surface and in the bulk of the insulating ring. Furthermore, the resistance provided by the insulating ring is too high, by at least an order of magnitude, to provide a 2-h RC time constant. Therefore, we added a discrete resistor between the input electrode and ground (Figure 4-6) to swamp out the undesirable characteristics of the insulating ring material and to provide the proper RC time constant.

Figure 4-7 shows the RC time constant of the input electrode under conditions simulating the SPM being in the sun. The simulation consists of the SPM being in a vacuum chamber with ultraviolet light shining on the dielectric sample (VDA-backed 2-mil Kapton) with a 2.7×10^{13} ohm resistor from the input electrode to ground. While this resistance value is low enough to eliminate the zero-offset problems, figure 4-7 shows a time constant of approximately 12 h, which is a factor of 6 too long. A proper value resistor was not available at the time of the test to provide the required 2-h time constant.

4.5 SPM ELECTRONICS DESIGN

A block diagram of the SPM is shown in Figure 4-8. The circuit is basically a servo-amplifier providing an output of 0 to ± 10 V which is used to drive the sensed signal to a null. The signal from the sensing electrode is buffered by a high-input-impedance amplifier, amplified in two stages (preamplifier and voltage amplifier), demodulated by a phase sensitive demodulator, and fed back to the compensating electrode(s) through the integrating feedback amplifier and the autorange circuit. The output of the instrument is derived directly from the ± 10-V feedback signal through the output buffer where it is attenuated by a factor of 4 and offset by 2.5 V to provide a 0- to 5-V telemetry signal corresponsing to -2 kV to 2 kV or -20 kV to 20 kV. The range output from the autorange circuit indicates on which range the instrument is set.

A means of driving the tuning fork is also required. To get the maximum amplitude of oscillation with minimum power, the fork is driven at its self-resonant frequency. This is accomplished by deriving a feedback signal from the motion of the fork and using it to generate the drive. A pair of piezoelectric crystals are used as both the drive and feedback elements, and are mounted on the bottom tine of the fork. Piezoelectric drive, as opposed to magnetic drive, has the advantages of ease of shielding and the absence of external magnetic fields that might influence other spacecraft instruments. The limiting amplifier and the power amplifier comprise the remainder of the tuning fork drive oscillator.

The schematic diagram of the SPM electronics is shown in Figure 4-9. Q4 is the input buffer; AR2 is the pre-amplifier; AR4 is the voltage amplifier; U2 is the phase-sensitive demodulator; AR6 is the feedback amplifier; AR7 is the output buffer; U1, AR10, and AR11 form
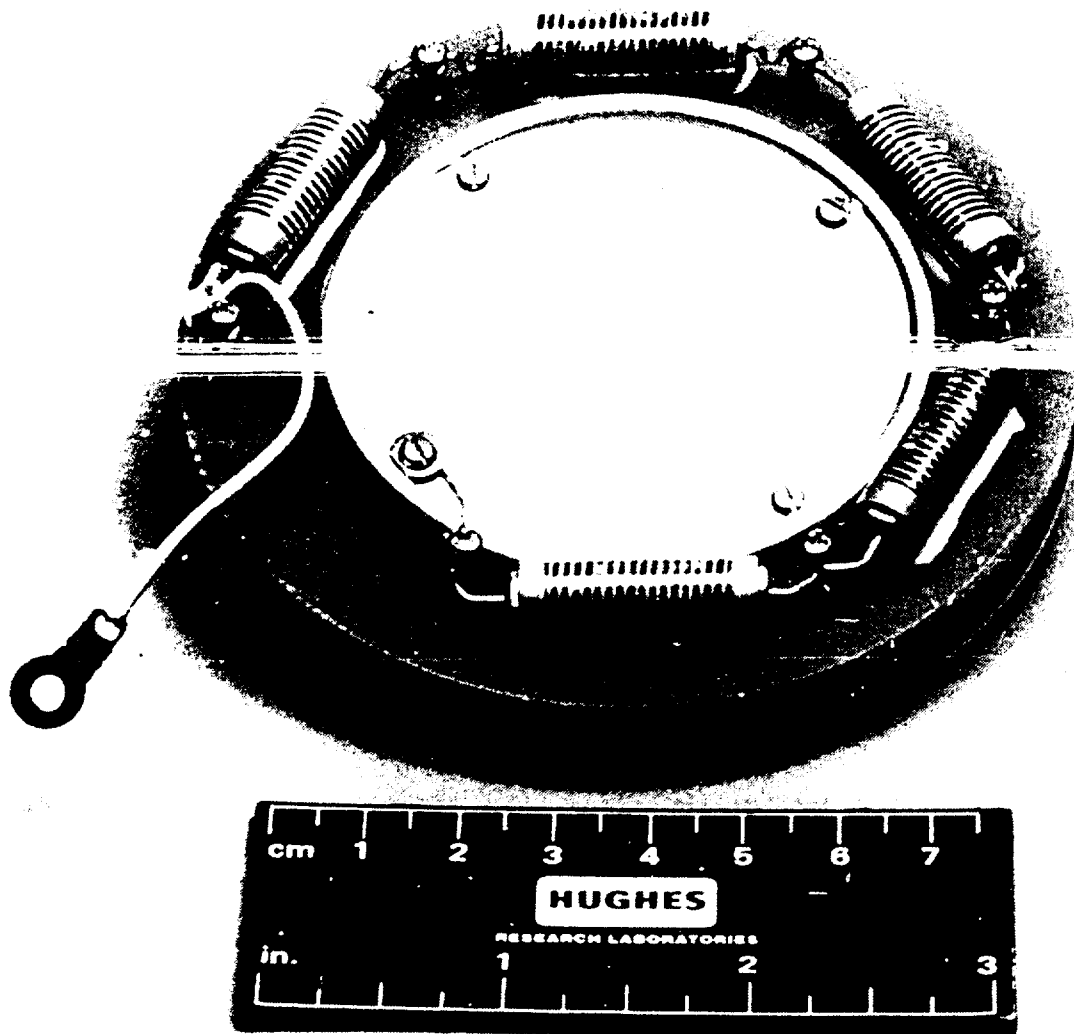
61

Figure 4-6. SPM input electrode assembly showing the discrete resistor (5 resistors in series) between the input electrode and ground (flying lead).
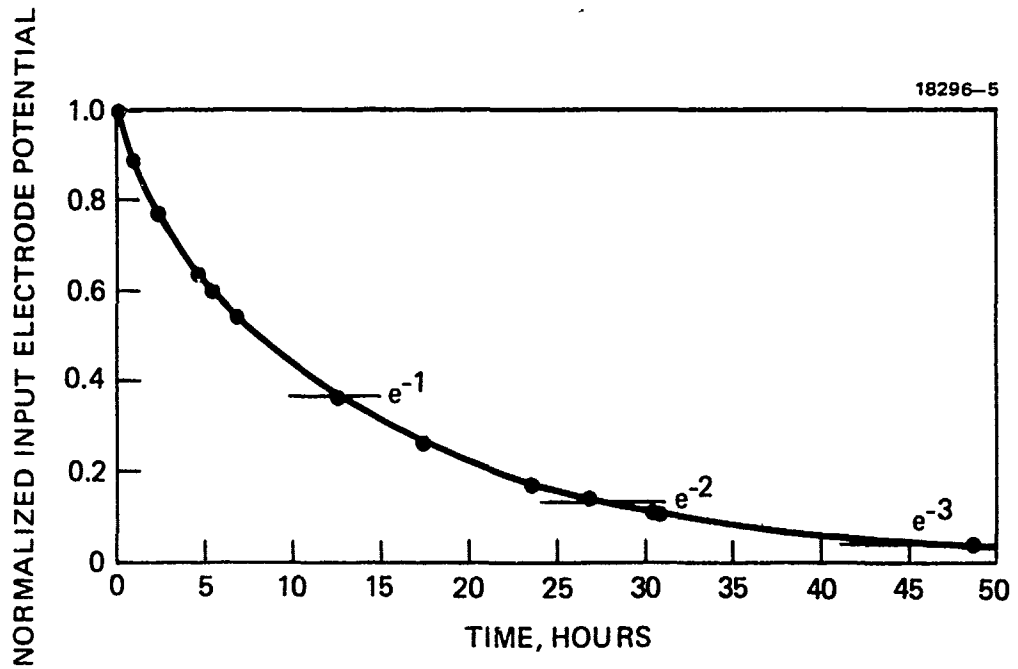
Figure 4-7. SPM input electrode time response under simulated sunlight conditions.
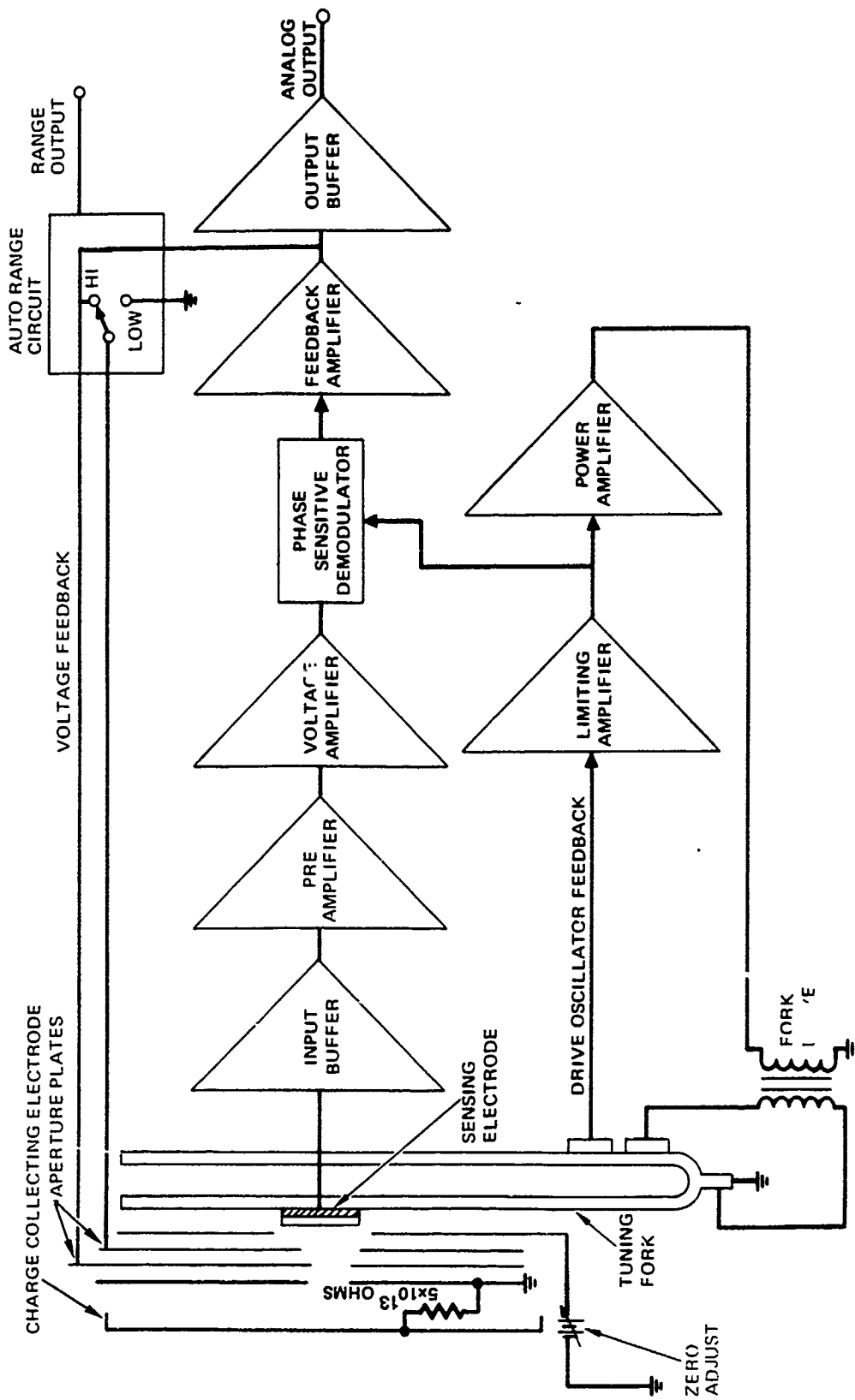
Figure 4-8. SPM block diagram.

13006–40R4

64

Figure 4-9. Schematic of the SPM electronics.

the autorange circuit; AR8 is the limiting amplifier; AR9 is the power amplifier; and Q5 is a photo transistor to detect when the SPM is in sunlight.

4.6 SPM FLIGHT TESTING

The flight SPMs were tested in a vacuum bell jar to determine the values of the SBT resistors and to obtain a calibration curve. This testing revealed a drift problem with the zero setting of the SPMs which consisted of two parts. One part of the drift was due to temperature and was associated with how the wire from the sensing electrode was connected to the preamp. The wire was originally routed along the tuning fork and epoxied to it. The wire now is suspended in free space and the associated component of temperature drift is no longer present.

The second part of the drift was a slow (days) steady drift in one direction. This drift was traced to operation of the ionization gauge (for measuring vacuum chamber pressure). When the ionization gauge was turned off, the SPM started drifting back toward its nominal zero point. The SPM was not fully closed up in its flight configuration during these tests; this allowed electrons and/or ions from the ionization gauge to enter the detection head and presumably collect on some surface causing a change in the electrostatic field. Completely assembling the SPM eliminated this problem. It is remarkable that partial assembly of the SPM, which provided a torturous path for any charged particle entering the detection head, was not good enough to prevent this drift problem. With these fixes, a zero offset was still observed immediately after pumpdown; however, this offset decayed with a 26-hr time constant and did not reappear.

The final calibration data taken in air for SPM S/N 001 and S/N 002 are shown in Figures 4-10 and 4-11 respectively. The zero points (for the low range) for the SPMs under vacuum conditions are also shown on the figures. The low range curves need to be shifted up or down to pass through these zero points to obtain the final calibration curves under vacuum conditions. The zero points for the SPMs under vacuum conditions were reproducible, but the zero points in air varied from day to day. The high range curves very nearly pass through the ideal zero point of 2.5-V output for zero input voltage. Final data on the high range were only taken for positive input voltages; however, earlier testing showed the high range to be symmetrical. The SPMs changed from the low range to the high range at approximately 4.4-V (0.6-V) output and back to the low range at approximately 2.64-V (2.36-V) output for positive (negative) input voltages. A fully assembled (without a front surface dielectric) flight SPM is shown in Figure 4-12.
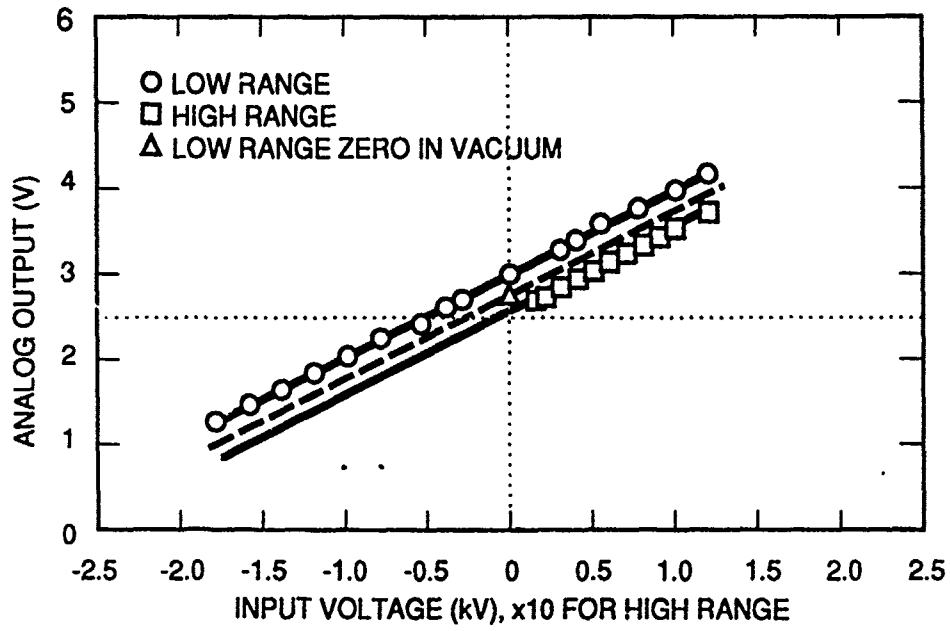
Figure 4-10. Calibration curves for SPM S/N001.
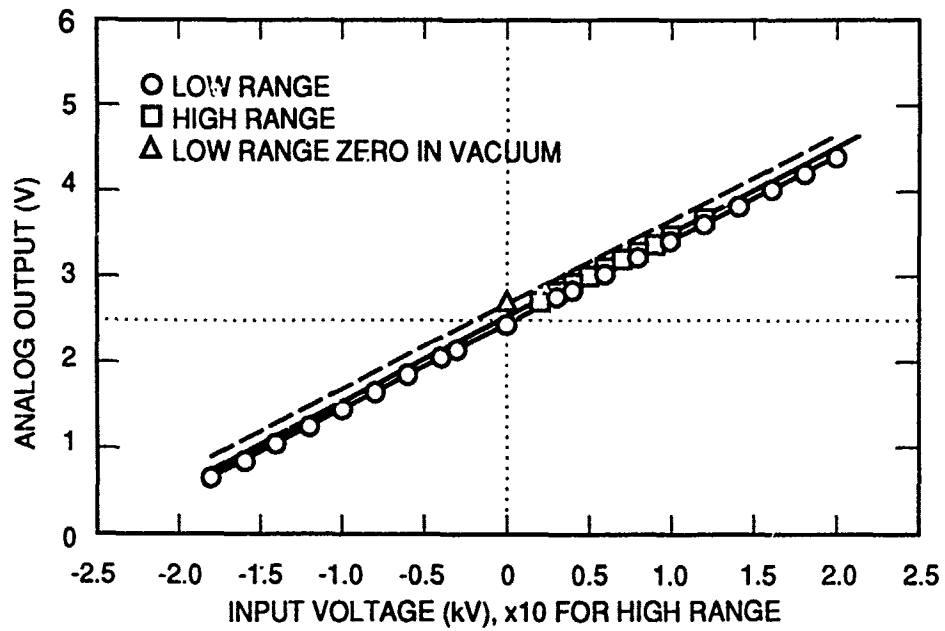
Figure 4-11. Calibration curves for SPM S/N 002.
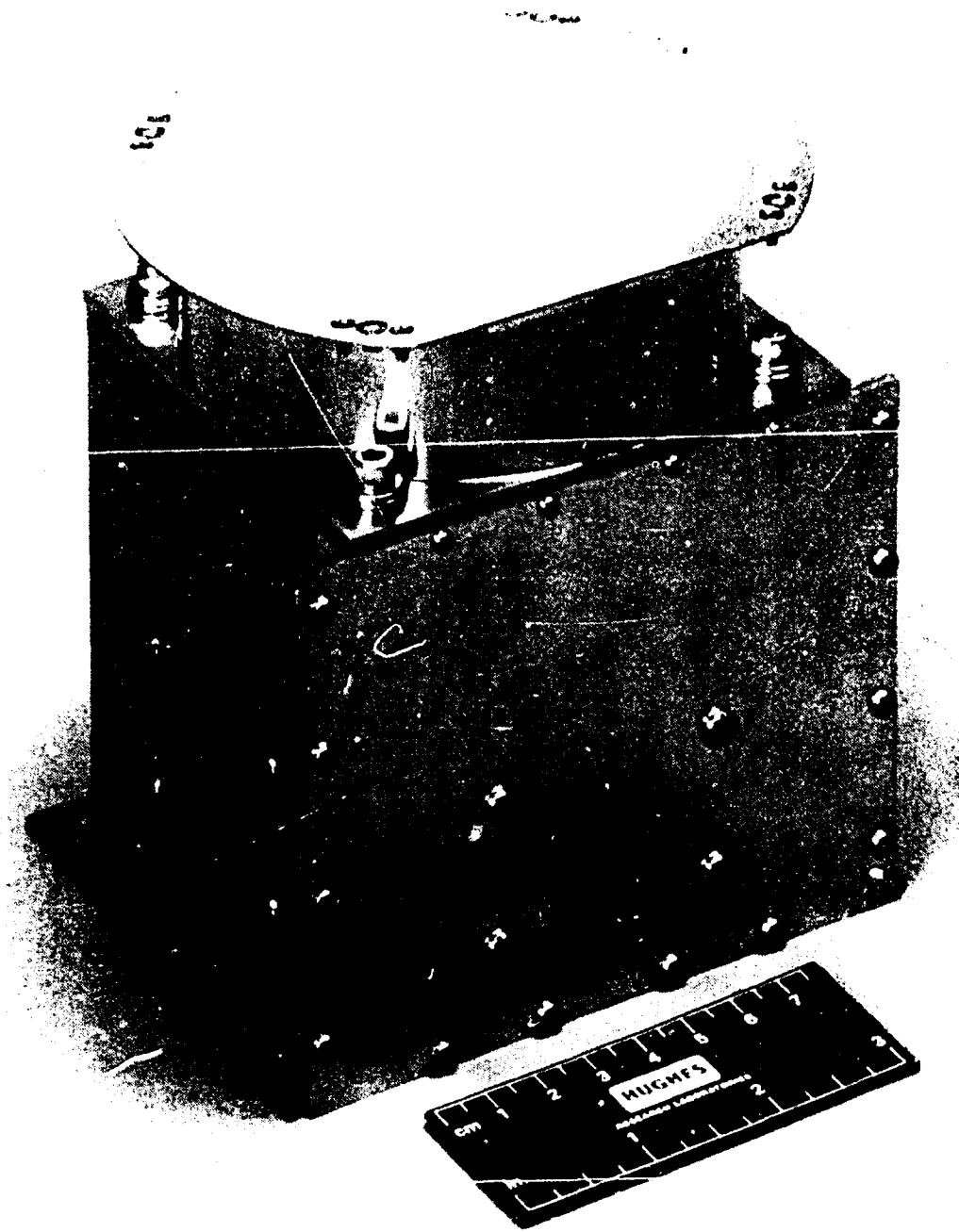
Figure 4-12. A fully assembled (without a front surface dielectric) flight SPM.

SECTION 5
TRANSIENT PULSE MONITOR (TPM)

The Transient Pulse Monitor (TPM) is included as part of the FMDS to detect the onset of arcing on spacecraft surfaces. The main requirement for the selection of the TPM sensor design is maximized ability to discriminate between signals generated by arcing events and signals due to "legitimate" spacecraft circuit transients. A secondary consideration is the need to register arcs occuring anywhere on the spacecraft surface with a minimum number of sensing elements.

A review of the literature revealed that the main types of effects caused by arcing on a spacecraft are those in which:

(1) The arc causes "blow-off" of a cloud of electrons which rapidly disperses. This geometrical change causes a pulse of electrostatic field which can be detected by capacitive coupling to an electrometer plate. This electrostatic field can be detected, weakly perhaps, beyond the line of sight.

(2) The arc creates a plasma that radiates at high frequency. This in turn causes a pulse of wideband rf energy to appear, with its source in the plasma cloud and randomly polarized. This energy can be detected by antennas (horns, dipoles, monopoles, etc.); for the most part, the radiation can be sensed in line-of-sight only.

(3) During the pre-arc stage, an increasing electrostatic potential appears (probably at the surface of dielectric materials). The arc causes a substantial collapse of this potential, which can be detected by capacitive coupling to an electrometer plate. The width of the detected pulse is determined by the low frequency response of the detection equipment, rather than any characteristic of the arc signature itself. The collapse of the potential can be detected beyond the line of sight.

(4) The arc causes replacement currents, which can be detected by current sensors, to flow in the conducting skin of the satellite.

Effect (4) has been employed on several satellites (e.g. SCATHA and the Canadian Technology Satellite) as a means of detecting arcs. The major problem encountered with this technique is its inability to differentiate between arcs and legitimate spacecraft transients, particularly in real time. Therefore, it was not seriously considered for this application.

The remaining effects can be classified by the type of detector required. Effects (1) and (3) utilize an electrometer plate (E-field antenna) which is broadband, while effect (2) requires an rf antenna, which is narrow band. The relative merits of these two detection methods are as follows:

• If only a single detector with a single antenna outside the Faraday cage of the spacecraft is used, the ability to discriminate correctly between arcs and transients appears to be equally limited for both detection methods.

70

- A single broadband antenna is more likely than a single rf antenna to pick up a detectable signal from an arcing event occurring at a location far below the horizon of the antenna (i.e., far from having a line-of-sight connection with it).

- Regardless of the detection method, the addition of a second antenna inside the spacecraft Faraday cage, in conjunction with a simple pulse-analysis circuit, offers a much increased probability of correct discrimination between arcs and transients by permitting a comparison of signals received inside and outside of the Faraday cage.

- It is more likely that the signals received by two broadband antennas, rather than by two rf antennas, will have amplitude ratios that will characterize arcs and transients properly, irrespective of the location of the event relative to the antennas.

- Additional practical points in favor of the broadband approach are the ease of protection from destructive overloads due to arcs adjacent to the antenna, and the lower power consumption.

The TPM design for FMDS is based on the broadband detection approach utilizing a 123-cm^2 E-field antenna outside the spacecraft Faraday cage connected to a 250-Hz to 75-MHz broadband amplifier and pulse analysis circuitry, and a second 123-cm^2 E-field antenna with greatly simplified pulse analysis capabilities inside the Faraday cage. The design is discussed in more detail in the following sections, along with test results.

5.1 TPM DESIGN

The TPM consists of two remote signal sensors and microprocessor-based pulse analysis circuitry as shown in Figure 5-1. The remote signal sensors each consist of a 123-cm^2 plate driving a buffer amplifier (AR1 of Figure 5-2). These remote sensors are connected to the TPM electronics unit via a coaxial signal cable and wires for ±5-V power. The sensors act as capacitive potential dividers from the electrostatic field of the arc to the spacecraft frame. The scaling input capacitors of 45 pF (parasitic capacitance of the wiring and AR1) or 1400 pF (C4 and C15) to ground are selected by a relay (K1) to provide two dynamic ranges of 10 to 300 V/m and 300 to 10,000 V/m. The input signal to the buffer has a dynamic range of ±0.025 to ±0.75 V. The mechanical design of the sensor is shown in Figure 5-3.

The TPM electronics unit contains the circuitry to detect positive and negative pulses above a commandable threshold setpoint, the pulse width of signals above threshold, and the positive and negative peak amplitudes. D/A converters set the threshold levels, a multiplexed A/D converter is used to convert analog signals to digital, and a dedicated microprocessor controls the TPM and exercises the transient pulse algorithms for arc discrimination.

The threshold detectors are fast comparators (AR10 or AR12 of Figure 5-4) that compare the positive and negative pulses with the commanded threshold setpoints and produce an "above-

71
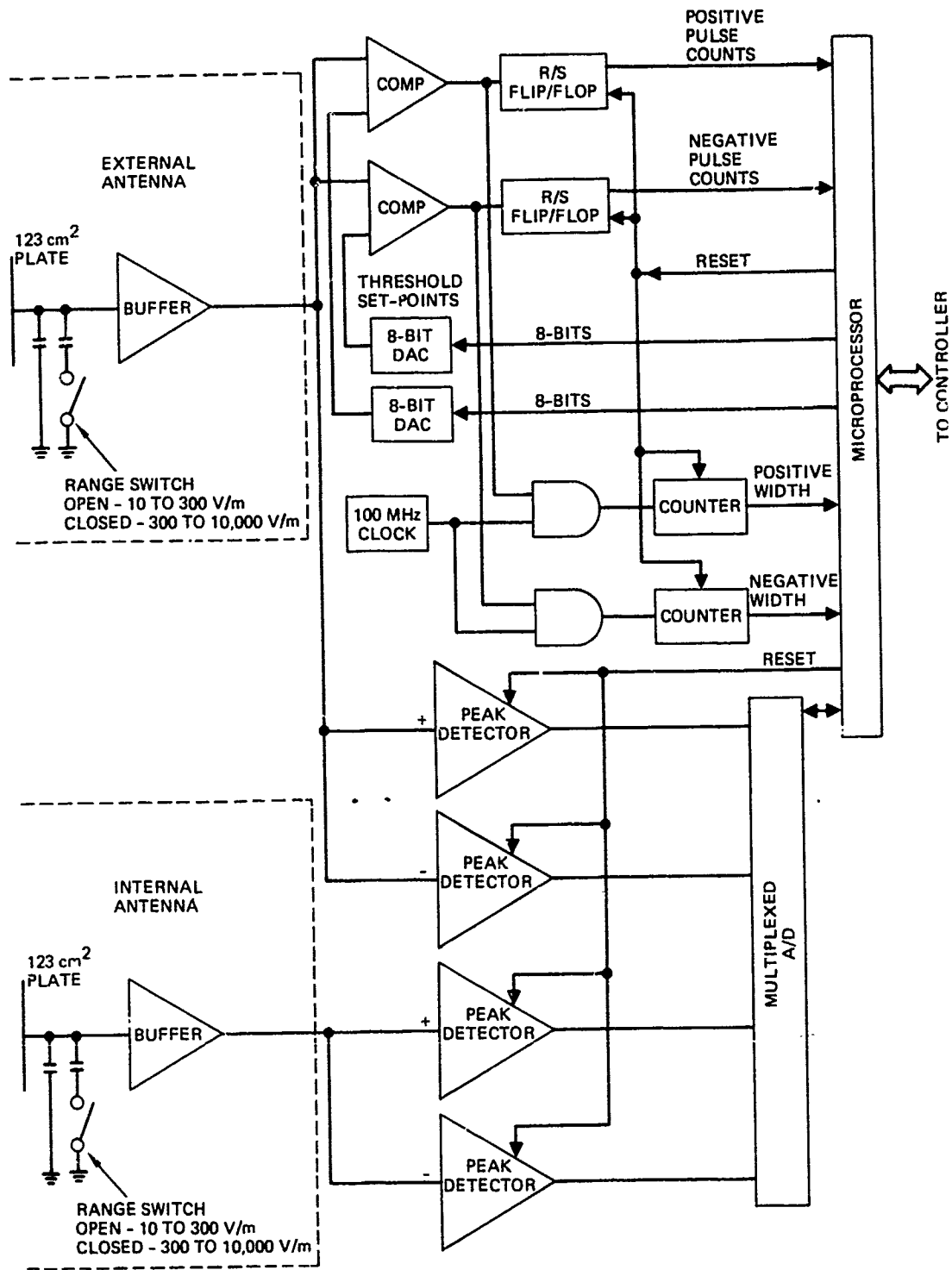
Figure 5-1. Block diagram of the TPM.

Figure 5-2. Schematic of the TPM input buffer.

73

15866-30

123 cm^2 SENSING PLATE

GROUNDED
SHIELD

PC CARD WITH BUFFER
AMP AND RANGE SWITCHING

CONNECTOR
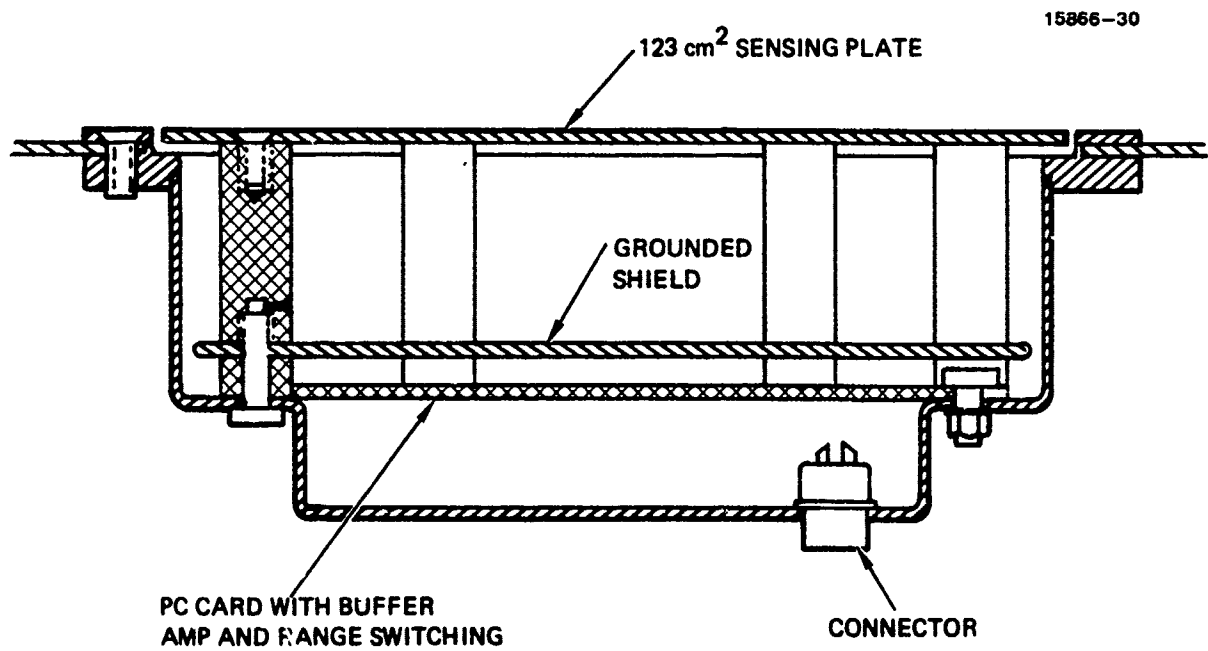
Figure 5-3. Cross section of the TPM sensor head.

Figure 5-4. Schematic of the TPM threshold detectors and width measurement circuitry.

75

threshold" logic signal. The comparators each drive an RS latch (U11 or U12) which provides a 5-ms lockout before another pulse can be detected. The microprocessor resets the RS latch after 5-ms and also stores the pulse count in memory. The positive and negative threshold levels are set by digital-to-analog converters (U29, U30, and AR13 or U31, U32, and AR14).

The pulse width detectors use the "above-threshoid" logic signal to gate a 100-MHz clock (U13) into a counter (U15, U16, and U17 or U18, U19, and U20). The counter then counts until the signal pulse drops back below the threshold setpoint at which time the 100-MHz clock is gated OFF. The width of the pulse is then the counts in the counter times 10 ns. The microprocessor stores the counts in memory (via bus buffers U24, U25, and U26) and resets the counter at the end of the 5-ms lockout.

The peak-amplitude detectors each consist of two stages of peak amplitude detection where the first stage (Q4, Q5, C2, and AR1 or Q6, Q7, C12, and AR4 of Figure 5-5) has a very fast risetime and consequently a rather fast decay time. The second stage (AR2, AR3, and C7 or AR5, AR6, and C17) has a slower rise time and hence a slower decay time but is fast enough to detect the peak amplitude reached by the first stage, and has a decay time which is slow enough to allow the microprocessor to read the peak amplitude by means of the A/D converter. The peak amplitude detectors are really two stages of peak reading voltmeter which allow the amplitudes of 20-ns to 10-μs pulses to be read by the microprocessor. The output signals of the four peak detectors are multiplexed (U1 and U2) and sent to an analog-to-digital converter. The detectors are reset to zero at the end of the 5-ms lockout by Q1 and Q2.

The microprocessor and its interfaces consist of a radhard 80C85 (U40 of Figure 5-6) with 2K of CMOS RAM (U53), 2K of CMOS EEPROM (U52), 2K of CMOS PROM (U48), 8-bit A/D converter (AR20, U49, U60, U61, U42, and U50), and a parallel interface to the system controller (U55, U56, U57, U58, U59, and U62).

Telemetry data provided by the TPM is measured anytime that the external signal is above the threshold setpoint (whether caused by an arc or a spacecraft transient) and is accumulated over a 4-s time period. The data provided by the TPM are as follows;

Data from the external antenna:
- No. of positive pulses above threshold
- No. of negative pulses above threshold
- Amplitude of the largest-amplitude positive pulse
- Amplitude of the largest-amplitude negative pulse
- Width of the largest-amplitude positive pulse
- Width of the largest-amplitude negative pulse
- Amplitude of the widest positive pulse

Figure 5-5. Schematic of the TPM peak amplitude detectors.

77
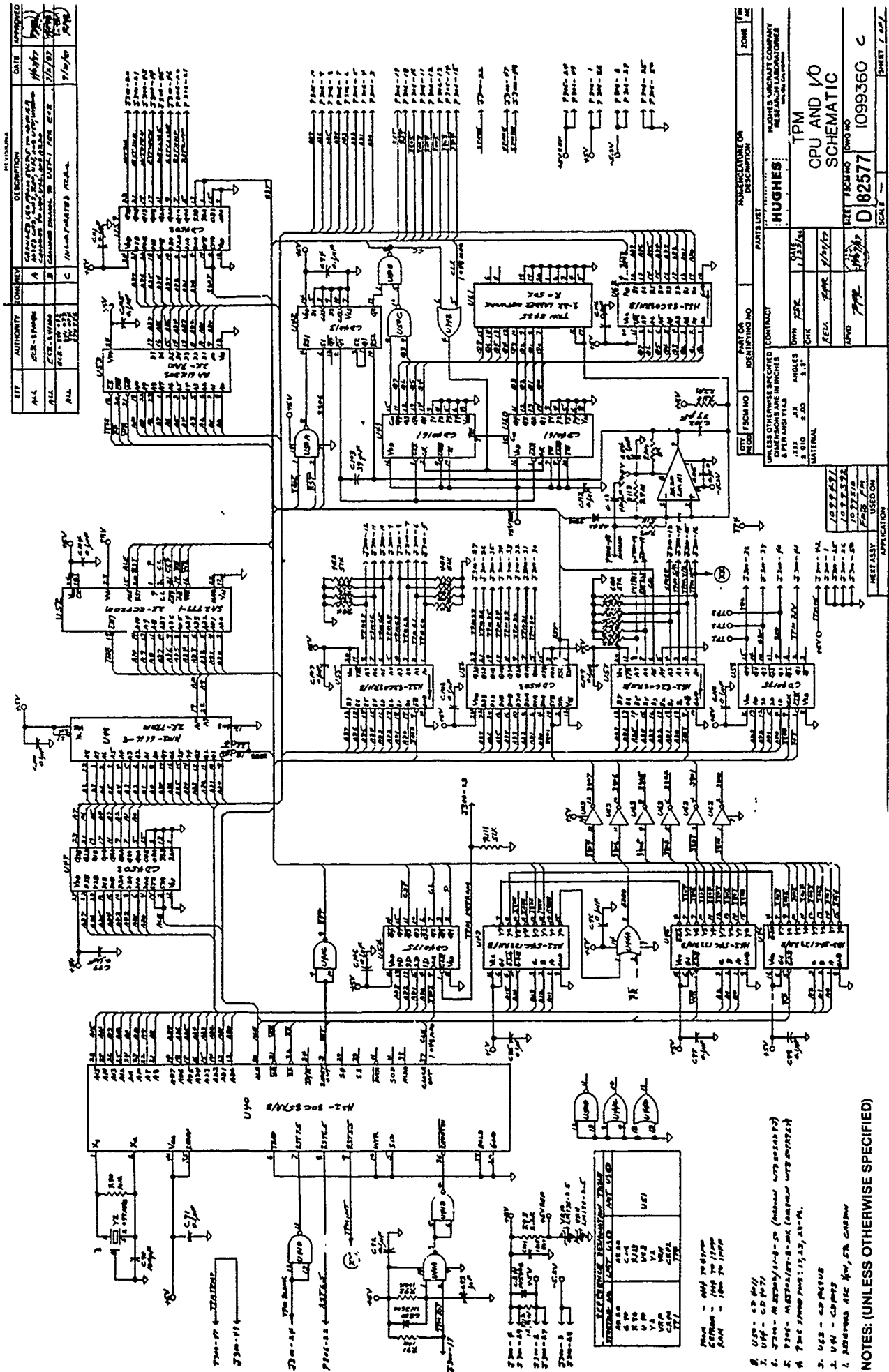
Figure 5-6. Schematic of the TPM microprocessor.

78

- Amplitude of the widest negative pulse
- Width of the widest positive pulse
- Width of the widest negative pulse.

Data from the internal antenna:

- Amplitude of the internal pulse corresponing to the largest-amplitude external positive pulse

- Amplitude of the internal pulse corresponding to the largest-amplitude external negative pulse

- Amplitude of the internal pulse corresponding to the widest external positive pulse

- Amplitude of the internal pulse corresponding to the widest external negative pulse.

General data:

- Relay status (readback of relay setting command).

5.2 BREADBOARD TEST RESULTS

The TPM was tested in a metallic vacuum chamber using real arcs from a dielectric sample. The test setup for performing this test is shown in Figure 5-7. The dielectric sample was irradiated with a 15-keV monoenergetic electron beam, causing it to charge up and arc approximately every 15 s. The external antenna had full view of the vacuum chamber interior while the internal antenna was mounted behind a grounded plate. The replacement current to the dielectric sample and the output of the external antenna's buffer amplifier were viewed on an oscilloscope.

Typical waveforms and data produced by an arc are shown in Figure 5-8. The replacement current rings for approximately 1 μs and is zero from then on (Figure 5-8(a)). The buffer-amplifier output goes negative and then positive within 1 μs (Figure 5-8(a)), after which it rings out at a low frequency (Figure 5-8(b)). The initial negative and then positive signal is in response to the radiated E-field generated by the arc and the low-frequency ring out is the response of the flat-plate antenna and the buffer amplifier settling out to a lower steady-state E-field (the arc lowers the voltage on the dielectric sample and therefore lowers the E-field that it generates). We do not have enough data to determine if the low-frequency ring-out is associated with all arcs. If it is, then this might be a characteristic that could distinguish arcs from other spacecraft transients. Spacecraft transients would not be expected to change the steady-state E-field seen by the antenna.
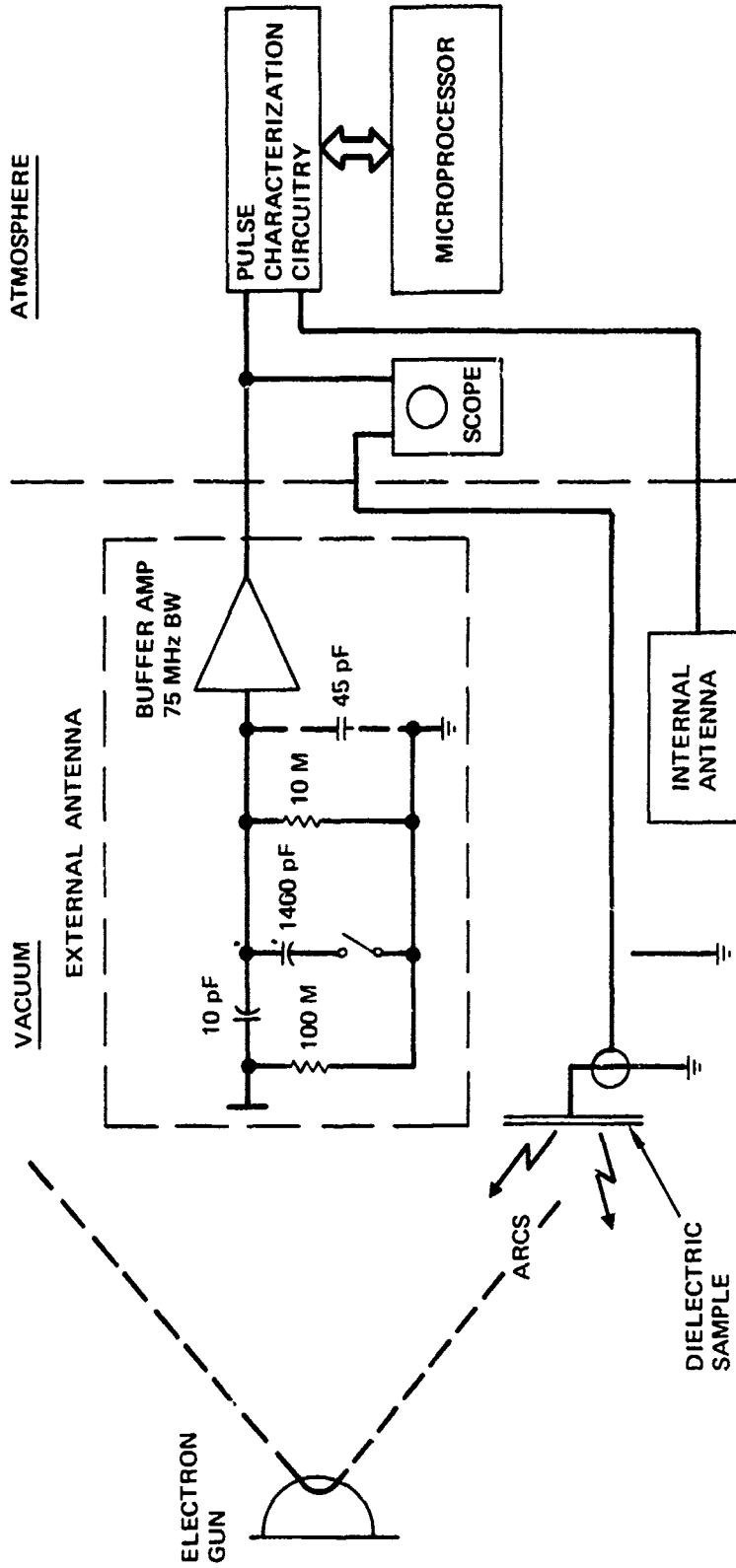
Figure 5-7. Test setup for testing the breadboard TPM in a metallic vacuum chamber.

80
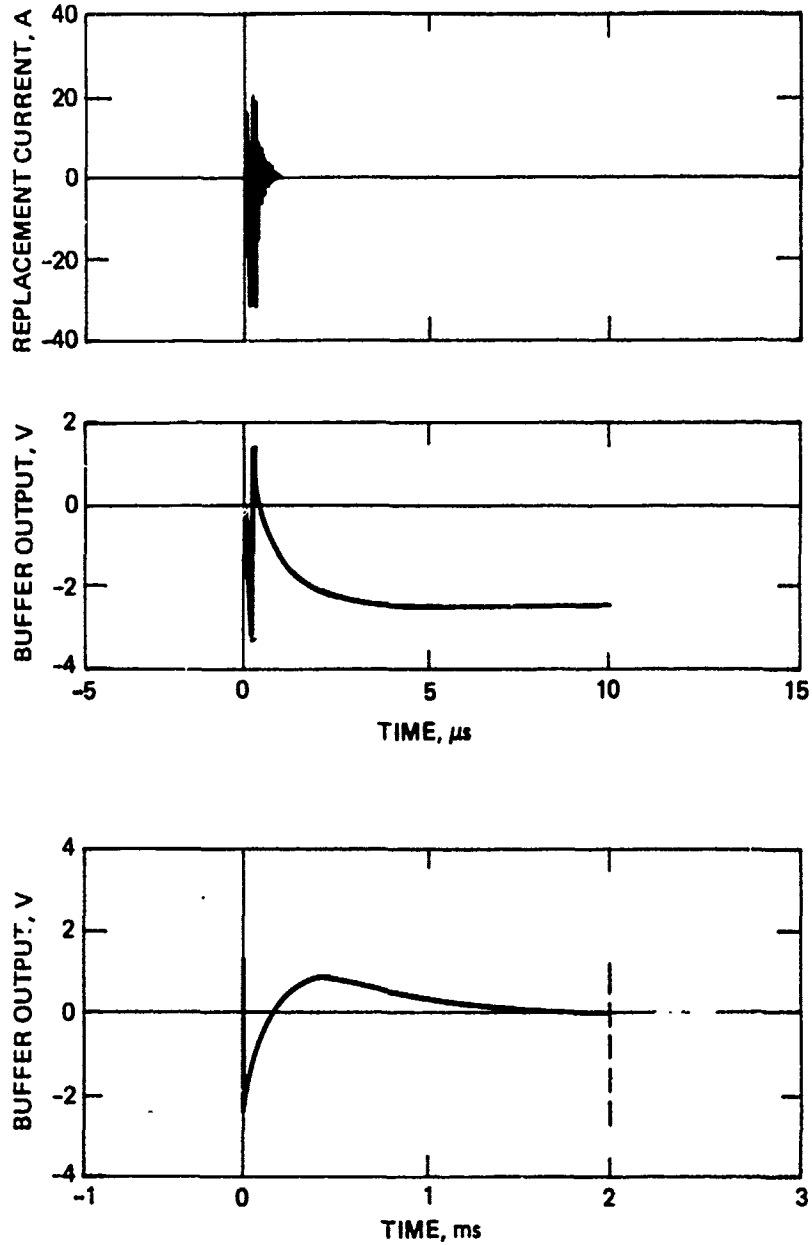
Figure 5-8. Typical waveforms produced by an arc.

The pulse-characterization circuitry interpreted the signal from the buffer amplifier as a negative pulse of 2.1 V and 100 ns, and a positive pulse of 1.11 V and 180 ns. Since the pulse-characterization circuitry is blanked for 5 ms after a pulse occurs, the low-frequency ring-out is ignored. The internal antenna picked up a signal that was lower in amplitude by a factor of >3 and therefore the algorithm of "external > internal" would have interpreted this data as an arc.

A test was made to simulate a normal spacecraft transient where a 28-V dc relay coil was actuated. The TPM responded to this transient and the output of the buffer amplifier showed 1 to 2 μs of high-frequency noise, after which it was zero. The low-frequency ring was not present. This particular test was not performed in a manner suitable to evaluate the "external > internal" algorithm.

The TPM was also tested with pulses of known polarity, amplitude, and width injected into the pulse characterization circuitry and with arcs created inside the vacuum chamber as part of the breadboard demonstration. The telemetry data read out on the GSE correlated closely with the injected pulses. When arcs were created inside the vacuum chamber, both the internal and external antennas detected the arcs. The amplitude detected by the external antenna was approximately 1.5 times higher than the amplitude detected by the internal antenna; therefore, the "external > internal" algorithm determined that it was an arc.

The cables between the two antennas and the electronics were interchanged so that the electronics for the internal antenna would receive the larger of the signals when an arc occured. The algorithm determined that it was not an arc since the internal signal was larger than the external signal. In this configuration the TPM never detected what was interpreted as an arc.

5.3 FLIGHT HARDWARE TEST RESULTS

Initial testing of the flight TPM revealed that the sensitivity of the TPM was lower than expected (200 V/m instead of 10 V/m), especially for narrow pulses (<100 ns). This was mainly due to higher capacitance to ground in the flight design of the antenna plate and front-end electronics circuitry. Increasing the spacing between the antenna plate and ground, and bootstraping the ground plane under the front-end electronics circuitry helped the sensitivity but made the antenna prone to oscillations and/or ringing; therefore these ideas were abandoned.

It was determined that the main problem was in the design of the peak amplitude detectors. The original design used a very fast diode (1N5711) to charge a 39-pF capacitor as the first of three pulse-stretching and peak-detecting stages. At low signal levels (<200 mV), the impedance of the diode is approximately 25,000 ohms giving a time constant of approximately 1 μs which is way to slow to detect 10-ns pulses. The diode was replaced with the Q4-Q5 amplifier of Figure 5-5 charging a 180 pF capacitor (C2 of Figure 5-5). This increased the sensitivity to approximately 20 V/m; however, this final design was never completely tested. A

82

decision was made not to expend any further program resources on the TPM and therefore the TPM hardware and software were never completed.

It is estimated that the TPM would consume 6.4 W (7.6 W from the spacecraft bus) and have a mass of 1.8 kg in its final configuration. The controller, ESA, and SPMs only consume 5.6 W from the spacecraft bus; therefore, the TPM also represents a severe power penalty for an instrument that is only intended to operate as a backup for the ESA and SPMs. A flight TPM antenna assembly is shown in Figure 5-9 and a flight input buffer circuit board in Figure 5-10.
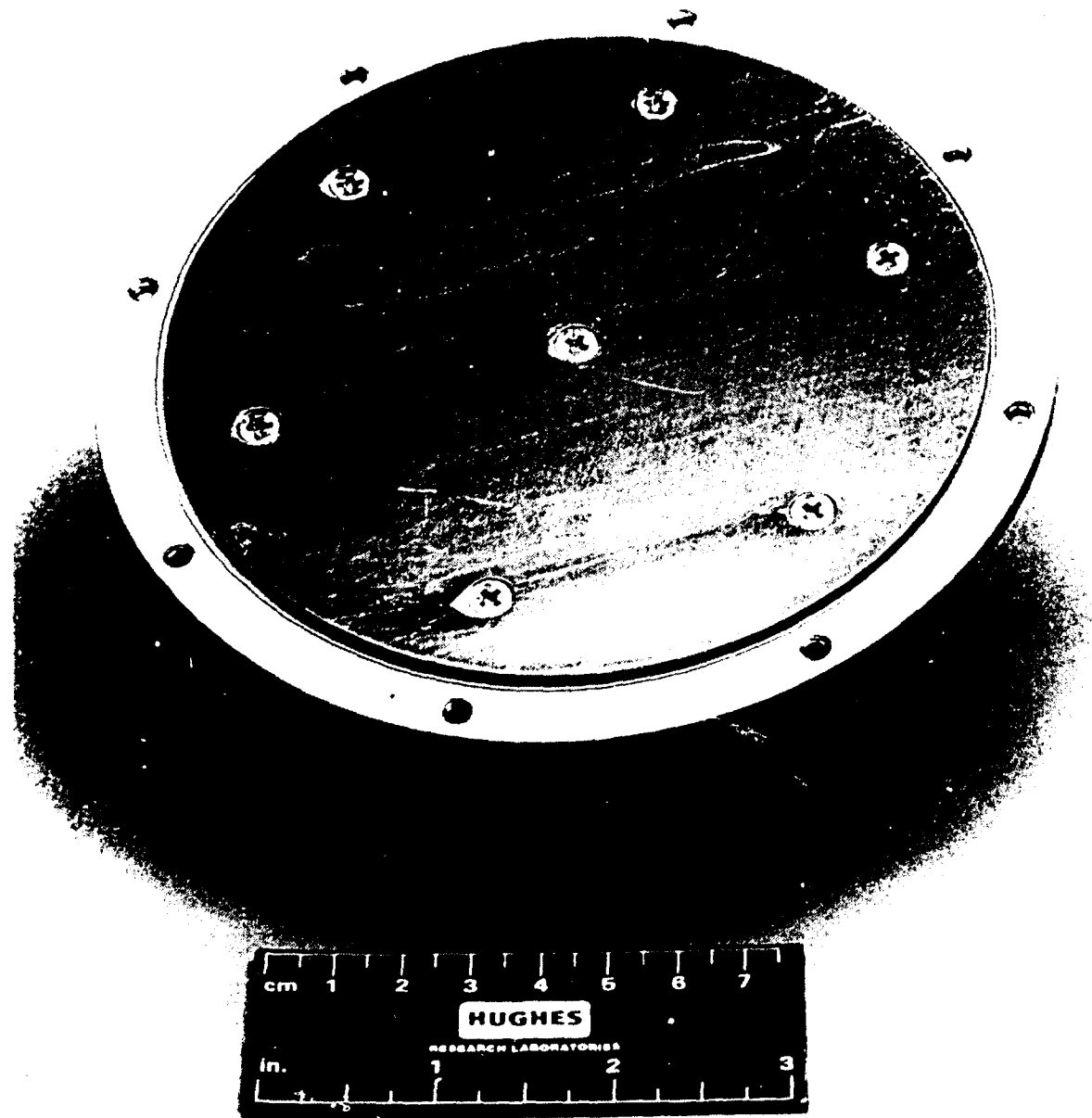
Figure 5-9. A flight TPM antenna assembly.
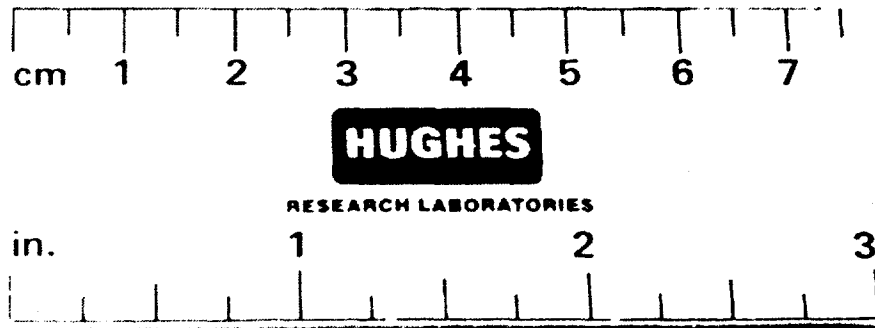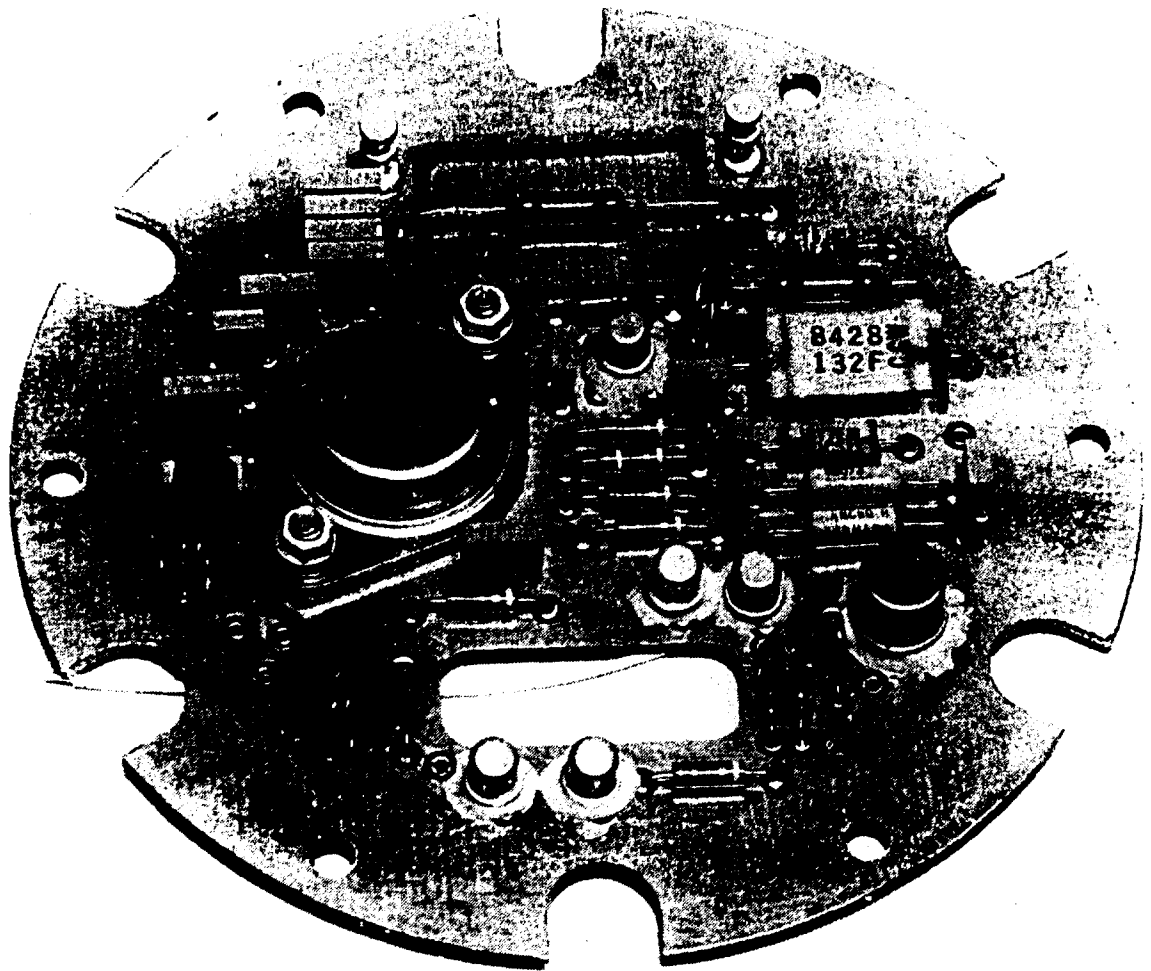
Figure 5-10. A TPM input buffer circuit board.

SECTION 6
CONTROLLER

The controller provides autonomous control of the FMDS relative to the remainder of the satellite, and also ties together the other units of the FMDS. The "brain" of the controller is a microprocessor which contains the algorithms necessary to interpret the data from the sensors and command the plasma source to turn ON when spacecraft charging is occuring. It then monitors and maintains the stability of the operation of the plasma source. The controller turns the plasma source OFF after a programmable time-out, when the emission current from the plasma source has been less than a threshold value for a specified period of time, and/or the ambient electron environment returns to a quiescent condition. The controller has the ability to accommodate certain instrumental faults and failures and to adjust instrument parameters. It is also the command and telemetry interface with the satellite.

In this section we describe the hardware design and software architecture for the FMDS controller. Flow charts of the major software routines and algorithms are also presented.

6.1 CONTROLLER HARDWARE DESIGN

Figure 6-1 shows the hardware architecture of the FMDS Controller. It is designed to survive 10 years at geosynchronous orbit from both a reliability and radiation standpoint. It contains a watchdog timer for CPU errors; redundant storage, error checking, and correction for RAM bitflips; instrument mask, powerdown, and subroutine timer for instrument failures; EEPROM write capability for altering algorithms and setpoints; and redundant command checking and command interlock for command errors or bitflips during transmission. It does not contain any hardware redundancy.

The design employs two seperate HS80C85RH microprocessors: one microprocessor ("ESA") services the ESA, producing a "vehicle potential" signal; and the second microprocessor ("master") serves the functions of operating the plasma source, maintaining command and telemetry contact with the spacecraft, and determining when to activate the plasma source based on inputs from the ESA processor, SPMs, and TPM. This two-processor approach was chosen because the comparitively heavy total computational requirement (which is dominated by processing ESA spectra to determine the vehicle potential) makes it impossible for a single microprocessor to handle the job. The use of one processor for the single activity of processing ESA data is a logically desirable approach which avoids excessive interrupts of the multitasking executive routine of the master microprocessor..

EEPROM (Electrically Erasable Programmable Read Only Memory) is used instead of the combination of PROM (Programmable Read Only Memory) and RAM (Random Access
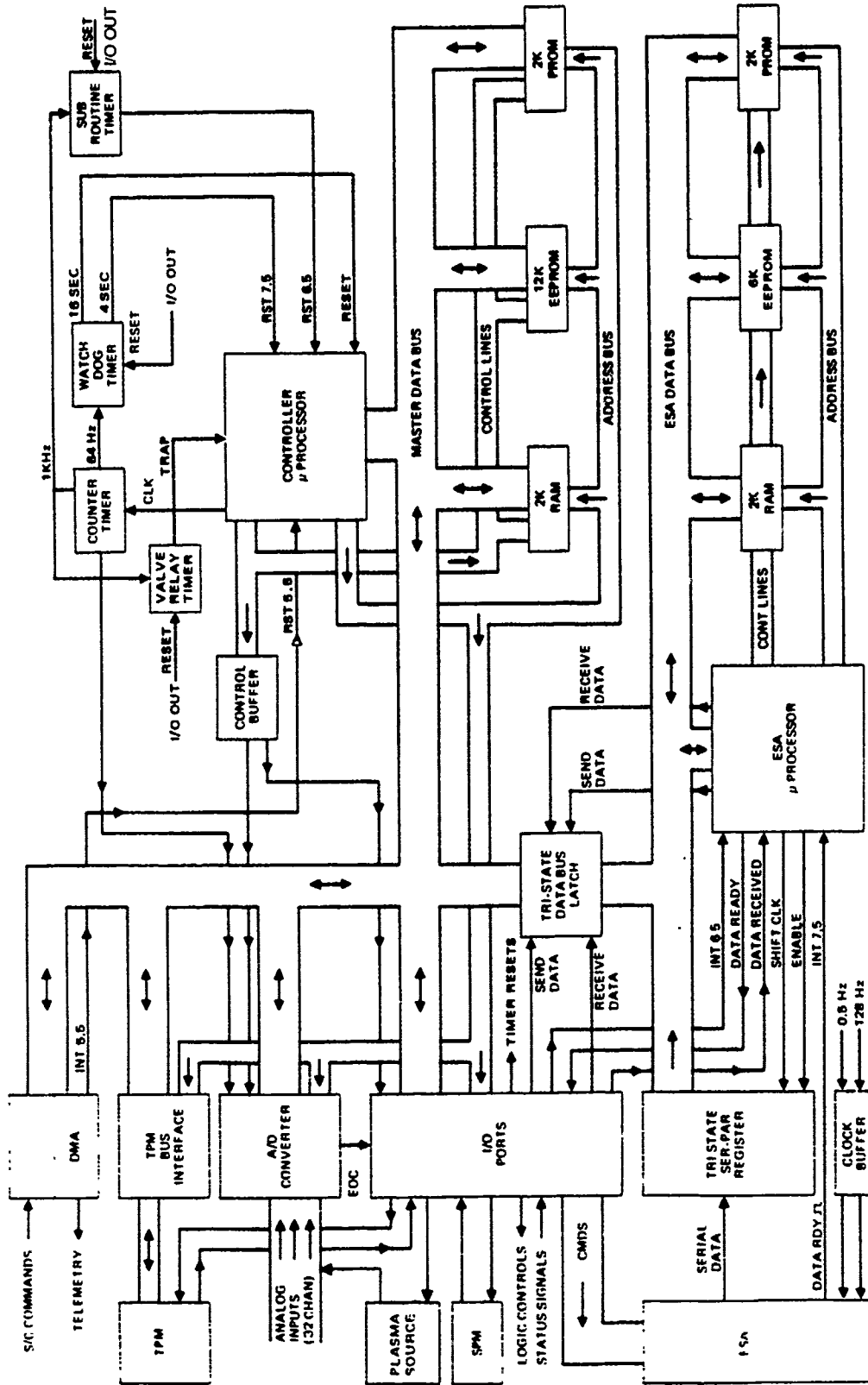
Figure 6-1. Block diagram of the FMDS controller.

87

Memory) that we have used in previous spaceborne systems. In these previous systems, default set points and logic decision thresholds were contained in PROM and were copied into RAM on system powerup. The RAM values were the ones actually used by the system, thus permitting new values to be uploaded into RAM from the ground (via a RAM-write command). Because of the extent of this RAM and the criticality of its contents, seperate error-correcting hardware was required to avoid system errors which could result from cosmic-ray-induced bitflips. The approach for the FMDS Controller exploited the availability of the radiation-hardened CMOS EEPROM from Sandia (SA2999). Both the FMDS operating algorithms and the default set points are housed in the EEPROM. This approach has several substantial advantages: (1) the amount of RAM is minimized; (2) the probability of bitflip-generated hazards to the system is small enough that seperate error-correcting hardware is not required, and a simplier measure provides more than adequate protection (i.e., storing critical parameters in three locations and using majority voting); (3) virtually all parts of the software can be rewritten from the ground, rather than just selected set points; and (4) a system reset or power outage will not cause unwanted default set points to reappear. The Sandia EEPROM is specified for 10,000 erase/write cycles and a 10-year retention period.

The PROM contains routines that are very basic and critical to operation of the system (initial boot up, commands and telemetry, and EEPROM write). If these routines were in EEPROM and the wrong location was accidentally written to, it would be a catastrophic mistake.

Telemetry data to the spacecraft is provided when it is requested by the spacecraft. This is done with DMA (Direct Memory Access). The DMA approach offers a simple interface with flexible timing to the spacecraft. The controller accepts one command byte every cycle (every 4 s). If commands are sent at a faster rate, then some of the command bytes will be lost.

The controller also contains I/O ports for the transfer of digital data between itself and the other units (ESA, SPMs, TPM, and plasma source) and a multiplexed analog-to-digital converter for digitizing analog parameters from the other units.

The master micropocessor schematic is shown in Figure 6-2, where U1 is the radiation-hard 80C85 microprocessor; U2 is the lower 8-bit address latch; U3 and U4 are the RAM; U8 is the PROM; and U13, U14, U15, U16, U17, and U18 are the EEPROM. In addition, U19, U20, and U21 are memory chip select decoders; U12 is a latch that controls the erase/write of the EEPROM; U22 forces the correct address bits and control signals unto the bus for DMA; and U23 is a bidirectional address/data bus buffer.

Figure 6-3 shows the ESA microprocessor schematic, where U40 is the microprocessor; U48 is the RAM; U41 is the PROM; and U45, U46, and U47 being the EEPROM. U52 is a latch controlling the EEPROM erase/write; U53 is the lower 8-bit address latch; U54, U65, and U56 are address decoders; and U60, U61, U62, and U63 are I/O ports to the master microprocessor.

Figure 6-2. Schematic of the master microprocessor.

Figure 6-3. Schematic of the ESA microprocessor.

The serial to parallel shift register, U57, inputs data from the ESA, U58 is the ESA data input port, and U59 is an output port to the ESA for the data clock and to the master microprocessor for handshaking (ESA R/V).

I/O address decoding is provided by U134, U135, U136, and U137 of Figure 6-4. Output ports U132 and U133 are used for the digital commands to the ESA, U130 is the output port for turning the valves and plasma source inverters ON/OFF, and U131 is the output port for turning the sensors (ESA, SPMs, and TPM) ON/OFF. Counters U139, U140, and U141 divide the clock signal from the master microprocessor for timing purposes, including the 4-s interrupt and watchdog timer. The subroutine timer and latching-solonoid timer are U143 and U144, respectively, with U142 being the latch to turn them ON/OFF, while U148 sends a 0.5 Hz timing signal to the ESA. Q130 resets a 16-s delay in the plasma source electronics every 4 s. If this delay is not reset for a period exceeding 16 s, all valves are closed and all instruments are turned OFF automatically (part of the watchdog timer).

The analog-to-digital (A/D) converter and more I/O is shown in Figure 6-5. U80 and U81 are 16 channel analog multiplexers (total of 32 channels), U83 is a sample-and-hold amplifier, and AR10, U84, U85, U90, and U91 comprise the A/D converter. U86 is the input port for the digitized analog data, U87 starts the conversion process, and U88 stores the channel address for the analog multiplexers. U82 is an output port that turns the plasma-source power supplies ON/OFF and selects their operating setpoint.

Figure 6-6 shows the interface with the TPM and the command/telemetry interface with the spacecraft. U111, U112, U113, and U114 are the I/O ports that transfer commands and data between the TPM and the master microprocessor. Optical isolation with the spacecraft for the command/telemetry interface is provided by U100, U101, U102, and U124. It is assumed that the optical isolation for the telemetry data line will be provided on the spacecraft end of the interface and U119, Q1, and Q2 form a line driver to drive that optical isolation. U103, U106, and U108 are edge-triggered D-type flip/flops to provide noise immunity for the incoming signals. U104 converts the serial command byte to parallel and U105 is the command input port. Flip/flops U107 and U110 and shift register U109 control the DMA timing which is shown in Figure 6-7. U115 is the parallel to serial telemetry shift register, U116 is the counter that selects the telemetry word for the DMA, U118 is the port that forces the counter data unto the memory address bus, and U123 is the input port for the DMA counter. U117 is an input port for the SPM ranges and the ADC conversion complete (not CC) signal.

The command timing shown in Figure 6-7 is straightforward and involves a command-enable signal, a command clock, and the command data. The command-enable allows eight clock pulses to shift the eight data bits into the shift register. The clock can be either a continuous stream of pulses or an 8-bit burst. The trailing edge of the command-enable signal

Figure 6-4. Schematic of the controller I/O circuitry.

92
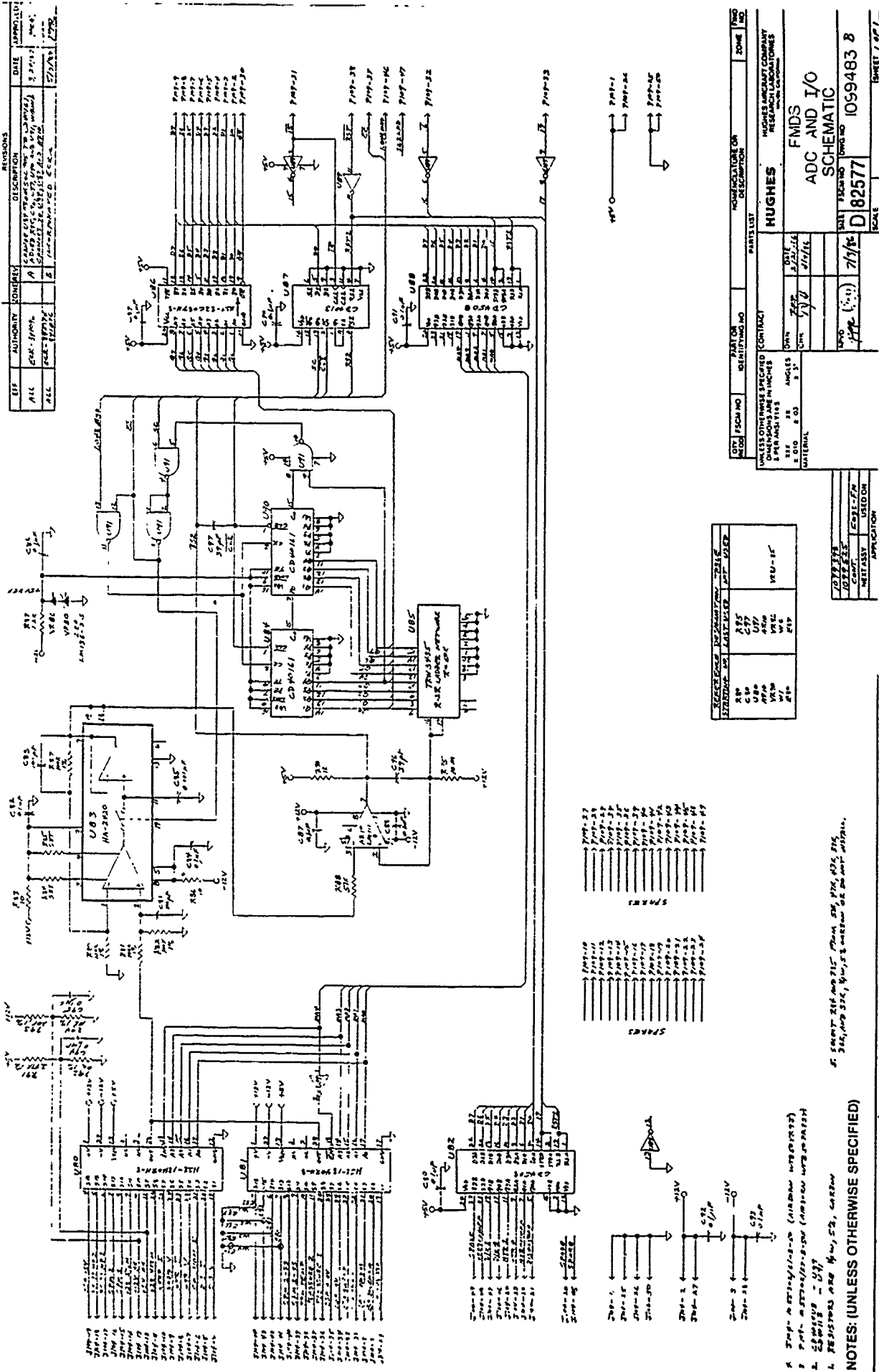
Figure 6-5. Schematic of the analog-to-digital converter schematic.

93
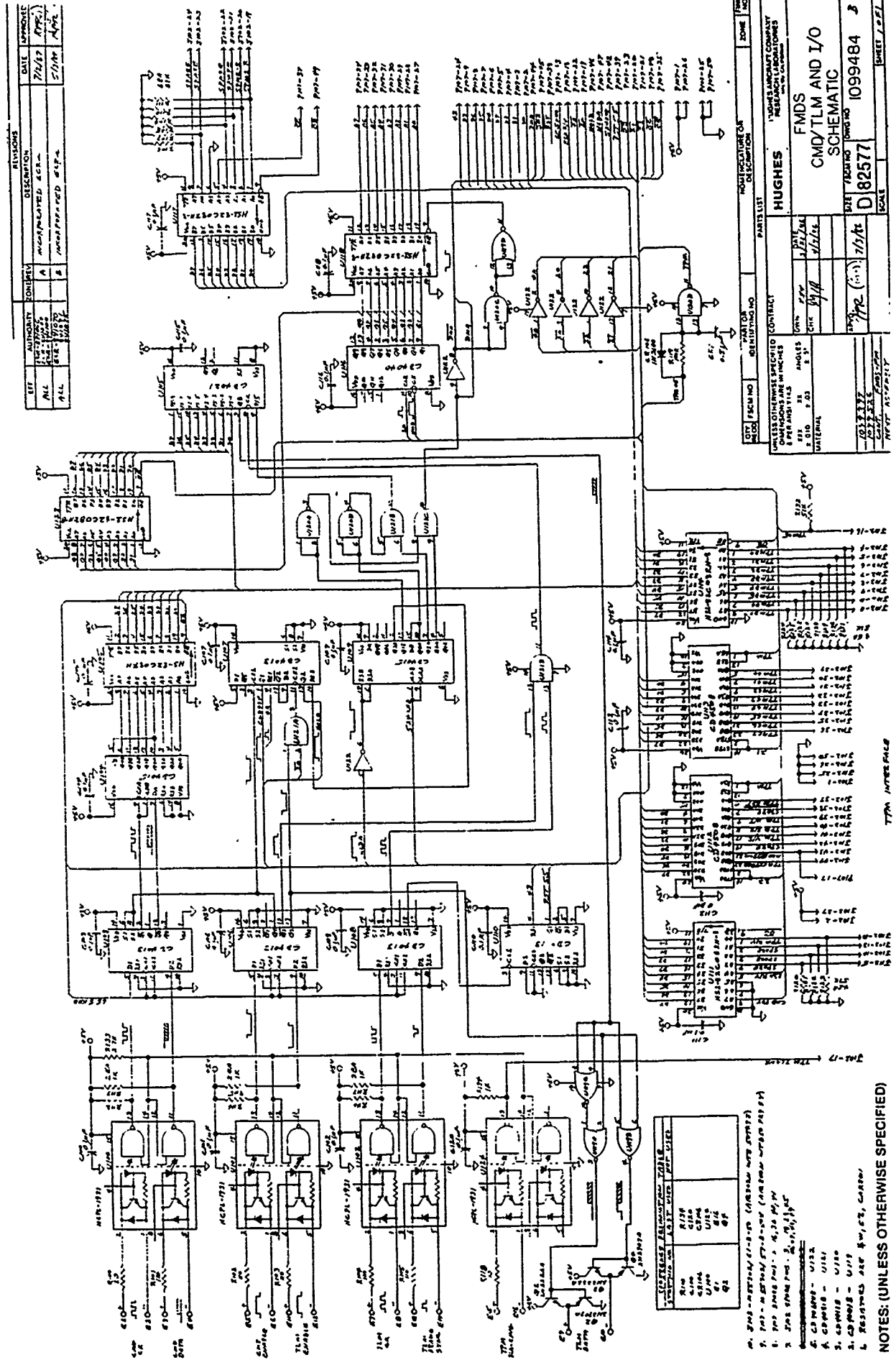
Figure 6-6. Schematic of the command and telemetry circuitry.

94

Figure 6-7. Command and telemetry timing.

NOTES: (UNLESS OTHERWISE SPECIFIED)

1. REFER TO DWG. NO. 109944 - FMDS CMD/TLM AND I/O SCHEMATIC

HUGHES AIRCRAFT COMPANY
RESEARCH LABORATORIES
MALIBU, CALIFORNIA

FMDS
CMD/TLM TIMING

SIZE C | FSCM NO 82577 | DWG NO 109944
SHEET 1 OF 1

sets F/F U107A to indicate to the master microprocessor that a command has been received. U107A is reset by the master microprocessor after it has read the command. The commands that the FMDS will accept and the telemetry data it provides are listed in Appendix A.

The telemetry timing is more complex because of the DMA function. Whenever the spacecraft issues a frame-sync pulse, F/F U110A is set which interrupts the master microprocessor, causing it to load the DMA area of memory with a new set of telemetry data, provided the last set has all been sent. After updating the DMA memory, U110A is reset and a DMA cycle is initiated. F/F U107B is set which requests the bus from the master microprocessor. When the master microprocessor relinquishes the bus, shift register U109 is enabled which starts shifting "1s" down its outputs. These "1s" successively force the counter data unto the address bus, clock the data in memory into the output shift register (U115), increment the DMA counter (U116), and reset F/F U107B which terminates the bus request allowing the master microprocessor to resume operation. The first telemetry data word is now in the shift register and can be clocked out by the spacecraft at any time. When the present word is clocked out, the trailing edge of the telemetry enable signal will initiate another DMA cycle so that the next telemetry data word will be ready for the spacecraft.

The mechanical packaging of the controller is on five PC boards which are contained in a 8.38-cm W x 15.24-cm D x 13.97-cm H (3.3 x 6.0 x 5.5 in.) box as shown in Figure 6-8. The box has a mass of 1.415 kg (3.12 lb) and consumes 0.86-W of power.

6.2 CONTROLLER SOFTWARE DESIGN

The software design is heavily modularized, consistent with modern design practices. An "executive" routine is present, which simply calls other modules in sequence. The advantage of this approach is that individual modules can be altered, added, deleted, or relocated with very little or very minor alteration of the overall code. The software is realized in a machine-intimate hign-level language, "C"; however, some portions are coded in assembly language for additional speed and memory-use efficiency requirements. A high-level language was used because it is essentially self-documenting, while even well-documented assembly coding is frequently impregnable and not maintainable.

6.2.1 Master Microprocessor

The master microprocessor (μP) is responsible for interrogating the several charging-detection instruments, determining whether or not a charging hazard exists, controlling the plasma source, and communicating with the ground (i.e., making telemetry data available and receiving and executing commands). The overall organization of the software is shown in Figure 6-9; we discuss the individual sections in a little more detail in the sections below.

96
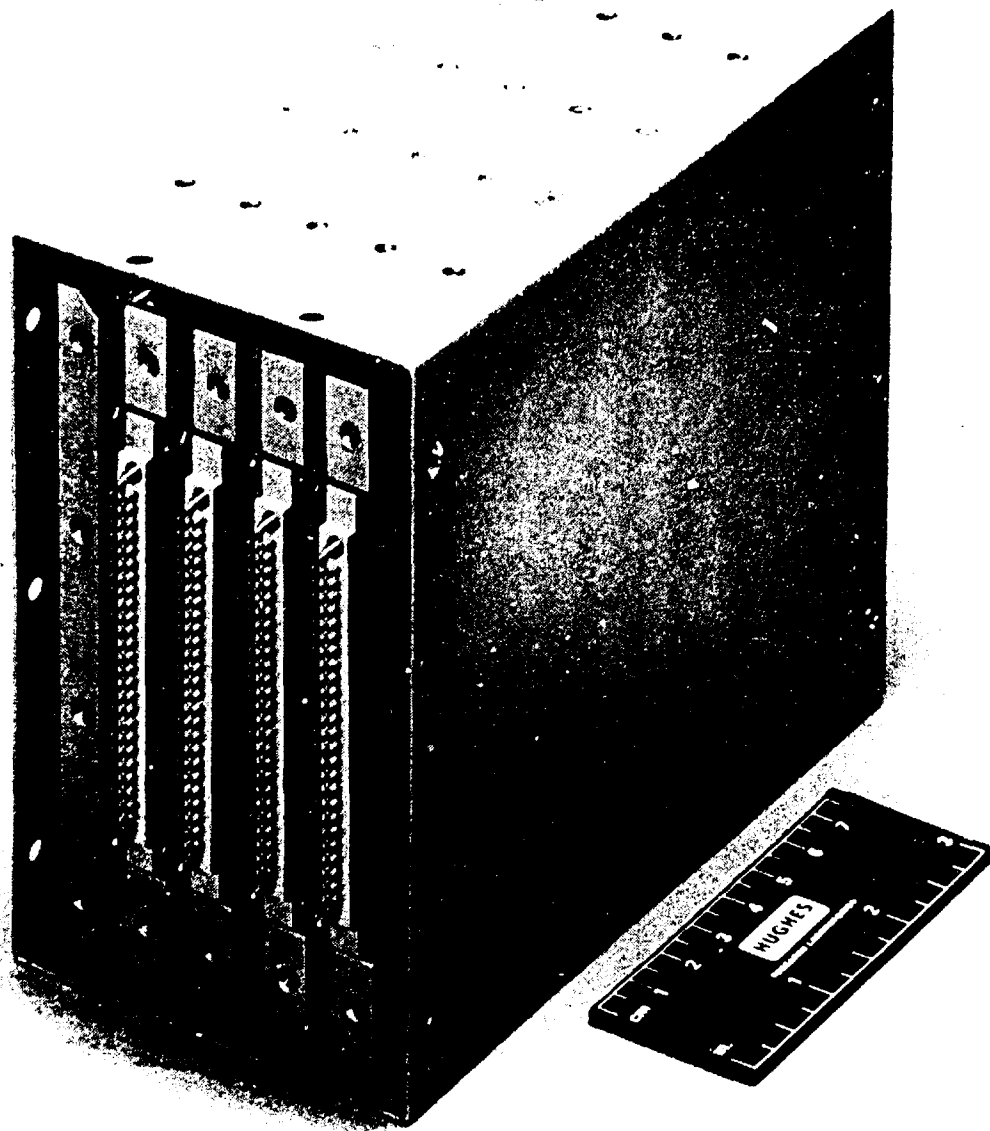
Figure 6-8. Controller electronics box without the box end-plate.
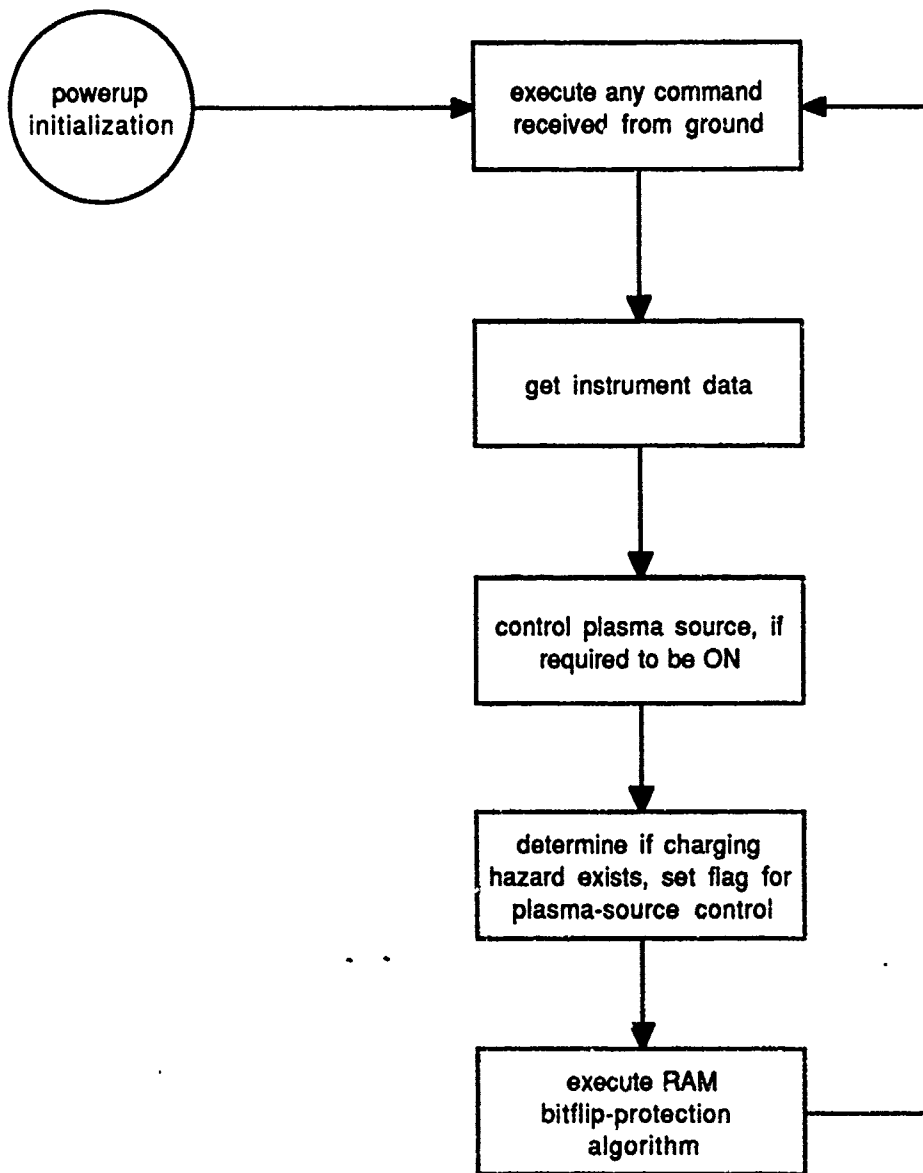
Figure 6-9. Overall organization of the FMDS controller software.

6.2.1.1 Powerup: *main*

On powerup, an initialization routine copies initialized data from PROM to RAM and jumps to the C function called *main*, shown in Figure 6-10 (we will use italics to denote C function names). *Main* is responsible for powering up the instruments (using the routine called "powerup") and for correcting any RAM bitflips that have occured since the previous 4-s cycle. Two flags are tested in main: one (auto-start) allows for enabling or inhibiting automatic instrument powerup when FMDS is powered up; the other (stop-flag) can be set by ground control to prevent code in EEPROM from being executed (Figure 6-11 shows the response to the stop-flag being set). This capability permits EEPROM-writing without the risk of incompletely-modified code being executed. Having completed its bitflip-protection task, main sits in an endless loop awaiting the 4-s interrupt (hardware interrupt RST 7.5). This interrupt generates a jump to the *executive* routine shown in Figure 6-12.

6.2.1.2 Master Task-Calling Routine: *Executive*

The *executive* routine is the controlling force of the master microprocessor. Upon entering the routine, the 4-s flag is checked and if it is set, this indicates that the microprocessor did not have time to execute all of the *executive* routine the last time before it was interrupted again by the 4-s interrupt. This will not normally occur, but if it does an error bit is written to the System Status Byte (SSB). The "watchdog timer" is reset next (the watchdog timer is implemented in hardware; if it is not reset at least once every 16 s, it resets the entire system). The 4-s flag is then set to facilitate checking for completion of the executive. Next the executive checks to see if a command has been received from the ground (and if it has, *executive* calls the command processor to execute the command). If the stop-flag is not set, executive calls the function *exec2* , shown in Figure 6-13 (the executive functions are partitioned in this manner because of PROM vs. EEPROM considerations).

6.2.1.3 Continuation of Executive: *Exec2*

In *exec2*, the various bits that comprise the SSB are specified, and the SSB is placed in a data stack called stack1, the various timers that are in the code are decremented if they are running, and then *exec2* calls a function to get data from the analog-to-digital converter (ADC). A hardware "subroutine timer" is included to protect against the possibility of the microprocessor becoming trapped in an endless loop (in case, for example, of an ADC fault). When the subroutine timer times out, it generates an interrupt and causes a jump to the location in *exec2* just after the function call that caused the problem. *Exec2* then calls the function *mode_mgr*, which is responsible for maintaining the plasma source in the desired operating condition. Next,
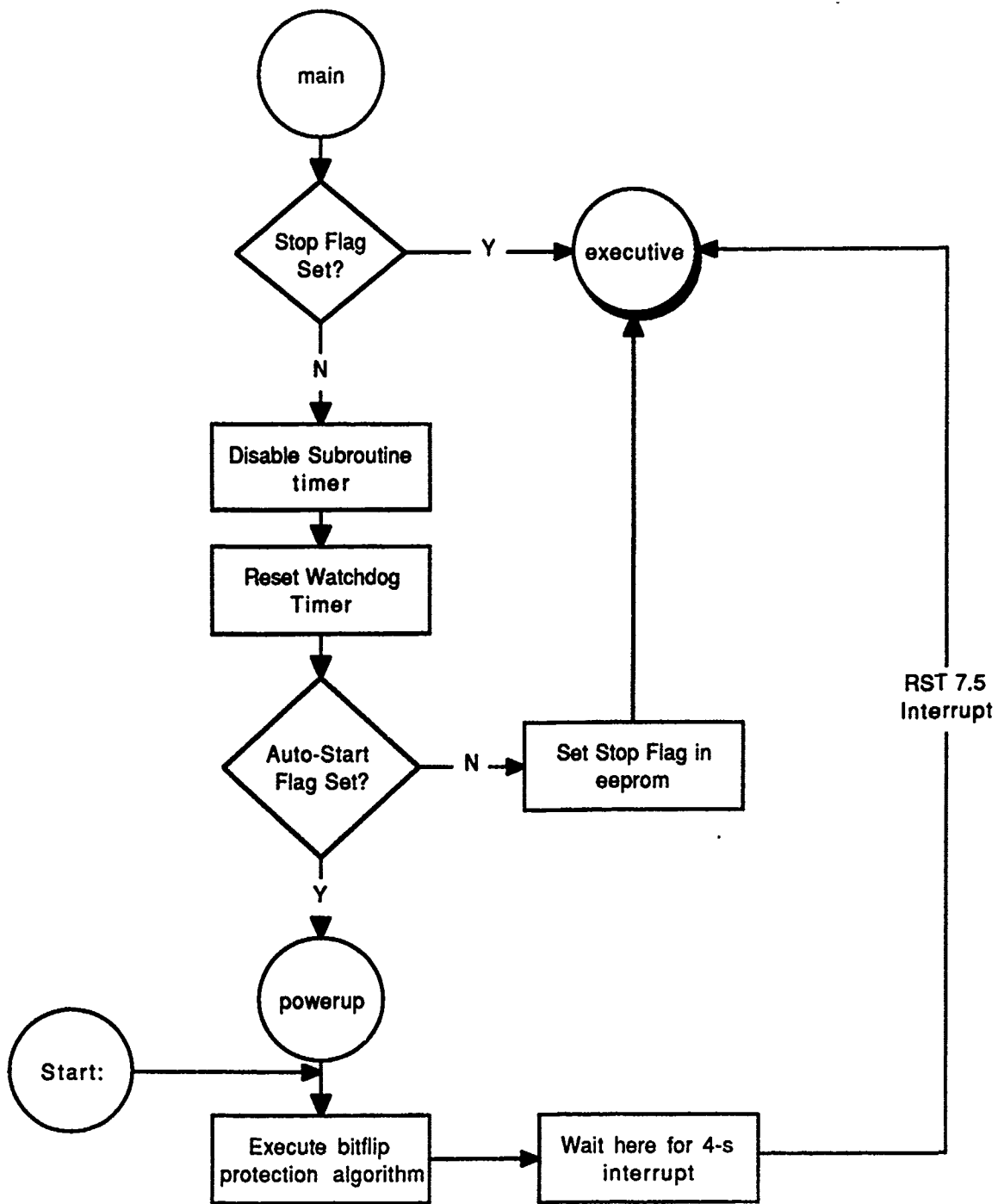
Figure 6-10. "Main" software routine.
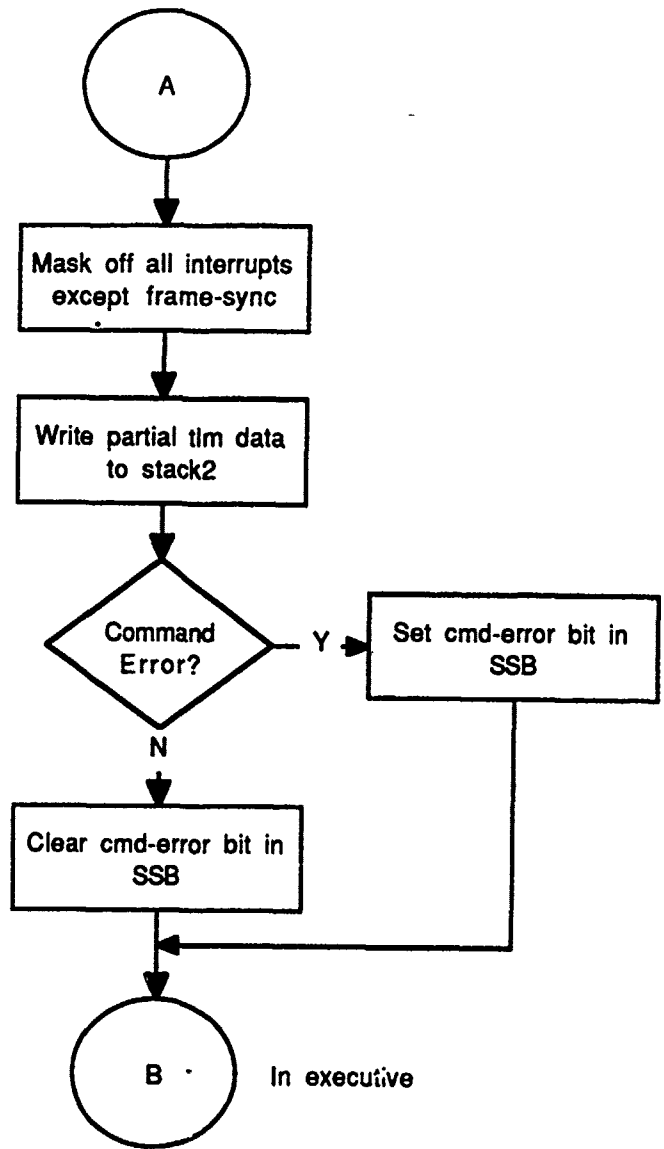
Figure 6-11. Response of the software to the stop-flag being set.
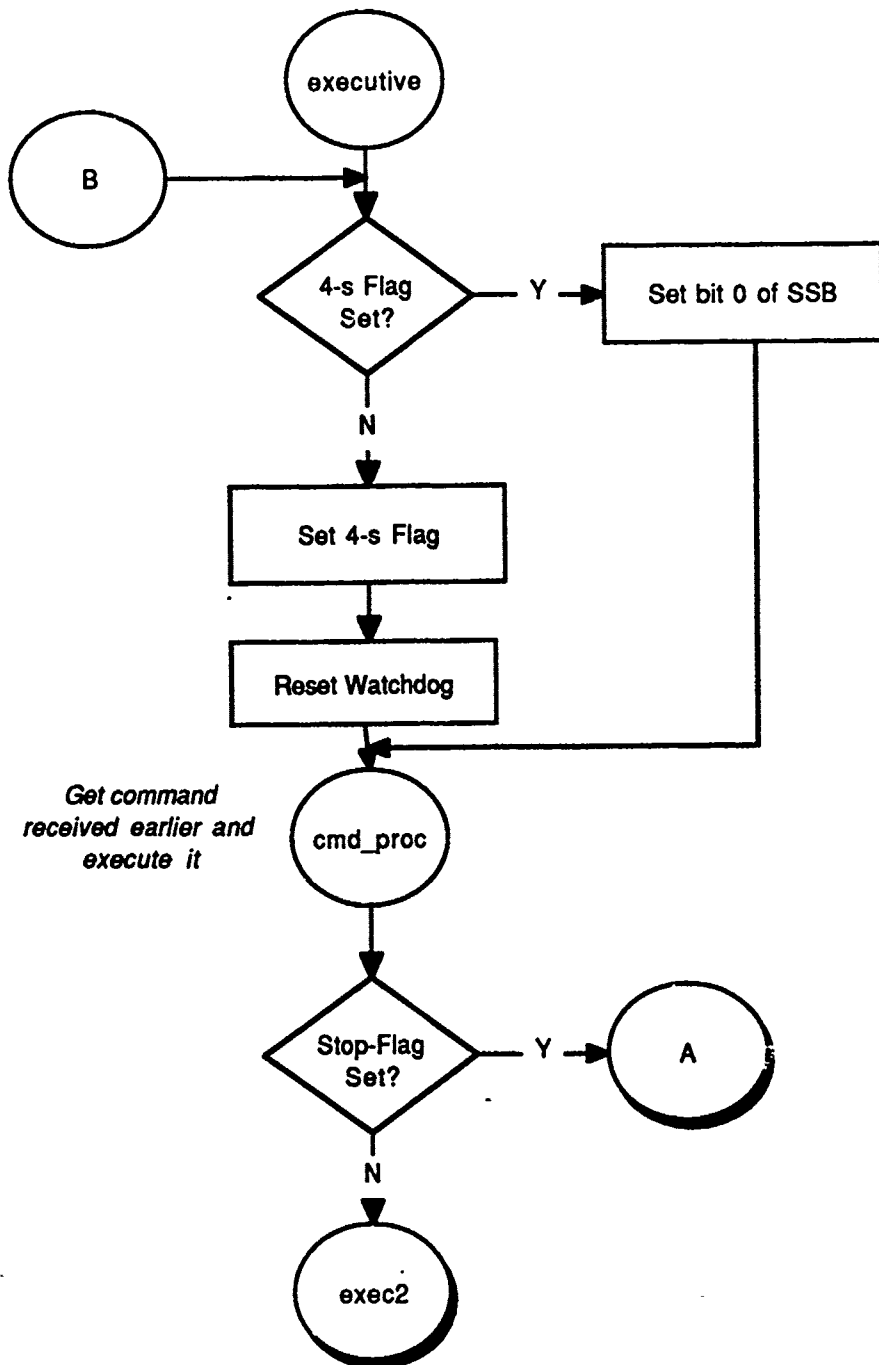
Figure 6-12. Software "executive" routine.

102
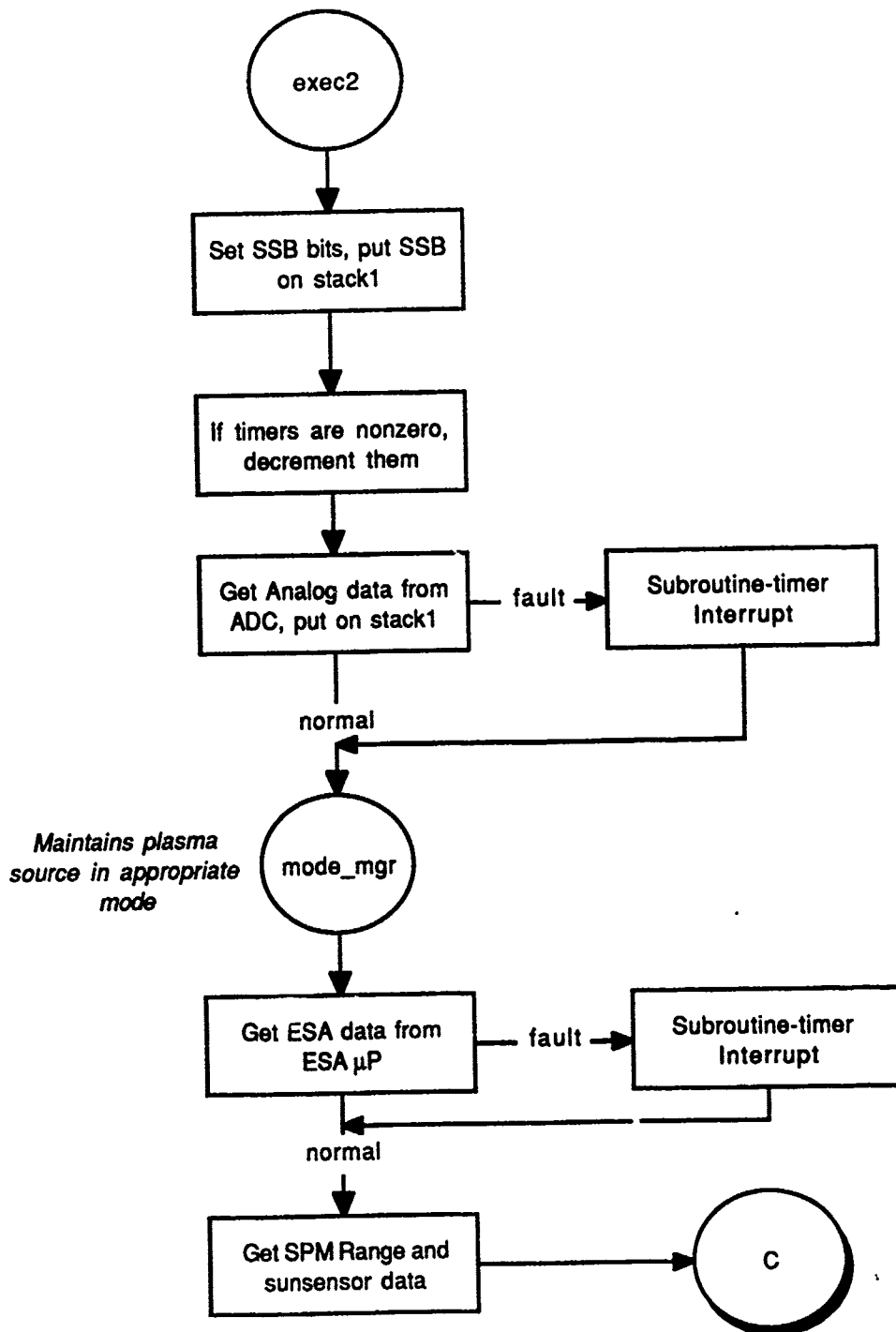
Figure 6-13. Continuation of the executive routine, "exec2".

the master μP communicates with the ESA μP to gather the next data set, if one is present. Finally *exec2* gets the SPM data and (see flowchart continued in Figure 6-14) calls the *hazard* algorithm. *Hazard* examines the set of data just collected and makes a determination that a charging hazard either does or does not exist. If a charging hazard is determined to be present, the charging flag is set; this will cause *mode_mgr* to ignite the plasma source on the next pass.

Following execution of the *hazard* algorithm, *exec2* divides the 16-bit counters that count charging indications and the source of plasma-source ignition indications into iupper and lower bytes and places them on stack1. *Exec2* then examines the ADC temperature-indicator data to determine if any instrument has exceeded its temperature limit. If overheating instruments are detected, they are turned OFF unless a ground-commandable mask bit has been set (this permits ignoring data from a faulty temperature sensor). *Exec2* then calls *SPM_zero*, which determines whether the SPMs should read zero (in case the plasma source has been in operation for a predetermined period); if they should, *SPM_zero* stores the SPM readings to be used as zero offsets for subsequent readings. Finally, exec2 places the power-relay status and other data on stack1 and calls the function *map*. *Map* takes the data in stack1 and reorders it according to a preset priority list. The reordered data is placed in stack2; these data are then copied into DMA RAM in servicing a frame-sync interrupt (see next paragraph). When *map* is complete, exec2 clears the 4-s flag, indicating completion, and jumps to the label "start" which is in *main*; here the bitflip protection algorithm will be executed, and the μP will await the 4-s interrupt, which begins the next cycle.

6.2.1.4 Charging Identification: *Hazard*

Hazard, shown in Figure 6-15, successively examines data from each instrument: if the instrument's power relay is closed, the ground-setable instrument mask bit corresponding to that instrument is not set, and a subroutine-timer fault has not been registered. For each active instrument, *hazard* maintains a software counter which determines the number of uninterrupted positive charging indications that are required to make a charging-hazard determination. Both these counters and the thresholds are ground-adjustable. In the case of the ESAs, the required counts are automatically adjusted according to the ESA sweep time. The functions *h_iESA*, *h_eESA*, *h_SPM1*, *h_SPM2*, and *h_IPS* are shown in Figures 6-16 to 6-19 (*h_SPM2* is not shown since it is identical to *h_SPM1* except for the counter variable). (Note that these functions are defined for flowcharting clarity only; these algorithms are embedded entirely within *hazard* in the actual code.)
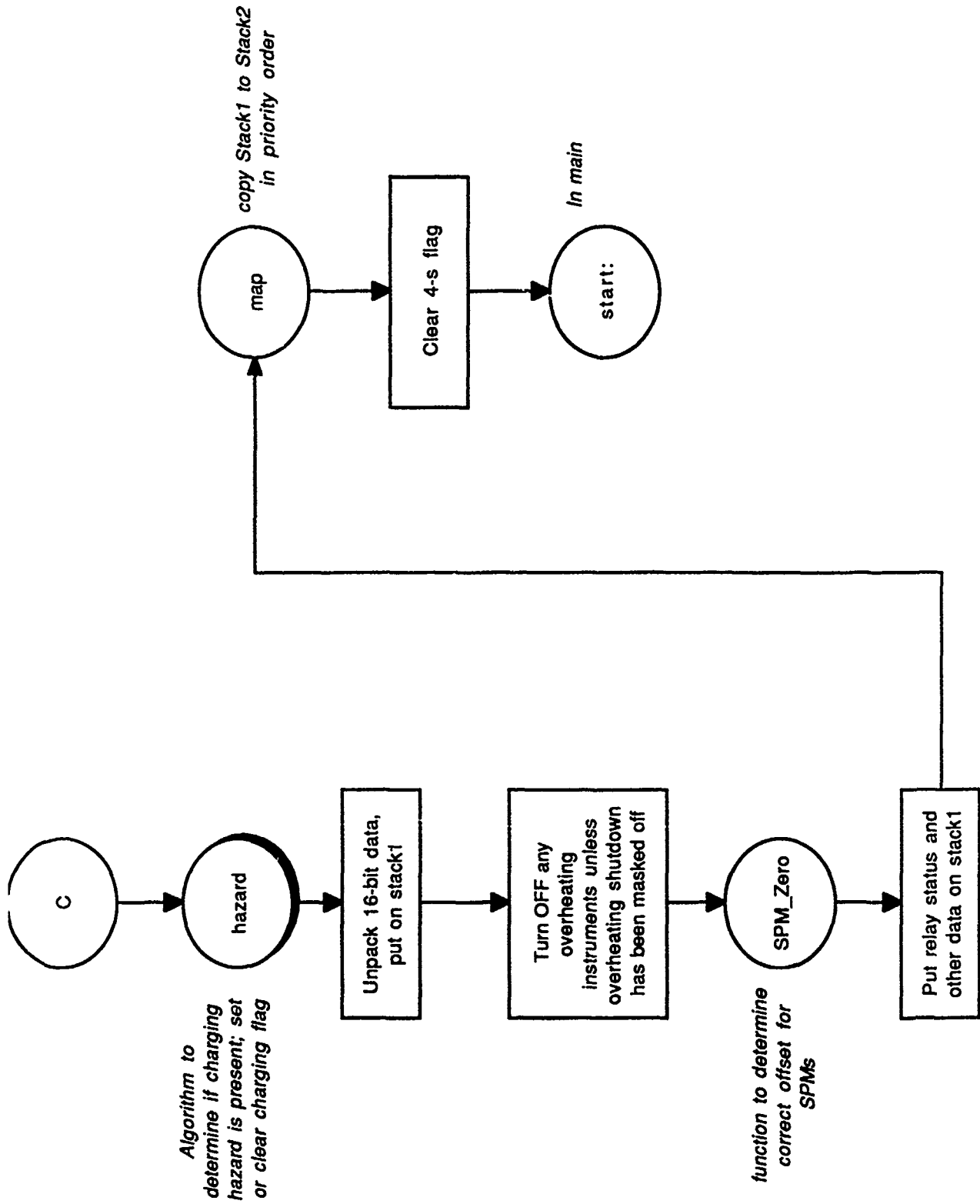
Figure 6-14. Continuation of the "exec2" routine.
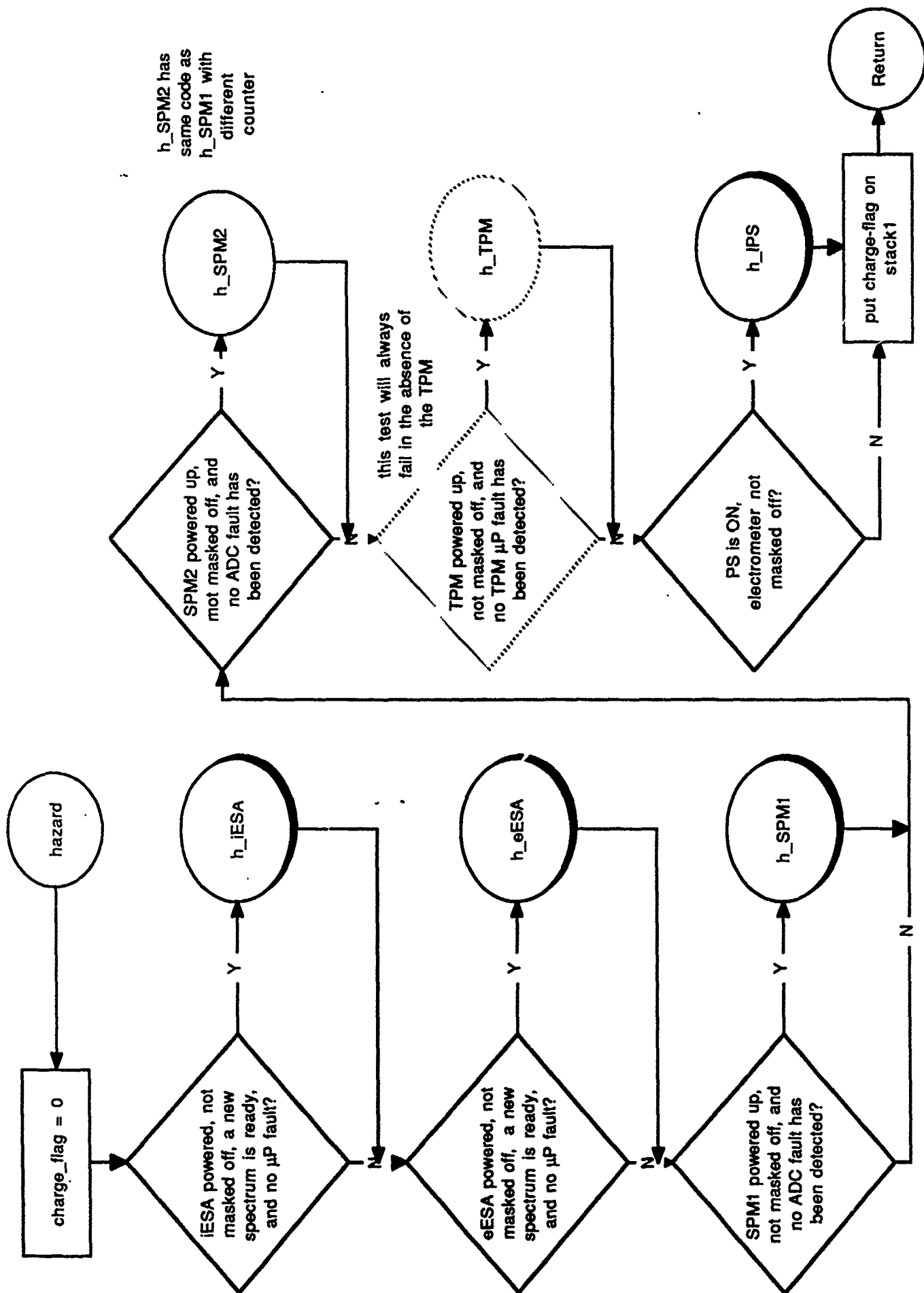
Figure 6-15. "Hazard" software routine.

hazard

charge_flag = 0

iESA powered, not masked off, a new spectrum is ready, and no μP fault? — Y → h_iESA

eESA powered, not masked off, a new spectrum is ready, and no μP fault? — Y → h_eESA

SPM1 powered up, not masked off, and no ADC fault has been detected? — Y → h_SPM1

SPM2 powered up, not masked off, and no ADC fault has been detected? — Y → h_SPM2

h_SPM2 has same code as h_SPM1 with different counter

TPM powered up, not masked off, and no TPM μP fault has been detected? — Y → h_TPM

this test will always fail in the absence of the TPM

PS is ON, electrometer not masked off? — Y → h_IPS

N → put charge-flag on stack1 → Return

Figure 6-16. Ion-ESA hazard-present routine.
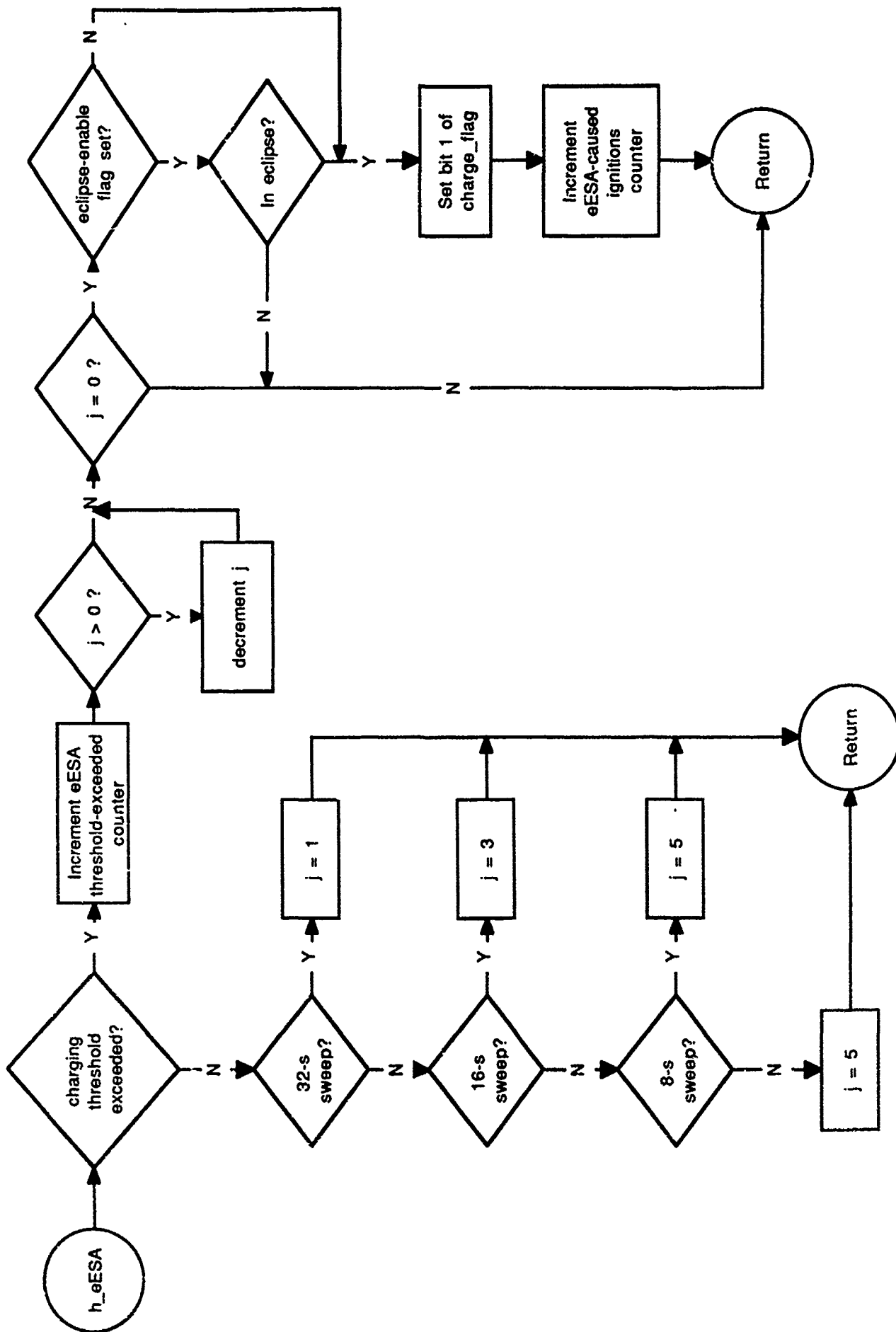
Figure 6-17. Electron-ESA hazard-present routine.

108
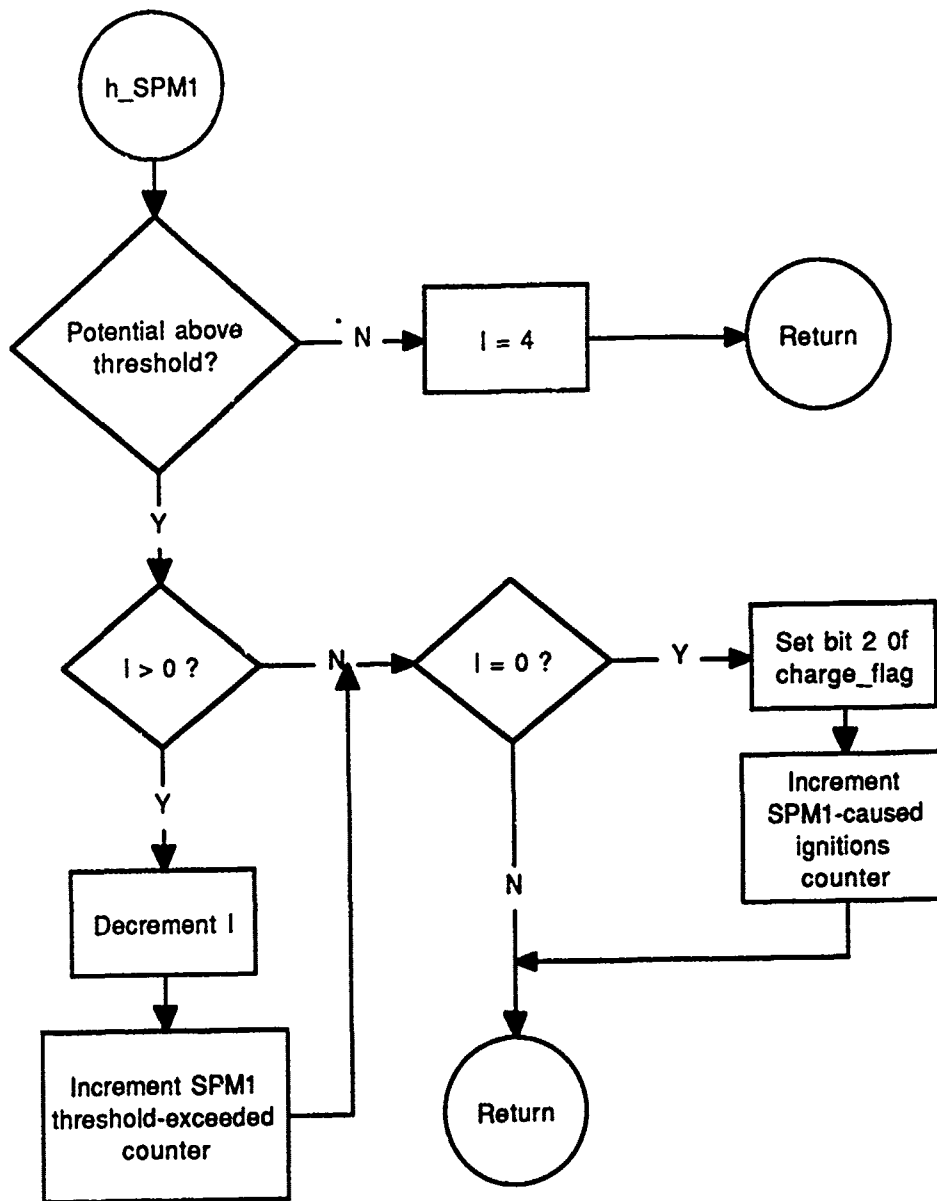
Figure 6-18. SPM1 hazard-present routine.

109
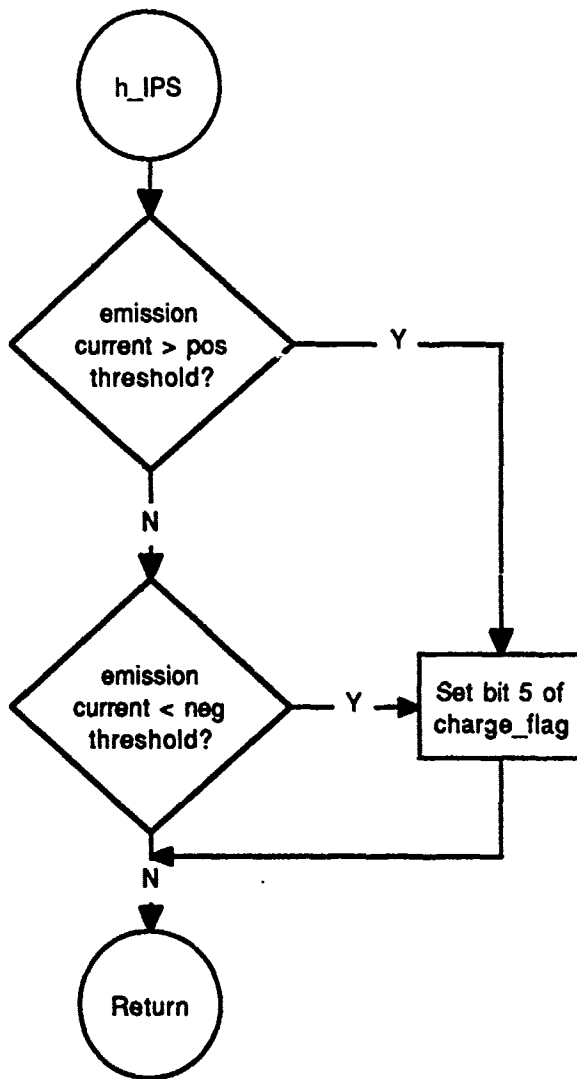
Figure 6-19. Plasma-source hazard-present routine.

6.2.1.5 Servicing the Frame-Sync Interrupt: *Telemetry_out*

The frame-sync interrupt service routine shown in Figure 6-20 interrupts the master μP and forces a jump to the *telemetry_out* function. *Telemetry_out* copies a new telemetry data set from stack2 into the DMA area of memory, resets the DMA counter, and initiates a DMA cycle before allowing the μP to return to its previous activity. The DMA cycle consists of a DMA bus request, loading a telemetry byte into the telemetry shift register, incrementing the DMA counter, and return of the bus to the microprocessor.

6.2.2 ESA Microprocessor

The ESA μP provides the master μP not only with ion and electron spectra, but also with a numerical estimate of the vehicle potential (iESA) and a yes-no assessment of the charging threat (eESA). Figure 6-21 is a simplified view of the ESA software. Basically, the μP spends its time waiting for interrupts. The RST 5.5 interrupt causes the μP to communicate with the master μP, either sending a spectrum and other data, or receiving an EEPROM-write command. The RST 6.5 interrupt is used to signal the μP that one channel's worth of data is ready to be read out of the ESA electronics. The ESA data are partially unpacked when they are received, unless any of several error conditions are detected, in which case the current spectrum is ignored. When a complete spectrum (16 channels) is complete, the vehicle potential is computed and the electron algorithm is executed. On completion of these actions, a flag is set to inform the master μP that a new spectrum is ready on its next receive-mode communication.

6.2.2.1 Computing Vehicle Potential from iESA Data

The algorithm used for determining vehicle potential based on the iESA data is shown in Figure 6-22. This "distribution-function-algorithm" (DFA)[4] was authored by Gussenhoven of AFGL and Spiegel of the University of Lowell. It examines adjacent iESA energy channels to find an abrupt increase in ion counts from one channel to the next. The algorithm calculates the difference of counts between adjacent channels and determines whether this difference is both large enough and of adequate statistical significance. The sharp rise in count rate is assumed to result from the acceleration of ambient low-energy ions through the potential difference between the spacecraft and local space plasma. If this potential difference is V_S, then no space-potential ions can traverse the ESA when it is tuned to an energy lower than eV_S. This situation creates an ion energy spectrum which has a characteristically sharp edge below which there are (ideally) no ion counts (some counts are, however, found in the "impossible" region between energies of 0 and eV_S; these counts are probably due to spacecraft generated charges). The DFA seeks to identify the spectral edge at energy eV_S by looking for a large and statistically significant increase in count rate between adjacent channels.

111
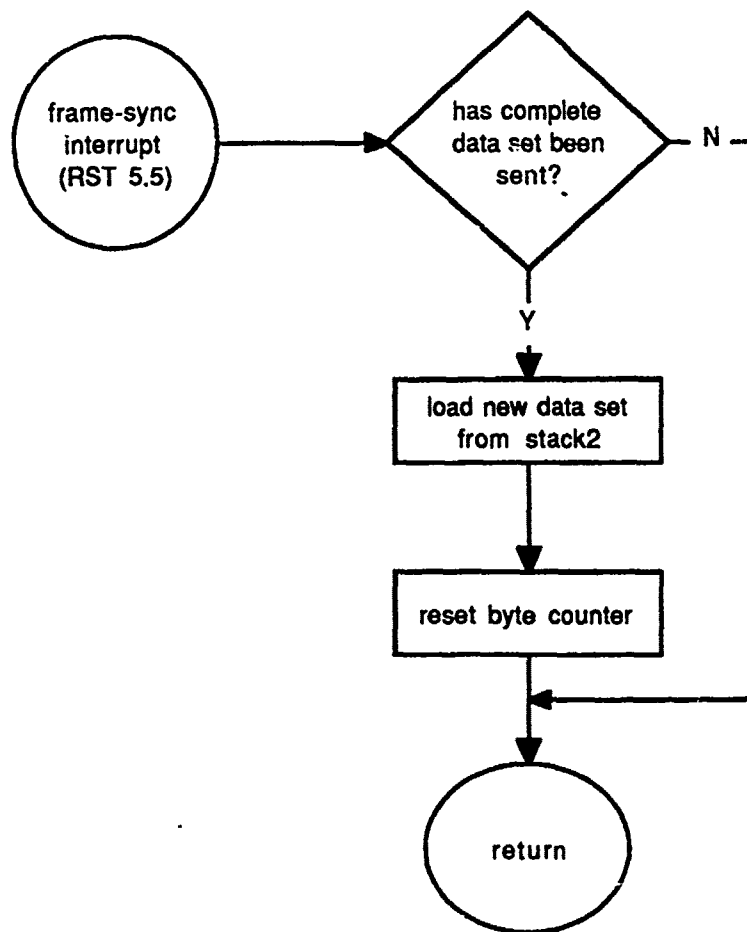
Figure 6-20. Frame-sync interrupt-service routine.

112
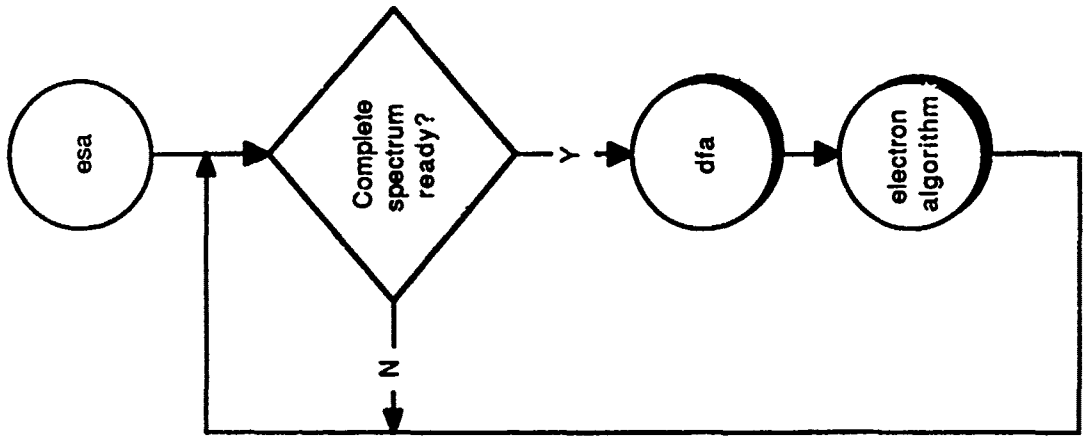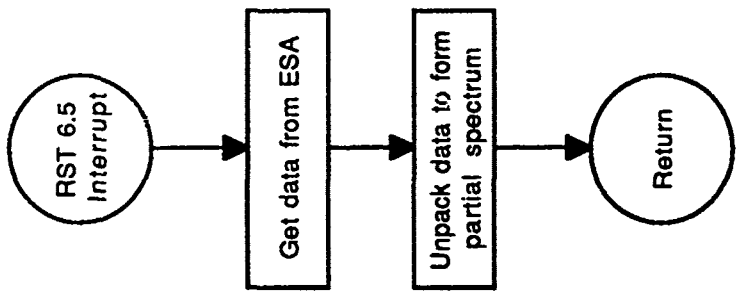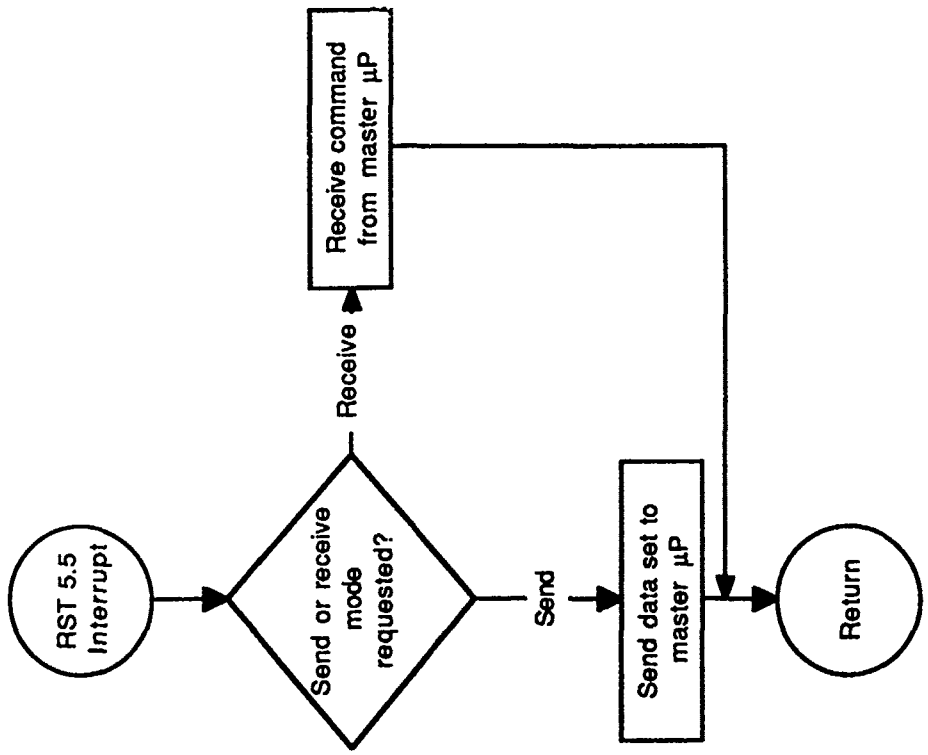
Figure 6-21. ESA microprocessor software.

113
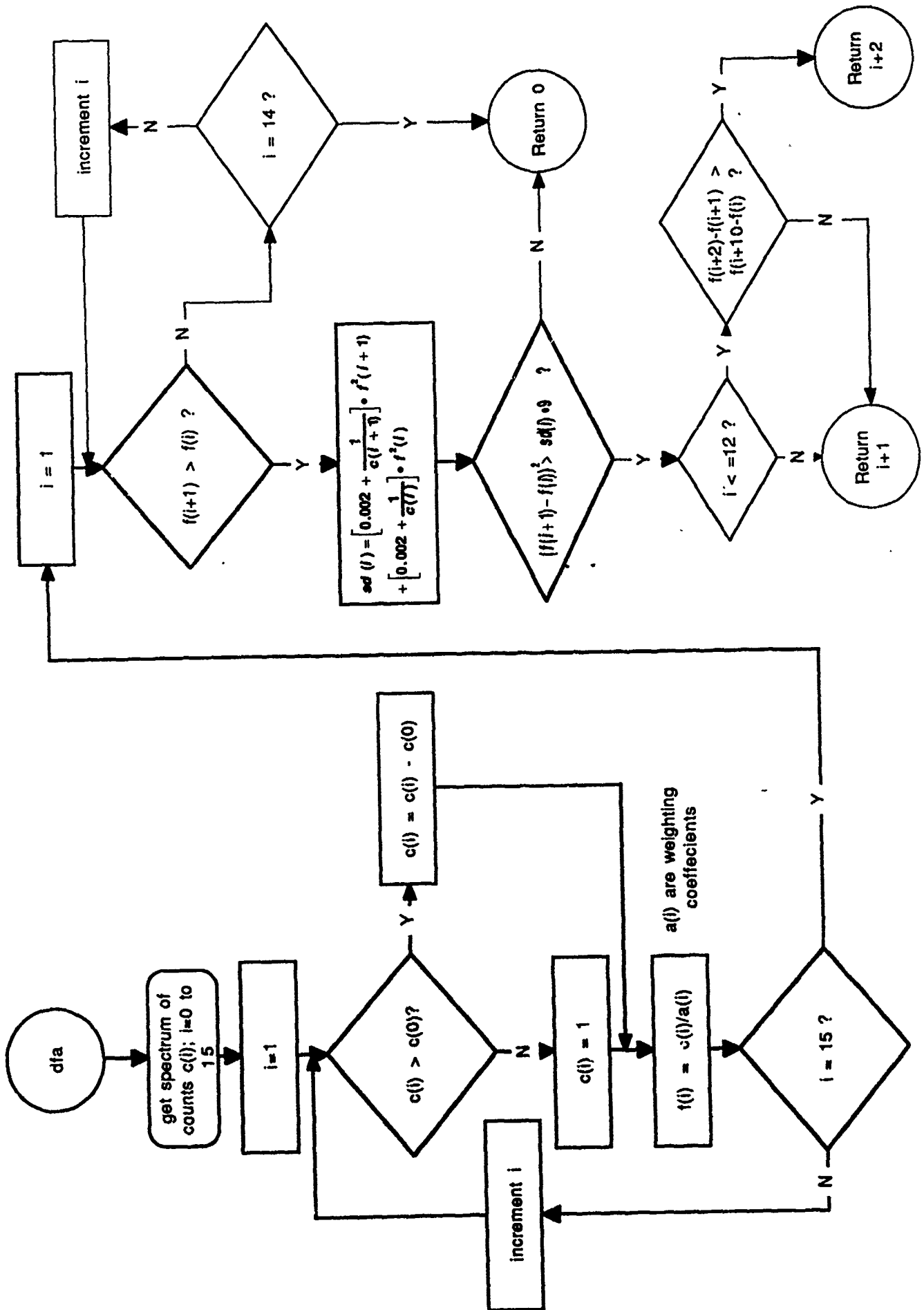
Figure 6-22. Flowchart of the distribution-function algorithm (DFA).

114

The other algorithm which we considered seriously was a template-matching-algorithm (TMA) which was implemented by preparing a number of templates -- dummy spectra which have calculated edges and shapes corresponding to varying degrees of spacecraft charging. The TMA sequentially compared the actual ion-energy spectrum with each of the templates and produced a vehicle potential which corresponded to the closest match between a template and the actual spectrum.

6.2.2.2 iESA Algorithm Testing

We tested these two algorithms (DFA and TMA) using SC-9 data which was reformatted into the FMDS channel widths and energy range. These data were accompanied by a "visual" analysis: an estimate of vehicle potential for each spectrum, as determined by an expert. The visual analysis served as our reference for accurate charging-algorithm operation. The tests indicated that the DFA was more accurate than the TMA on a spectrum-by-spectrum basis, as shown in Table 6-1. On a charging-event basis the DFA was found to determine charging above threshold 100% of the time. A few spectra might not agree, but the charging event was always detected. Two typical charging events and a comparison of the visual and DFA determined vehicle potentials are shown in Figure 6-23. As can be seen from the figure, the DFA closely tracks the visual.

6.2.2.3 Electron Algorithm

The algorithm used by the ESA μP for interpreting the eESA data is shown in Figure 6-24. It is a simple algorithm that compares the sum of the counts in the two highest energy channels with the sum of the counts in the lower energy channels (excluding the background channel). If the two highest energy channels contain more counts than the lower energy channels, then it is probable that a charging environment exists. This algorithm is based on results by Olsen[5] but has been tested (with good success) with only one day of SC-9 data.

6.3 BREADBOARD TESTING

The controller and its software were debugged, tested, and modified as the complete FMDS system was being checked out and prepared for the breadboard demonstration. Modifications were made as their need was pointed out by the testing or when worthwhile improvements were uncovered. In general, it performed very well as shown by the breadboard system test results presented in Section 10. Two notable exceptions are discussed below.

One of the major glitches during the breadboard demonstration was loss of sync for the telemetry data and latchup of the command and telemetry UART in the controller. This problem resulted in abandoning the UART in favor of the conventional enable signal, clock signal, and

Table 6-1. Comparison of the DFA and TMA Ion ESA Algorithms.

15866—17

SPECTRUM-BY-SPECTRUM

ALGORITHM	THRESHOLD ENERGY (eV)	VISUAL	AGREE	DISAGREE	MISS	ACCURACY
DFA	2000	873	760	79	113	87.1%
	1000	2025	1933	168	92	95.5%
	448	3020	2813	120	207	93.2%
	200	3819	3458	178	361	90.6%
TMA	1000	2025	1805	655	220	89.1%

VISUAL — NUMBER OF SPECTRA WHICH INDICATE CHARGING ABOVE THRESHOLD AS DETERMINED BY AFGL VISUAL INSPECTION OF AVAILABLE DATA.

AGREE — ALGORITHM AGREES WITH VISUAL.

DISAGREE — ALGORITHM INDICATES CHARGING ABOVE THRESHOLD WHEN VISUAL DOES NOT.

MISS — ALGORITHM DOESN'T INDICATE CHARGING ABOVE THRESHOLD WHEN VISUAL DOES.

116
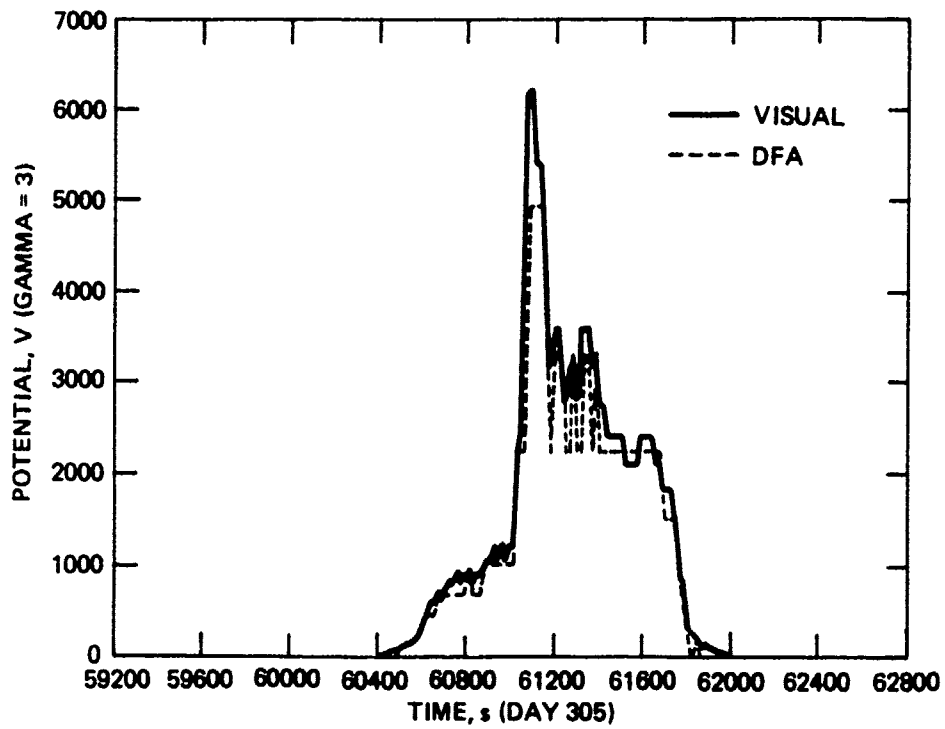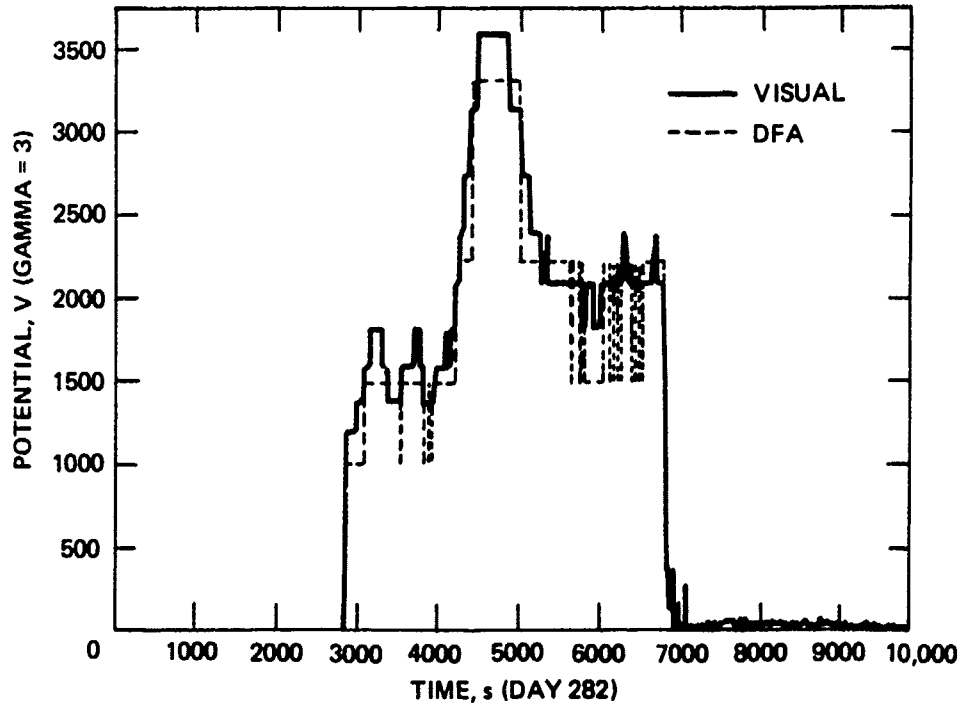
Figure 6-23. Comparison of the visual and DFA-determined vehicle potential.

117
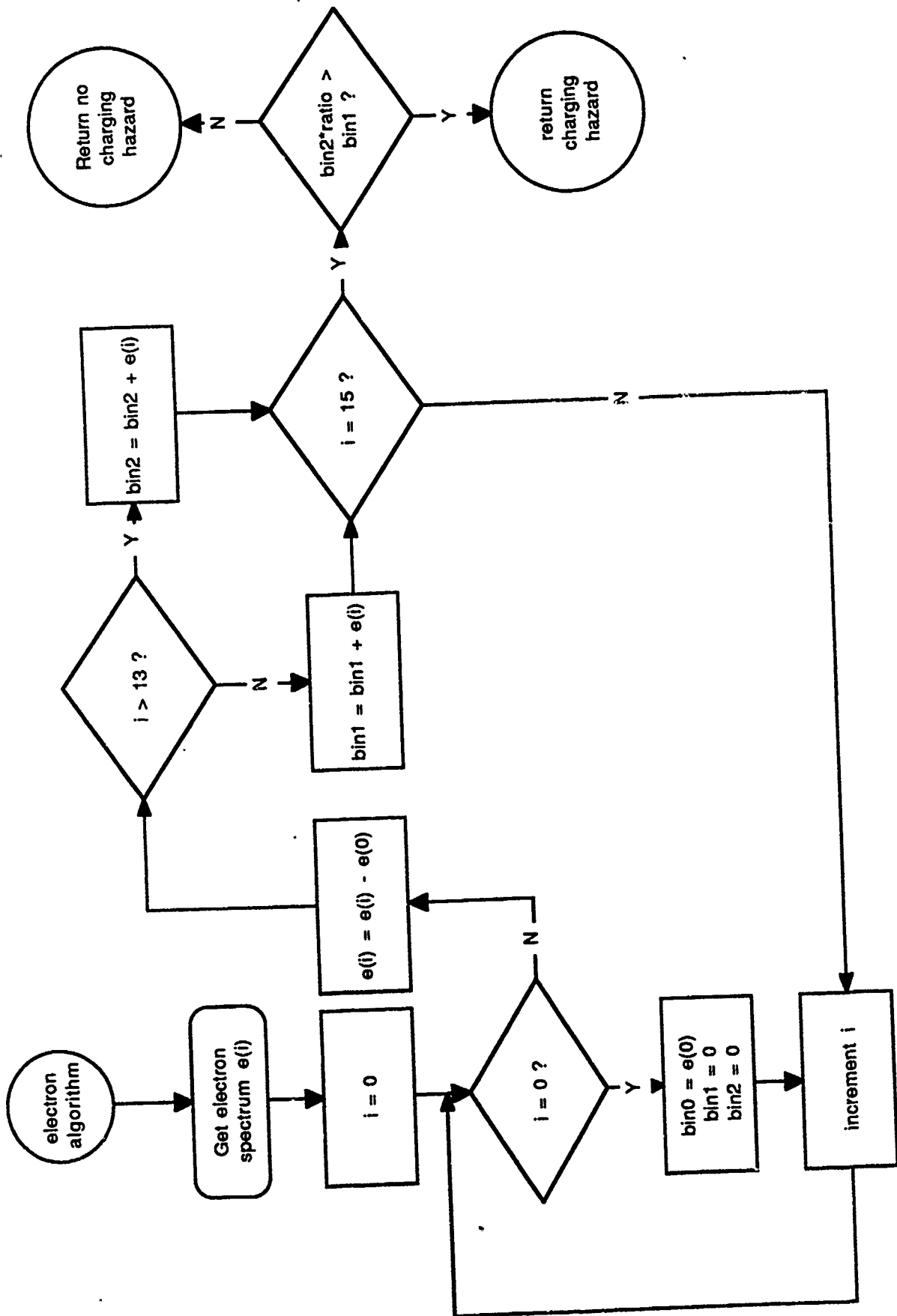
Figure 6-24. Flowchart of the electron-ESA algorithm.

118

data signal type of interface discussed in Section 6.1. We have used this type of interface before without the problems that were experienced with the UART.

The ion-ESA algorithm that we wrote along the lines of Spiegel's Distribution Function Algorithm (DFA) called for subtracting the background channel counts from the other channels before looking for a statistically significant edge. Since the count in the background channel was equal to or larger than some of the other channels and the DFA returned a count of 1 for subtractions that were negative or zero, then going from 1 to 3 or 4 counts after the subtraction appeared to be statistically significant, when in reality there was no edge at that channel in the raw data. When the subtraction of the background channel was eliminated, the DFA determined the correct level of spacecraft charging.

6.4 FLIGHT TESTING

The controller hardware and software were tested on the bench before being integrated with the remainder of the FMDS subsystems. One major hardware problem and one major software problem were discovered and fixed during this testing. Both problems were associated with the EEPROM. The hardware problem resulted in the complete contents of the EEPROM being lost. This problem was discovered the first time that we had the software loaded into EEPROM. We shut the controller OFF and went to lunch. When we returned approximately one hour later, the contents of the EEPROM was all "0"s. This problem was traced to the fact that the +18 V to the EEPROM (used during write and erase operations) normally had no load on it and therefore decayed with a very long time constant (hours) when the power was turned OFF. With the +18 V present and the normal operating supply (+5 V) at zero, the contents of the Sandia SA2900 EEPROM are lost. This was verified by separate tests on an engineering model SA2900. The problem was remedied by adding a 1K resistor from the +18 V to the +5 V powering the EEPROM.

The software problem with the EEPROM resulted from the microprocessor being interrupted by the TRAP interrupt during the time that the EEPROM write routine was being executed. The TRAP interrupt doesn't save the contents of any of the registers and also changes the stack pointer; therefore, the software never returned to finish the EEPROM write routine, causing portions of the software in EEPROM to be erased and not rewritten. The software was changed to prevent any of the interrupts from interrupting the microprocessor during the EEPROM write routine.

The remainder of the bench testing of the controller consisted of fixing minor coding problems in the software. Software integration problems with the other FMDS subsystems are covered in Section 10.

SECTION 7
PLASMA SOURCE

The FMDS plasma source consists of three subsystems: the plasma generator, the power electronics required to operate and control the plasma generator, and the expellant storage and control assembly. The plasma generator was developed under a Hughes IR&D project and this technology was provided to the FMDS program for the flight plasma generator design.

7.1 PLASMA GENERATOR DESIGN

The plasma generator is regarded as the major element of the system, since its design and operating characteristics determine the requirements for the other two elements (power supplies and feed system). The plasma generator has the general characteristics shown in Table 7-1.

The plasma generator (Figure 7-1) is a compact arrangement of a hollow-cathode, keeper and anode electrodes, a magnetic structure, and a ground shield. Xenon/hydrogen gas flowing through the plasma generator is ionized by bombardment with electrons released from a low-work-function surface within the hollow cathode. The ionized gas flows out of the plasma generator, providing a medium density ($\approx 10^{10}$/cm^3), inert-gas plasma to neutralize differential charge buildup between various surfaces of the spacecraft, and also to form an electrically conducting "bridge" between the spacecraft and the natural space plasma.

A <1-s plasma generator turn-ON time is achieved by gas-burst ignition. Approximately 1000 V is applied between the keeper and the cathode, and then a burst of high-pressure gas (few hundred Torr) is admitted to the cathode. The keeper voltage falls almost immediately (<1 ms) to <20 V. We believe that the ignition process consists of the formation of an arc that runs on a small spot on the insert until the insert temperature is raised to the point of thermionic emission. At this point, cathode operation undergoes a rapid transition to a low-voltage hollow-cathode mode. The total energy input during the high-voltage portion of the ignition transient is about 0.25 J, which is nondestructive to the insert. The gas pressure and flow settle out to the nominal 0.5 sccm condition in approximately 120 s.

The rolled-foil insert consists of 0.013-mm- (0.5-mil)-thick rhenium foil with a sputter deposited linear platinum grid deposited on one side. A Hughes proprietary emissive mix is sprayed on both sides of the foil to provide a low work function medium for electron emission. The rhenium foil is then rolled into a cylindrical structure for insertion into the cathode.

Table 7-1. SPACECLAMP Plasma Generator Characteristics.

T9234-15

Parameter	Value	Unit
Expellant flow rate	<40	mA Equiv
Discharge voltage	<40	V
Discharge current	<250	mA
Keeper voltage	<25	V
Keeper current	<400	mA
Total power (run)	<10	W
Total power (conditioning)	20	W
Ignition time	<1	S
Expected lifetime	>1200	Hours
Expected restart capability	>1000	Starts
Ion-emission current (max)	>1	mA
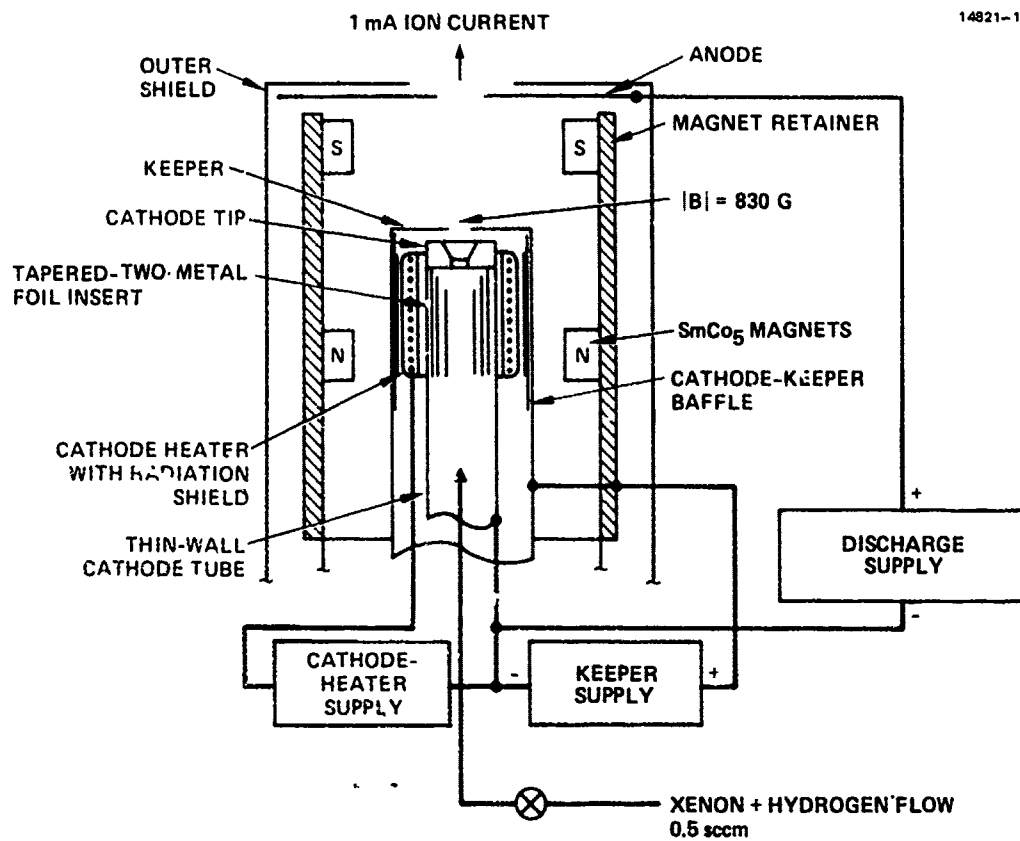
Figure 7-1. Simple schematic of the plasma generator.

The flight design of the plasma generator is shown in Figure 7-2 and an exploded view of a flight source in Figure 7-3. The plasma generator is designed as a hermetically sealed unit so that it can be evacuated (through a remove-before-launch cap) and operated during ground testing and spacecraft integration. The cathode, keeper, and anode are all electrically isolated from the outer shell so the return current from the spacecraft can be measured.

7.2 EXPELLANT STORAGE AND CONTROL SYSTEM

The expellant feed and control system consists of the storage tank, valves, pressure regulator, flow impedance, and pressure transducers required to provide the source with gas-burst ignition and a steady-state 0.5-sccm flow rate (Figure 7-4). The storage tank is a Department of Transportation (DoT) approved pressure vessel (rated for transportation on commercial aircraft) with a volume of approximately 2 liters and containing 90 standard liters of xenon and 10 standard liters of hydrogen at a pressure of approximately 4.1 MPa (600 psia). The tank is fitted with a pressure transducer (to indicate the quantity of remaining expellant) and a manually operated fill valve.

The xenon/hydrogen flows from the tank through the high pressure valve, which is intended to save the expellant if a slow downstream leak should develop, to the pressure regulator. The pressure regulator reduces the xenon/hydrogen pressure to a constant 69 kPa (10 psia). The 69 kPa is applied to the upstream side of a constant flow impedance to maintain a steady state flow rate of 0.5 sccm. The low-pressure valve is the valve that actually turns the flow to the plasma generator ON/OFF.

The low pressure transducer measures the pressure in the gas-burst volume and is used to indicate if the low-pressure valve is open or closed. With the valve closed, the pressure in the gas-burst volume builds up to 69 kPa which indicates that the valve is closed. If the valve is open, then the pressure in the gas-burst volume is approximately zero and indicates that the valve is open. The gas-burst volume provides the burst of gas required for gas-burst ignition and the bypass valve is used to quickly fill this volume. The low-pressure valve and the bypass valve are never both open at the same time.

The tank is removable from the remainder of the FMDS so that it can be filled and/or transported separately. Sectional drawings of the flight valves and flight pressure regulator are shown in Figures 7-5 and 7-6, respectively. The same valve is used for both the high-pressure and low-pressure portions of the feed system.

7.3 PLASMA GENERATOR ELECTRONICS DESIGN

The Plasma-Generator electronics block diagram is shown in Figure 7-7. It contains a discharge supply, keeper supply, and a heater supply for operation of the plasma generator, a
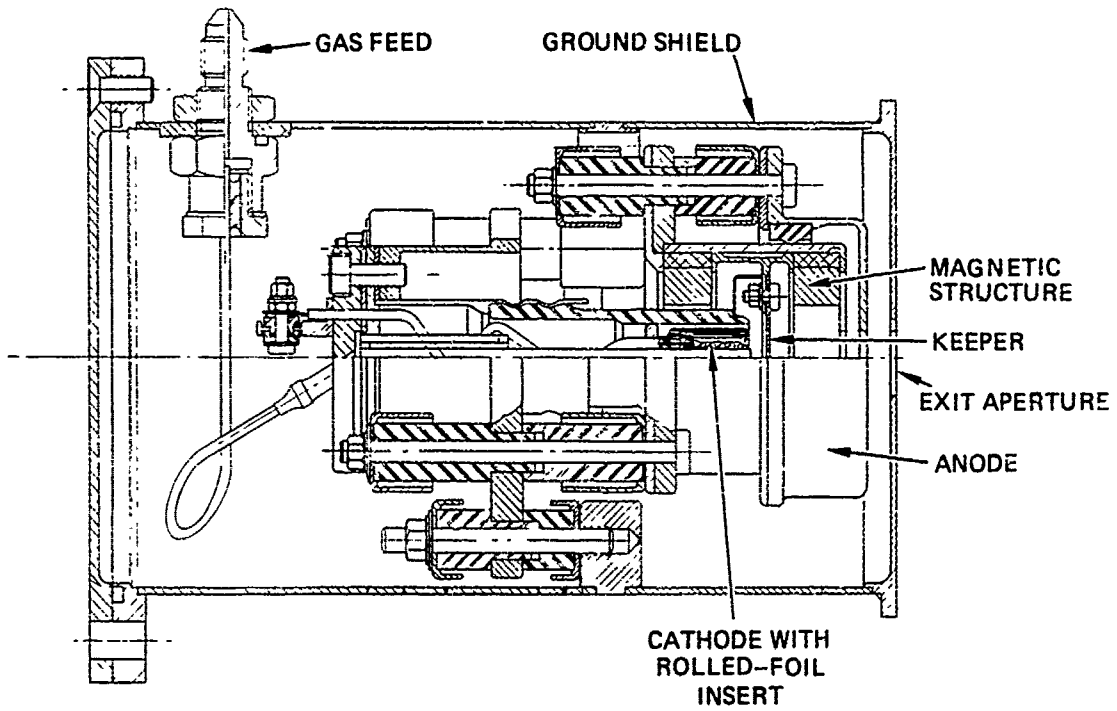
Figure 7-2. Cross section of the flight plasma generator.

124
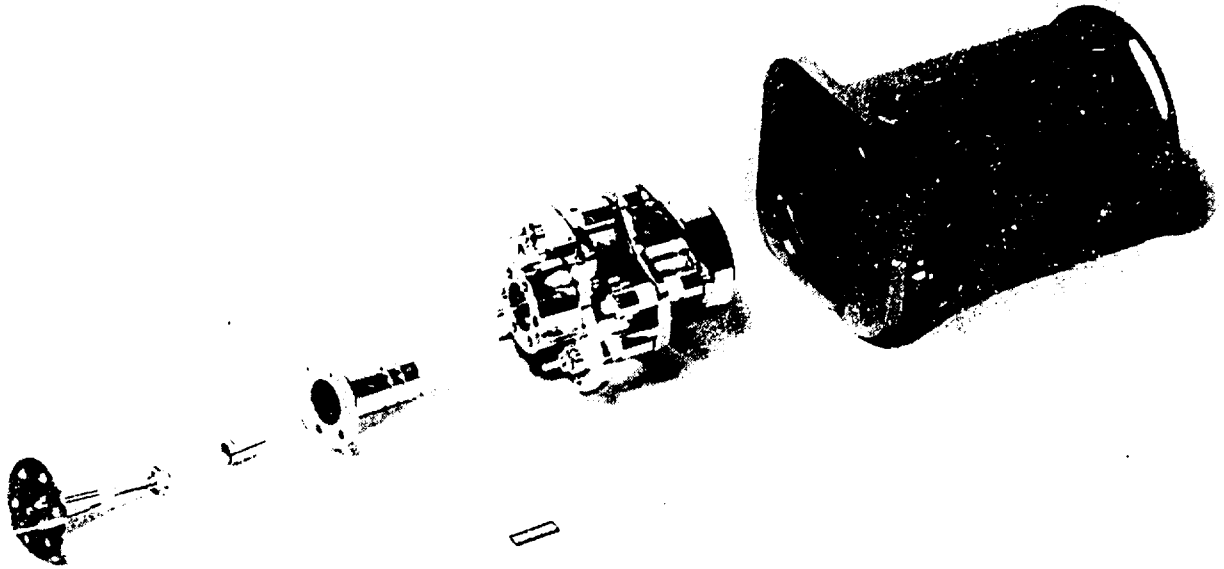
Figure 7-3. A flight plasma generator in an exploded configuration.

14961—17R3

XENON AND HYDROGEN TANK

FILL VALVE

HIGH PRESSURE TRANSDUCER

HIGH-PRESSURE VALVE

REGULATOR

BYPASS VALVE

FLOW IMPEDANCE

GAS-BURST RESERVOIR

LOW PRESSURE TRANSDUCER

LOW-PRESSURE VALVE

PLASMA SOURCE
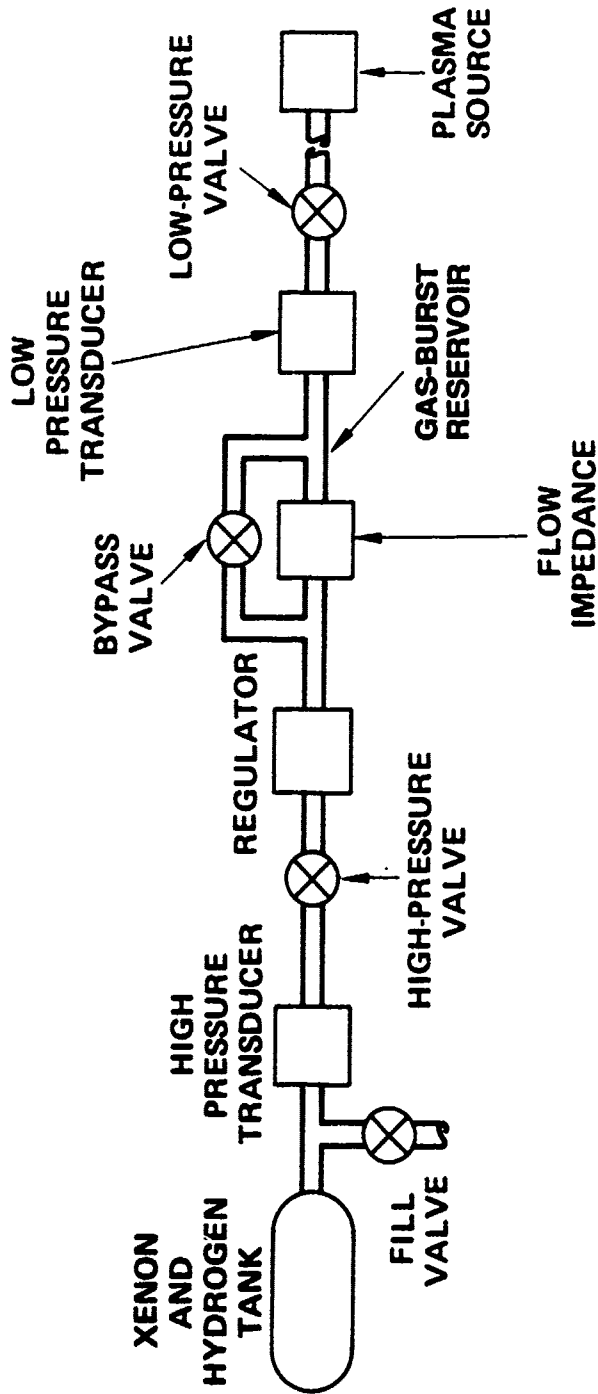
Figure 7-4. Block diagram of the expellant storage and feed system.

14961-3

1.19 DIA   IN

MACHINE PLUNGER
TO OBTAIN .018 - .024
STROKE

0.33

.060
WITH ENDS
FLUSH (REF.)

0.727
0.663

1.62

3.117
3.073

1 MEDIUM_____PURE XENON GAS

2. PRESSURES:
     OPERATING _____10 psig TO 850 psig
     PROOF _____1275 psig
     BURST _____2125 psig

3 TEMPERATURES
     AMBIENT _____OPERATING _____ -40°C TO +71°C
                                  NON-OPERATING __-40°C TO +85°C

4 FLOW_____.020 DIA ESEO (MIN) (Cd= .65)

5. LEAKAGE _____INTERNAL__1.0 x 10^{-5} SCC/sec G He AT 0 TO 850 PSIA
                                EXTERNAL__1.0 x 10^{-6} SCC/sec He AT 850 psig

6 POWER _____30 W MAX. AT 27.2 vdc AND 20°C
     VOLTAGE _____24.8 TO 27.2 vdc
     DUTY _____INTERMITTENT; 100 ms ON 100 ms OFF
     RESPONSE TIME (ELECTRICAL) AT 27 Vdc, 70°F AND 372 PSID
                                  OPENING__40 ms MINIMUM PULSE
                                  CLOSING__40 ms MINIMUM PULSE

7. FILTRATION _____10 μm(NOMINAL)

8 WEIGHT_____0.65 lb (CALCULATED)

9 MATERIALS IN CONTACT WITH MEDIA:
   ST. STL. 302, 304, 304L, AND 430 CHROME PLATE SEAL POLYIMIDE

10. INSULATION RESISTANCE _____100 MΩ AT 500 Vdc

11. DIELECTRIC 500 VRMS (60 Hz) 1 min ____5 mA MAX.
                                         LEAKAGE

Figure 7-5. Cross section of the flight valves.

127

DESIGN DATA

1. MEDIA —————— XENON
2. INLET PRESSURE —————— 25 TO 850 psia
3. REGULATED PRESSURE —————— 5–15 psia (±10% OF SET POINT)
4. FLOW —————— 0.5 ssc/min AT FULL RANGE OF INLET PRESSURE
5. PROOF PRESSURE —————— 1200 psi
6. BURST PRESSURE —————— 2400 psi
7. LEAKAGE:
   INTERNAL —————— 1×10^{-5} scc/s He MAX
   EXTERNAL —————— 1×10^{-6} scc/s He MAX
8. TEMPERATURE RANGE:
   NON-OPERATING —————— -40°C TO +85°C
   OPERATING —————— -25°C TO +71°C
9. WEIGHT, ESTIMATED —————— .32 lb

Figure 7-6. Cross section of the flight pressure regulator.

128
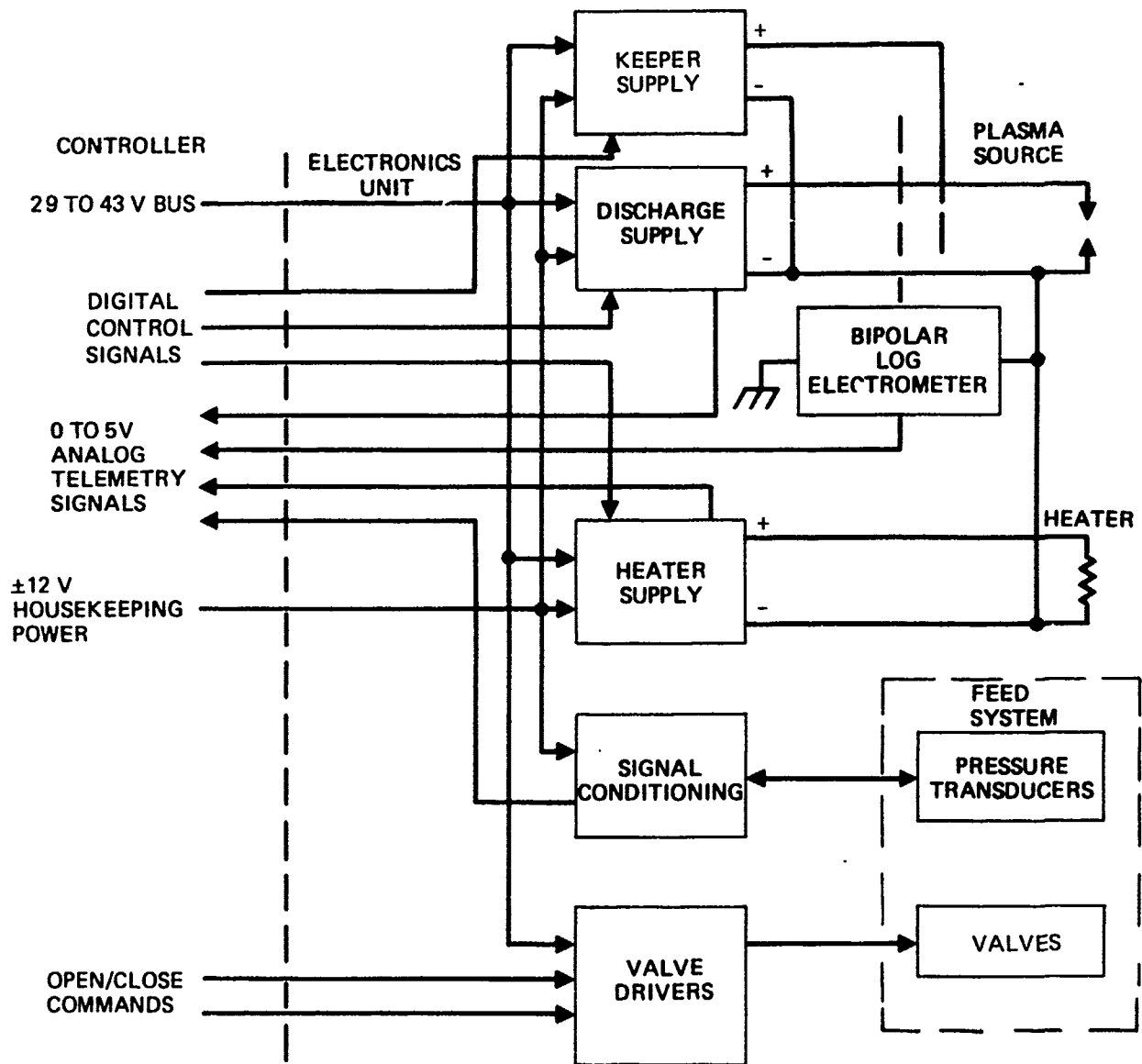
Figure 7-7. Block diagram of the plasma generator electronics.

bipolar log-electrometer to measure the emission from the plasma generator (return current from the spacecraft), valve drivers for the valves, and analog telemetry signal conditioning.

7.3.1 Power Supplies

The plasma generator power requirements are relatively low (<20 W), which rules out the need for complex inverters in order to obtain reasonable efficiencies. Therefore, half-wave flyback inverters are used for all three power supplies. The half-wave flyback inverter (Figure 7-8) is the simplest type of inverter which provides isolation and high reliability while requiring a minimum number of components. Since it operates in a current-source mode rather than a voltage-source mode, it exhibits inherent output short-circuit protection. Only four power-handling components are required:

- One transformer (T1)
- One transistor switch (Q1)
- One blocking diode (CR1)
- One filter capacitor (C1).

The flyback inverter functions by cyclically storing energy in the magnetic field of transformer T1 while Q1 is turned ON and then transferring this stored energy to T1's secondary through diode CR1 to the output filter (C1) and the load when Q1 is OFF. By varing the Q1 ON time, the amount of energy stored and transferred to the load in each cycle can be controlled or regulated in proportion to changes in input voltage, output load, or commanded setpoint.

The heater supply is shown schematically in Figure 7-9. The supply produces a maximum constant-current output of 10 V at 3 A and is controlled by an integrated circuit (U1) which is a pulse-width-modulator (PWM). Regulation is accomplished by sensing the output current with T3 and U3 and feeding this signal back to the PWM. The output of U3 is also used to provide the current telemetry signal.

Optical isolation (U2) is used to isolate the output of U1 which is referenced to control-and-telemetry common from the gate of the switching MOSFET (Q1) which is referenced to input-power common. Q2, Q3, and Q4 interface the output of U2 with the gate of Q1. The peak current through Q1 is limited by sensing this current with T2 and feeding it back to the current limit input of U1.

The voltage telemetry is derived from a seperate winding on the output transformer (T1D). A synchronous sample/hold circuit (Q5 and Q6) is used to minimize the effects of the
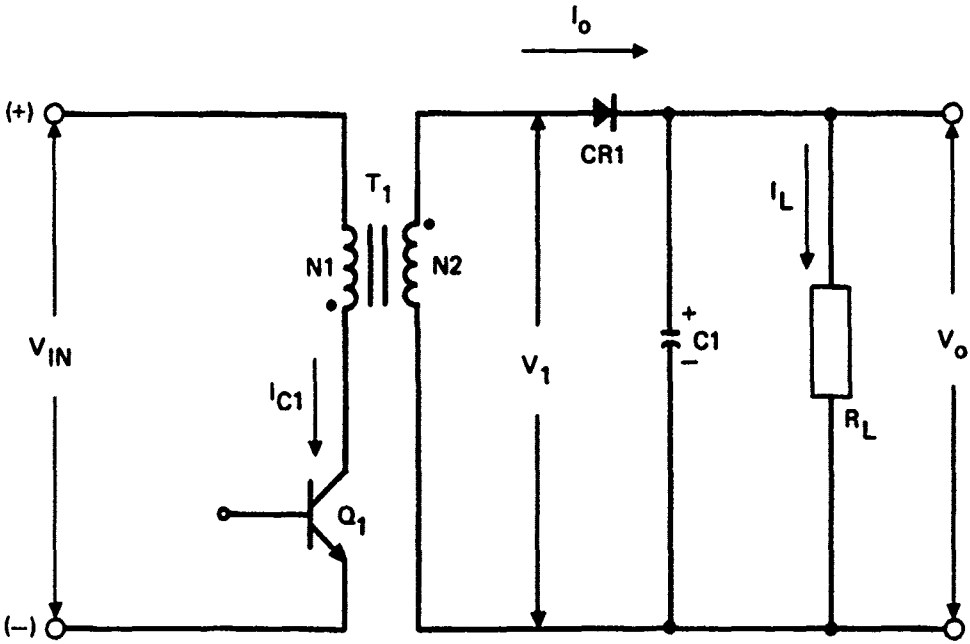
Figure 7-8. Simplified schematic of a half-wave flyback inverter.

Figure 7-9. Heater supply schematic.

leading-edge transient spike. This telemetry voltage is also fed back to the PWM to limit the output voltage under open-circuit conditions.

The ON/OFF command and the setpoint command from the controller are buffered and decoded by U4. U4 is a CMOS quad switch allowing it to function as normally open switches.

The discharge supply design shown in Figure 7-10 is very similar to the heater supply. It produces a constant-current output of up to 0.3 A at up to 40 V and an open circuit output of 100 V. The output voltage is limited to 100 V via VR6 and U6 feeding back to U1. The voltage telemetry signal is not fed back to U1. The peak transient current to the Plasma Generator is limited to less than 1 A by way of Q7, Q8, Q9, and R42.

The keeper supply is similar to the discharge supply and is shown in Figure 7-11. It produces a constant-current output of up to 0.4 A at up to 30 V with an open circuit voltage of 1000 V. The 1000 V is produced by a patented Hughes circuit which automatically turns ON/OFF. If the output is open circuited, then the voltage on T1E will flyback to at least 100 V higher than the input bus voltage, appling 100 V to T2 which is a 10:1 step up transformer which produces the 1000 V output. As the output is loaded down, the flyback voltage on T1E drops below the input bus voltage removing all drive to transformer T2. Peak transient currents to the plasma generator are limited to 400 mA from the 1000 V through R2 and to less than 1.5 A from the low voltage section through Q5, Q4, and R4. Under open-circuit conditions, Q5 turns ON turning Q4 OFF and placing R4 into the circuit. Approximately 30 s after the plasma generator ignites, Q5 turns OFF which turns Q4 ON removing R4 from the circuit. Output inductor L1 also limits transient currents and provides instantaneous voltage spikes to the keeper if it should try to extinguish.

7.3.2 Bipolar Log Electrometer

The bipolar log electrometer measures currents in the ranges of -1 µA to -10 mA and 1 µA to 10 mA. It has a 0 to 5-V analog telemetry output with zero-V out equal to -10 mA, 2.5-V out equal to -1 µA to 1 µA, and 5-V out equal to 10 mA.

Current is converted from being linear to being logrithmic via the base-emmitter junction of a transistor (Q1A or Q2A of Figure 7-12) in the feedback loop of an operational amplifier (AR1). Q1, Q3, and AR3 are used for positive currents and Q2, Q4, and AR2 are used for negative currents. Q1B (Q2B) and R12 (R27) provide temperature compensation for the circuit. Q3 (Q4) is a constant-current source that sets the low end of the logrithmic range (1 µA) while R13 (R10) sets the high end of the range (10 mA) by adjusting the gain of amplifier AR3 (AR2) The outputs of AR3 and AR2 are summed by amplifier AR4 to provide the bipolar function.

133

Figure 7-10. Discharge supply schematic.

134

Figure 7-11. Keeper supply schematic.

Figure 7-12. Schematic of the bipolar log electrometer.

Figure 7-12 also shows the signal conditioning for the plasma generator electronics temperatures and the feed system pressure transducers. Shunt regulator VR7 provides closely regulated 5-V power for both the temperature and pressure measurements. The temperatures are simply measured with a thermistor (R63 or R64) in series with a fixed resistor (R65 or R66) providing a temperature sensitive voltage divider of the regulated 5 V. The regulated 5 V is also applied to the strain gauge bridges of the pressure transducers.. The floating voltage signals from the pressure transducers are amplified and converted to single ended signals by AR5 and AR6 or AR7 and AR8.

7.4 BREADBOARD TEST RESULTS

During the FMDS breadboard testing we used a cylindrical Langmuir probe, which was 7.5 in. from the plasma source, to measure the plasma density. The electron density was measured by biasing the probe tip to collect electron current, which was then used to estimate the electron density. When the source was not biased relative to the vacuum chamber (simulating an uncharged condition) we measured an electron density of $1.5 \times 10^8/cm^3$ and an electron temperature of approximately 1.5 eV. When the source was biased to 30 V relative to the vacuum chamber, the resultant net ion current was about 1 mA, and the electron density and temperature were about $9.5 \times 10^7/cm^3$ and 0.8 eV respectively.

The net ion emission current from the plasma source was measured during ignition and at its throttled setpoints. The emission current was measured by biasing the plasma source 30 V positive relative to the vacuum chamber walls. A plot of net emission current versus bias voltage is shown in Figure 7-13 for the nominal operating point. Figure 7-14 shows a stripchart recording of the emission current during ignition. The emission current starts at 0.4 mA, falls to 0.1 mA at 5 s, increases to 0.8 mA at 8 s and finally steadys out at 1.8 mA at 20 s. The variation in emission current is the result of the pressure inside the source decreasing to its steady-state value after the gas-burst-ignition.

The emission current from the breadboard source was measured for its various operating points. It was:

- 1.8 mA at setpoint 2 (nominal operating point)
- 0.84 mA at setpoint 1
- 0.80 mA at setpoint 0
- 0.45 mA at setpoint 2 with the discharge supply OFF
- 2.05 mA at set point 3.
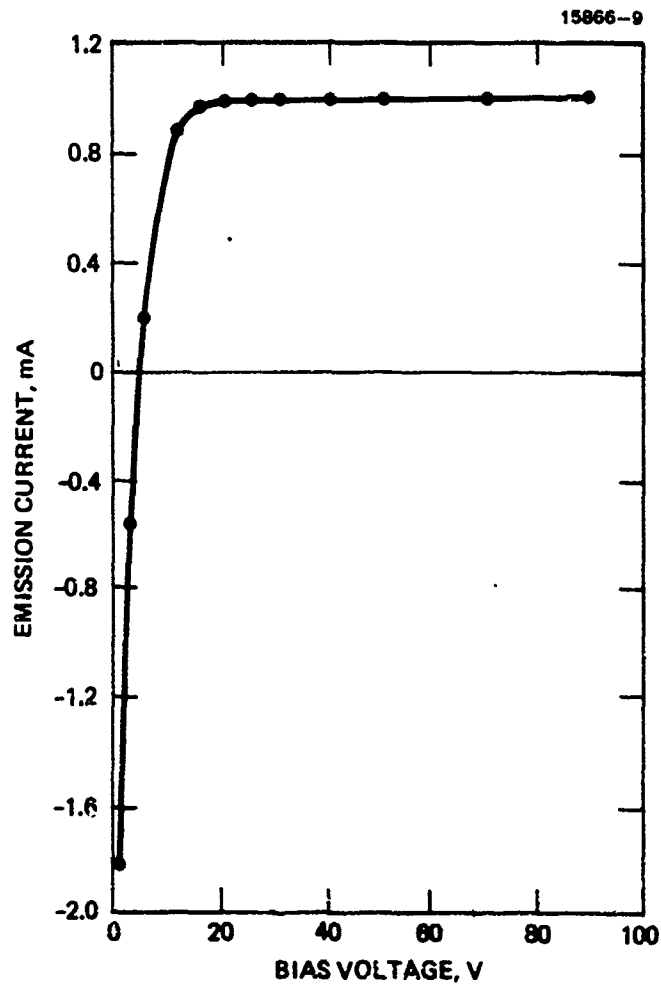
Figure 7-13. Plasma source net emission versus bias voltage for the nominal operating point.
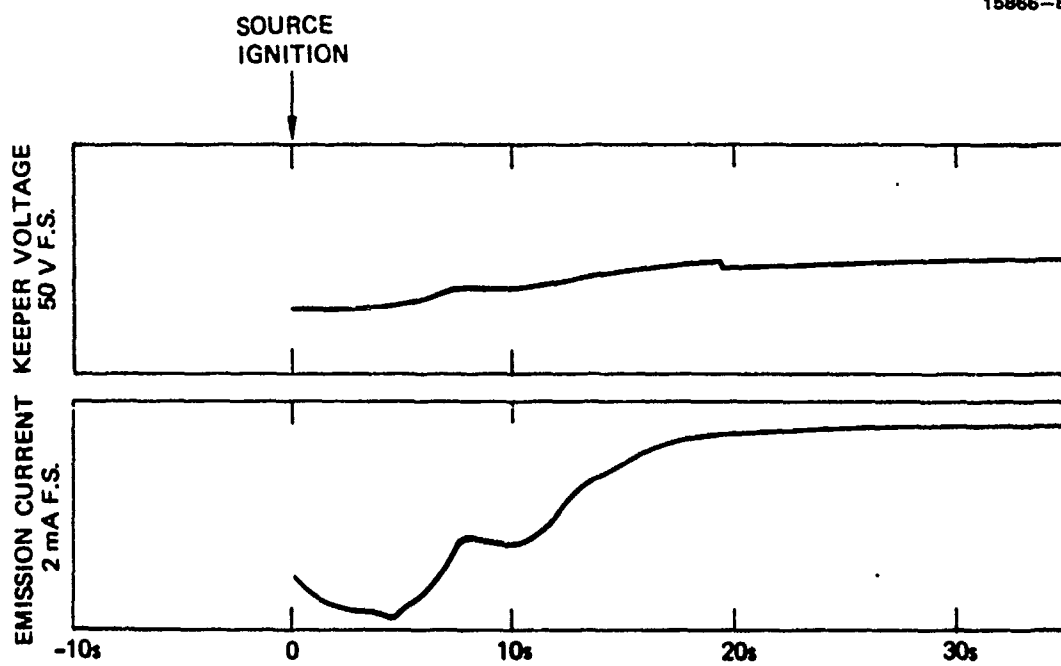
Figure 7-14. Plasma generator emission current during ignitron.

139

For the plasma generator, ion emission as a function of discharge current for a keeper current of 250 mA is shown in Figure 7-15. Some optimization of the plasma source was performed between the breadboard data and the 1 Oct 85 data shown in Figure 7-15. This optimization was performed to improve the ignition and operating characteristics of the plasma generator and as a result of data collected during the breadboard demonstration. The optimization consisted of:

- Incorporating a ceramic insulator between the cathode and keeper and optimizing the gas-burst volume; these changes increase the interelectrode gas pressure to reliably produce the Paschen breakdown that initiates cathode ignition.

- Developing a new cathode-insert fabrication technique in which 0.051-mm-thick foil is used to space and thermally isolate different layers of the rolled-foil insert.

- Tapering the downstream edge of the insert, thereby exposing a greater number of layers of foil to the cathode plasma.

- Improving the discharge-chamber gas feed by providing several gas-diversion holes in the keeper (i.e., post-cathode gas diversion), resulting in increased ion emission from the source.

- Installing a new current-limiting circuit in the keeper power supply to reduce the peak current delivered to the source during ignition, because we have found that ignition currents greater than a few amperes lead to degraded source performance.

A prototype source was operated for a total of 730 hours and 913 gas-burst ignitions as part of a lifetest. The lifetest was terminated after the source operation became unreliable. Upon disassembly of the source, we found that the cathode tube had become brittle and fractured. We utilized SEM and EDAX techniques to carefully examine the cathode, which consisted of a tantalum tube with a tungsten tip and the rolled-foil insert. The elements found within the tube and in the neighborhood of the fracture included aluminum, barium, copper, tantalum, rhenium, and iron. The presence of each element can be explained by the manufacturing techniques used to fabricate the cathode, except for the iron which may have been residual contamination from the SEM vacuum vessel. We concluded that foreign materials were not introduced into the cathode, and that the fragile condition of the tube was probably a result of a reaction between the emissive mix on the rolled-foil insert and the tantalum cathode tube.

140
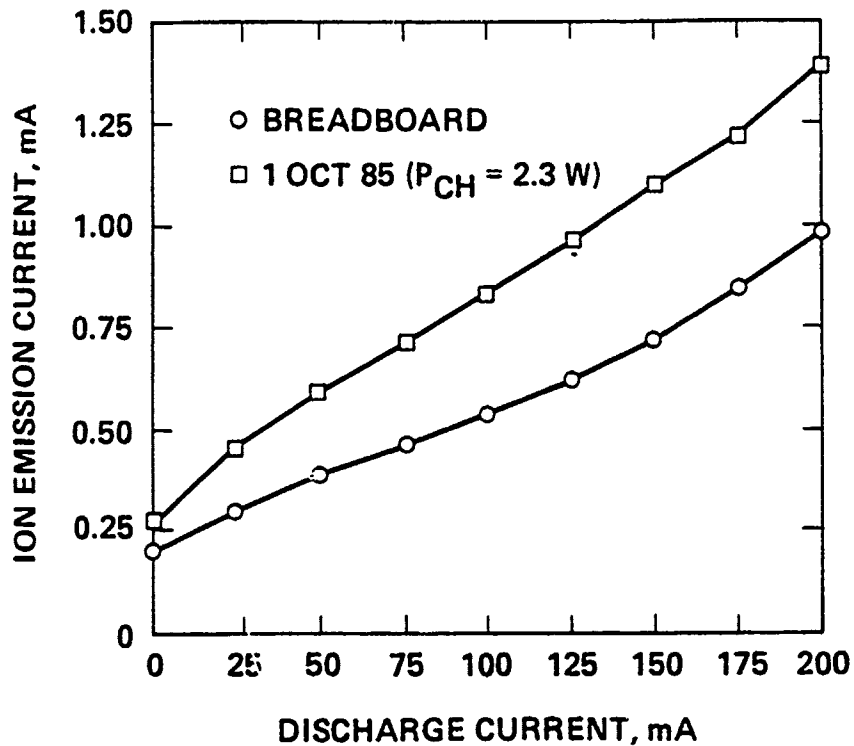
Figure 7-15. Plasma generator ion-emission current as a function of discharge current.

We also found that the 0.010-in.-diameter cathode orfice in the tungsten tip had become partially occluded. However, since we found only aluminum, copper, and tantalum within the orfice and did not measure traces of rhenium or platinum, the occluding material was probably not a remnant of the rolled-foil insert.

The brittle state of the cathode tube indicated that the design of the plasma source should incorporate a cathode tube assembly which is fabricated from an alternative material which is less subject to becoming brittle than tantalum. Therfore the design was changed to 50/50 molybdenum-rhenium; a material that has shown a greater resistance to becoming brittle in testing by Hughes under a NASA-LeRC ion propulsion contract (NAS 3-22474).

141

7.5 CYCLIC LIFE TEST

A cyclic lifetest was performed to demonstrate the required source performance of over 1200 hours of operation and 1000 gas-burst ignitions. The test utilized the plasma generator which was part of the FMDS breadboard demonstration, a new cathode employing moly-rhenium, flight-type power supplies, and a flight regulator (set to 69 kPa) in the feed system. Prior to performing the lifetest, we corrected the less-than-ideal gas-burst ignition properties of the source observed during the breadboard demonstration by optimizing the keeper and discharge power supply load lines.

The test had demonstrated 1,562 hours of operation and 1,582 cold gas-burst starts when we voluntarily terminated the test to permit detailed inspection of the plasma source. The cathode and cathode insert were both in excellent condition, indicating that we had not yet reached the end of lifetime for these critical plasma source components.

The significant aspects of this lifetest relative to previous tests were:

(1)   Use of a 90% xenon and 10% hydrogen gas mixture (as opposed to pure xenon) to ameliorate what we believe to be water vapor deconditioning of the cathode insert.

(2)   The cathode tube was made of a molybdenum-rhenium alloy, chosen for its resistance to chemical attack from the emissive mix and embrittlement by hydrogen.

(3)   The peak keeper current from the 1-kV ignitor supply was reduced from 1 A to 0.4 A.

(4)   An inductor was added to the output of the keeper supply to accommodate short duration instantaneous voltage transients required by the plasma generator during the first 20 s after ignition.

As a result of this life test, several observations can be made.

(1)   The 90/10 xenon/hydrogen gas mixture improved the gas-burst-ignition characteristics while not affecting other operating parameters.

(2)   A minimum ON time of 1 hour improved the gas-burst-ignition characteristics of subsequent cycles.

(3)   Periodic reconditioning of the plasma generator was necessary for reliable ignitions. We recommend after every 100 ignitions since the vast majority of ignition faults during this lifetest occured after 100 cycles since the last reconditioning. Reconditioning consisted of applying 20-W of tip heat for 1 hour and then operating the plasma generator for 1 hour without tip heat.

142

(4)   Steady-state performance (after being ON for approximately 120 s) was very
        reliable.

Throughout the course of the lifetest, we utilized a variety of computer-controlled operating modes. The ON times ranged from 2 minutes to 2 hours, and the OFF times from 1 to 59 minutes. The computer system was capable of performing an immediate restart of the plasma generator if it did not start successfully. After three successive failures, the computer shut the test down and waited for operator-controlled reconditioning to be performed. Reconditioning, which refreshes the layer of work-function-reducing emissive mix on the cathode insert surfaces, returned the ignition characteristics to a satisfactory condition, and was performed several times during the lifetest.

The ion-emission characteristics of the prototype plasma source are shown in Figure 7-16 for various keeper and discharge current setpoints. The ion-emission current is relatively insensitive to keeper current and is mainly a function of discharge current over the range of parameters tested. The keeper and discharge voltages as a function of expellant flowrate are shown in Figure 7-17 (keeper current = 255 mA, discharge current = 202 mA). The voltages start to rise rapidly below 0.5 sccm which is the nominal operating point and a good compromise between input power and expellant consumption.

The keeper current and voltage (on a fast time scale) are shown in Figure 7-18 during gas-burst ignition. On this time scale, both are well behaved and quickly settle out. However, Figure 7-19 shows that the plasma generator is quite noisy and its operating parameters varying during the first two minutes of operation. This is believed to be associated with the cathode coming up to operating temperature and the flowrate decreasing to 0.5 sccm (after the gas burst for ignition).

FMDS is ultimately intended for use on operational spacecraft where hydrogen in the expellant will not be a problem. However, the use of hydrogen in the expellant could be a problem if FMDS is used on some scientific spacecraft. The plasma generator will expel protons and protons are the dominant natural species in space. If hydrogen were a problem, then deuterium might be acceptable, depending on the scientific measurements being made. Deuterium has the same ameliorating effects on the plasma generator as hydrogen.

Hydrogen is also always a concern from the safety standpoint. The FMDS expellant tank will contain 10 standard liters of H_2 and explosive mixtures in air or oxygen require H_2 concentrations greater than 4%. Therefore if all 10 standard liters were immediately dumped into a volume greater than 250 liters (9 ft^3 or a cube 2.1 ft on a side), the mixture would not be explosive. For this reason, we believe the quantity of hydrogen carried by FMDS is not a safety hazard.

143
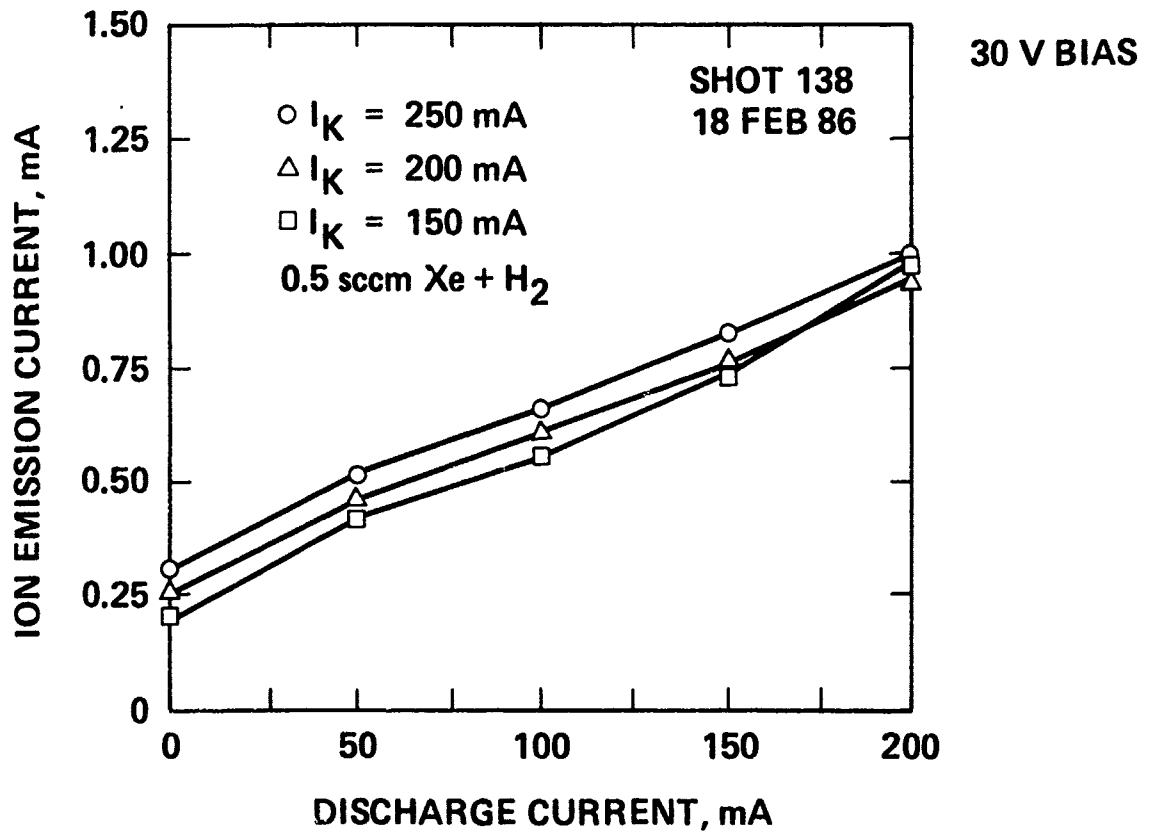
Figure 7-16. Ion emission current characteristics of the prototype plasma source for various keeper and discharge currents.

144
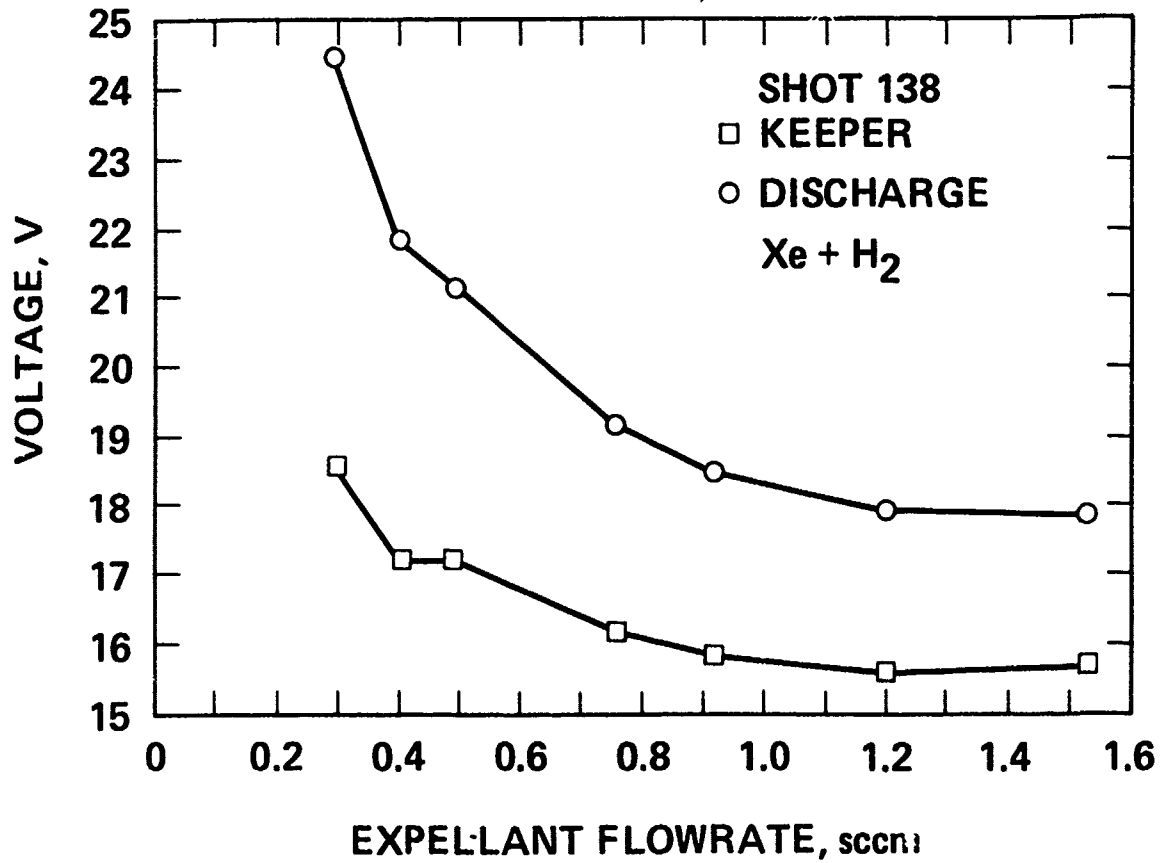
Figure 7-17.   Keeper and discharge voltages of the prototype plasma source as a function of expellant flow rate.

145

SHOT 66

CURRENT
0.5 A/DIV

VOLTAGE
20 V/DIV

5 ms/DIV

IGNITION

SHOT 143

CURRENT
0.5 A/DIV

VOLTAGE
20 V/DIV

5 ms/DIV
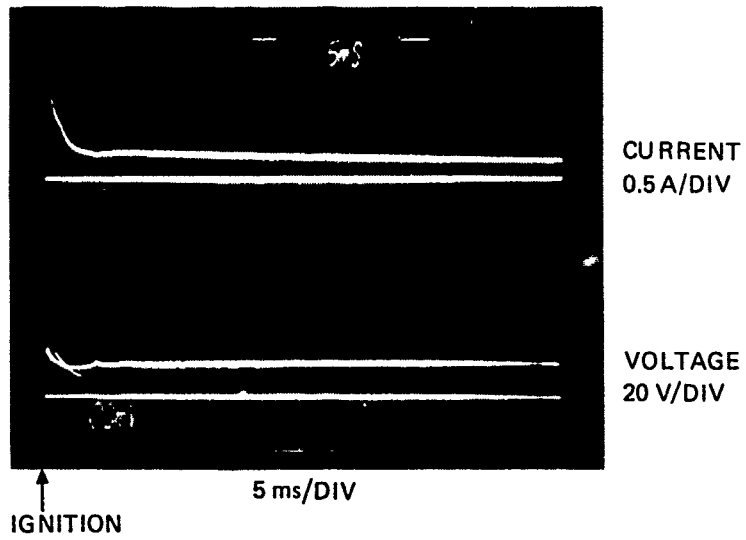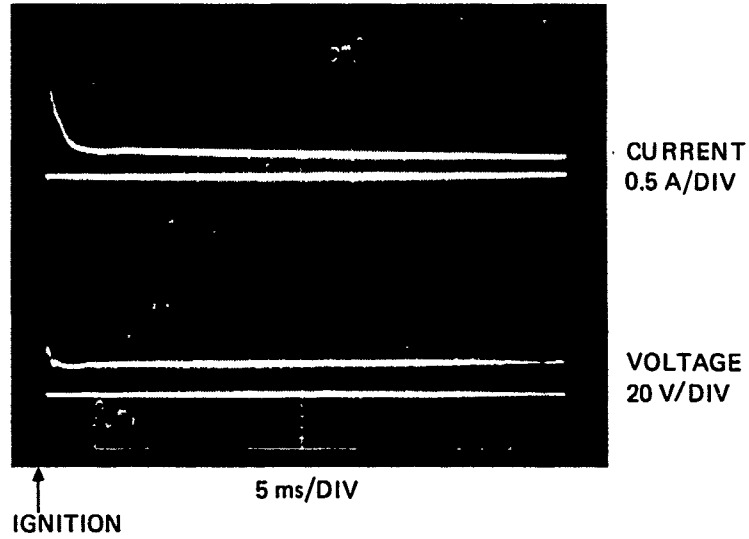
IGNITION

Figure 7-18. Keeper current and voltage during gas burst ignitron.

146
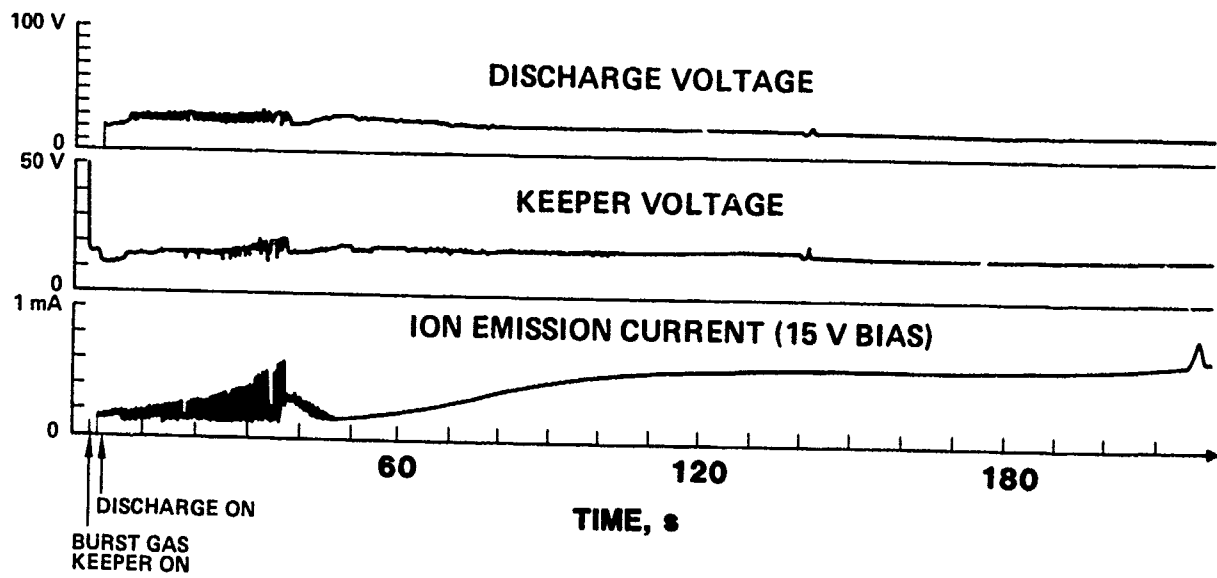
Figure 7-19.   Prototype plasma source voltages a:id ion emission during the first few minutes after starting.

7.6 FLIGHT PLASMA SOURCE TEST RESULTS

The first flight plasma source to be tested was S/N 903. S/N 903 is not planned to be flown, but is identical to S/N 901 and S/N 902 which are the flight sources. It was tested to verify the flight design which is structurally modified from the breadboard source in a manner which was not expected to significantly effect operating characteristics. However, the first operation of S/N 903 was very erratic and unacceptable as shown in the stripchart recording of Figure 7-20. The keeper voltage continuously drifted, jumped around, and never stabilized. In addition, the keeper and discharge voltages were both higher than expected. This type of operation was thought to be indicative of contamination of the cathode and its insert; however, a problem with the design was still a possibility at that time.

We were in the process of replacing the cathode insert with one we knew was good (from the breadboard source), when we discovered that some of the components in the source were very discolored and abnormal looking. We had these parts analyzed and concluded that an air leak in the feed system, which was later discovered, had contaminated the source, as evidenced by the copper and rhenium oxides present. We also concluded that a dark material on the heater-lead outer conductor and the mounting collar was stainless steel that was vapor deposited on those components during fabrication. When the heater lead was brazed into the mounting collar, the brazing fixture had stainless steel screws, which disappeared during the brazing operation. These parts were grit blasted to remove the stainless steel; however, the presence of some stainless steel in these areas is not considered to be a problem.

All parts of the source were cleaned, a new cathode insert was installed, and the source was reassembled. As an additional guard against contamination, we cleaned the vacuum chamber in which the source was tested. Figure 7-21 shows a stripchart recording of the keeper voltage and emission current during subsequent testing. It is very stable and well-behaved (after the normal ignition transients), and the keeper and discharge voltage levels are very acceptable.

Ion emission current (I_E) as a function of keeper current (I_K) and discharge current (I_D) is shown in Figure 7-22. The two operating points depicted in this figure and Figures 7-23 and 7-24 are detailed in Table 7-2. We can see from Figure 7-22 that higher I_E (than the nominal of approximately 1 mA at I_K = 250 mA and I_D = 200 mA) can be obtained by going to a lower keeper current and a slightly higher discharge current (I_E = 3.5 mA at I_K = 50 mA and I_D = 250 mA). Figure 7-23 shows total input power to the source as a function of I_K and I_D. It is interesting to note that the higher I_E region from Figure 7-22 actually requires less power than the nominal point. Specific ion emission current in μA/W is plotted against I_K and I_D in Figure 7-24. This figure shows that the source performance is definitely much better at lower keeper currents; however, flight source S/N 901 had a low amplitude oscillation when

148

18296—6
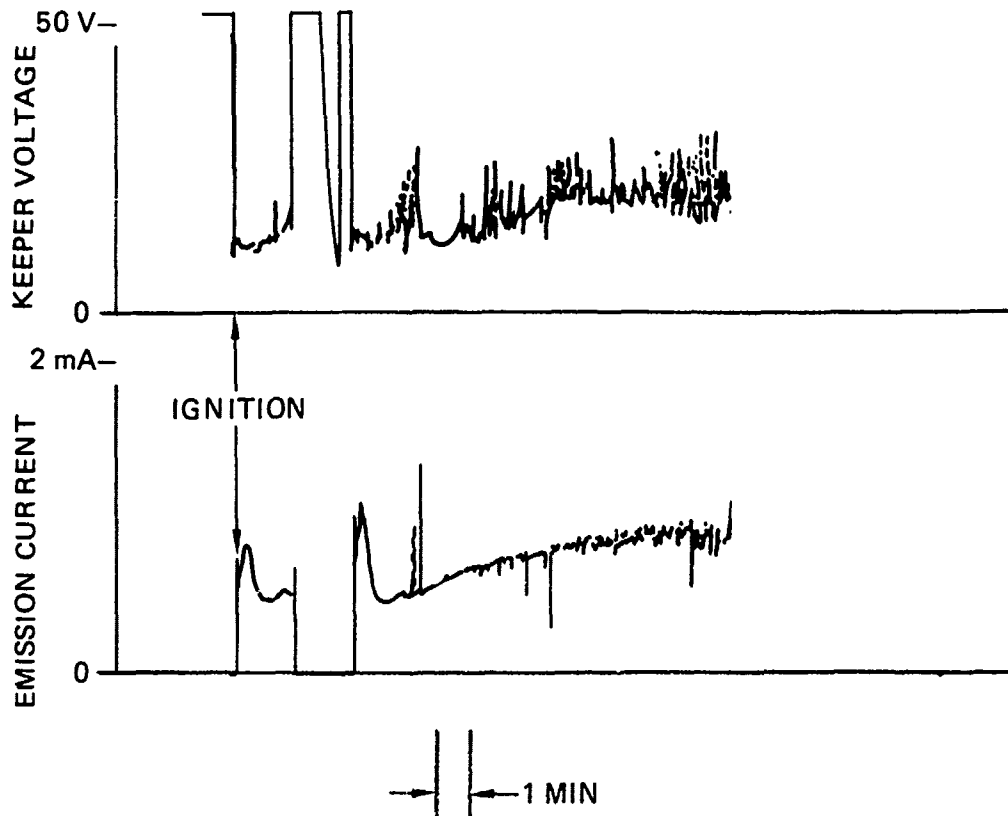
Figure 7-20.   Stripchart recording of the keeper voltage of source S/N 903 during initial and unacceptable operation (contaminated cathode and insert).
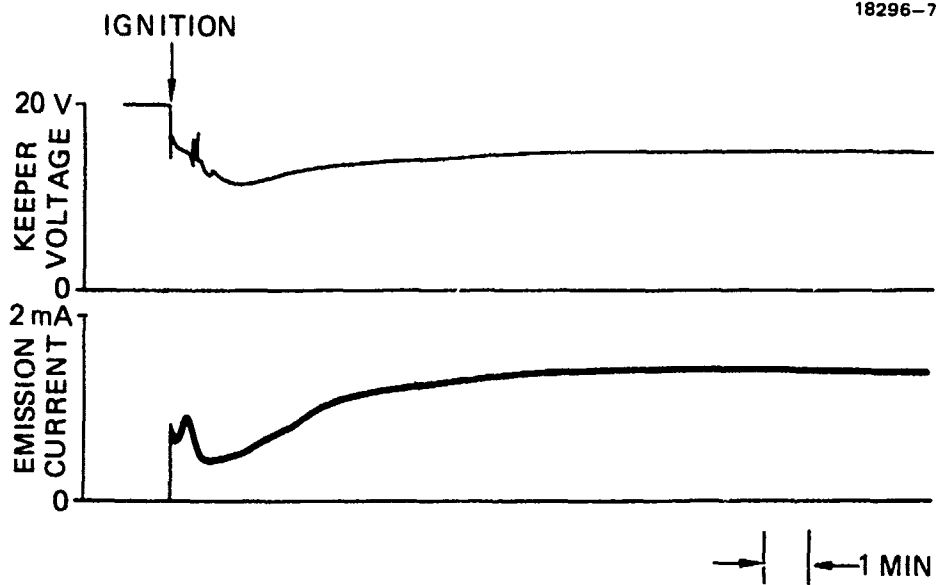
Figure 7-21. Stripchart recording of the keeper voltage of source S/N 903 after elimination of the contamination problems, showing very good performance.
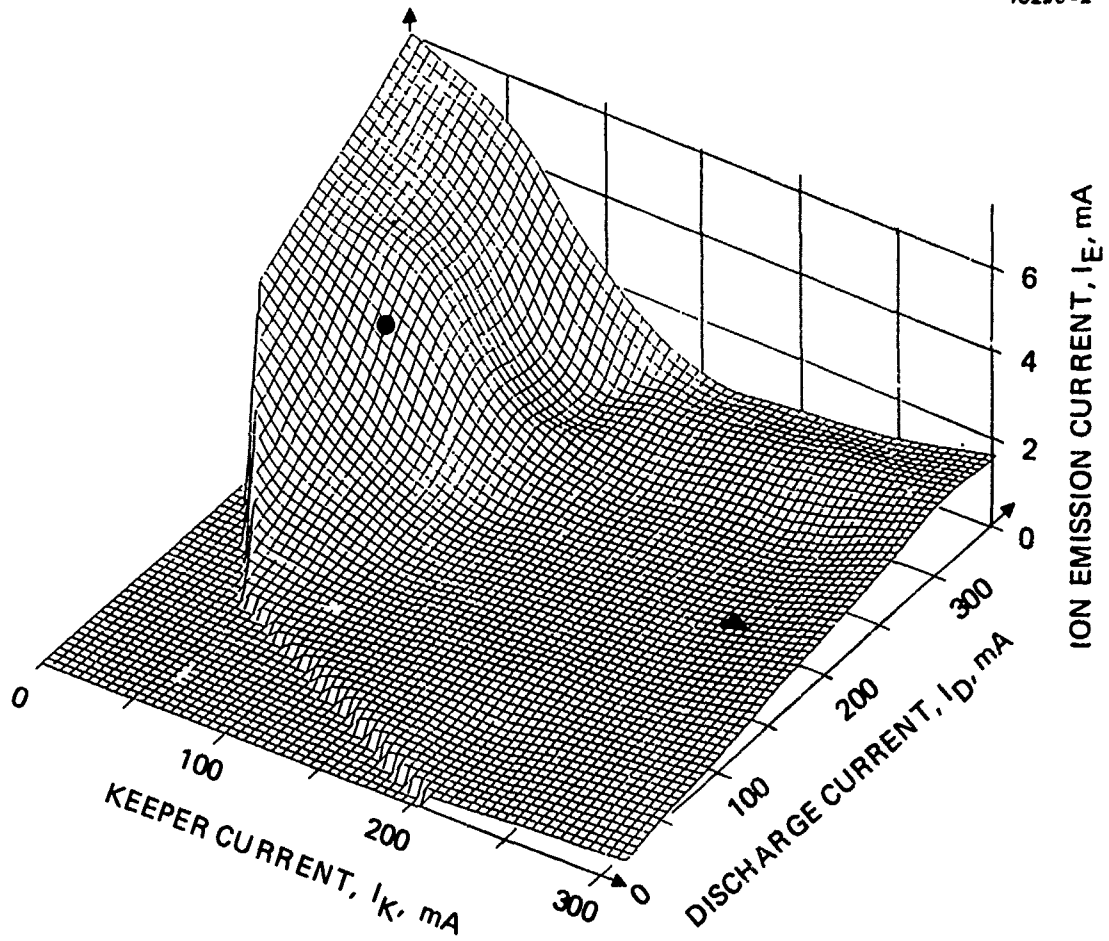
Figure 7-22. Ion emission current as a function of keeper current and discharge current for source S/N 903.

18296—3
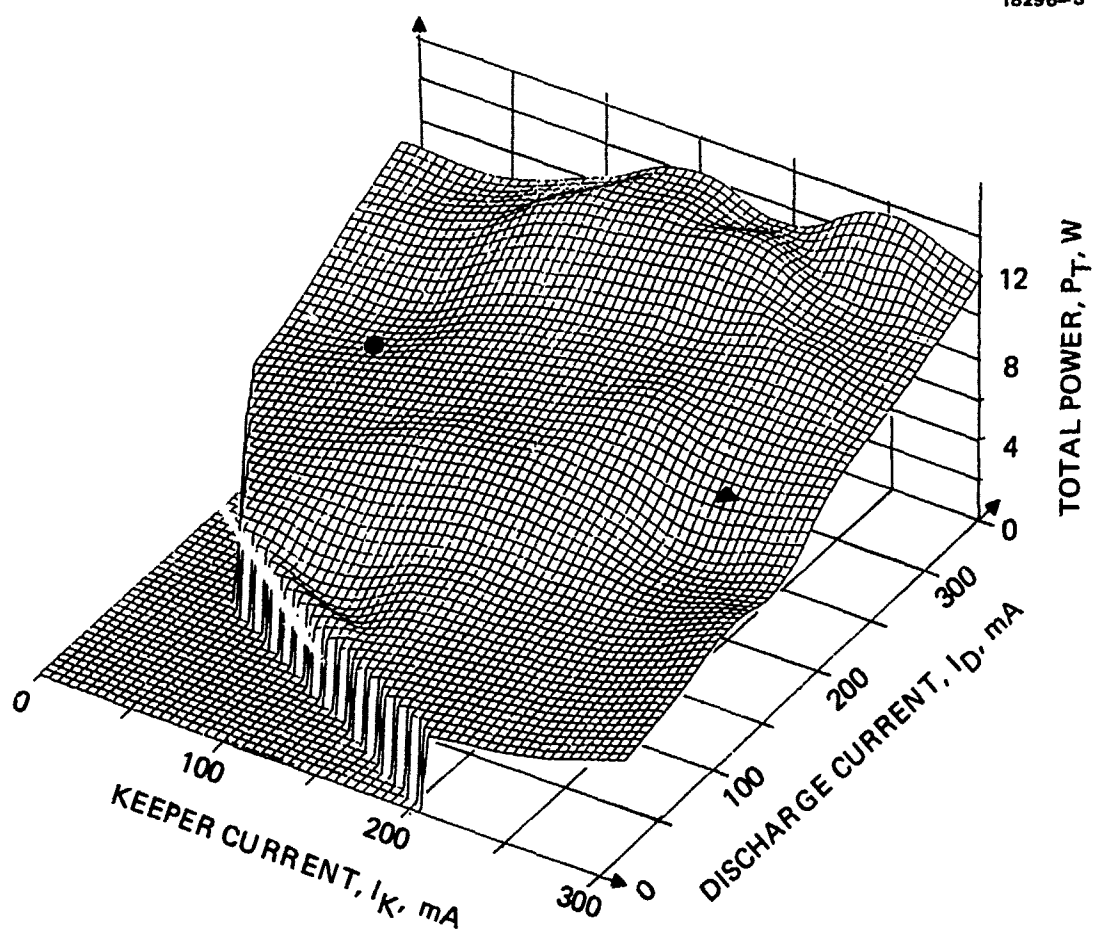
Figure 7-23. Total input power to source S/N 903 as a function of keeper current and discharge current.

152
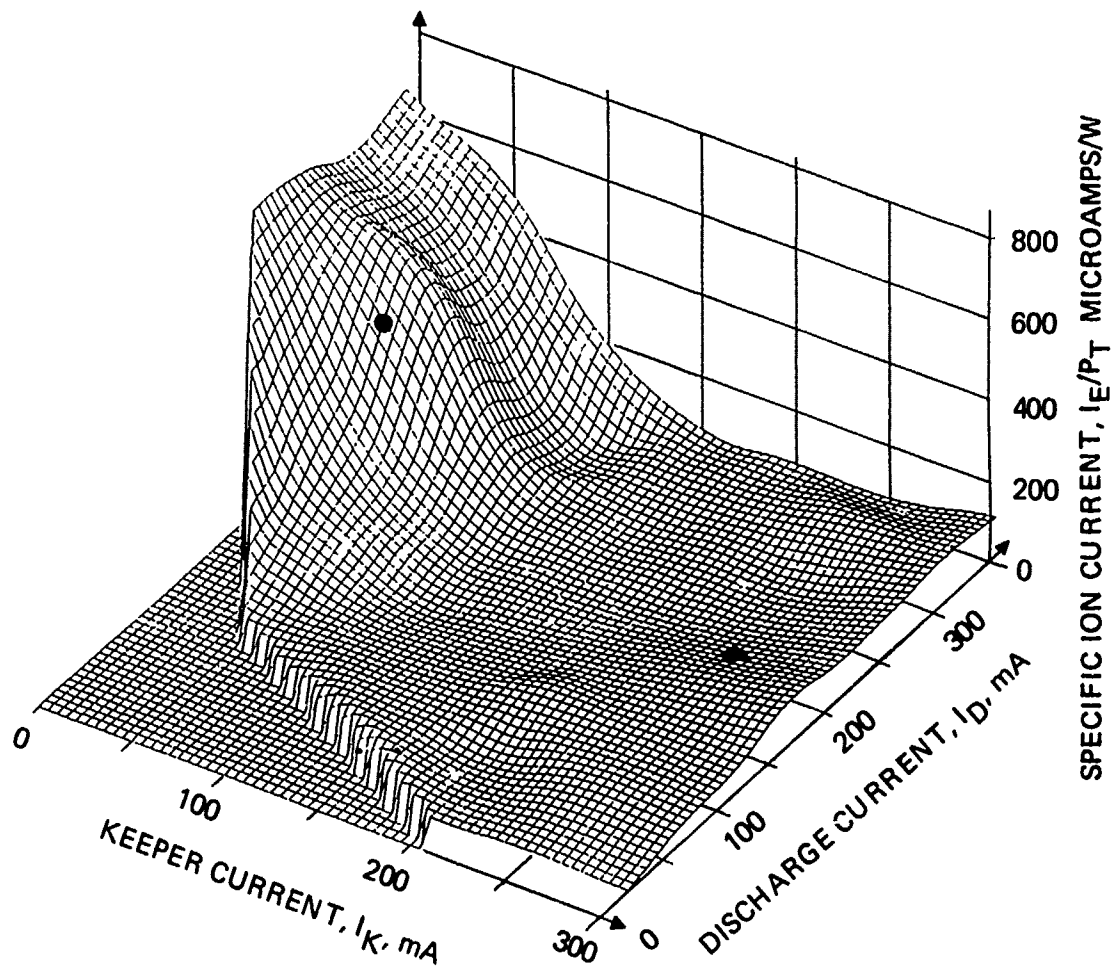
Figure 7-24. Specific ion emission current (μA/W) as a function of keeper current and discharge current for source S/N 903.

Table 7-2. Operating Points Illustrated in Figures 7-22, 7-23, and 7-24.

T9234-16

Point:	●	▲
Keeper:	11.4 V, 50 mA	13.9 V, 250 mA
Discharge:	23.4 V, 250 mA	23.7 V, 200 mA
Ion emission:	3.49 mA	0.967 mA
Gas flowrate:	0.46 sccm	0.46 sccm
Total power:	6.42 W	8.22 W

operated with the flight power supplies at $I_K = 50$ mA and $I_D = 250$ mA. It is also necessary to start the source at the nominal operating point and then switch to the lower I_K point after the ignition transient is complete (1 to 2 minutes).

Testing of the delivered flight plasma source (S/N 901) was accomplished without any problems. Its initial operation was very stable and well-behaved. The initial discharge voltage of ≈ 28 V was quite high but dropped to an acceptable level of ≈ 17 V within the first few hours of operation. The ion-emission characteristics of this plasma source are shown in Figure 7-25 for various keeper and discharge current setpoints. The high emission-current output for low keeper current (50 mA) is readily apparent in this figure. The plasma source has a nominal operating point (SP 10) of:

$$V_K = 14.8 \text{ V} \qquad I_K = 258 \text{ mA} \qquad P_K = 3.82 \text{ W}$$
$$V_D = 18.5 \text{ V} \qquad I_D = 177 \text{ mA} \qquad P_D = 3.27 \text{ W}$$

Therefore the plasma source nominally consumes and dissapates ≈ 7.1 W. This power is dissipated by conduction through the plasma source mounting base and by radiation from its surfaces.

A photograph of the flight source is shown in Figure 7-26. It has a mounting base that is 9.6 cm (3.78 in.) square with rounded corners, a main body diameter of 8.13 cm (3.25 in.), and is 14.0 cm (5.5 in.) high. It has a measured mass of 1.72 kg (3.80 lb).

7.7 FLIGHT SOURCE ELECTRONICS AND FEED SYSTEM TEST RESULTS

The flight source electronics were bench tested before being integrated with the plasma source and controller. This testing revealed a major problem in the keeper power supply; the components on the primary side of the transformer in the high-voltage (1000 V) section were being overstressed by voltage. This overstress resulted when the design was changed from an input bus of 28±4 Vdc to a 29- to 43-Vdc bus. Higher voltage-rated components were not readily available; therefore, the design was changed from being a separate flyback inverter for the HV section to the Hughes' patented circuit shown in Figure 7-11 and discussed in Section 7.3.1.

The output characteristics of the heater, discharge, and keeper supplies are shown in Figures 7-27 through 7-29 respectively. The efficiencies of these supplies are also shown on the figures for the various operating points measured and are all nominally 60%. The plasma source power supplies are housed in an electronics box along with the input filter, housekeeping inverter, and bipolar log electrometer. This box (without covers) is shown in

155
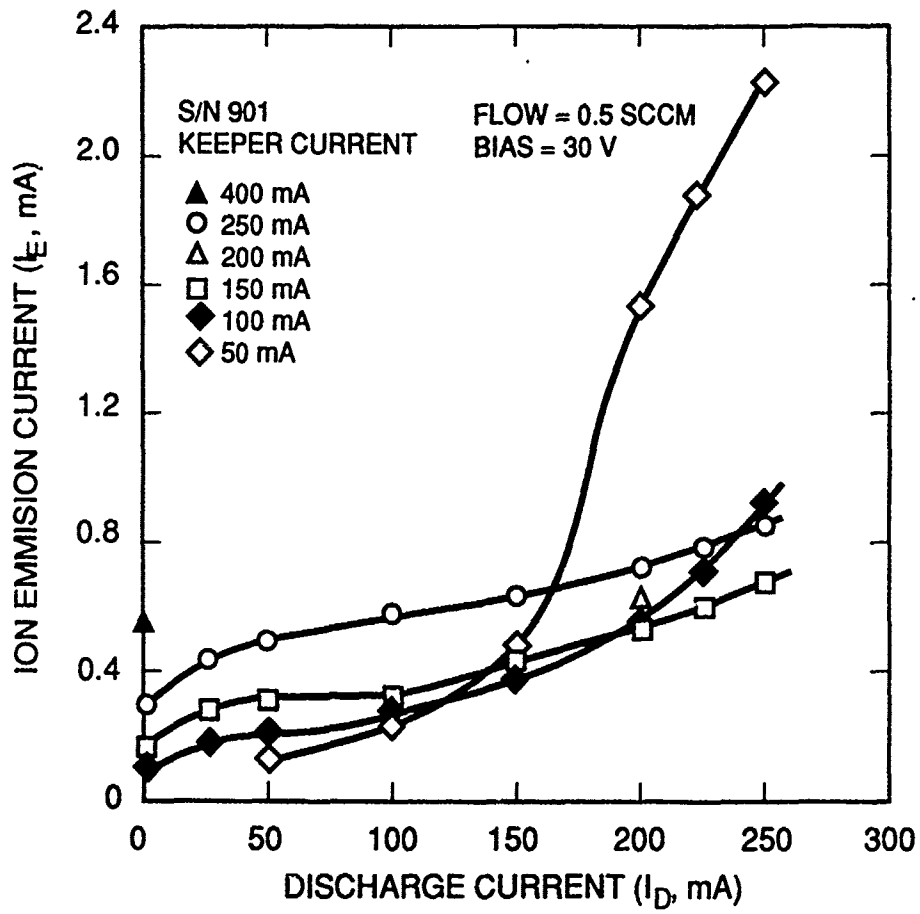
Figure 7-25. Ion emission current characteristics of flight source S/N 901 for various keeper and discharge currents.
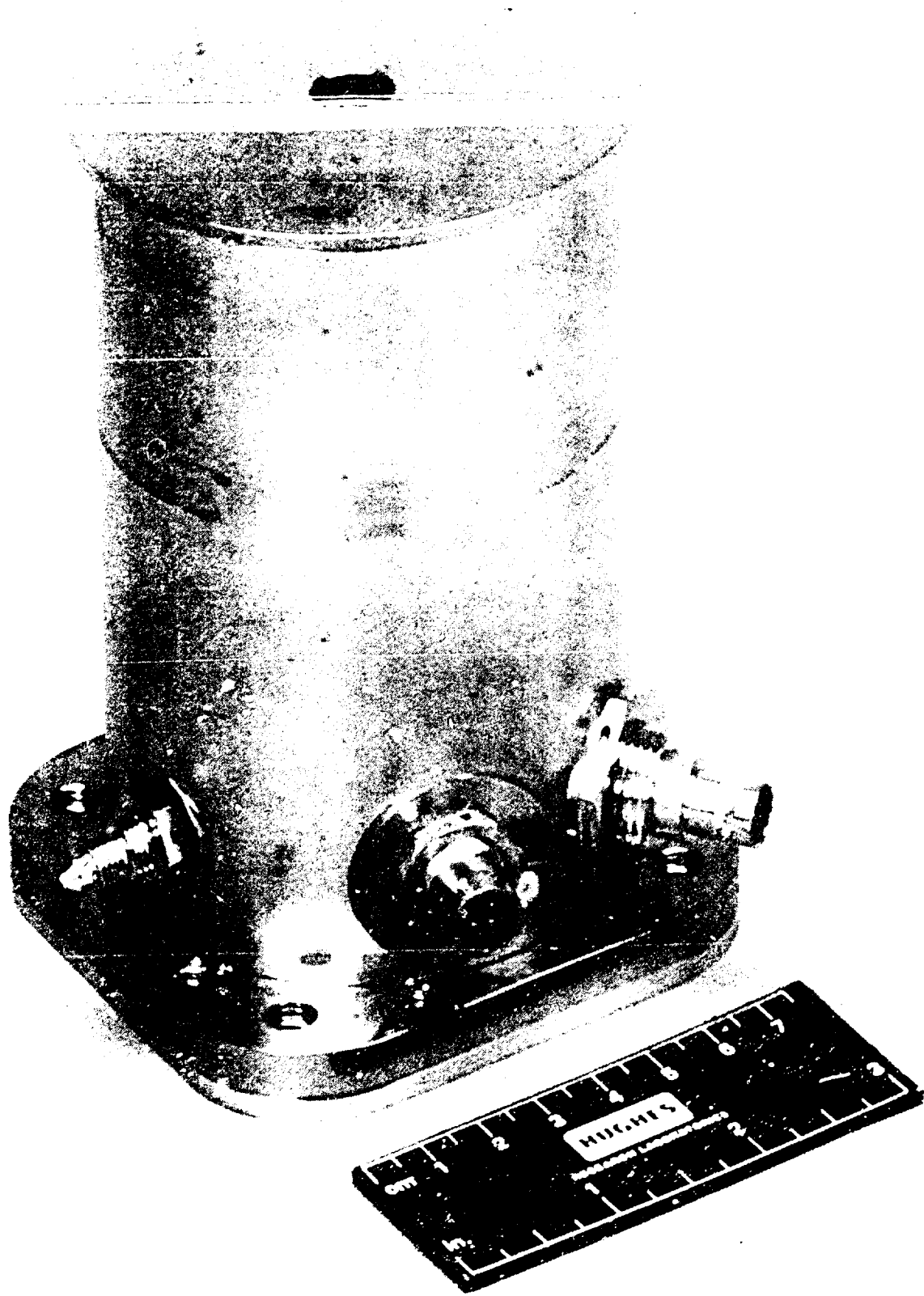
Figure 7-26. Photograph of flight plasma source S/N 901.

C8912-14-07
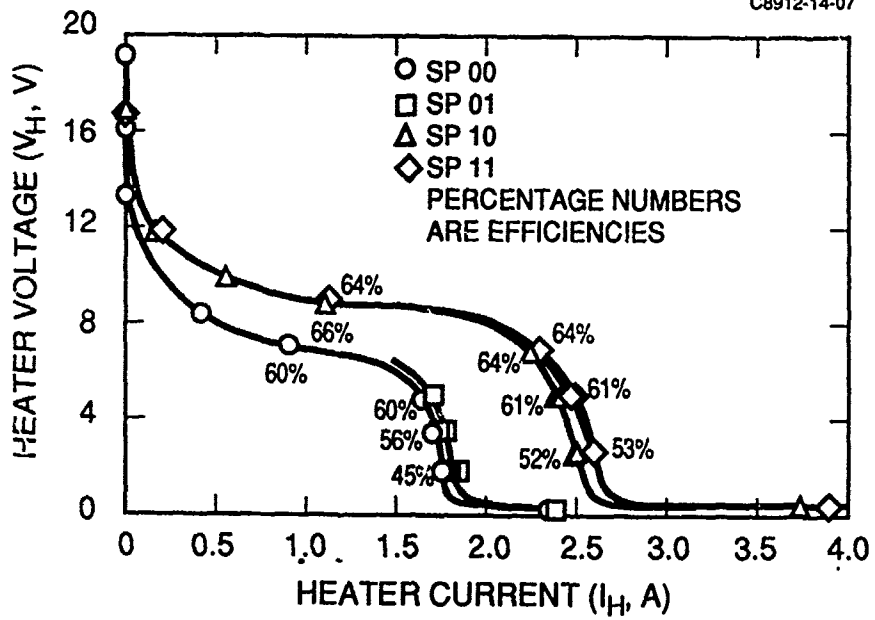
Figure 7-27. Output characteristics and efficiency of the heater supply.

158
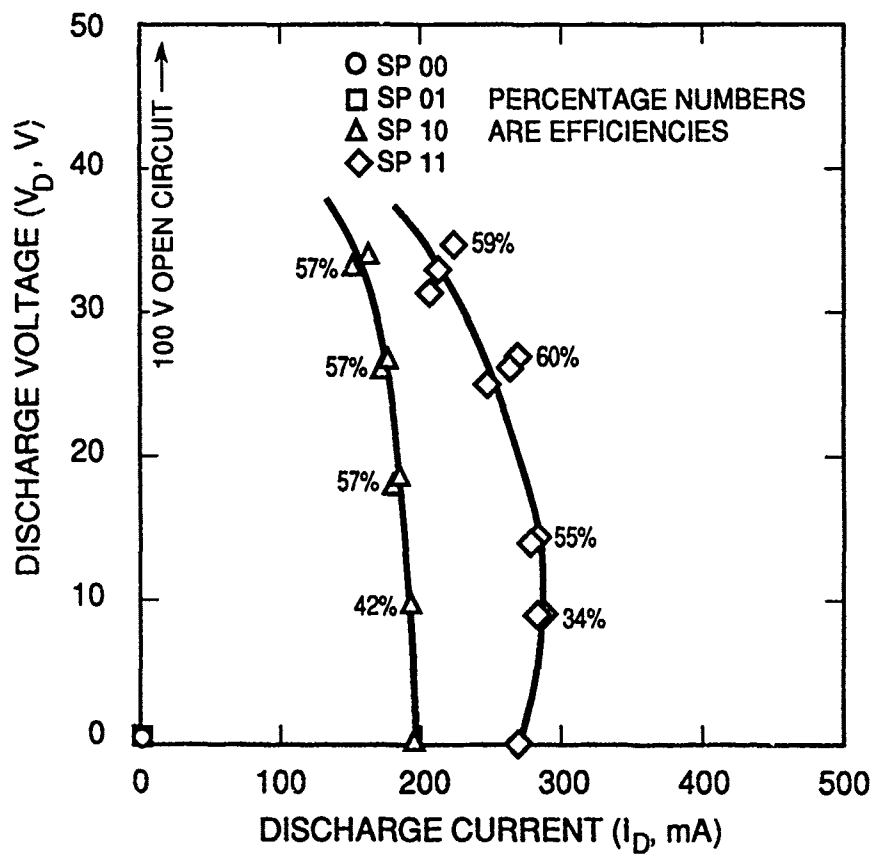
Figure 7-28. Output characteristics and efficiency of the discharge supply.
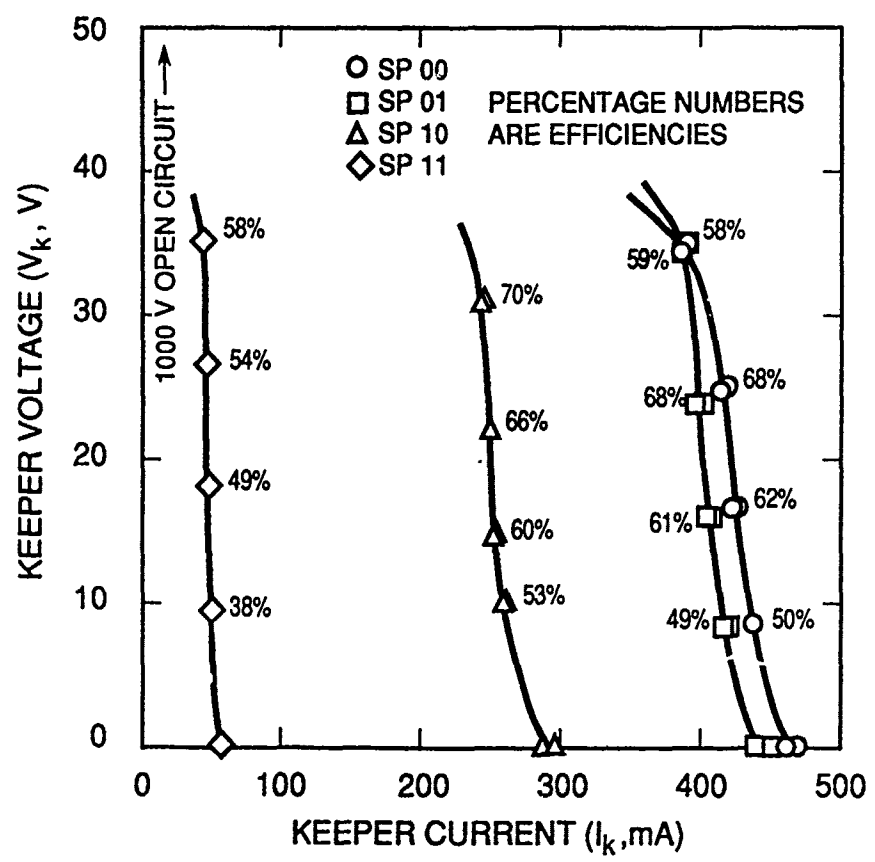
Figure 7-29. Output characteristics and efficiency of the keeper supply.

Figure 7-30. It is 17.78-cm L x 15.24-cm D x 13.97-cm H (7.0 x 6.0 x 5.5 in.) and has a mass of 3.461 kg (7.63 lb).

The expellant tank was filled by Cryogenic Rare Gas Co. with 495 g (90 standard liters) of xenon and 10 standard liters of hydrogen. The expellant tank has a volume of 2.048 liters, resulting in an expected tank pressure of 4.02 MPa (583 psia) at 21°C. The tank pressure measured using the high pressure transducer (and its manufacturers calibration data) was 3.66 MPa (530 psia). The expected tank pressure due to the partial pressure of xenon was calculated using the correction values for the compressability of xenon that were presented in a paper by Juza and Sifner and is 3.52 MPa (510 psia) at 21°C. The partial pressure of the hydrogen was calculated by treating it as an ideal gas and was 0.50 MPa (73 psia) at 21°C. These pressures lead to a calculated temperature of -23°C where the xenon will start to liquify in the tank. This temperature was also obtained from the data in the paper by Jusa and Sifner.

The gas in the tank was certified by Cryogenic Rare Gas Co. to be 10% hydrogen and 90% xenon on a mol/mol basis with the following impurity concentrations:

Krypton	<25 ppm
Nitrogen	<5 ppm
Oxygen	<2 ppm
Methane	<1 ppm
Carbon Dioxide	<1 ppm
Water	<1 ppm.

We also measured the flow rate provided by the flight pressure regulator and the flight flow impedance. With 1.1 MPa (150 psig) on the upstream side of the pressure regulator and the downstream side of the flow impedance at vacuum, the measured flow rate was 0.655 sccm.

The expellant tank and the pressure regulator can be seen in Figure 2-2. The feed system has a mass of 4.067 kg (8.97 lb) dry and contains an additional 0.496 kg (1.10 lb) of expellant when fully loaded.

7.8 CONTAMINATION MEASUREMENTS

The possibility of contaminants emanating from a plasma generator is always a concern to spacecraft designers, especially where optical and thermal control surfaces are involved. Therefore, during the lifetest of the breadboard plasma generator, we installed three glass "witness" slides within the vacuum chamber to measure the deposition of any contaminating substances that might emanate from the plasma generator.
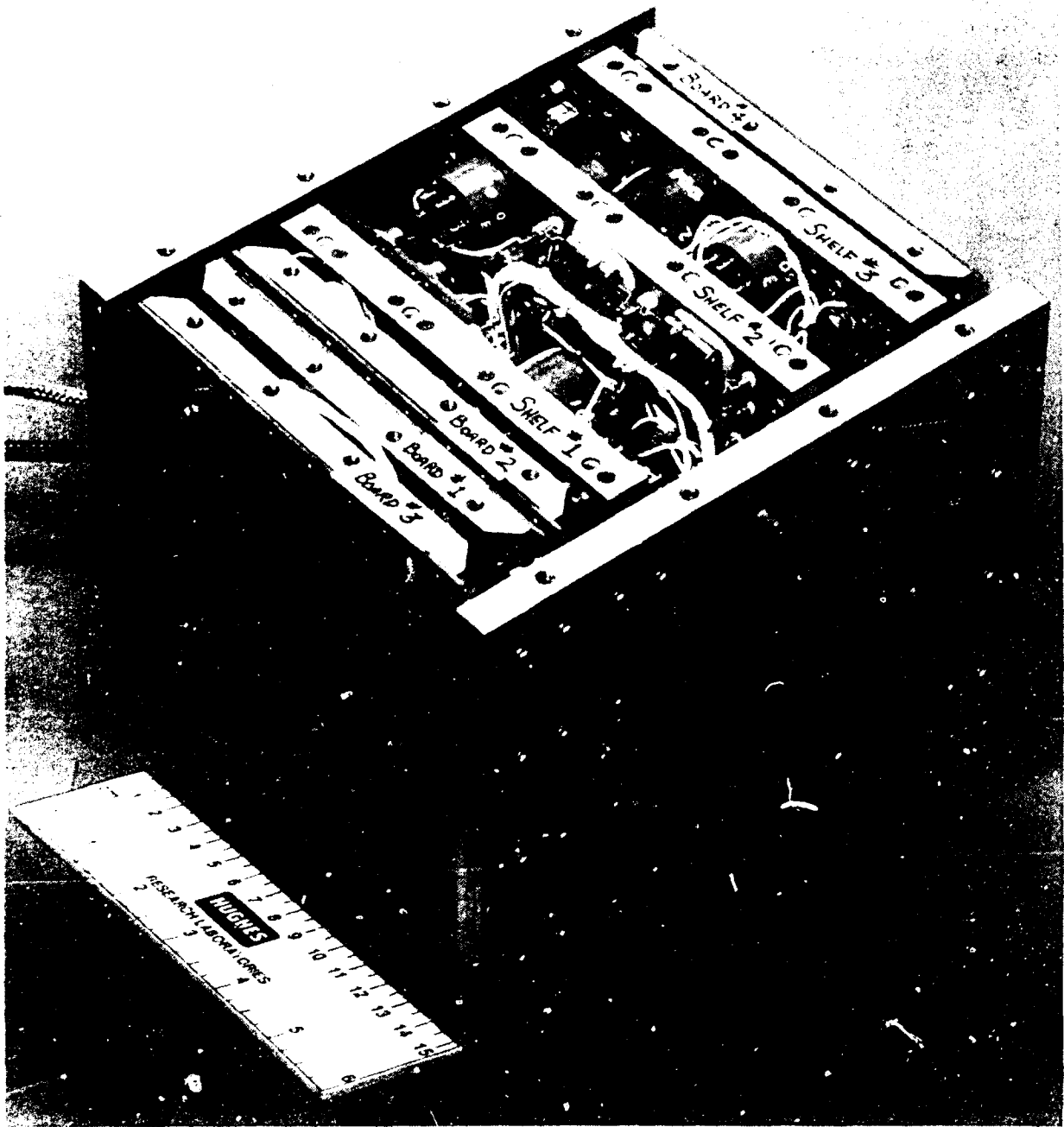
Figure 7-30. Plasma source electronics box without its cover.

The slides were placed in the positions shown in Figure 7-31. Slide #3 was directly below the exit aperature of the plasma generator and slide #4 was approximately 17 cm further downstream. Both slides were mounted on a perforated steel mesh vacuum-chamber liner (diameter = 23.4 cm). Slides #1 and #2 were control slides, with #2 being placed within the vacuum chamber but upstream of the plasma generator and isolated from the emitted plasma by a perforated mesh. Slide #1 was never placed in the vacuum chamber.

After the lifetest, we found that slide #3 had become coated with a brownish material while slides #2 and #4 still appeared clear. Light transmission analysis of all four slides indicated that slides #1, #2, and #4 all had similar characteristics, while slide #3 showed transmission loss compared to the other three. This transmission loss as a function of wavelength is shown in Figure 7-32. We used electron spectroscopy for chemical analysis (ESCA) to measure the relative amounts of any surface-deposited elements on slides #1, #3, and #4. No contaminants were identified on slides #1 and #4 while slide #3 was found to have carbon and sodium on it. We believe that this contamination is due to vacuum-pump oil that backstreamed onto the slide and subsequently decomposed under bombardment by plasma ions and electrons.

Contaminants that might be emitted from the plasma generator are barium, strontium calcium, platinum, rhenium, molybdenum, iron, samarium, colbalt, stainless-steel, tantalum, and tungsten. None of these were found on the witness slides.

We also used optical spectroscopy to determine if there were sputtered-metal contaminants present in the efflux of the FMDS plasma source during operation. These contaminants, if present, would pose a potential deposition hazard to nearby sensitive spacecraft surfaces. While we do not expect sputtering within the FMDS plasma source (because the voltages present in the source are generally below the sputtering threshold for the materials that compose the discharge chamber), we have had only limited experimental confirmation of this expectation. In the present work, we found no contaminant spectra in the FMDS plasma source optical emissions. This finding is in agreement with the above results for the glass "witness" slides, giving us a high level of confidence that the FMDS plasma source efflux is free of contaminants.

Figure 7-33 shows the simple apparatus that we used for the measurements. Light from the FMDS plasma source Penning-discharge plasma is imaged onto the slit of a 0.25-m Jarrell-Ash monochromator, which is equipped with a stepping-motor grating drive. As the grating moves, spectral lines fall on the exit slit where they are detected by an R212A photomultiplier tube. The photomultiplier output is recorded on a strip-chart recorder. We calibrated the system by placing commercial neon and krypton calibration lamps at the location of the plasma source and recording their spectra. By using these known spectra as

163
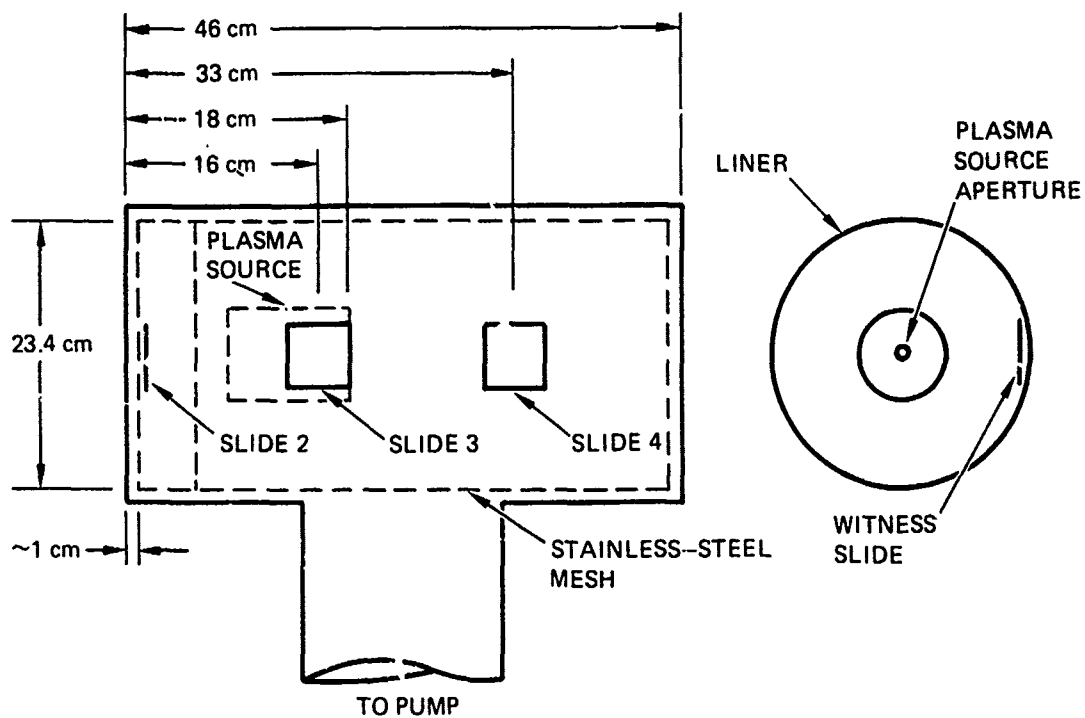
Figure 7-31   Positions of the contamination "witness" slides during the plasma generator
lifetest.

17155—4
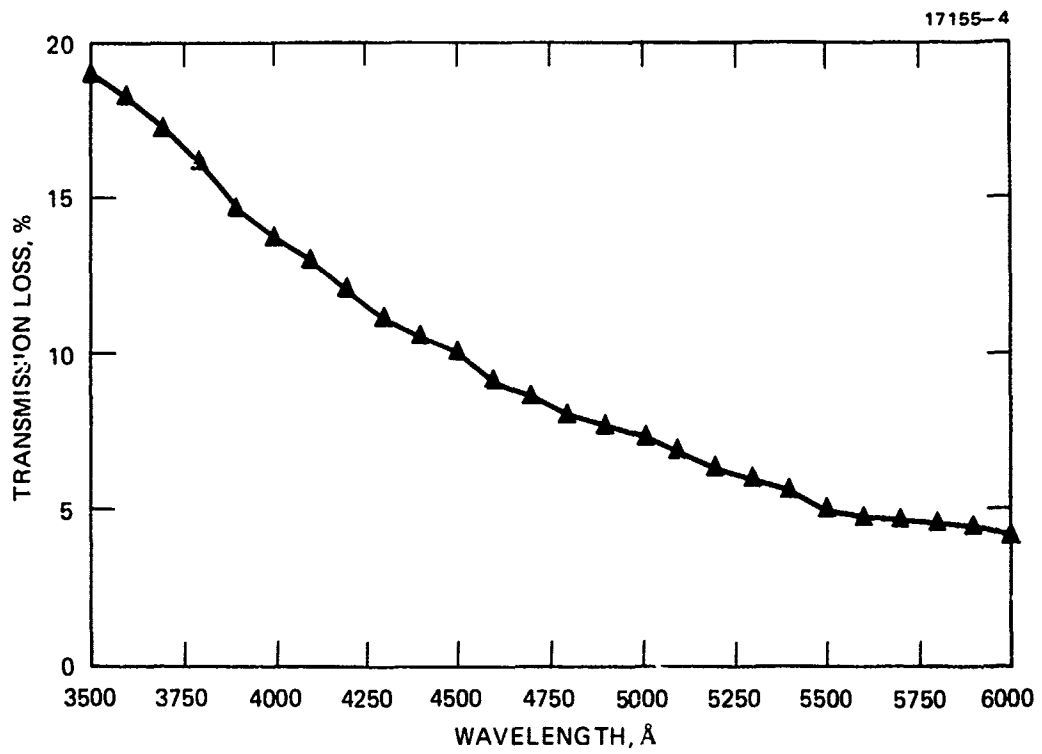
Figure 7-32. Optical transmission ?... of contamination "witness" slide 3.

165

18296—8

PLASMA SOURCE
POWER SUPPLIES

1.2-m VACUUM CHAMBER

FMDS PLASMA SOURCE

LIGHT FROM DISCHARGE
IN PLASMA SOURCE

EMISSION
SPECTRUM

STRIP-CHART
RECORDER

VACUUM
WINDOW

LENS

GRATING DRIVE

ENTRANCE SLIT

MONOCHROMATOR

PHOTOMULTIPLIER

POWER SUPPLY
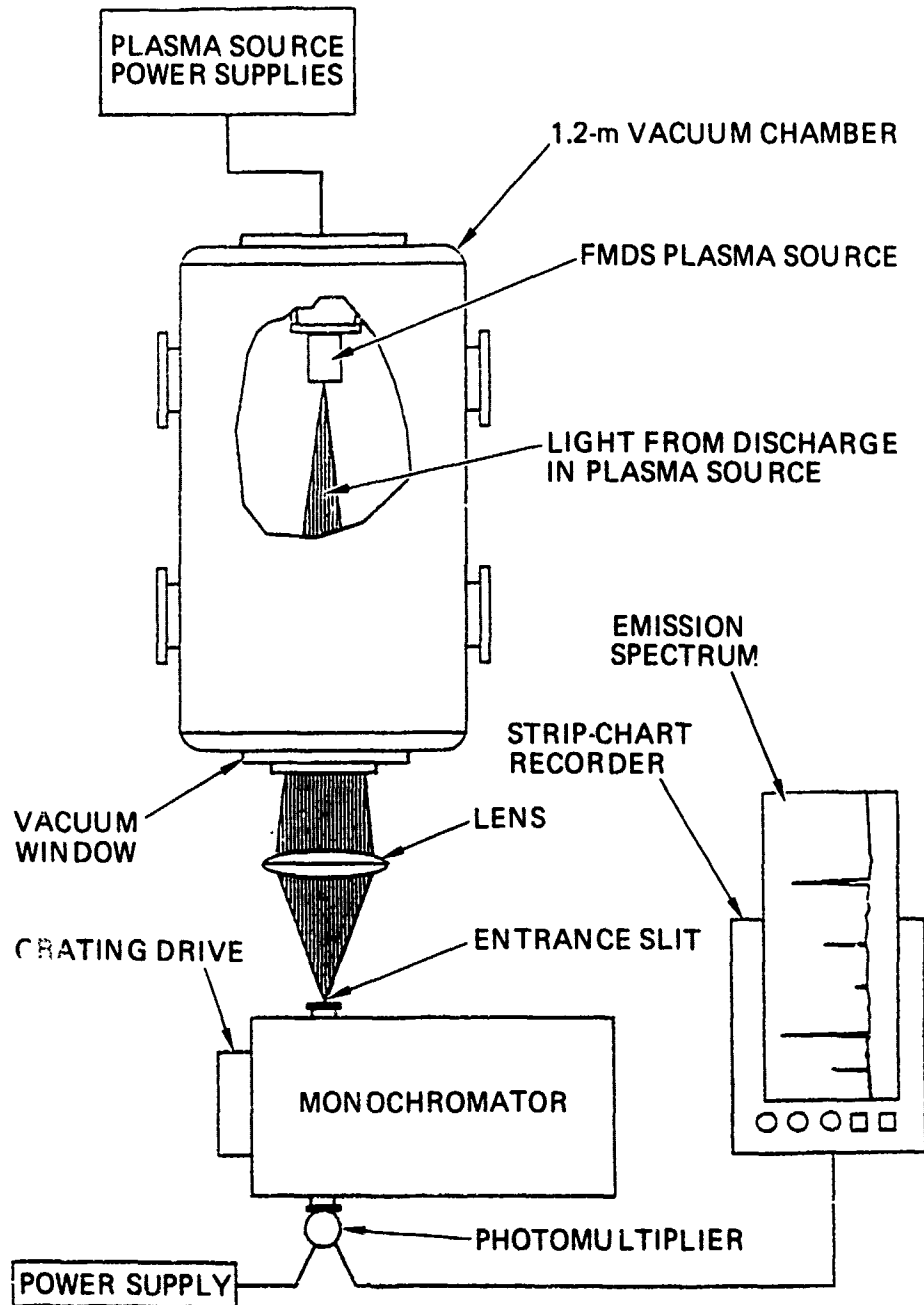
Figure 1-33. Apparatus used in FMDS spectroscopic measurements.

166

guides, we could determine the wavelengths of lines emitted by the FMDS plasma source with a high degree of accuracy.

To determine if contaminants were present, we compared the observed spectrum with published atomic and ionic persistent-line spectra for xenon and hydrogen and for the candidate contaminantes of iron, tungsten, molybdenum, tantalum, platinum, and rhenium. Generally, if a given species is present in a Penning discharge, it will be represented by multiple spectral lines, because electrons in the discharge are sufficiently energetic to excite a large number of atomic energy levels. In some cases individual spectral lines of the candidate contaminants may coincide with those of xenon or hydrogen lines (within the resolution of our instrument), making unambiguous identification of those particular lines impossible. For tentative species identification, we required the presence of at least one unambiguous spectral line; positive identification required multiple unambiguous lines. Using this criterion, we found no evidence (tentative or otherwise) of any of the candidate contaminants. Each of the candidate contaminants has strong persistent lines which fall into regions of the spectra that would make them clearly distinguishable from xenon and hydrogen lines; none of these lines were detected.

The occurrence of a null result, as obtained above, always brings with it the question of whether the apparatus was sufficiently sensitive. While more sensitive measuring techniques (photon counting, laser fluorescence, etc.) certainly exist, we have previously used the same spectroscopic apparatus to detect contaminants in the emissions spectra of ion-thruster Penning discharges which run at slightly higher discharge voltages. In these measurements, we easily detected iron and molydenum spectral lines when voltages within the ion thruster were above the sputtering threshold. These previous results lend confidence in our ability to detect contaminant atoms at levels which (for the ion-thruster application) have been judged not hazardous to a spacecraft.

Another possible concern to a spacecraft is the condensation of xenon expellal on cryo-temperature surfaces. Neutral xenon gas released from the plasma generator will condense and freeze (xenon has a 161 K freezing point) on cold (100 K) optical surfaces, potentially forming a thin xenon-ice coating that could degrade the optical properties of the cold optical elements. We present very simple calculations below that indicate no buildup of condensing xenon will occur at the 100 K optical-surface temperature and that only a small fraction of a monolayer of xenon surface coverage can be expected.

The rate of buildup of xenon on a cold surface can be computed by evaluating the xenon arrival rate (as a result of xenon diffusion from the plasma generator) and loss rate (as a result of xenon evaporation at 100 K from the cold optical surface).

The flux of neutral xenon arriving on an exposed surface is

$$f_{arriving} = n_o <v_o>/4,$$

where $n_o = 10^{11}/m^3$ is the assumed neutral-xenon density, and $<v_o> = 194$ m/s is the mean xenon-atom velocity (assuming a 300 K temperature). These approximate numbers give an arriving flux of about

$$f_{arriving} = 5 \times 10^{15}/m^2s.$$

The loss flux can be estimated by assuming that there is a thin xenon-vapor layer above the cold surface that is in equilibrium with the adsorbed xenon immediately below it. This layer will have a pressure equal to the vapor pressure of xenon at 100 K (i.e., 100 Pa). This pressure corresponds to a gas density near the surface of

$$n_s = P/kT_s = 10^{23}/m^3,$$

giving a flux of leaving xenon atoms of

$$f_{leaving} = n_s<v_s>/4 = 3 \times 10^{24}/m^2s.$$

These simple calculations predict that if there were a surface la_er of adsorbed xenon, it would desorb approximately 10^9 times faster than it could be replenished from ambient xenon. This calculation confirms what intuition suggests: unless the pressure of xenon gas that reaches cryogenic surfaces exceeds the 100-Pa vapor pressure of xenon at 100 K, no frozen-xenon buildup will occur. Xenon pressures this high exist only inside the plasma generator itself, and only for a few seconds during gas-burst ignition.

While the foregoing calculations show that no macroscopic xenon-ice buildup can be expected, a small fraction of a monolayer of xenon will form on exposed surfaces, because arriving atoms spend a finite time on the surface before they are evaporated off. The equilibrium surface coverage increases with incident on flux, decreases with temperature, and varies somewhat with the composition of the optical surface. In a typical result,[6] investigators found 0.08 monolayers of xenon on a palladium substrate at 100 K; however, their incident xenon-atom flux was $f_{arriving} = 3 \times 10^{17}/m^2s$, which is greater than our expected flux by a factor of ≈ 40. Very sophisticated experiments are required to detect even one monolayer; therfore, the buildup of xenon from the plasma generator should not effect the operation of any optical surfaces or sensors.

7.9 MAGNETIC FIELD MEASRUEMENTS

One of the specifications for the FMDS is that magnetic fields should be less than 100 nT at 1 m in any direction from the unit. Since the plasma generator contains permanent magnets, this specification is of primary concern. Measurements made on the unshielded flight magnetic field structure (using flight hardware) gave readings of 150 to 200 nT at 1 meter. The magnetic field structure is housed in a 3.25-inch-diameter by 5.5-inch-high cylinder that is closed on each end (except for the 0.5-inch-diameter exit aperature on the downstream end). Various methods of magnetically shielding this cylinder using Netic and/or Conetic materials were investigated and rejected because of fabrication problems. Fabricating the cylinder and downstream end plate from soft steel works as well as the special materials and is easy to fabricate. The final enclosure design is shown in Figure 7-2 and was expected to reduce the magnetic field to less than 50 nT at 1 meter. Measurements made by Southwest Research Institute were nominally 200 nT at 0.5 m. Assuming that we are dealing with a dipole magnetic field, its field strength will fall off as $1/r^3$, and therefore will be nominally 25 nT at 1 m.

SECTION 8
SYSTEM DESIGN

The FMDS is designed as a self-contained system. This approach minimizes the interfaces with the satellite and makes the FMDS more attractive as a "housekeeping" function that performs the task of keeping the satellite in a neutral charge state. The command-and-telemetry interfaces are accomadated through the controller and the power interface is accommodated through the Plasma-Source electronics box. This enables single types of command, telemetry, and power interfaces with the satellite. Any differences in command and/or telemetry format required by the sensors or the Plasma Source are provided by the Controller and not the satellite. All of the components of the FMDS are mounted on a flat plate as discussed in Section 2.1. This flat plate is the mechanical and thermal interface with the satellite.

The SPACECLAMP plasma source for the FMDS turns ON in 1 s or less once the power supplies have been turned ON and the burst valve opened; therefore, the response time of the FMDS (the time-span from the satellite reaching the threshold level selected as the critical charging level until low-energy plasma is emitted) is mainly determined by the instrument response times, the time required for the controller to process the appropriate algorithms, and the time required for the controller to operate valves and turn the power supplies ON.

The controller operates on a 4-s cycle and closes the plasma source relay during the cycle following the one in which charging is detected, and the high pressure valve is opened during the next cycle. The bypass valve is closed and the keeper supply turned ON during the next cycle, followed by opening of the burst valve and emission from the plasma source during the subsequent cycle. Therefore, it takes approximately 16 s from the time that an algorithm determines that charging is present until the plasma source is turned ON. The ESA has sweep times of 4, 8, 16, and 32 s, and the algorithms associated with it require 5, 5, 3 and 1 sweeps respectively to detect charging. The SPM responds almost immediately and its algorithm requires 4 cycles to detect a hazard. The TPM also responds immediately and one detected arc sets the charging flag. The total FMDS response time from a hazard being present, being detected by the various FMDS instruments, and plasma source turn-ON is listed in Table 8-1. The desired response time is 30 s or less. It is obvious from Table 8-1 that the ESA does not meet this requirement for any of its sweep rates. Nothing can be done about the 32-s sweep since at least one sweep of the instrument is required to obtain data. The 16-s sweep response could be lowered to 48 s or 32 s by lowering the required number of sweeps from 3 to 2 or 1 respectively. The response for the 8-s sweep could be lowered to 40 s or 32 s

by lowering the required number of sweeps from 5 to 3 or 2 respectively. Similarly the 4-s sweep response can be lowered to 32 s or 28 s by reducing the required number of sweeps from 5 to 4 or 3. The required number of sweeps can easily be modified by changing the appropriate value of k or j in Figures 6-16 and 6-17 with EEPROM write commands.

Table 8-1. Response Times of the FMDS for the
Various Charging Sensors.

CHARGING SENSOR	FMDS RESPONSE TIME, s
ESA (4-s SWEEP)	36
ESA (8-s SWEEP)	56
ESA (16-s SWEEP)	64
ESA (32-s SWEEP)	48
SPM	28
TPM	16

8.1 ELECTRICAL DESIGN

Since the exact vehicle and/or satellite on which the FMDS will be flown is not known, the exact power, command, and telemetry interfaces are not known. Therefore, we have designed for the case we consider to be standard and resonable interfaces.

The primary power return, the command signals, and the telemetry signals to the FMDS are all isolated from the chassis and from each other by at least 1 megohm. The one telemetry data line from the FMDS is referenced to chassis inside the FMDS under the assumprtion that isolation for this line will be provided on the satellite end. The satellite structure is not used as an intentional current carrying conductor. The ground-return-isolation scheme is shown in Figure 8-1.

The design of the housekeeping inverter isolation and regulation is shown in Figure 8-2. This inverter provides transformer isolation between the spacecraft power bus and the FMDS electronics and regulated housekeeping power (± 5 V, ± 12 V, 28 V) to the sensors and plasma source electronics. Primary power for the plasma source power supplies is taken directly from the spacecraft bus with isolation provided by the individual inverter output transformers. Relays are provided to turn the power to the sensors and the plasma source ON/OFF via commands from the controller. Power (nominally 28 Vdc) to operate the valves and relays is obtained by placing a 10-V zener diode in series with the input bus to provide 19- to 33-Vdc power. This approach, although very lossy during the 125-ms pulse to a valve or

15571-7
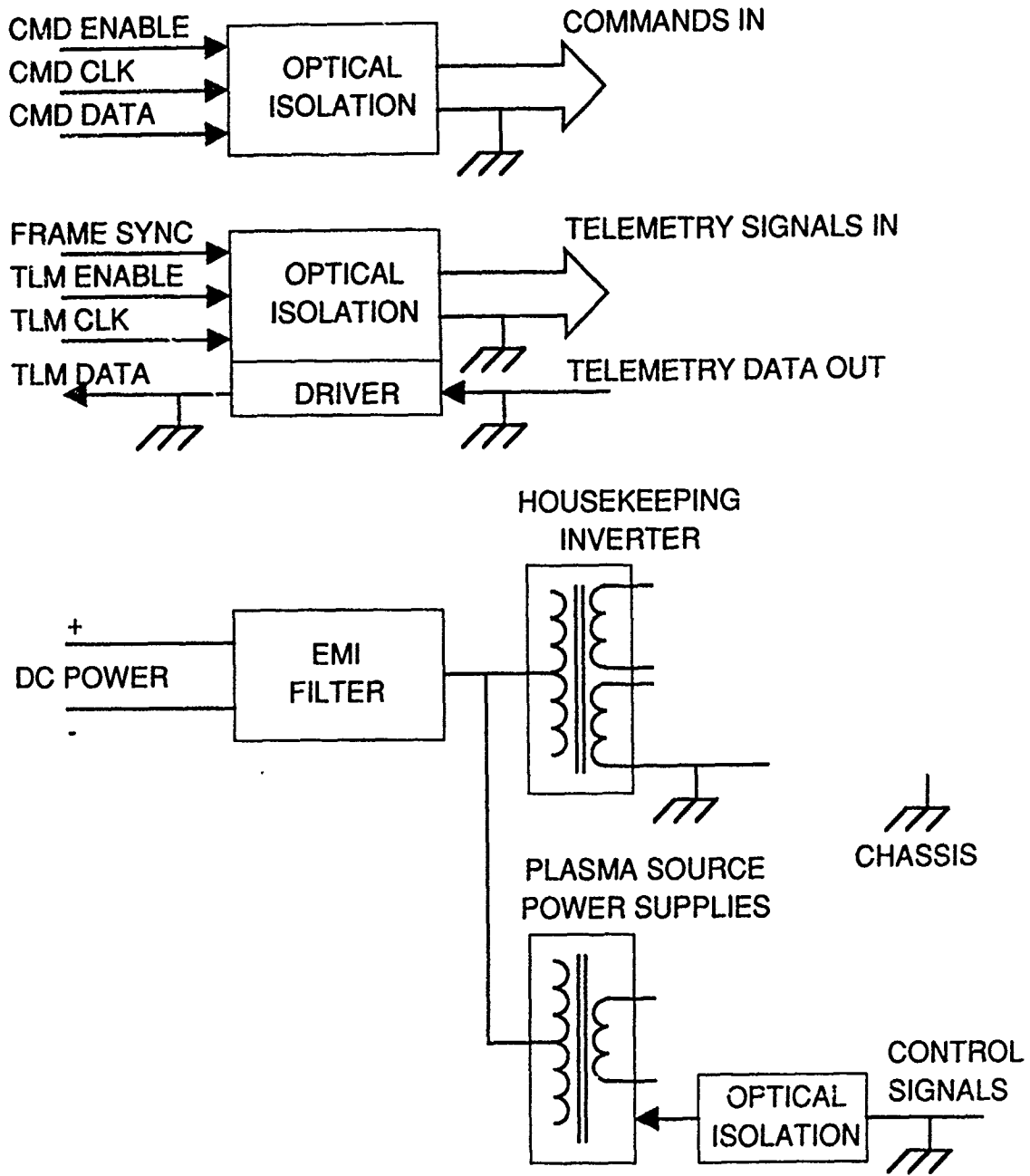
Figure 8-1. Ground return isolation scheme for the FMDS.

172

29-43 Vdc
INPUT

INPUT FILTER		STEP-DOWN PREREGULATOR	20 V	CURRENT-FED SQUARE-WAVE INVERTER		MULTIPLE WINDING OUTPUT SECTION

+28 V
+5 V REG.
±12 V
+15 V
±12 V
±5, +18 V

PMW CONTROL

VALVE AND RELAY DRIVERS
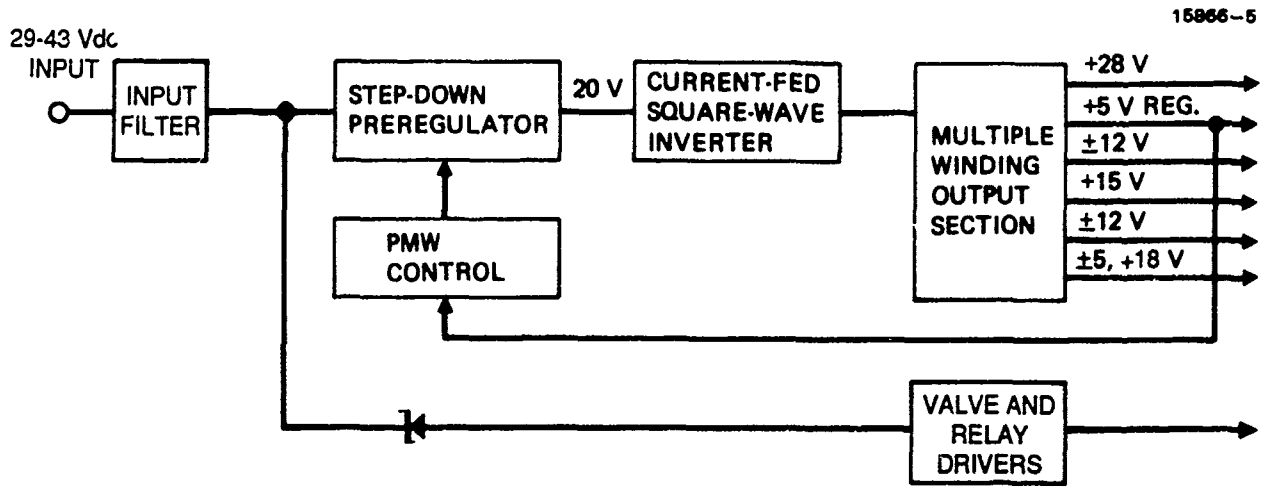
Figure 8-2. Housekeeping inverter isolation and regulation block diagram.

relay, actually dissipates very little average power, since pulses occur on an average of less than one per hour.

The inverter consists of three basic sections as shown in the block diagram of Figure 8-2: (1) A pulse-width-modulated (PWM) step-down preregulator which provides a constant 20-V input to the inverter section; (2) a current-fed, square-wave-inverter section which chops the 20-V power at a 50-kHz rate and provides power to (3) multiple secondary output windings.

The current-fed, push-pull, square-wave converter provides all the characteristics required of this isolation regulator:

- Transformer isolation between input power and output power
- Multiple output capability
- Good cross regulation between outputs
- Minimum complexity.

In addition, this configuration minimizes the high-power stresses imposed on the switching elements during switching intervals by placing a filter choke in the input power line where it can limit the current through the transformer and the switching elements. It also prevents damage due to unbalanced dc currents and effectively turns the converter into a current source which aids in maintaining stable operation over a wide operating range. Minimum complexity is achieved by using one choke in the primary which current feeds all outputs in parallel. Since each secondary winding drives its load directly (without a choke), cross coupling between outputs is very tight, resulting in excellent cross regulation. To achieve good cross regulation, however, it is necessary to maintain a continuous, low-impedance across the primary winding which dictates driving the primary winding at maximum duty cycle (50% each side) at all times. This requirement precludes using PWM for output regulation. Instead, the step-down converter must be used to regulate the voltage to the current-fed converter, which in turn regulates all secondaries in parallel.

A schematic of the housekeeping inverter is shown in Figure 8-3. U1 is the pulse-width-modulator integrated circuit that controls the step-down converter to regulate the 5 Vdc for the controller. All the other housekeeping voltages track this regulated voltage. Q4 is the switching MOSFET that alternately connects L1 to common or to the input bus (via CR1) thereby controlling the average current flowing in L1. L1 is then the current source that feeds the output inverter which is comprised of Q2, Q3, and T3. Q2 and Q3 are alternately switched ON/OFF by flip-flop U2 and T1 which are syncronized to U1. Startup power is applied to U1 and U2 via Q1 and then the circuit is bootstraped via R19 and CR3 to provide

174

Figure 8-3. Schematic of the housekeeping inverter (Sheet 1 of 2).

175

Figure 8-3. Schematic of the housekeeping inverter (Sheet 2 of 2).

NOTES: (UNLESS OTHERWISE SPECIFIED)

higher efficiency. The secondary windings of T3 are rectified and then capacitively filtered to provide the appropriate dc voltages for operating the various FMDS subsystems. Most of the dc outputs are controlled by relays to turn the subsystems ON/OFF. These relay contacts have a small impedance in series with them to limit the transient current when they are closed into the capacitive loads.

VR14 is the zener diode which lowers the input voltage for driving the valves and relays. U6 through U21 are optical isolators which provide ground isolation for the valve and relay drivers. U23, U22, and Q11 comprise a time delay circuit which opens all relays and closes all valves if it is not reset at least once every 16 s. This is part of the controller watchdog timer and is intended to place the FMDS in a safe mode if execution of the controller software has gotten lost, and to disconnect an instrument that is shorting the output of the housekeeping inverter and thereby preventing any of the FMDS subsystems (including the controller) from operating.

The signal from the input current shunt (R103) is amplified and chopped by AR1, CR42, and Q44. The signal is stepped up in voltage and isolated by T4, and then rectified and filtered to provide an analog telemetry signal of input bus current. The input bus voltage is measured by limiting the voltage on the T5 windings to the input bus voltage with CR47. The output of T5 is then rectified and filtered to provide the telemetry signal.

To minimize high frequency EMI radiation from power-distribution lines, all rectification and filtering is performed within the housekeeping subsystem. Only dc power is distributed to the subsystems. Ground returns internal to the FMDS are connected to its case in a manner consistent with minimizing EMI and avoiding internal ground loops. The plasma source must be referenced to the satellite frame (through the bipolar-log electrometer to the FMDS mounting plate) for proper operation.

An input filter is provided for the spacecraft bus and is designed to meet the requirements of MIL-STD-461B and MIL-STD-1541. The Filter, shown in Figure 8-4, is a two stage LC filter and feeds all of the FMDS inverters. Its calculated attenuation characteristics are shown in Figure 8-5.

The housekeeping inverter and the input filter are housed in the plasma source electronics box discussed in Section 7.7.

8.2 COMMANDS AND TELEMETRY

All commands and telemetry to and from the FMDS are in the form of serial digital signals. Ground isolation of digital signals is easily performed with optical isolators while ground isolation of analog signals is a much more complicated process. The use of serial digital signals (as opposed to parallel digital signals) and multiplexing the commands or

Figure 8-4. FMDS input filter schematic.
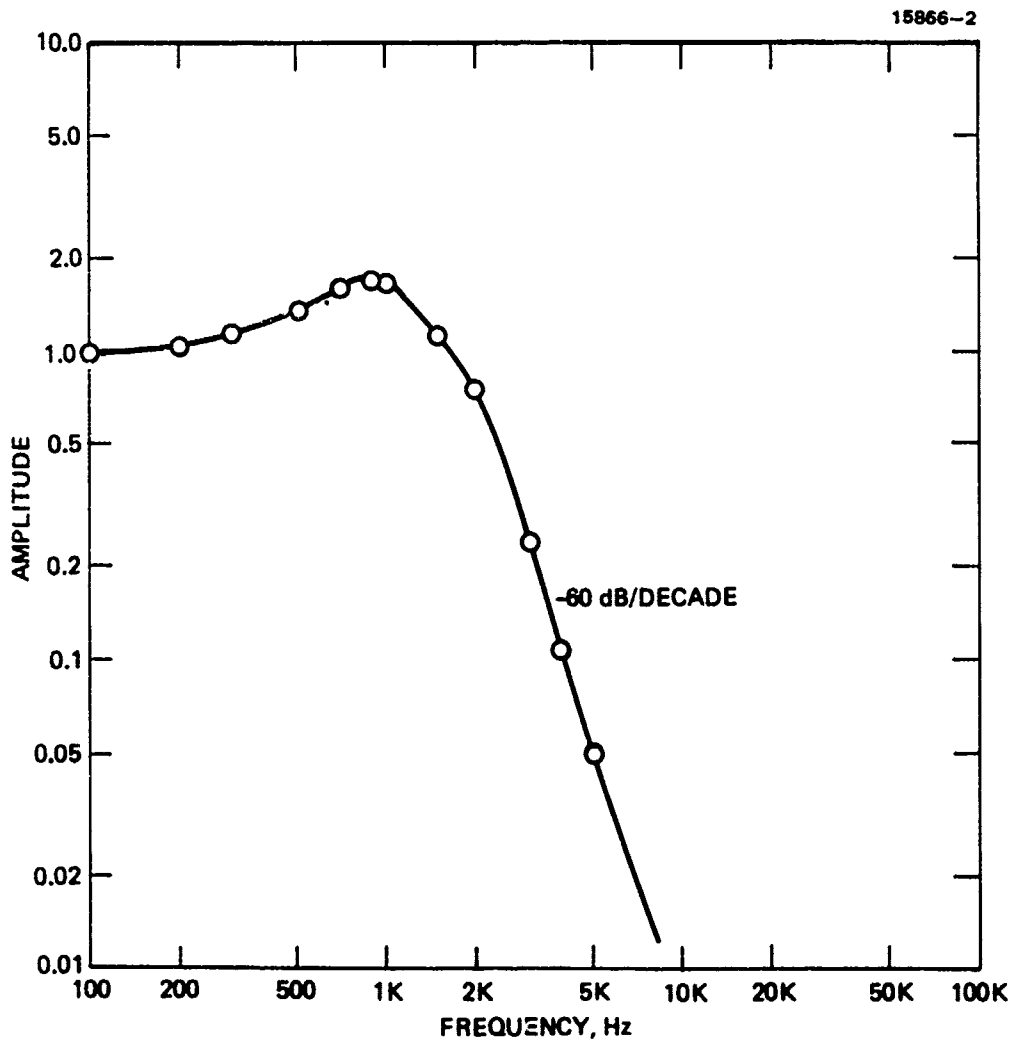
Figure 8-5. Attenuation characteristics of the input filter.

179

telemetry words sequentially over the same wires significantly simplifies the command and telemetry interfaces with the spacecraft. The command interface requires three lines (an enable, a clock, and a data line) and the telemetry interface requires four lines (an enable, a clock, a data, and a frame-sync line).

The optical isolation and driver circuits are shown in Figure 6-6. The telemetry data line requires optical isolation on the spacecraft end, while the other six lines have their optical isolation on the FMDS end. Futher details of the command and telemetry interface were presented in Section 6.1 and a listing of the commands and telemetry words is in Appendix A.

8.3   MECHANICAL DESIGN

The mechanical design of the FMDS was discussed in Section 2.1 and the FMDS is shown in Figure 2-2. The overall dimensions, masses, and power consumption are also detailed in Section 2.1. The thermal design is discussed in Section 9.

SECTION 9
SYSTEM THERMAL ANALYSIS

The following sections summarize the results of the FMDS thermal analysis study from its inception in 1983 until its completion in September 1986. Figures and tables are included which show predicted system temperatures under various conditions.

In addition to the development of an FMDS thermal model, certain key modules were analyzed. Steady state analyses of the TPM Threshold Detector, Master Microprocessor, and Plasma Generator Electronics (Shelf 2) Assemblies were performed. The purpose of these module analyses was to predict component operating temperatures and compare the results with the maximum acceptable component derated temperatures per Hughes S&CG document PA201. The CINDA thermal models used to calculate these temperatures were delivered as a separate report under the contract.

9.1 ANALYSIS INPUTS

This section contains the physical and thermal configurations assumed for the thermal analyses.

9.1.1 Physical Design

The FMDS system components mounted on the honeycomb mounting plate are shown in Figure 9-1. With the exception of the plasma generator, the system is covered with an aluminum enclosure. The enclosure sides are blanketed with Multi Layer Insulation (MLI) while the top is covered with quartz radiator and/or MLI. The normalized radiator area, A_R, is a key parameter in the presentation of the results to follow. The primary system components in Figure 9-1 are:

> Plasma Generator
> Plasma Generator Electronics
> Electrostatic Analyzer (ESA)
> Transient Pulse Monitor (TPM)
> Surface Potential Monitors (SPMs)
> Controller.

The mounting position of the FMDS must be on an external surface of the satellite so that the ESA, TPM, SPMs, and plasma generator will have a view of the natural space environment. One such mounting position is shown in Figure 9-2.

Figure 9-1. FMDS power dissipation map.

WEST SPOT
REFLECTOR

FMDS

FEED ARRAY
APERTURE
COVER

EAST SPOT
REFLECTOR
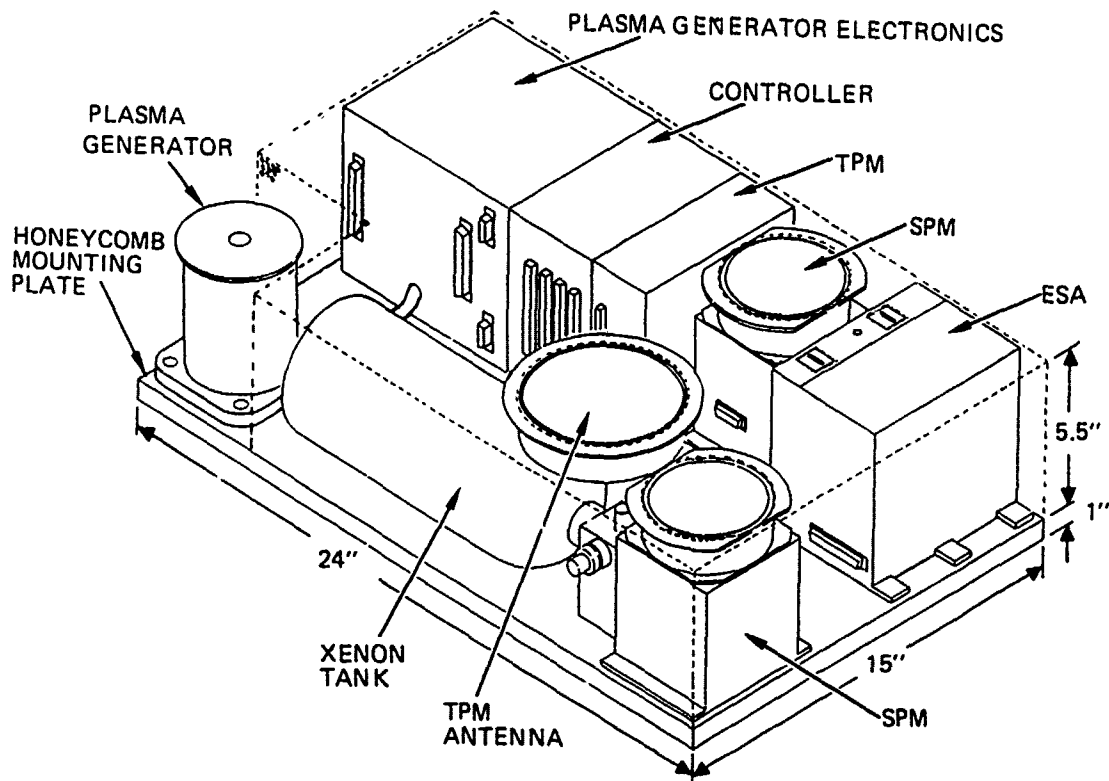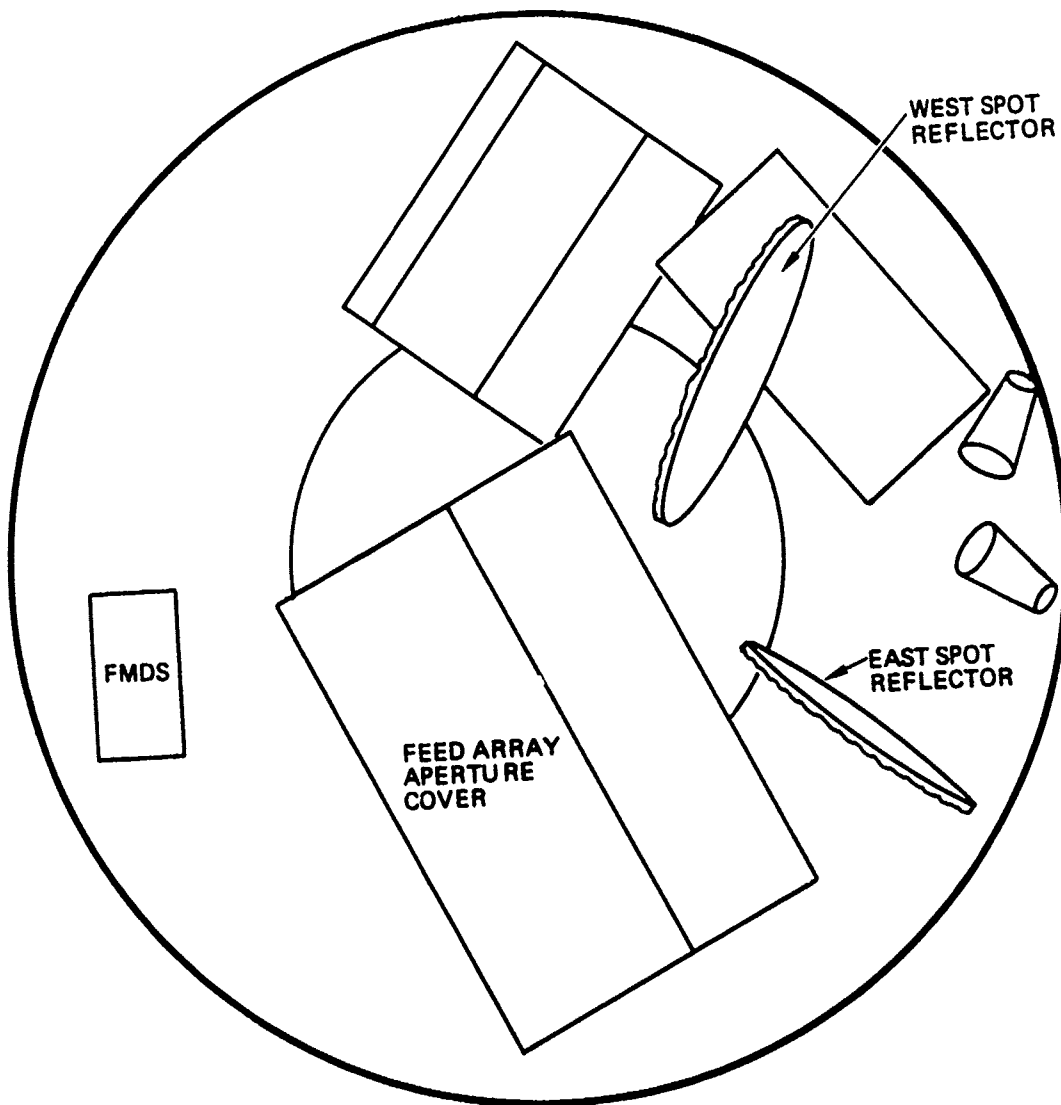
Figure 9-2. FMDS mounted near the antenna farm of a spin stabilized communications satellite.

The TPM Threshold Detector and Master Microprocessor Assemblies consist of a Multiwire board[7] mounted at the top and bottom to right angle brackets. A cross section of a typical Multiwire board is shown in Figure 9-3. A polyimide core 0.030 in. thick is coated on both sides with 2 ounce copper layers which serve as power and ground planes. A typical ground plane with cutouts for component and via holes is shown in Figure 9-4. Each layer of copper is covered with 0.006 in. of prepreg (adhesive layer) and glass epoxy which forms the outer surface of the board. A Multiwire board provides the conductive interconnections between electrical components through the use of insulated #34 AWG magnet wire embedded in the surface layer of the board.

The components in the Source Electronics Assembly are mounted on a 0.050 in. thick aluminum mounting plate which is 5.9 by 5.4 in.

9.1.2 Thermal Configuration

Figure 9-5 shows a simplified thermal model of the FMDS with boundary conditions at the satellite/FMDS interface as well as the space/FMDS and satellite-structure/FMDS interfaces which interact radiatively with the system. The top of the aluminum enclosure is tightly coupled to space when it is entirely covered with radiator.

The relationship between system-level and board-level analysis is shown schematically in Figure 9-6. The electronics boxes which are conductively connected to themselves, the top of the enclosure, and the honeycomb mounting plate are also radiatively connected to their interior surroundings. The latter point is true for all system components within the enclosure.

The Master Microprocessor and TPM Threshold Detector Assemblies are shown in Figures 9-7 and 9-8 respectively. Multiwire boards are used for both assemblies and details of the different board layers are shown below. These boards are mounted by front-surface right-angle aluminum brackets 0.050 in. thick. It is assumed that all of the component generated heat must flow through the board and exit at one of the right-angle brackets. The two copper layers of the board provide most of the lateral heat path.

BOARD LAYER	MATERIAL	THICKNESS(inches)
1	epoxy	0.006
2	prepreg	0.006
3	copper	0.0028
4	polyimide	0.030
5	copper	0.0028
6	prepreg	0.006
7	epoxy	0.006
	TOTAL	0.0596
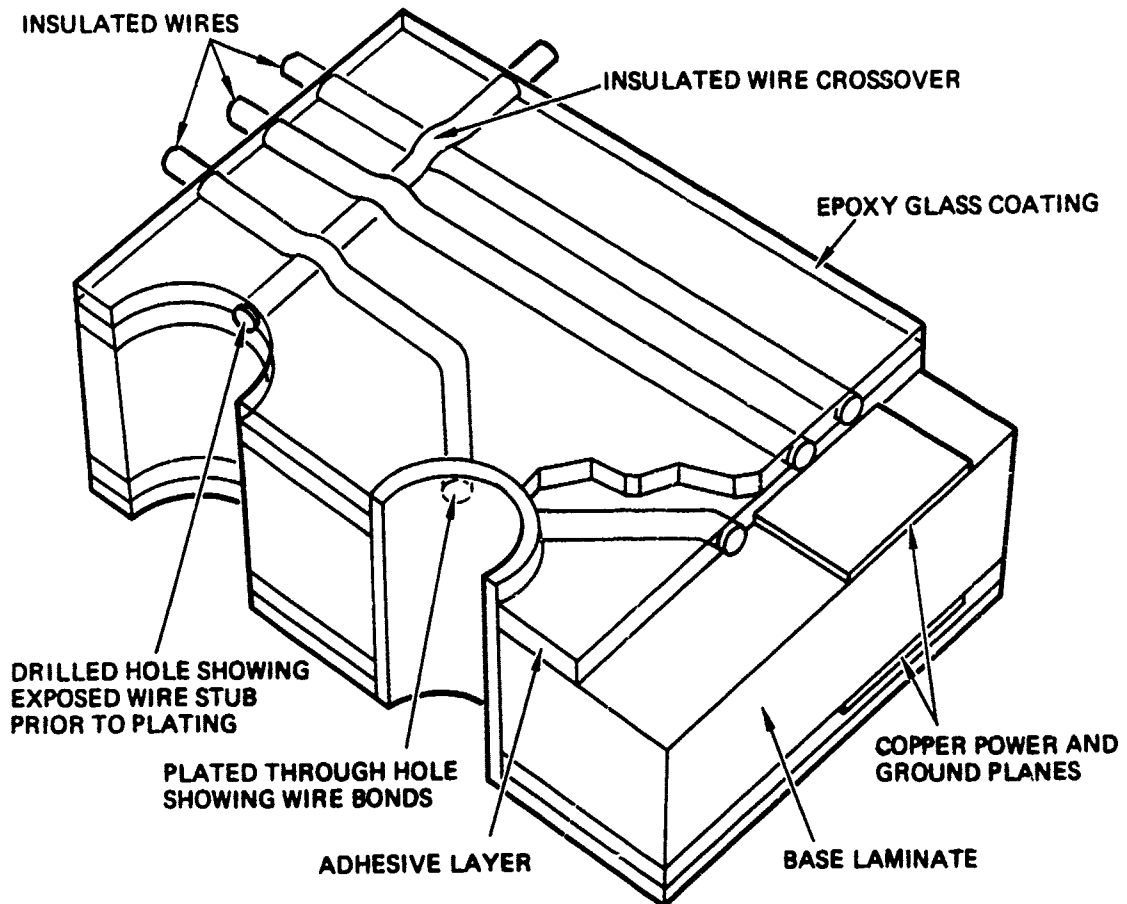
Figure 9-3. Cross section of a multiwire board.
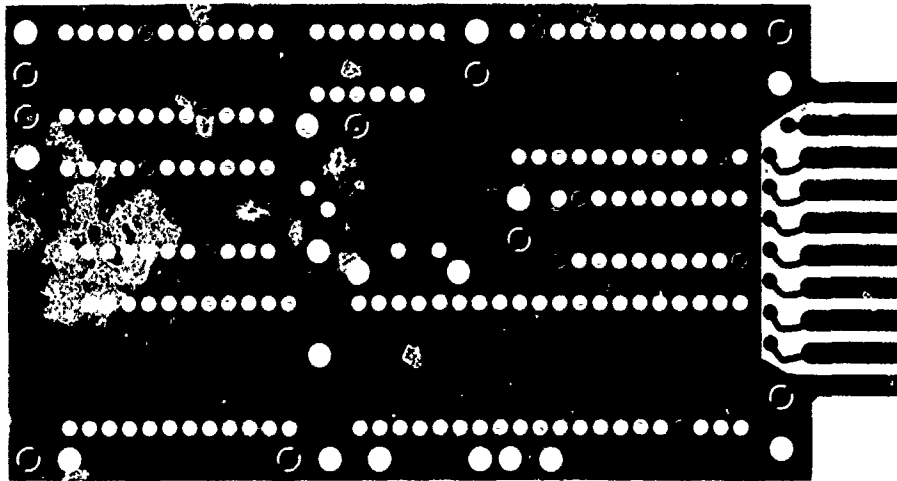
Figure S-4. Typical multiwire board ground plane.

16980–5

SPACE
σT^4

ANTENNA FARM
σT^4

$\dfrac{1-\epsilon}{A\epsilon}$

$\dfrac{1-\epsilon}{A\epsilon}$

$\dfrac{1}{AF}$

$\dfrac{1}{AF}$

$\dfrac{1}{AF}$

Q
DIRECT SOLAR
ALBEDO
EARTH IR

QUARTZ RADIATOR

$\dfrac{1-\epsilon}{A\epsilon}$

MLI BLANKET
FOUR SIDES

$Q_{electronics}$

Q_{heater}

R_m $\left\{\begin{array}{l} \text{I – INSULATED} \\ \text{R – RADIATIVE} \\ \text{C – CONDUCTIVE} \end{array}\right.$

SATELLITE
T_m
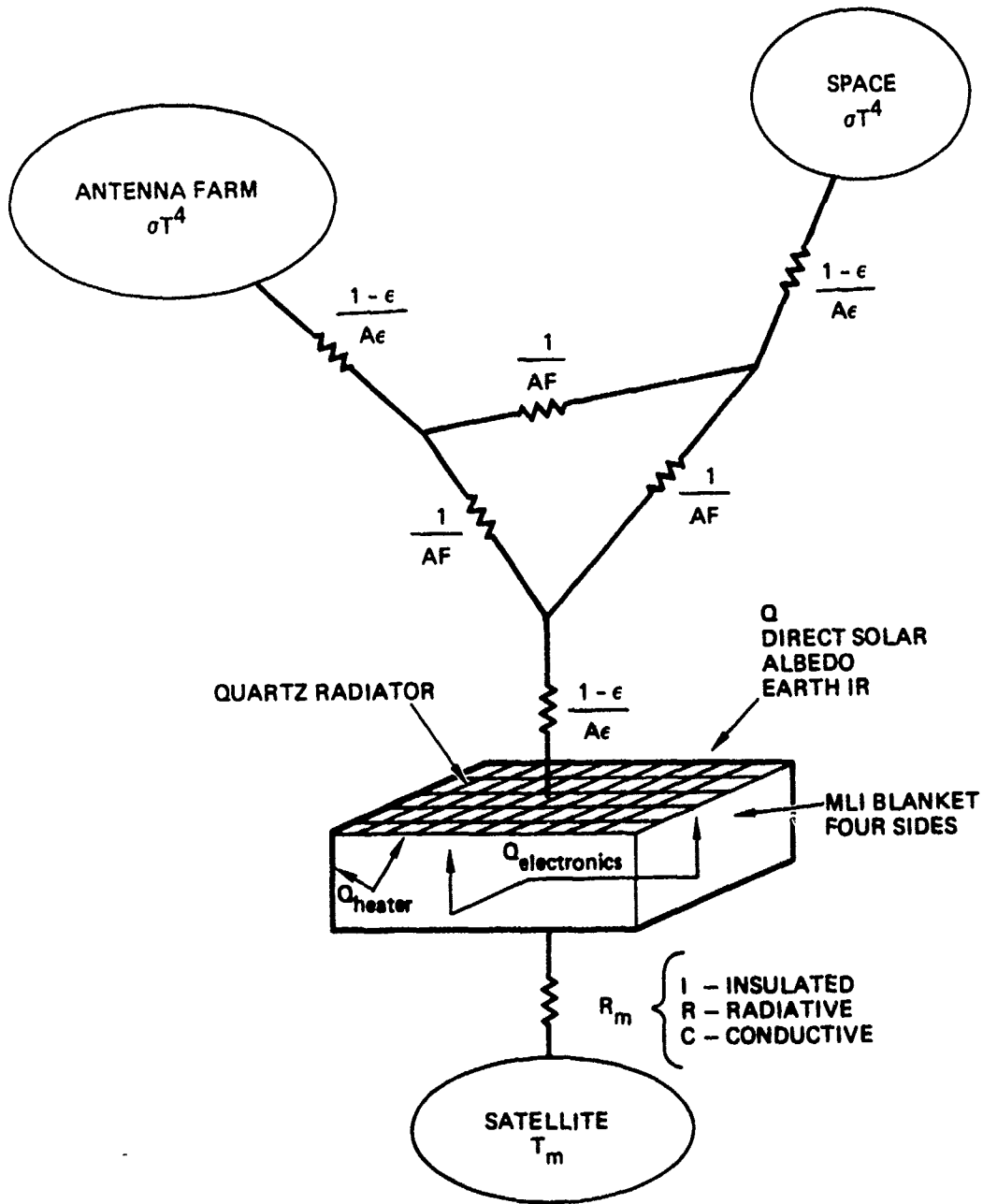
Figure 9-5. Simplified thermal model of the FMDS.

187
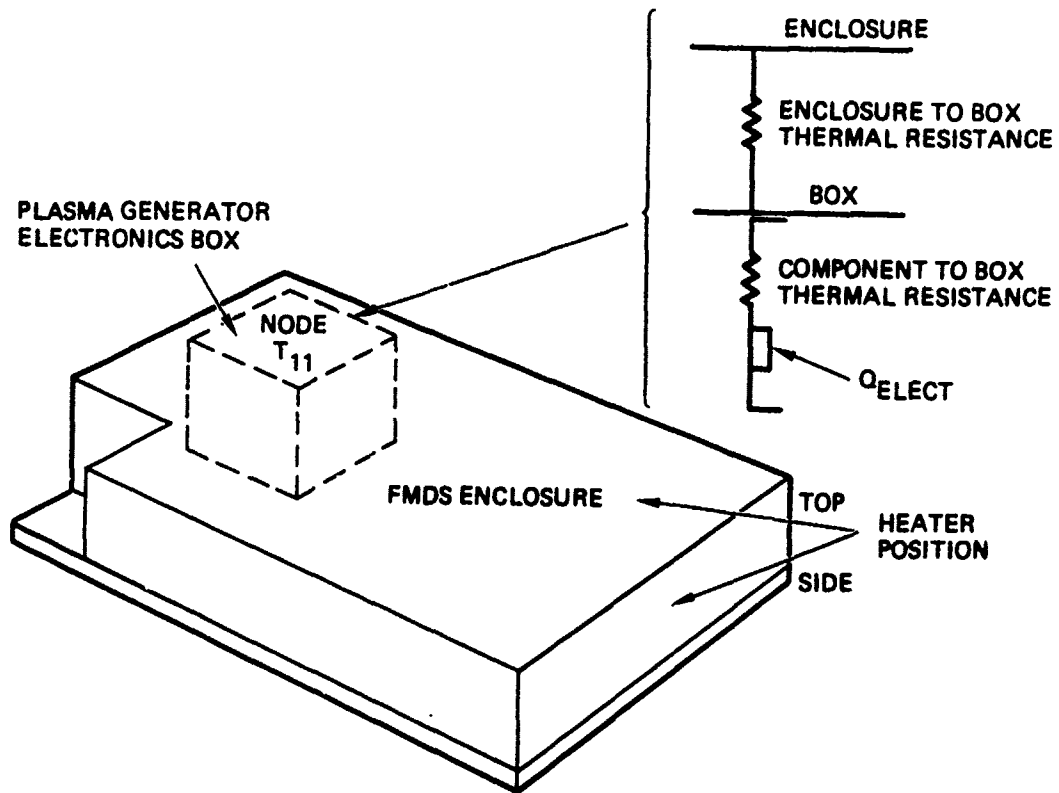
Figure 9-6. Typical enclosure/electronics-box/component thermal interface.

16980—7
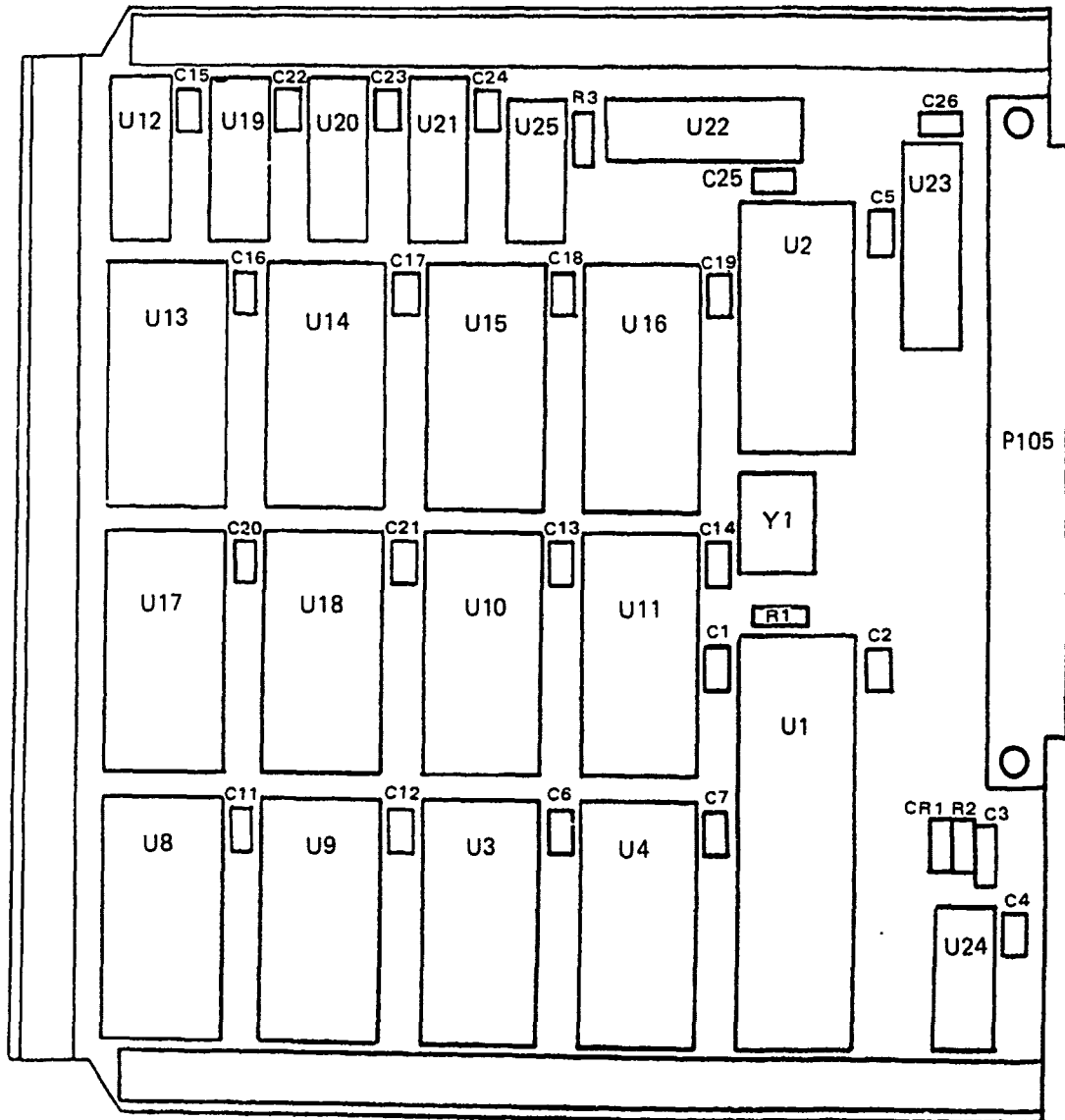
Figure 9-7. Master microprocessor assembly component layout.

189
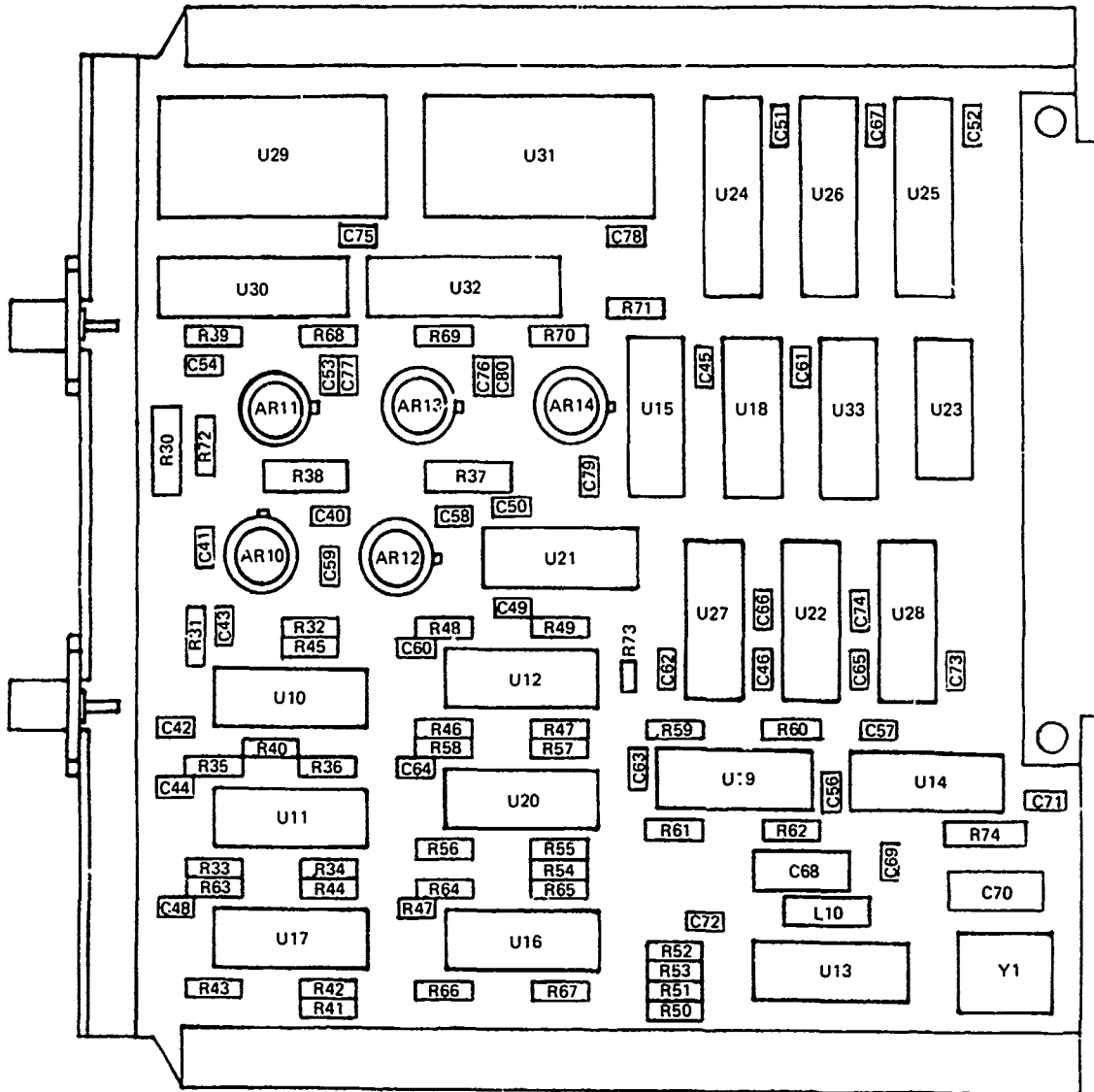
Figure 9-8. TPM threshold detector assembly component layout.

The Plasma Generator Electronics (Shelf 2) Assembly (shown in Figure 9-9) is constructed around a 0.050 in. thick aluminum plate with the heat dissipating components bonded and/or stud-mounted to the plate. Interconnections between electrical components are hard wired with insulated via holes providing passage through the aluminum plate. Two components are mounted on transformer T1-CH and for these the mounting temperature is taken to be the transformer case temperature.

9.2 OPERATING CONDITIONS

A power dissipation map of the FMDS system is shown in Figure 9-10. Some minor changes to this map have occurred, however, this map is the baseline for the thermal analysis. The system has two basic modes of operation that are considered. The first, the "operating" mode, corresponds to operation of the plasma source and has the maximum dissipation (25.5 W). The second mode is the "monitoring" mode during which time the plasma source and its electronics are off and therefore not dissipating any power. The system dissipation for this mode is 10.5 W.

Two thermal cases are considered for these operating modes. For the first, the hot case, operating and environmental conditions are chosen to result in the highest system temperatures. The system is considered to be in the "operating" mode with a 43°C mounting surface temperature, and under a solar load at the End-of-Life (EOL). For the second case, the cold case, the mounting surface temperature is -13°C, there is no solar load, and the system is in the "monitoring" mode.

The TPM Threshold Detector, the Plasma Generator Electronics (Shelf 2), and the Master Microprocessor Assemblies are assumed to dissipate a worst case of 4.8, 11.4, and 0.3 W respectively. In actual practice, they will dissipate less power than this. The boundary temperatures for the TPM Threshold Detector Assembly are 54°C at the bottom bracket and 50°C at the top bracket. The boundry temperatures for the Plasma Generator Electronics and Master Microproccesor Assemblies are 57°C at the bottom bracket and 61°C at the top bracket. These boundary temperatures were calculated using the system thermal model for the hot case and are both (top and bottom) within 4°C of each other. Junction and case temperatures for the parts are compared to component derated temperatures per Hughes S&CG document number PA201.

191
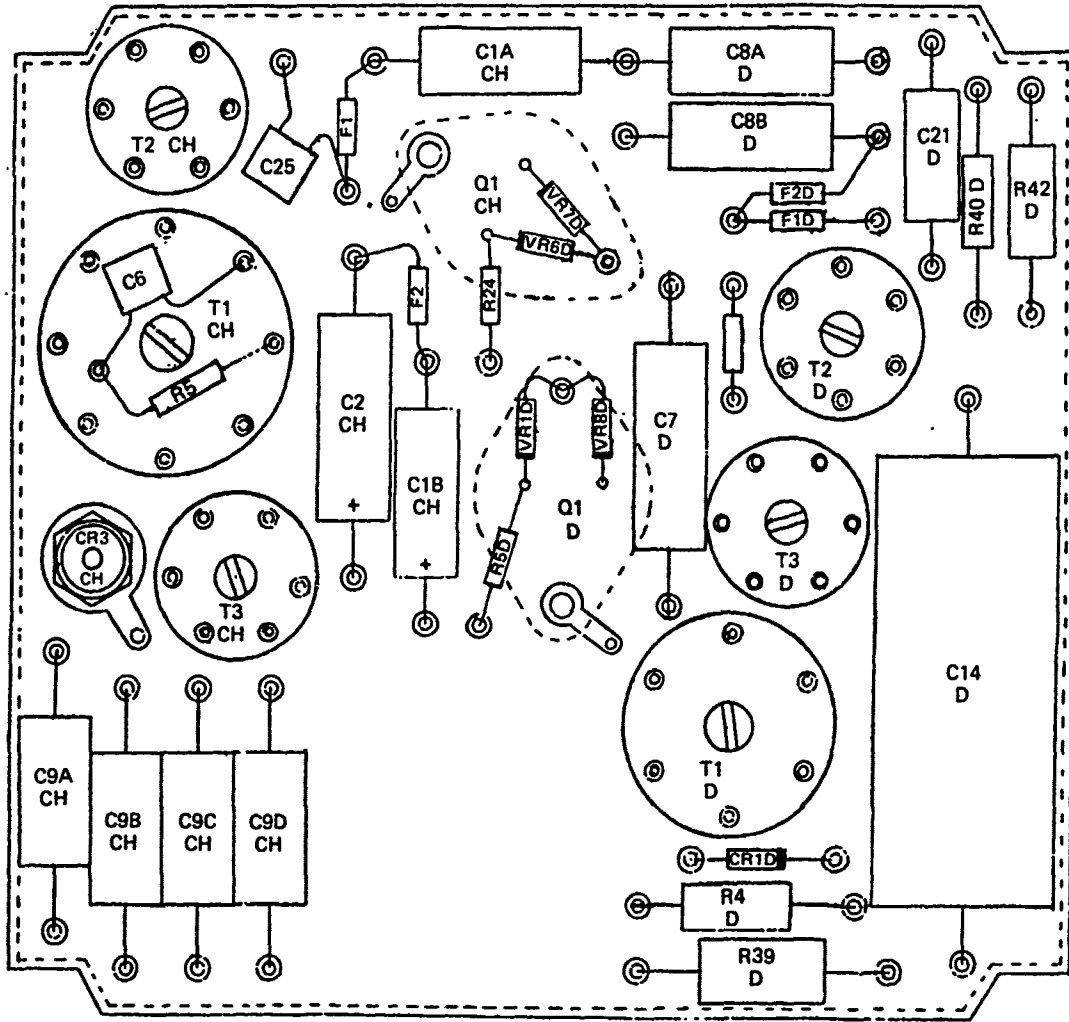
Figure 9-9. Plasma generator electronics (shelf 2) assembly component layout.
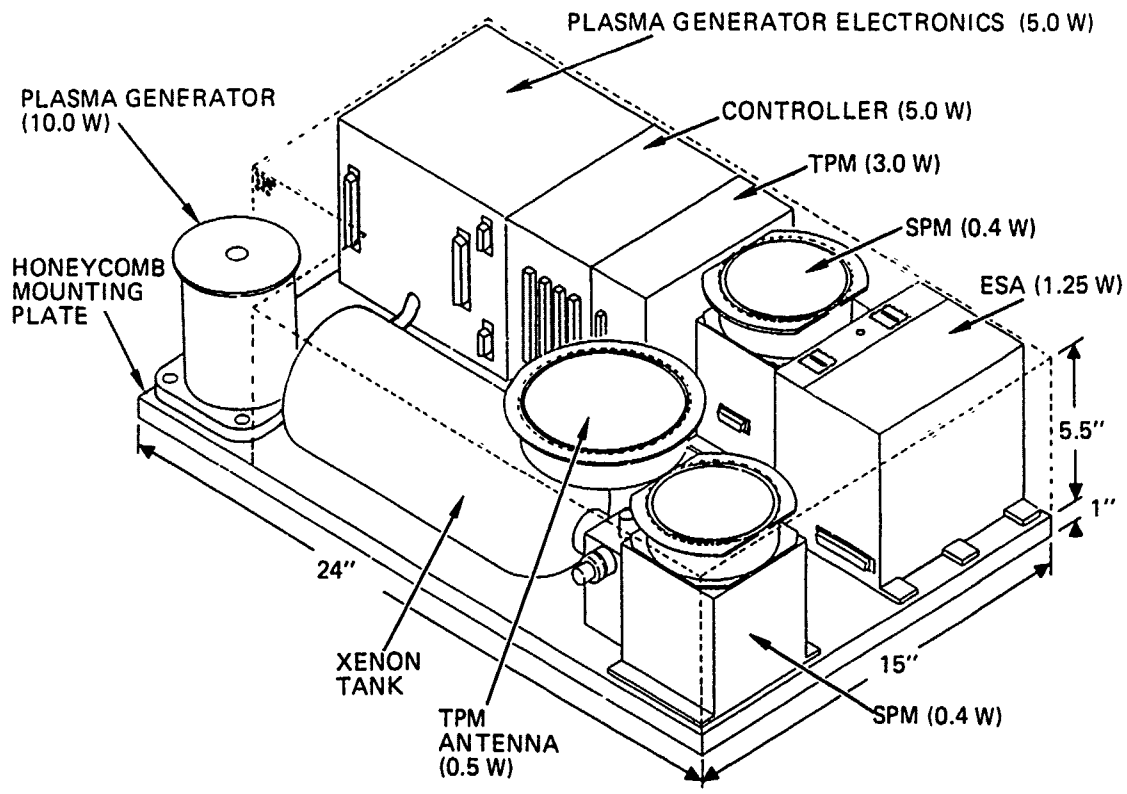
Figure 9-10. Flight Model Discharge System (FMDS).

9.3 ASSUMPTIONS

The following assumptions were made in the system analysis:

1) Off normal solar incidence (23.4°)

2) Unobstructed view of space

3) No concentration of solar load

4) Internal subassemblies painted black

5) Surface properties:

	Emissivity	Absorption
Radiator	0.8	0.1(BOL)/0.2(EOL)
MLI blanket	0.65	0.1(BOL)

6) Aluminum wall thickness:

Enclosure - 0.050 in.

Electronics box - 0.050 in.

The following assumptions were made in the board analyses:

1) There is negligible thermal contact resistance between the board and its mounting bracket.

2) The copper planes extend throughout the board (except where cutouts occur) and under the area in contact with the mounting brackets - the latter point should not be over looked with regard to its impact on board temperature deltas.

3) All component maximum allowable temperatures are taken to be 100°C for the Master Microprocessor Assembly.

4) The junction-to-case thermal resistance (θ_{JC}) for U1, U3-U11, and U19-U23 of the Master Microprocessor Assembly was assumed to be 80°C/W. The actual value was unknown at the time of analysis, however, this is a typical value for military approved dual-in-line packages.

5) The junction-to-case thermal resistances (θ_{JC}) for the TPM Threshold Detector Assembly are shown in Table 9-1.

9.4 ANALYSIS METHOD

The system-level thermal model was shown in Figure 9-5 and represents a simplified version of the more detailed system nodal map as shown in Figure 9-11. Predicted temperatures at the nodes of Figure 9-11 were calculated using the CINDA thermal analyzer program available at Hughes.

194

Table 9-1. TPM Threshold Detector Assembly Steady State Component operating Temperatures.

CIRCUIT SYMBOL	PART NUMBER	THETA JC (DEG C/W)	POWER (WATTS)	MOUNTING SURFACE TEMP (DEG C)	CASE TEMP (DEG C)	JUNCTION TEMP (DEG C)	MAXIMUM ALLOWABLE TEMP (DEG C)
U10	M38510/06301BEB	50.000	0.380	74.	81.	100.	105.
U11	M38510/06002BEB	50.000	0.100	71.	72.	77.	105.
U12	M38510/06002BEB	50.000	0.100	74.	76.	81.	105.
U13	M38510/10516/BEBJC	35.000	0.250	63.	65.	74.	105.
U14	M38510/06301BEB	50.000	0.380	73.	78.	97.	105.
U15	CD4040BD/3AR	50.000	0.002	71.	71.	71.	105.
U16	M38510/06101BEB	50.000	0.250	65.	70.	82.	105.
U17	M38510/10578/BEBJC	35.000	0.375	66.	73.	86.	105.
U18	CD4040BD/3AR	50.000	0.002	71.	71.	72.	105.
U19	M38510/06101BEB	50.000	0.250	73.	76.	89.	105.
U20	M38510/10578/BEBJC	35.000	0.375	73.	80.	93.	105.
U21	M38510/06302BEB	50.000	0.380	74.	81.	100.	105.
U22	M38510/06302BEB	50.000	0.380	75.	82.	101.	105.
U23	M38510R/17101BCB	50.000	0.001	70.	70.	70.	105.
U24	HS1-82C08RH-8	50.000***	0.004	65.	65.	65.	105.
U25	HS1-82C08RH-8	50.000***	0.004	64.	64.	64.	105.
U26	HS1-82C08RH-8	50.000***	0.004	65.	65.	65.	105.
U27	M38510/06302BEB	50.000	0.380	75.	82.	101.	105.
U28	M38510/06302BEB	50.000	0.380	74.	81.	100.	105.
U29	M38510R/17602BJB	40.000	0.004	62.	62.	62.	105.
U30	TRW5435**		0.001	66.	66.		105.
U31	M38510R/17602BJB	40.000	0.004	62.	62.	62.	105.
U32	TRW5435**		0.001	66.	66.		105.
U33	M38510R/05553BEB	50.000	0.001	71.	71.	71.	105.
Y1	909146-13		0.000	62.	62.		105.
L10	M39010/06ER33LR		0.000	67.	67.		105.
AR10	LM161H/883B	45.000	0.100	73.	77.	81.	105.
AR11	HS2-3530RH-8	45.000***	0.020	69.	70.	71.	105.
AR12	LM161H/883B	45.000	0.100	73.	77.	82.	105.
AR13	HS2-3530RH-8	45.000***	0.020	68.	69.	70.	105.
AR14	HS2-3530RH-8	45.000***	0.020	69.	70.	71.	105.
R30	RNC60H1500FR		0.013	71.	84.		110.
R31	RCR07G102JS		0.013	72.	87.		95.
R32	RCR07G511JS		0.013	73.	87.		95.
R33	RCR07G511JS		0.013	68.	82.		95.
R34	RCR07G511JS		0.013	68.	83.		95.
R35	RCR07G511JS		0.013	73.	85.		95.
R36	RCR07G511JS		0.013	73.	86.		95.
R37	RNC60H3162FR		0.013	72.	86.		110.
R38	RNC60H3162FR		0.013	71.	85.		110.
R39	RCR07G153JS		0.013	69.	83.		95.

NOTE: THE MAXIMUM ALLOWABLE TEMPERATURE IS THE UPPER LIMIT OF THE "ACCEPTABLE" TEMPERATURE REGION.

** THIS COMPONENT IS A RESISTOR NETWORK AND DOES NOT HAVE A JUNCTION.

*** θ_{JC} WAS ASSUMED FOR THIS COMPONENT

Table 9-1. TPM Threshold Detector Assembly Steady State Component operating Temperatures (Continued).

CIRCUIT SYMBOL	PART NUMBER	THETA JC (DEG C/W)	POWER (WATTS)	MOUNTING SURFACE TEMP (DEG C)	CASE TEMP (DEG C)	JUNCTION TEMP (DEG C)	MAXIMUM ALLOWABLE TEMP (DEG C)
R40	RCR07G511JS		0.013	73.	87.		95.
R41	RCR07G511JS		0.013	59.	73.		95.
R42	RCR07G511JS		0.013	59.	73.		95.
R43	RCR07G511JS		0.013	59.	73.		95.
R44	RCR07G511JS		0.013	68.	83.		95.
R45	RCR07G511JS		0.013	74.	88.		95.
R46	RCR07G511JS		0.013	73.	87.		95.
R47	RCR07G511JS		0.013	73.	87.		95.
R48	RCR07G511JS		0.013	74.	88.		95.
R49	RCR07G511JS		0.013	74.	88.		95.
R50	RCR07G511JS		0.013	58.	73.		95.
R51	RCR07G511JS		0.013	58.	73.		95.
R52	RCR07G511JS		0.013	63.	78.		95.
R53	RCR07G511JS		0.013	63.	78.		95.
R54	RCR07G511JS		0.013	68.	83.		95.
R55	RCR07G511JS		0.013	68.	83.		95.
R56	RCR07G511JS		0.013	68.	83.		95.
R57	RCR07G511JS		0.013	73.	87.		95.
R58	RCR07G511JS		0.013	73.	87.		95.
R59	RCR07G511JS		0.013	73.	87.		95.
R60	RCR07G511JS		0.013	73.	87.		95.
R61	RCR07G511JS		0.013	70.	83.		95.
R62	RCR07G511JS		0.013	70.	83.		95.
R63	RCR07G511JS		0.013	68.	82.		95.
R64	RCR07G511JS		0.013	68.	83.		95.
R65	RCR07G511JS		0.013	68.	83.		95.
R66	RCR07G511JS		0.013	59.	73.		95.
R67	RCR07G511JS		0.013	58.	73.		95.
R68	RCR07G243JS		0.013	69.	83.		95.
R69	RCR07G394JS		0.013	69.	83.		95.
R70	RCR07G243JS		0.013	69.	83.		95.
R71	RCR07G394JS		0.013	65.	80.		95.
R72	RCR07G394JS		0.013	71.	84.		95.
R73	RCR07G511JS		0.013	73.	88.		95.
R74	RNC50H4021		0.001	69.	69.		119.
C40	M39014/01-1553		0.000	71.	71.		100.
C41	M39014/01-1553		0.000	72.	72.		100.
C42	M39014/01-1553		0.000	71.	71.		100.
C43	M39014/01-1553		0.000	73.	73.		100.
C44	M39014/01-1553		0.000	70.	70.		100.
C45	M39014/01-1553		0.000	69.	69.		100.

NOTE: THE MAXIMUM ALLOWABLE TEMPERATURE IS THE UPPER LIMIT OF THE "ACCEPTABLE" TEMPERATURE REGION.

(Continued)

Table 9-1. TPM Threshold Detector Assembly Steady State Component operating
Temperatures (Continued).

CIRCUIT SYMBOL	PART NUMBER	THETA JC (DEG C/W)	POWER (WATTS)	MOUNTING SURFACE TEMP (DEG C)	CASE TEMP (DEG C)	JUNCTION TEMP (DEG C)	MAXIMUM ALLOWABLE TEMP (DEG C)
C46	M39014/01-1553		0.000	75.	75.		100.
C48	M39014/01-1553		0.000	67.	67.		100.
C49	M39014/01-1553		0.000	74.	74.		100.
C50	M39014/01-1553		0.000	72.	72.		100.
C51	M39014/01-1553		0.000	62.	62.		100.
C52	M39014/01-1553		0.000	61.	61.		100.
C53	M39014/01-1553		0.000	69.	69.		100.
C54	M39014/01-1553		0.000	69.	69.		100.
C56	M39014/01-1553		0.000	70.	70.		100.
C57	M39014/01-1553		0.000	73.	73.		100.
C58	M39014/01-1553		0.000	72.	72.		100.
C59	M39014/01-1553		0.000	73.	73.		100.
C60	M39014/01-1553		0.000	73.	73.		100.
C61	M39014/01-1553		0.000	68.	68.		100.
C62	M39014/01-1553		0.000	73.	73.		100.
C63	M39014/01-1553		0.000	72.	72.		100.
C64	M39014/01-1553		0.000	68.	68.		100.
C65	M39014/01-1553		0.000	74.	74.		100.
C66	M39014/01-1553		0.000	75.	75.		100.
C67	M39014/01-1553		0.000	62.	62.		100.
C68	908535-1		0.000	67.	67.		100.
C69	M39014/01-1553		0.000	66.	66.		100.
C70	908535-1		0.000	65.	65.		100.
C71	M39014/01-1553		0.000	69.	69.		100.
C72	M39014/01-1553		0.000	63.	63.		100.
C73	M39014/01-1553		0.000	71.	71.		100.
C74	M39014/01-1553		0.000	74.	74.		100.
C75	M39014/01-1553		0.000	66.	66.		100.
C76	M39014/01-1553		0.000	69.	69.		100.
C77	M39014/01-1553		0.000	69.	69.		100.
C78	M39014/01-1553		0.000	65.	65.		100.
C79	M39014/01-1553		0.000	72.	72.		100.
C80	M39014/01-1553		0.000	69.	69.		125.

TOTAL OF PART DISSIPATIONS: 4.841 WATTS
AVERAGE JUNCTION TEMPERATURE: 79.5   DEG C

NOTE: THE MAXIMUM ALLOWABLE TEMPERATURE IS THE UPPER LIMIT
OF THE 'ACCEPTABLE' TEMPERATURE REGION

16980–15R1

BACK
(1100)

RIGHT
(1090)

COVER

TOP
(1060)

LEFT
(1080)

FRONT
(1110)

PLASMA GENERATOR ELECTRONICS

CONTROLLER

PLASMA
GENERATOR

(11)

(12)

(13)

TPM

SPM

ESA

(21)

(22) (23)

(14)

(60)

(80)

(24)

(15)

XENON TANK

(70)

TPM ANTENNA

SPM

(41)

(42)

(51)

(43)

HONEYCOMB
MOUNTING PLATE

(52)

(44)

(53)

(54)

(45)

SPACECRAFT
MOUNTING SURFACE
(5000)

(55)

Figure 9-11. Detailed FMDS nodal map.

198

The board analyses were performed using CINDA with preprocessing accomplished through the use of Hughes Product Analysis Laboratory's NEWT5 and ATDP programs. NEWT5 permits the digitized input of board and component position data, while ATDP automates certain phases of input and output table format.

9.5 RESULTS

The system-level results are presented as curves of A_R (normalized radiator area) versus T_{HOT} and as curves of Q (heater dissipation in watts) versus T_{COLD} with A_R as a parameter. The variables T_{HOT} and T_{COLD} are taken at the top of the plasma generator electronics box, node 11 in Figure 9-11. This node was chosen to provide a reference electronics-module mounting temperature. If this value is too high, then the electronic components will have high operating temperatures resulting in reduced reliability and shorter life time. The curves of Figure 9-12 are labeled as follows:

C - FMDS conductively connected (thermally) to the satellite with mounting surface temperatures of 43°C and -13°C.

R - FMDS radiatively connected to the satellite with internal satellite subsystems at 43°C and -13°C.

I - FMDS insulated from the satellite.

The connection referred to here is from the FMDS honeycomb mounting plate to the satellite as shown in Figures 9-5 and 9-11. The radiator size A_R in Figure 9-12 was determined from the "hot case" by calculating the temperature T_{11} for which $T_{11} = T_{HOT}$. If the radiative area is less than this area then $T_{11} > T_{HOT}$; if the area is greater then $T_{11} < T_{HOT}$.

All curves exhibit a drop in temperature as the radiator area increases. The slopes of the curves vary with the insulated case showing the greatest variation in temperature with a change in radiator area. The conductive case provides the best thermal connection with the satellite and shows the least variation of T_{HOT} with a change in area.

The heater power in Figures 9-13 through 9-15, assumed to be distributed uniformly over the enclosure sides, was determined from the "cold case" with the radiator area as a given and calculating the node 11 temperature for which $T_{11} = T_{COLD}$. If the heater dissipation is greater then $T_{11} > T_{COLD}$; if the dissipation is less then $T_{11} < T_{COLD}$.

Figures 9-13 through 9-15 plot curves of Q versus T_{COLD} for the conductive, radiative, and insulated cases respectively. Depending on the mounting arrangement, these curves can be used to estimate the heater value that would be required to keep component temperatures within a specified operating temperature range.

Given the electronics box boundary temperatures for the "hot case", the three electronics assemblies were analyzed to provide board temperature maps for given component dissipations

16980-11
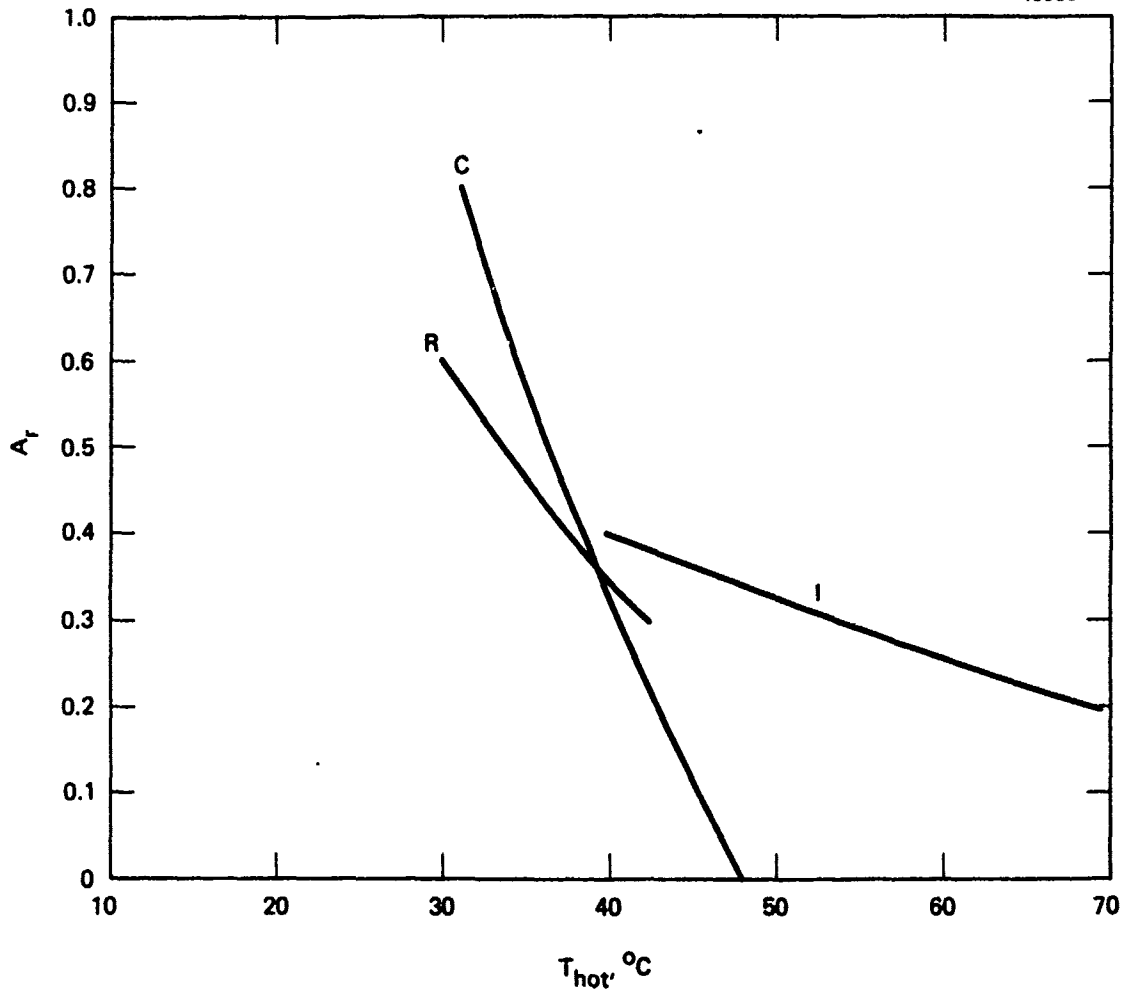
Figure 9-12.   Normalized radiator area versus T_{HOT} for the conductive, radiative, and insulated connections with $T_M = 43°C$.

200
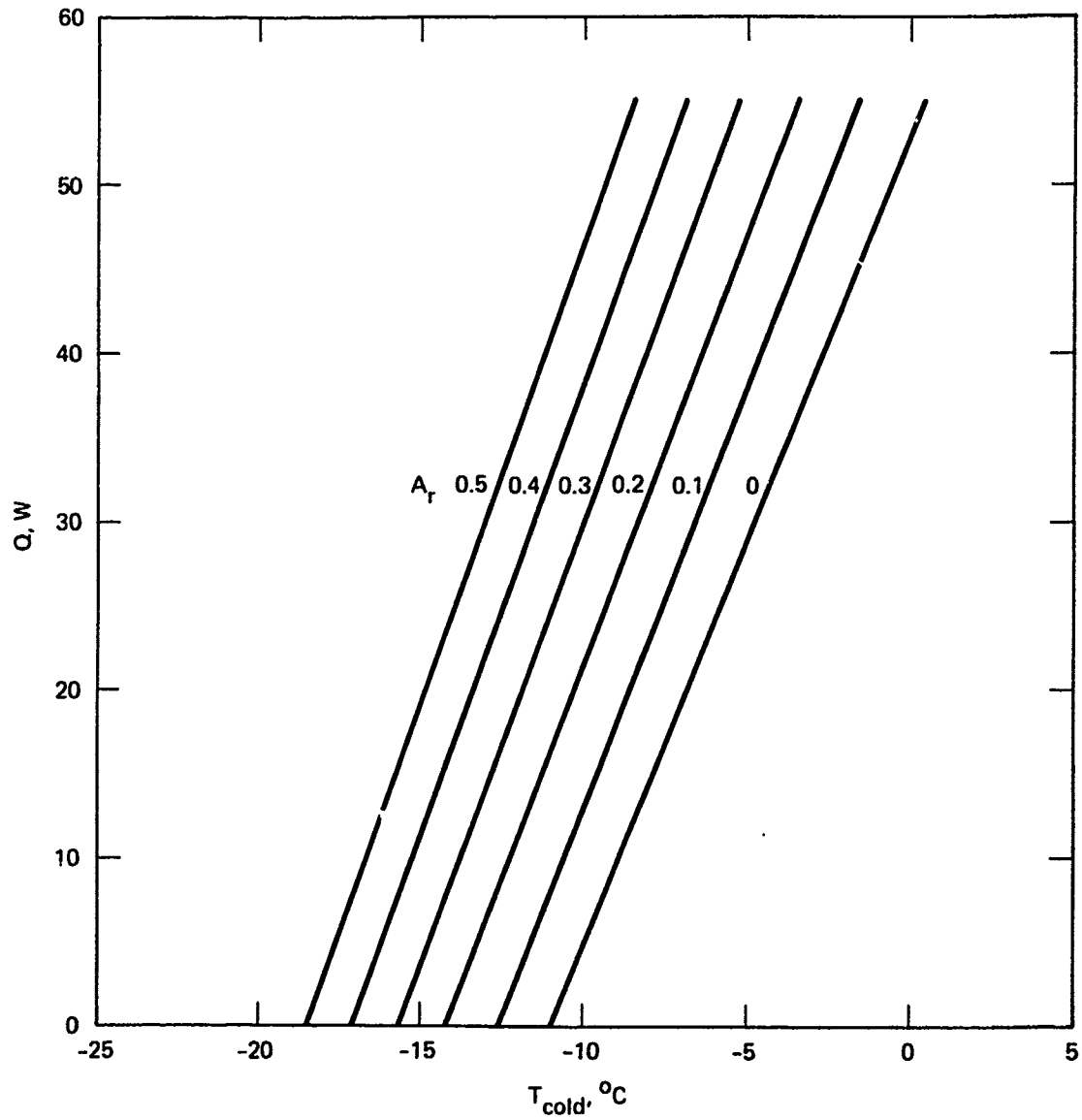
Figure 9-13. Heater power versus T_{COLD} for the conductive connection with $T_M = -13°C$.
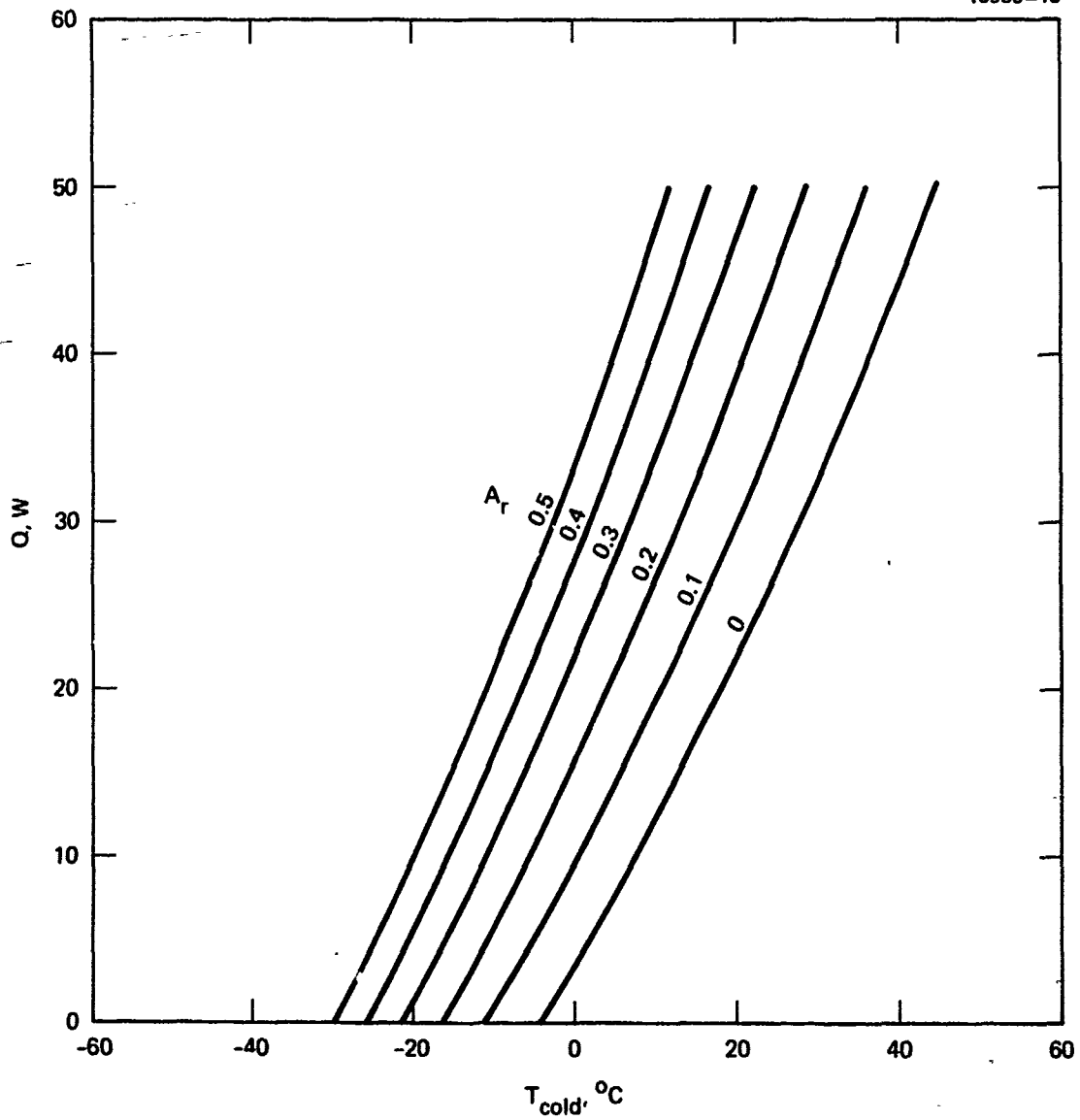
Figure 9-14. Heater power versus T_{COLD} for the radiative connection with $T_M = -13°C$.

202
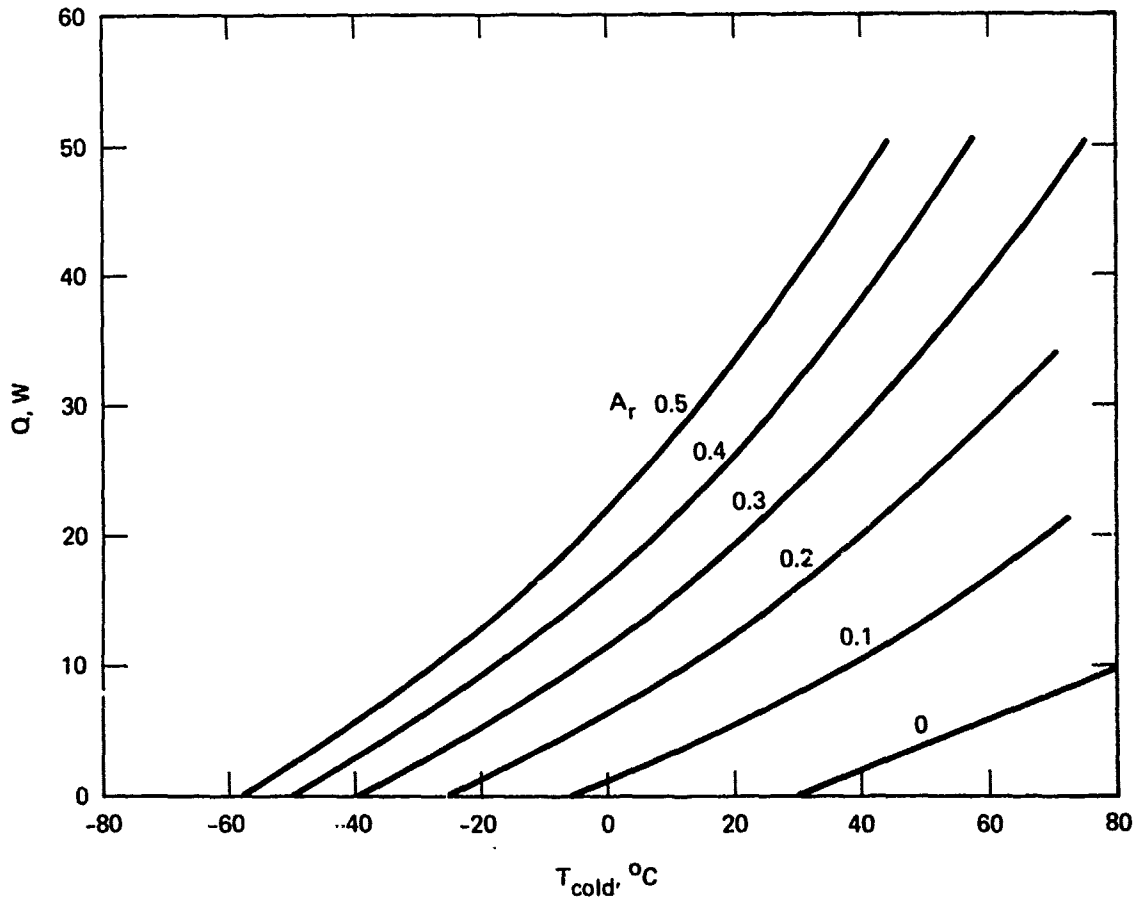
Figure 9-15.   Heater power versus T_{COLD} for the case where FMDS is insulated from the satellite.

and mounting technique. The results of the analyses are presented in Tables 9-1 through 9-3. Table 9-1 lists the component case and junction temperatures for the TPM Threshold Detector Assembly. These results indicate that all components are operating below their maximum allowable operating temperature limit. The same thing can be said for the Plasma Generator Electronics (Shelf 2) Assembly listed in Table 9-2 and for the Master Microprocessor Assembly listed in Table 9-3.

9.6 FMDS SYSTEM THERMAL DESIGN

From Figures 9-12 through 9-15, a radiator area (A_R) and a maximum required heater power (Q) can be determined that will allow the FMDS system to operate for any of the three mounting configurations (conductive, radiative, or insulated). The analysis of the three electronics assemblies shows that for a node 11 temperature (upper boundary of the Plasma Generator Electronics Assembly) of 61°C, that some of the TPM Threshold Detector Assembly component junction temperatures are within 5°C of the maximum allowed (Table 9-1). Therefore, T_{11} should be maintained at ≤ 61°C to keep the electronic components below an acceptable upper temperature limit.

Figure 9-12 shows that for $A_R = 0.25$, T_{HOT}(which is really T_{11}) will be ≤ 61°C for all three mounting configurations. If we choose $A_R = 0.3$ to allow for some margin in the design, then T_{11} for the three mounting configurations will be:

C - $T_{11} = 41$°C

R - $T_{11} = 43$°C

I - $T_{11} = 53$°C.

Minus 24°C is the lowest temperature that the system will be tested to; therefore, $T_{11} = -24$°C is the coldest temperature that can be allowed and still guarantee that the system will function properly when turned ON. With the system turned completely OFF, the electronic components will come to equilibrium at -24°C and then start to warm up immediately when turned ON. Figures 9-13 through 9-15 assume that the system is in the "monitoring" mode and dissipating 10.5 W. Under this condition with $A_R = 0.3$, the heater powers required to keep T_{11} (T_{COLD}) ≥ -24°C for the three mounting configurations are:

C (Figure 9-13) - Q = <0.0 W (i.e., heater not required)

R (Figure 9-14) - Q = <0.0 W (i.e., heater not required)

I (Figure 9-15) - Q = 4.0 W.

The heater powers required to keep $T_{11} \geq -24$°C with $A_R = 0.3$ when the system is completely OFF, can be determined from Figures 9-13 through 9-15 by extrapolating the curves to the point at which they intersect the value of -24°C and adding 10.5 W to the value obtained

Table 9-2. Plasma Generator Electronics (Shelf 2) Assembly Steady State Component Operating Temperatures.

CIRCUIT SYMBOL	PART NUMBER	THETA JC (DEG C/W)	POWER (WATTS)	MOUNTING SURFACE TEMP (DEG C)	CASE TEMP (DEG C)	JUNCTION TEMP (DEG C)	MAXIMUM ALLOWABLE TEMP (DEG C)
C1ACH	M39006/22-0568		0.100	61.	61.		85.
C1BCH	M39006/22-0568		0.100	65.	65.		85.
C2CH	M83421/01-2255S		0.000	65.	65.		85.
C6CH	M39014/01-1523		0.000	78.	78.		125.
C7D	M83421/01-2255S		0.000	63.	63.		85.
C8AD	M39006/22-0568		0.100	61.	61.		85.
C8BD	M39006/22-0568		0.100	61.	61.		85.
C9ACH	M39003/22-0554		0.100	62.	63.		85.
C9BCH	M39006/22-0554		0.100	62.	63.		85.
C9CCH	M39006/22-0554		0.100	62.	63.		85.
C9DCH	M39006/22-0554		0.100	62.	63.		85.
C14D	M83421/01-4317S		0.000	61.	61.		85.
C21D	M39003/01-3094		0.000	61.	61.		85.
C22D	M39014/02-1310		0.000	62.	62.		125.
C25CH	M39014/02-1310		0.000	61.	61.		125.
CR1D	JANTXVSDRIM		0.400	60.	66.		105.
CR3CH	JANTXV1N5816	1.500	2.000	69.	73.	76.	105.
F1CH	988244-13		0.000	61.	61.		85.
F2CH	988244-13		0.000	65.	65.		85.
F1D	988244-13		0.000	61.	61.		85.
F2D	988244-13		0.000	61.	61.		85.
Q1CH	JANTXV2N6766	0.830	2.000	61.	69.	70.	105.
Q1D	JANTXV2N6766	0.830	0.500	63.	65.	66.	105.
R4D	RCR32G511JS		0.000	57.	57.		98.
R5CH	RCR20G221JS		0.250	78.	80.		98.
R5D	RCR07G100JS		0.000	63.	63.		98.
R24CH	RCR07G100JS		0.000	63.	63.		98.
R39D	RCR42G223JS		0.050	57.	57.		98.
R40D	RWR80S1R00FR		0.000	61.	61.		140.
R42D	RCR32G101JS		0.000	61.	61.		98.
T1CH	1099467		4.000	71.	78.		85.
T1D	1099463		1.000	62.	65.		85.
T2CH	1099460		0.100	61.	61.		85.
T2D	1099460		0.100	62.	63.		85.
T3CH	1099460		0.100	69.	69.		85.
T3D	1099460		0.100	62.	63.		85.
VR1D	JANTXV1N4470		0.000	63.	63.		105.
VR6CH	JANTXV1N4470		0.000	61.	61.		105.
VR7CH	JANTXV1N4470		0.000	61.	61.		105.
VR8D	JANTXV1N4470		0.000	63.	63.		105.

TOTAL OF PART DISSIPATIONS: 11.400 WATTS
AVERAGE JUNCTION TEMPERATURE: 70.5 DEG C

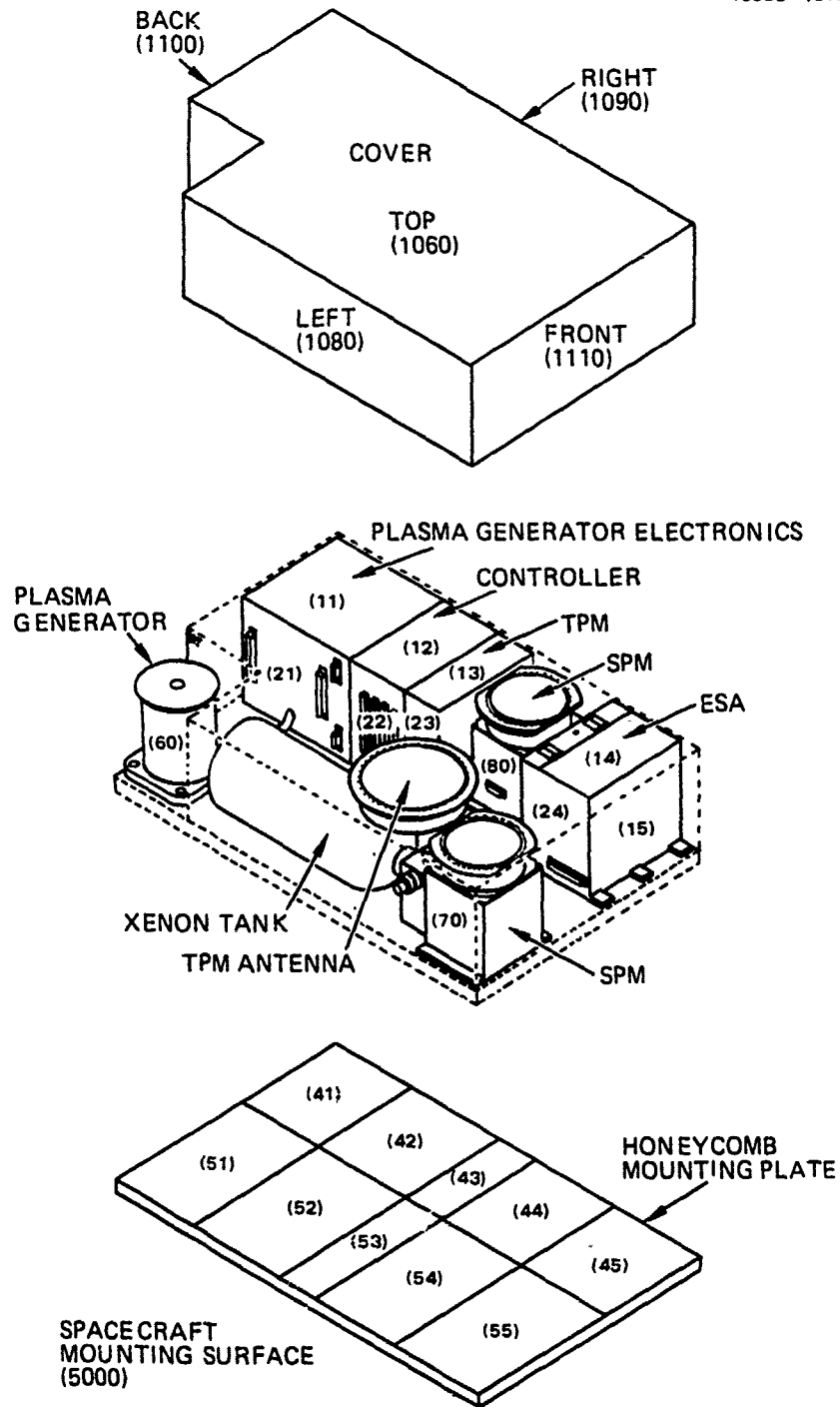NOTE: THE MAXIMUM ALLOWABLE TEMPERATURE IS THE UPPER LIMIT OF THE 'ACCEPTABLE' TEMPERATURE REGION

Table 9-3. Master Microprocessor Assembly Steady State Component Operating
Temperatures.

CIRCUIT SYMBOL	PART NUMBER	POWER (WATTS)	MOUNTING SURFACE TEMP (DEG C)	CASE TEMP (DEG C)	JUNCTION TEMP (DEG C)	MAXIMUM ALLOWABLE TEMP (DEG C)
U1	HS1-80C85RH/B	0.018	67.	67.	69. •	100.
U2	CD4508	0.004	66.	67.	67.	100.
U3	MA6116SOS	0.100	69.	72.	80. •	100.
U4	MA6116SOS	0.100	69.	72.	80. •	100.
U8	HS1-6641RH/B	0.005	68.	68.	68. •	100.
U9	HS1-6641RH/B	0.005	67.	67.	68. •	100.
U10	HS1-6641RH/B	0.005	67.	67.	68. •	100.
U11	HS1-6641RH/B	0.005	67.	67.	68. •	100.
U12	CD40175	0.000	66.	66.	66.	100.
U13	SA2999-1	0.005	67.	67.	68.	100.
U14	SA2999-1	0.005	67.	67.	67.	100.
U15	SA2999-1	0.005	67.	67.	67.	100.
U16	SA2999-1	0.005	67.	67.	67.	100.
U17	SA2999-1	0.005	68.	68.	68.	100.
U18	SA2999-1	0.005	67.	67.	68.	100.
U19	HS1-54C138RH/B	0.002	66.	66.	67. ○	100.
U20	HS1-54C138RH/B	0.002	66.	66.	67. •	100.
U21	HS1-54C138RH/B	0.002	66.	66.	66. •	100.
U22	HS1-82C08RH/B	0.004	66.	66.	67. •	100.
U23	HS1-82C08RH/B	0.004	66.	66.	67. •	100.
U24	CD4093	0.001	66.	66.	66.	100.
U25	CD4081	0.001	66.	66.	66.	100.
CR1	JANTX1N3600	0.000	66.	66.	66.	100.
R1	RESISTOR	0.009	67.	67.		100.
R2	RESISTOR	0.003	66.	66.		100.
R3	RESISTOR	0.000	66.	66.		100.
Y1	CRYSTAL	0.000	67.	67.		100.
C1	CAPACITOR	0.000	67.	67.		100.
C2	CAPACITOR	0.000	67.	67.		100.
C3	CAPACITOR	0.000	66.	66.		100.
C4	CAPACITOR	0.000	66.	66.		100.
C5	CAPACITOR	0.000	66.	66.		100.
C6	CAPACITOR	0.000	68.	68.		100.
C7	CAPACITOR	0.000	67.	67.		100.
C11	CAPACITOR	0.000	67.	67.		100.
C12	CAPACITOR	0.000	67.	67.		100.
C13	CAPACITOR	0.000	67.	67.		100.
C14	CAPACITOR	0.000	67.	67.		100.
C15	CAPACITOR	0.000	66.	66.		100.
C16	CAPACITOR	0.000	66.	66.		100.
C17	CAPACITOR	0.000	66.	66.		100.
C18	CAPACITOR	0.000	66.	66.		100.
C19	CAPACITOR	0.000	66.	66.		100.
C20	CAPACITOR	0.000	67.	67.		100.
C21	CAPACITOR	0.000	67.	67.		100.
C22	CAPACITOR	0.000	66.	66.		100.
C23	CAPACITOR	0.000	66.	66.		100.
C24	CAPACITOR	0.000	66.	66.		100.
C25	CAPACITOR	0.000	66.	66.		100.
C26	CAPACITOR	0.000	66	66.		100.

• JUNCTION TEMPERATURE APPROXIMATED BASED ON θ_{jc} = 80°C/W
TOTAL OF PART DISIPATIONS   0.288 W

206

(because the curves were calculated for the "monitoring" mode in which 10.5 W is disipated). This results in:

C (Figure 9-13) - Q = <0.0 W (i.e., heater not required)

R (Figure 9-14) - Q = 8.5 W

I (Figure 9-15) - Q = 14.5 W.

The FMDS system will be cold soaked during environmental qualification at -24°C and, therefore, its operation after being exposed to colder temperatures will not be guaranteed. However, the electronic components themselves have storage temperature ratings of -65°C. The heater powers required to keep $T_{11} \geq$ -65°C can be estimated for the three cases (again by extrapolation) as:

C (Figure 9-13) - Q = <0.0 W (i.e., heater not required)

R (Figure 9-14) - Q = <0.0 W (i.e., heater not required)

I (Figure 9-15) - Q = 6.0 W.

The above discussion leads to a FMDS system thermal design where 30% of the FMDS cover (A_R = 0.3) is covered with radiator to keep the system cool and a 15 W heater is included to keep the system warm.   This design will work for any one of the three mounting configurations (conductive, radiative, or insulated).

9.7 DISCUSSION AND RECOMMENDATIONS

It should be noted that the data presented in Figures 9-12 through 9-15 use one node temperature (T_{11}) to represent the temperature of a typical electronics mounting surface within the system. A detailed temperature map of the system is provided by the CINDA computer run.

The following factors can influence the temperatures presented in this report:

a)   Host vehicle and mounting -- effects of solar concentration, shading, etc.

b)   Launch and transport environment -- worst case conditions might be encountered in transport.

c)   Dissipation and mode of operation -- revised mission profile or operating experience might change these.

d)   Transient effects -- post-eclipse bus voltage can increase due to increased solar cell efficiency at low temperatures.

It is recommended but not required that bonding be used with all dissipating components on the TPM Threshold Detector Assembly and the Master Microproccesor Assembly. It is required and was assumed in the analysis that bonding (HP16-103, Type XIII is recommended) is used for all dissipating components on the Plasma Generator Electronics (Shelf 2) Assembly.

When the FMDS is integrated with a vehicle, emphasis should be placed on an understanding of items a-d above. A careful evaluation of these, keeping in mind the choice of

207

satellite and launch mode, will determine the applicability of the present data and curves for the particular application. If significant solar concentration, shading, changes in dissipation, etc. occur, the computer model should be updated to reflect these changes.

In particular the following differences between this analysis and the delivered hardware should be noted:

1)   The delivered hardware has no cover, the ESA and one SPM locations are interchanged, and the TPM was not installed (comparison of Figures 2-2 and 9-1).

2)   The system, without the TPM, dissipates approximately 5.6 W in the "monitoring" mode and 20.5 W in the "operating" mode. With the TPM installed, it would dissipate approximately 14 W in the "monitoring" mode and 29 W in the "operating" mode.

3)   The components are not painted black.

SECTION 10
SYSTEM TEST RESULTS

The results of system level testing of the breadboard and flight units of the FMDS are presented in this section. Only very limited thermal data and no vibration or EMI data are available.

10.1 BREADBOARD TEST RESULTS

There were two demonstrations of the breadboard hardware at Hughes Research Laboratories (HRL) during 1985. The first demonstration featured a review of the breadboard design and a limited demonstration of the hardware capability. The second demonstration featured the full capabilities of the breadboard FMDS system.

The plasma source and sensors for the breadboard demonstration are shown mounted on the test fixture in Figure 10-1. An aluminum plate was mounted flush with the plasma source and sensors to simulate a cover over the FMDS. This aluminum plate was then covered with VDA backed 5-mil Kapton to simulate a thermal blanket.

The test facility is shown in Figure 10-2. The FMDS plasma source and sensors were mounted on a plate inside the vacuum chamber while most of the electronics were mounted on a plate outside the vacuum chamber. The two plates were connected together with an 8-in aluminum tube and mounted to the chamber with a G-10 glass/epoxy flange. The aluminum tube shielded the interconnect wires between the sensors and the electronics and the G-10 flange allowed the entire FMDS to charge or be biased 20 kV relative to facility ground. The facility contained an electron gun, proton source, and UV source to simulate the space environment, and a Faraday cup and Langmuir probe for diagnostic measurements of the simulated environment and the plasma from the plasma source. The dielectric target was designed to charge up and create arcs for the TPM to detect.

10.1.1 Test Sequences

The first demonstration of the FMDS breadboard consisted of the following sequence of events:

1) Plasma Source in operation
2) Detection of protons by the ESA
3) Single command turn-OFF and burst volume fill of the Plasma Source
4) Detection of differential charging by the SPM
5) Simulation of spacecraft charging to -2.5 kV
6) Single command turn-ON of the Plasma Source and discharge of the simulated spacecraft
7) Turn-OFF of the Plasma Source and recharge of the simulated spacecraft.
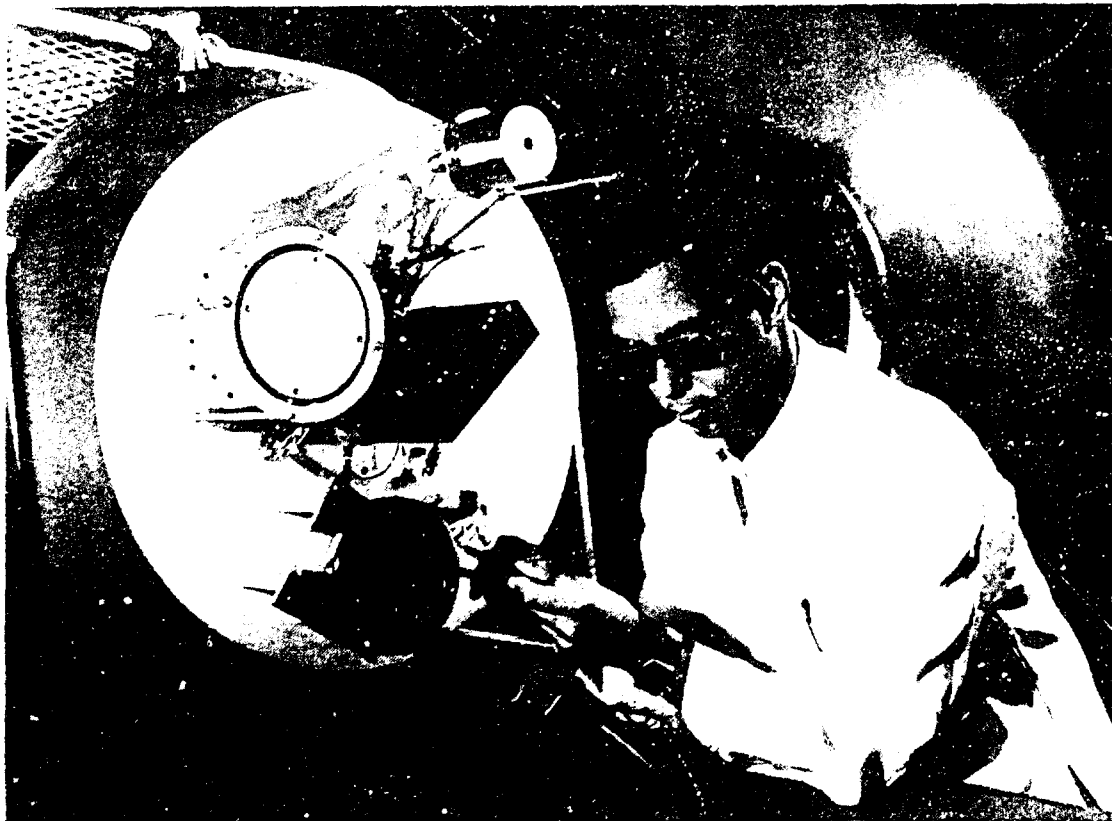
Figure 10-1. FMDS breadboard plasma source and sensors mounted on the test fixture.
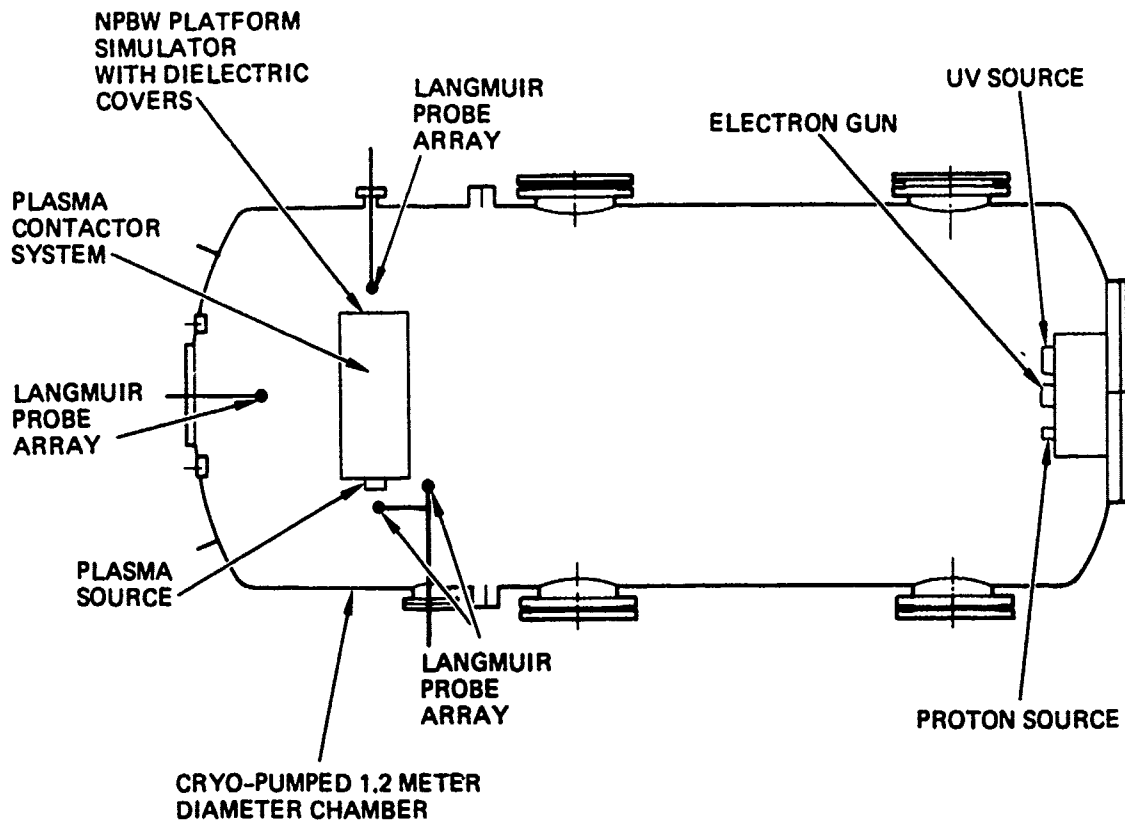
Figure 10-2. Test facility for testing the FMDS.

The second demonstration consisted of the following sequence which demonstrated all of the FMDS capabilities.

1. **Demonstration of Plasma Source**
   - <1s ignition
   - Steady state emission current
   - Emission current during ignition
   - Throttled operation
   - Emission current at throttled setpoints

2. **Demonstration of ESA Operation**
   - Operation of sun sensor
   - Detection of ions
   - Detection of electrons
   - Ion-ESA algorithm
   - Electron-ESA algorithm

3. **Demonstration of SPM Operation**
   - Charge Kapton front surface with e-gun
   - Turn ON UV source with e-gun ON; front surface discharges
   - Resetting of the SPM using UV and grounding relay

4. **Demonstration of TPM Operation**
   - Inject pulses of known amplitude, polarity, width, and repitition rate; correlate with telemetry
   - Produce arcs and detect with TPM
   - Reverse antennas; TPM does not detect the arcs

5. **Demonstration of Controller**
   - Output telemetry
   - Commands
   - Setting of charging flags
   - Masking of charging flags
   - Change charging-flag threshold level
   - Controller turn-ON of Plasma Source
   - Controller turn-OFF of Plasma Source
   - Manual control of Plasma Source

6. **Demonstration of System**
   - Plasma within 30 s of threshold level
   - Charge entire FMDS; detect charging with ion-ESA; auto turn-ON of Plasma Source; FMDS discharge
   - Detect high-energy electrons with electron-ESA; auto turn-ON of Plasma Source; Plasma Source stays ON until high energy electrons disappear
   - Charge the SPM; detect charging; auto turn-ON of Plasma Source; SPM discharge
   - Generate arcs; detect arcs with TPM; auto turn-ON of Plasma Source; elimination of arcs
   - Activate all sensors; see which one turns the Plasma Source ON

10.1.2 Demonstration Test Results

The first demonstration was very short (30 minutes) and demonstrated the seven items listed above. This demonstration served to show the basic capabilities of the FMDS and the test facility.

The system was operated in an autonomous manner for the second demonstration to show that it could autonomously detect spacecraft charging and turn ON its plasma source to negate that charging. Many of the test results from this demonstration have been discussed previously in the sections on the individual instruments. The other significant results of this demonstration are discussed below.

The ion ESA and its algorithm were tested by charging the entire FMDS negatively with respect to facility ground (spacecraft frame charging) using the electron gun while protons were present in the chamber. The sharp increase in the proton spectra moved to higher energy channels as the FMDS charged more negative. When the peak moved past the threshold charging level as determined by the ion-ESA algorithm, the plasma source was automatically turned ON. Upon ignition of the plasma source, the FMDS potential immediately returned to facility ground potential.

The electron ESA and its algorithm were tested by increasing the energy of the electron beam until the sum of the counts in the two highest energy channels of the electron ESA exceeded the sum of the counts in the lower energy channels. This indicated that a charging environment was present and the plasma source was automatically turned ON to prevent charging from occuring. The plasma source remained ON until after the simulated charging environment was removed and the plasma source preset ON time had expired. Both requirements had to be met before the plasma source would turn OFF.

The Kapton surface on the SPM was charged negatively (differential charging) using the electron beam and when the charging exceeded the threshold level the plasma source was automatically turned ON. The differential charge on the SPM was immediately removed and the SPM remained uncharged as long as the plasma source was ON. The UV source was also used to remove the charge from the SPM indicating that the SPM could be rezeroed during sunlight conditions. The UV source removed the charge with the electron gun ON or OFF.

The TPM was tested by charging Kapton surfaces inside the vacuum chamber using the electron beam until they arced to other surfaces or ground. The first arc was detected by the TPM and the plasma source was automatically turned ON. No further arcing was observed since the Kapton surfaces cannot charge with the plasma from the plasma source present. As discussed in Section 5, when the TPM antennas were reversed such that the internal antenna saw higher amplitude signals than the external antenna, the plasma source was not turned ON.

The Controller was tested by having it automatically control the FMDS as the other tests were being performed. The ability to mask instruments, change threshold levels, and manually control the plasma source by remote commands was also demonstrated during this testing.

The above tests were conducted with only one sensor at a time activated. All sensors were activated and the electron gun turned ON to see which sensor would respond fastest. With the FMDS system floating from facility ground, the ion ESA activated the plasma source as expected (spacecraft frame charging). With the FMDS floating, frame charging occurs much faster than differential charging, therefore, the SPM did not see a differential charge before the ESA activated the plasma source. The SPM activated the plasma source (differential charging) when the FMDS system was connected to facility ground. Under these conditions the ESA never sees a shift in the ion spectra because the FMDS frame cannot charge. However, differential charging does quickly occur; therefore, the SPM activated the plasma source. In both cases there was not time for dielectric surfaces to charge to high enough potentials for arcs to occur, and therefore, the TPM did not activate the plasma source.

10.2   FLIGHT HARDWARE TEST RESULTS

The flight hardware subsystems were integrated together, calibrated, and tested as a complete system. The TPM was not included in any of these.

10.2.1   Integration Testing

Several problems were discovered and solved during the integration testing. The first of these was the noise problem with the ESA when the plasma source power supplies were operated. This problem and its solution were discussed in Section 4.4.

When the two SPMs were connected into the flight harness, their telemetry outputs had a low-frequency ($\approx$0.5 Hz) oscillation on them. If only one SPM was connected into the harness, then the oscillation was not present. This was traced to a beat frequency between the tuning forks in the SPMs. The tuning forks oscillate at nominally 330 Hz, but are slightly different causing the beat frequency. This problem was solved by decoulpling the tuning forks from the $\pm$12-V power source and the remainder of the SPM circuitry using 200 ohm resistors and $\approx$50 μF capacitors. This fix added $\approx$40 g to the mass of each SPM.

The first time that we tried to start the plasma source using the flight feed system, the software tried to start it four times. The source came on each time but went out shortly thereafter. The stripchart recording of the discharge and keeper voltages indicated that the burst volume upstream of the burst valve was too small. The burst volume was determined to

214

be ≈ 3 cm^3 when it should be ≈ 16.5 cm^3 (1 in^3). The volume was increased by adding a hollow block to the top of the flow impedance assembly. We were able to manually start the source and keep it operating with this modification.

We were able to start the plasma source manually (sending separate commands to actuate each valve, power supply, and set point); however, when we tried to start the source under automatic control of the software, the software would turn it back OFF ≈ 6 s after startup. This was traced to the plasma-source mode-manager routine in the software which monitors the keeper voltage and current to determine the operating condition of the plasma source. The mode-manager routine did not shut the source OFF during manual startups because it is not active for manual startups. Several modifications were made to the mode-manager routine in the following order to fix this problem. It was first thought that the mode manager was shuting the source OFF because it detected that the keeper voltage was above 25 V, even for a short period of time. The software was modified to require that the keeper voltage be above 25 V for >1 minute or above 40 V for >8 s. One reading below these values also resets the timers. The software still turned the source back OFF. Then it was discovered that the 10Ω ohm resistor which is in the keeper output for ≈ 40 s after the source starts, was making the telemetry look like the keeper voltage was >40 V. The software was modified to raise the voltage limits during startup and then revert to the lower values when the plasma-source-ON flag gets set (≈ 3 minutes after startup). The software still turned the source back OFF. The final problems in the mode manager were: 1) that the executive routine called the mode manager before it called the ADC to update the analog telemetry data; therefore, the mode manager was operating on 4-s old data, and 2) that the software was detecting that the keeper current was <40 mA; mainly due to problem 1) but also only one time of detecting <40 mA would cause a shutdown. The software was modified to call the ADC before calling the mode manager and also to require three successive detections of <40 mA before shuting the source OFF. After these last modifications, we had no more problems with the software shutting the source OFF when it should not

Randomly occurring current spikes were observed on the input power bus. These spikes were actually 4-s wide pulses that were larger in amplitude for higher input bus voltages as shown in Figure 10-3. This was due to a hardware problem and a software problem. The time delay circuitry of Figure 8-3 (U23, U22, and Q11) is reset by a narrow pulse from the controller once every four seconds such that Q11 does not turn ON. A problem in the software was causing the controller to send a 4-s wide reset pulse on occasion. This wide pulse was allowing crosstalk between the two halves of U23 to partially turn Q11 ON, causing a large current draw through the coils of the valves and relays, but not large enough to actuate them. The second half of U23 (Figure 8-3) was an active part of the circuit at this

215
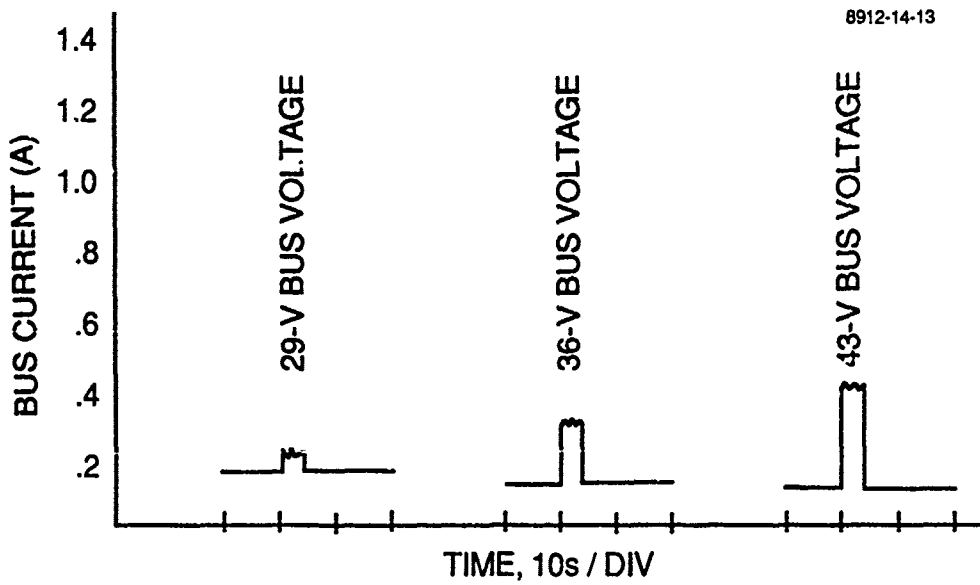
Figure 10-3. Current spikes observed on the input power bus.

time, and the current through the light-emitting diode between pins 7 and 8 was causing a few μA to flow (due to crosstalk that exists in these devices) through the transistor between pins 13 and 14 and partially turning Q11 ON. The second half of U23 was no longer needed for ground isolation (due to an earlier circuit modification) so it was removed from being an active part of the circuit, and the software problem was rectified. We did not observe any more anomolus current spikes.

The partial pressure of xenon in the vacuum facility during times when the burst valve was closed, led us to believe that there was a small leak in the feed system. The partial pressure was still high with the high-pressure valve closed and the bypass and burst valves open. This led us to believe that the leak was upstream of the high pressure valve in the expellant tank or bulkhead on the end of the tank. We were never able to find a leak in the feed system before the FMDS was delivered; however, this should be verified before the system is flown. The pressure transducers (high pressure and low pressure) in the feed system should also be replaced before flight. The pressure transducers in the system are psia units which are sealed on the outside (reference side) with a nonhermetic epoxy. Therefore, the atmospheric pressure trapped by the epoxy will slowly leak away when the FMDS is under vacuum conditions for a long period of time (e.g., when in space). This will cause the zero of the pressure transducers to slowly shift by ≈14.7 psi. This would not be a major problem for the high pressure transducer since it is 14.7 psi out of 530 psi (2.8%) at the start of life. For the low pressure transducer, however, this represents 14.7 psi out of 10 psi (147%). Pressure transducers of the psig type were purchased but were not delivered to Hughes until after the FMDS was delivered to the USAF. The psig units have a vent tube on the outside (reference side) and, therefore, can be calibrated under vacuum conditions to simulate the flight environment.

10.2.2   Software Startup Options

During testing of the full system it was determined that there was a possibility of losing some of the EEPROM write software since it was stored in EEPROM. If other parts of the software were lost from EEPROM at the same time, then there would be no way to recover from this loss and a catostrophic failure would have occurred. Therefore, a concentrated effort was undertaken to partition the software with all vital power-up, command and telemetry, and EEPROM write software in the 2K of PROM such that all of the software in EEPROM could be reloaded from the ground if necessary. This resulted in three startup options for the system.

1) If EB$_H$ is present at location 1002$_H$ in EEPROM, then the system will perform an automatic startup upon power being applied. The senors will be turned on, and the FMDS will go into its monitoring mode immediately.

2) If EB$_H$ is not present at location 1002$_H$, then the software will look for 28$_H$ FD$_H$ at memory locations 47A7$_H$ and 47A8$_H$ respectively. If 28$_H$ FD$_H$ is not present (which the odds are it will not be on power up since these memory locations are in RAM), then the software will write the stop-flag at location 1001$_H$ and trap the software in the lower 2K of memory (PROM). This will be indicated by the Plasma-Source Mode being F0$_H$ in the telemetry stream. Sending command 93$_H$ FF$_H$ FF$_H$ XX$_H$ will clear the stop-flag and the full software will be executed. If the microprocessor gets reset for any reason, 28$_H$ FD$_H$ will still not be present and the stop-flag will be set again.

3) If after sending command 93$_H$ FF$_H$ FF$_H$ XX$_H$, command 3C$_H$ is sent, then 28$_H$ FD$_H$ will be written to memory locations 47A7$_H$ and 47A8$_H$. If a reset of the microprocessor occurs now, then the software will not write the stop-flag and an automatic startup will occur. However, if the system is powered down and then back up, the 28$_H$ FD$_H$ will go away and the stop-flag will be set. After sending commands 93$_H$ FF$_H$ FF$_H$ XX$_H$ and 3C$_H$ there are two options; a) turn the instruments ON manually, or b) send command 37$_H$ which will halt the microprocessor. The watchdog timer will cause a reset of the microprocessor, and an automatic startup will occur.

10.2.3 Calibration Data

The calibration curves for the telemetry outputs from the plasma source power supplies, input bus voltage and current, temperatures of the plasma source electronics, and bipolar-log electrometer are presented in Figures 10-4 through 10-13. The calibration curve for the plasma source electronics temperatures was calculated from published data on the characteristics of the thermistors used. The other calibration curves were obtained by measuring the parameter with a DVM and plotting it against the output of the telemetry.

10.2.4 Input Power Profiles

The input power and/or input current for the various FMDS operating modes are presented below. The inrush current profile during application of bus power to the FMDS is shown in Figure 10-14. Current spikes of up to 3.7 A occur during the first several hundred ms after power application. The power profile during the automatic cathode-conditioning mode is presented in Figure 10-15. The FMDS draws 16.8 W for 3 hrs, 6.2 W for 0.5 hrs, 28.0 W for 1 hr, and then retuns to the monitoring mode where it draws 5.5 W. Figure 10-16 shows the bus current (for a 37-V bus) during startup and shutdown of the plasma source.

C8912-14-14
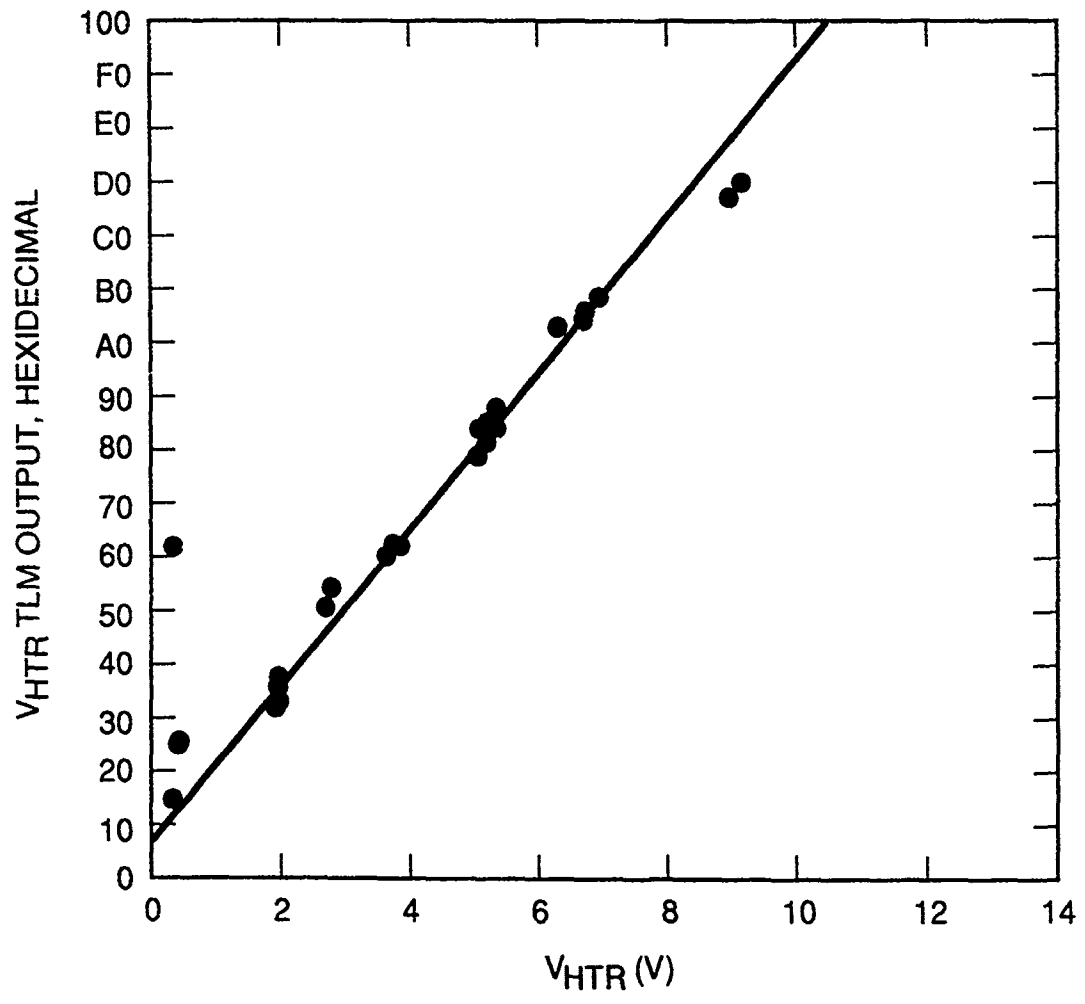
Figure 10-4. Telemetry calibration curve for the heater voltage.

219
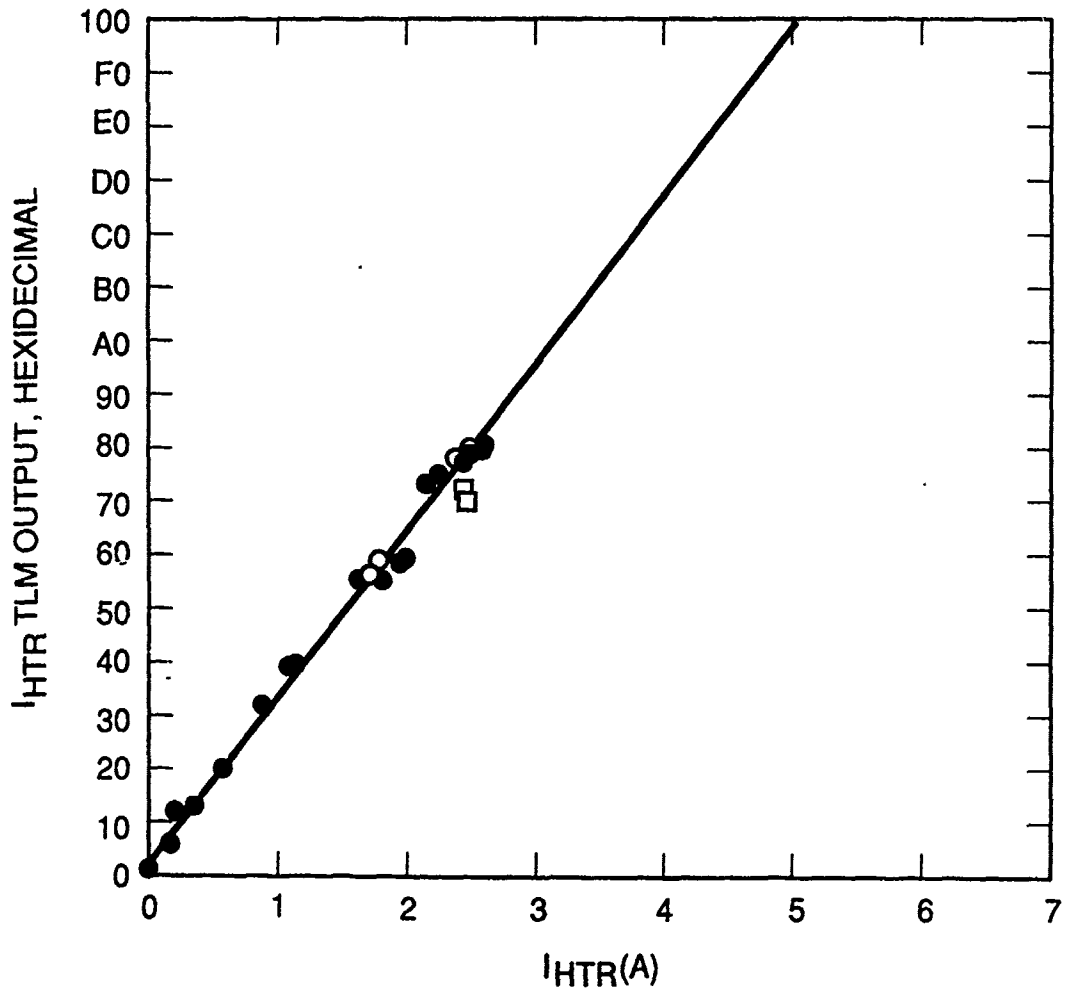
Figure 10-5. Telemetry calibration curve for the heater current.
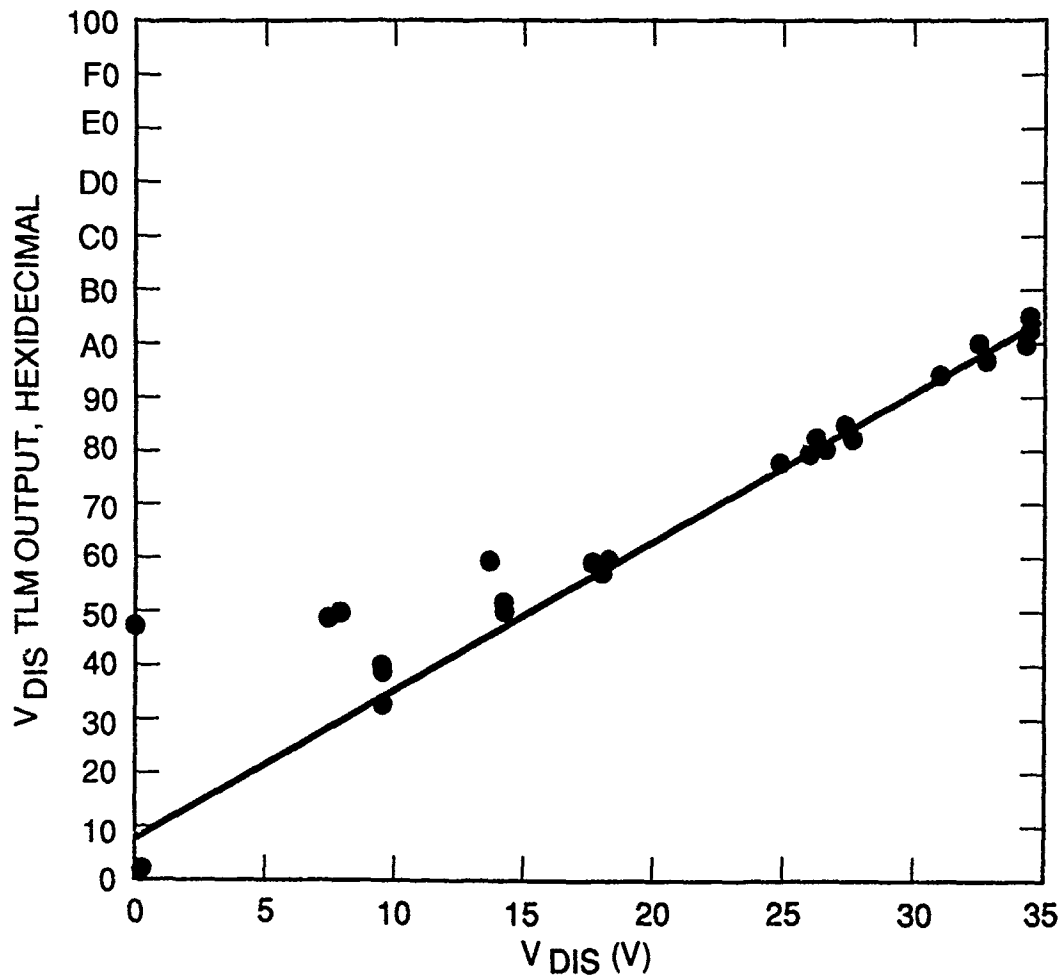
Figure 10-6. Telemetry calibration curve for the discharge voltage.
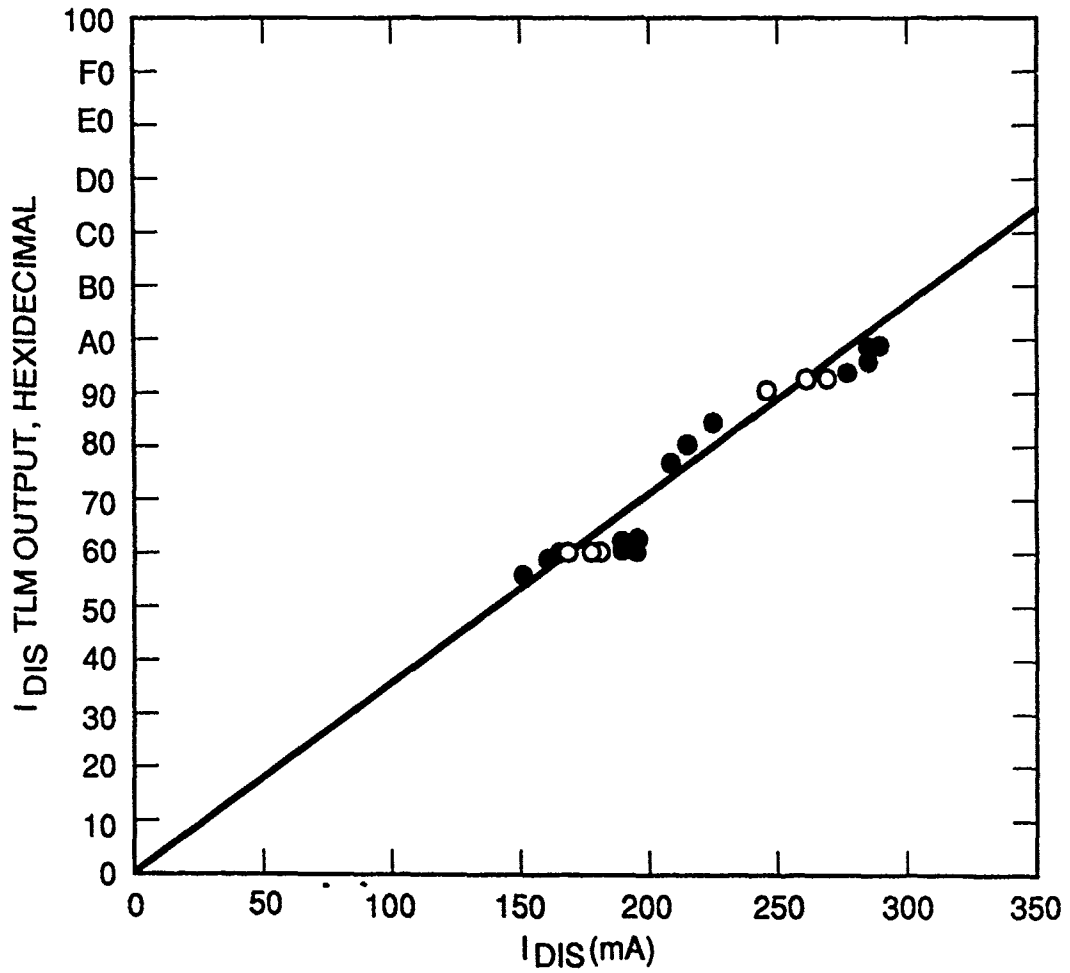
Figure 10-7. Telemetry calibration curve for the discharge current.

222

C8912-14-18
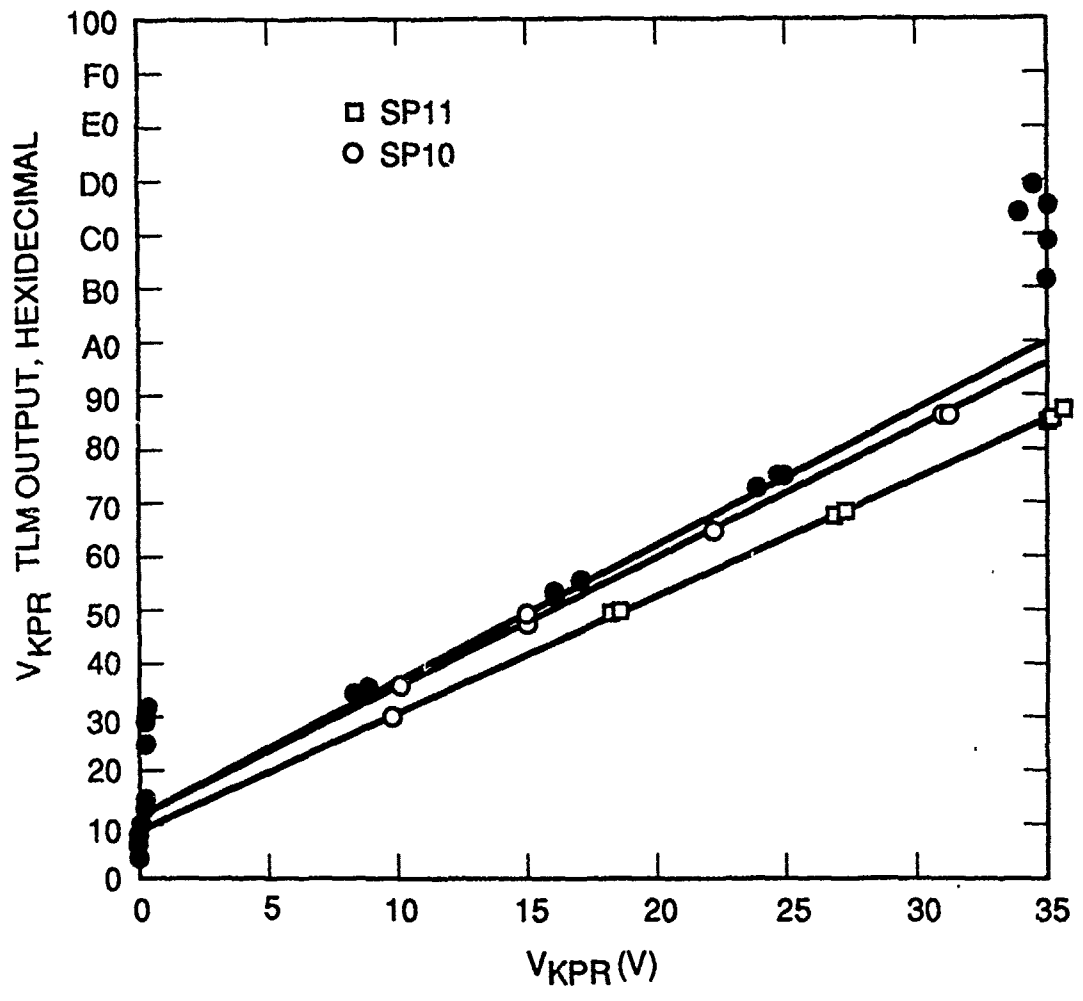
Figure 10-8. Telemetry calibration curve for the keeper voltage.

223
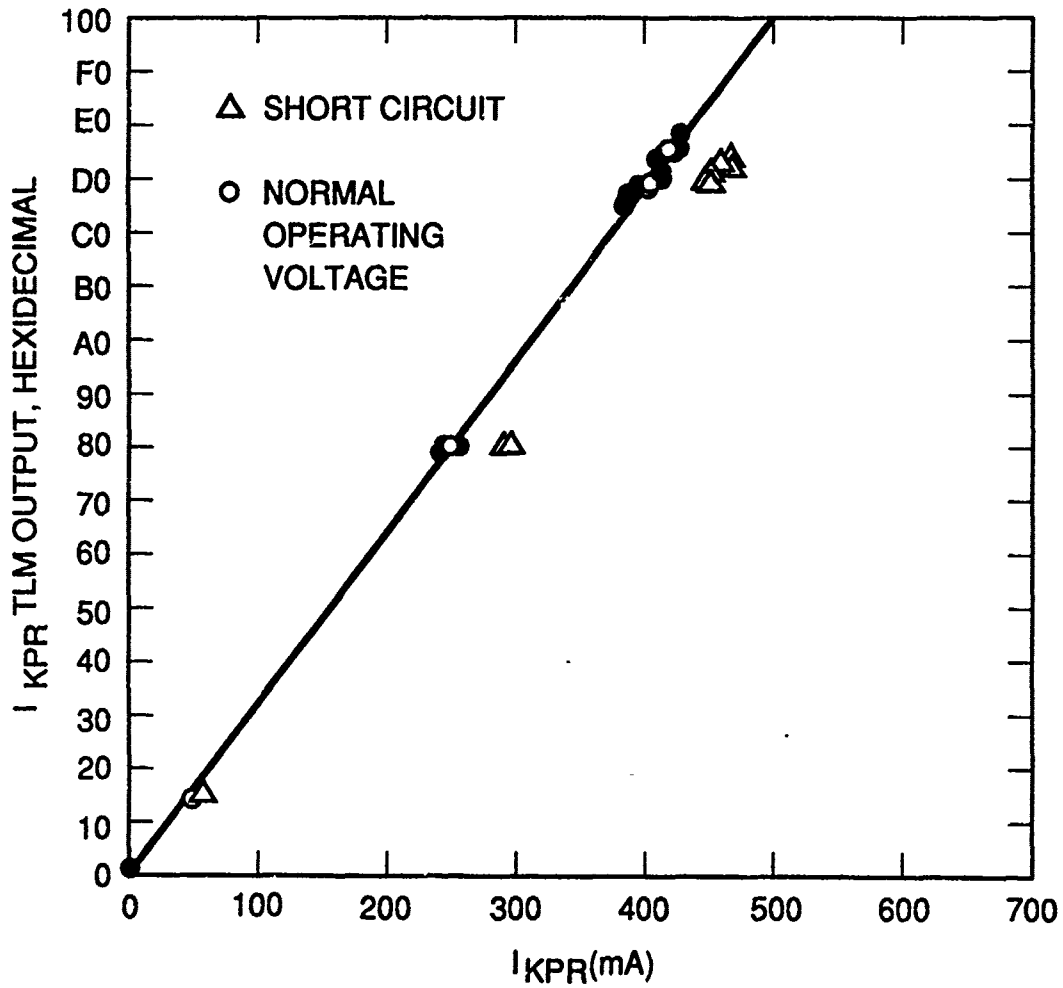
Figure 10-9. Telemetry calibration curve for the keeper current.
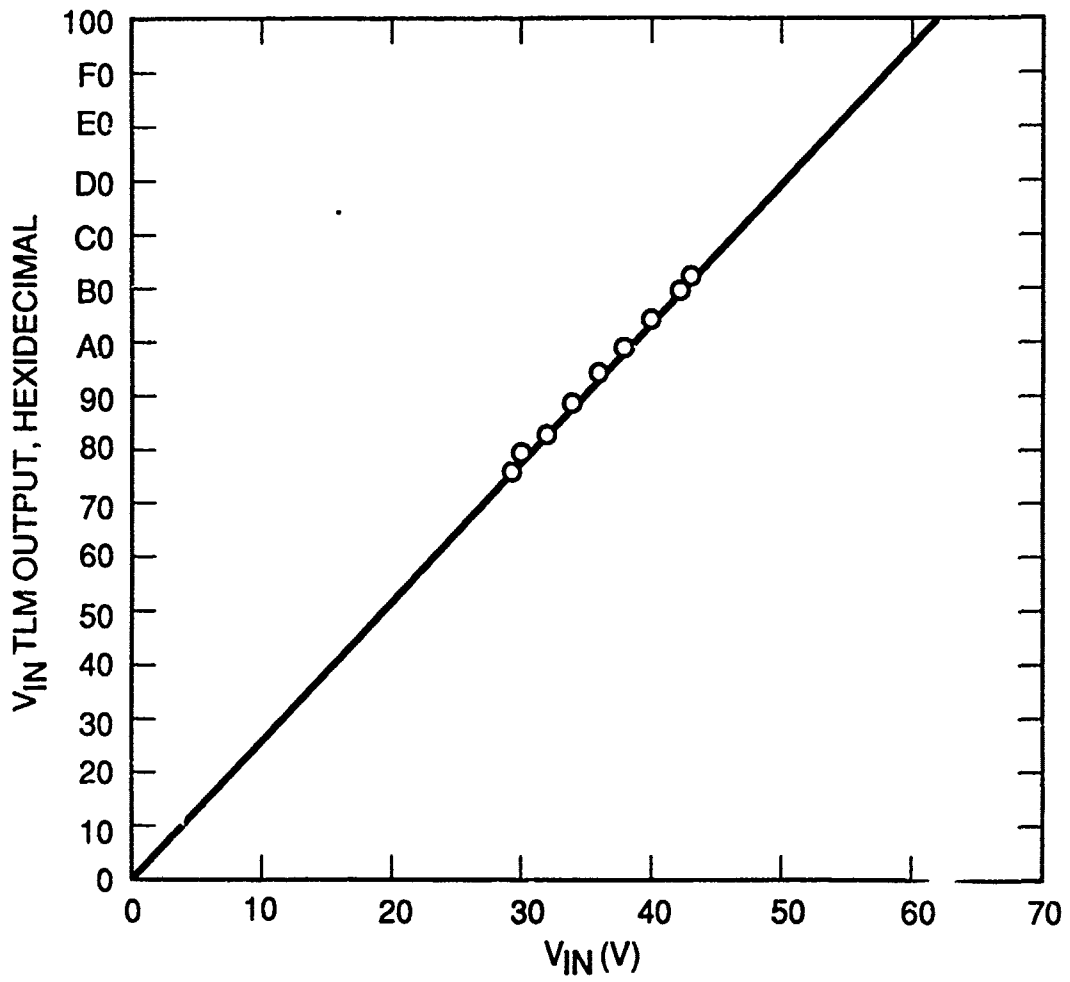
Figure 10-10. Telemetry calibration curve for the input bus voltage.
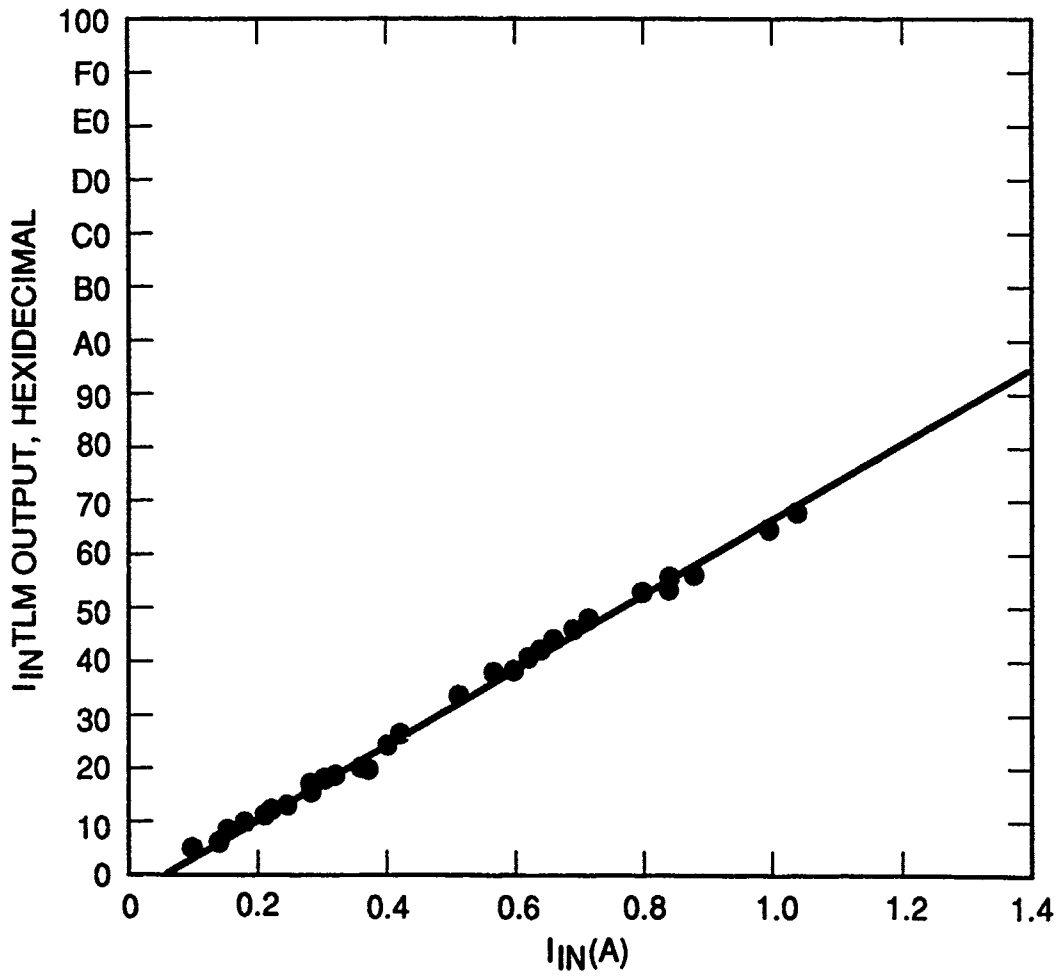
Figure 10-11. Telemetry calibration curve for the input bus current.
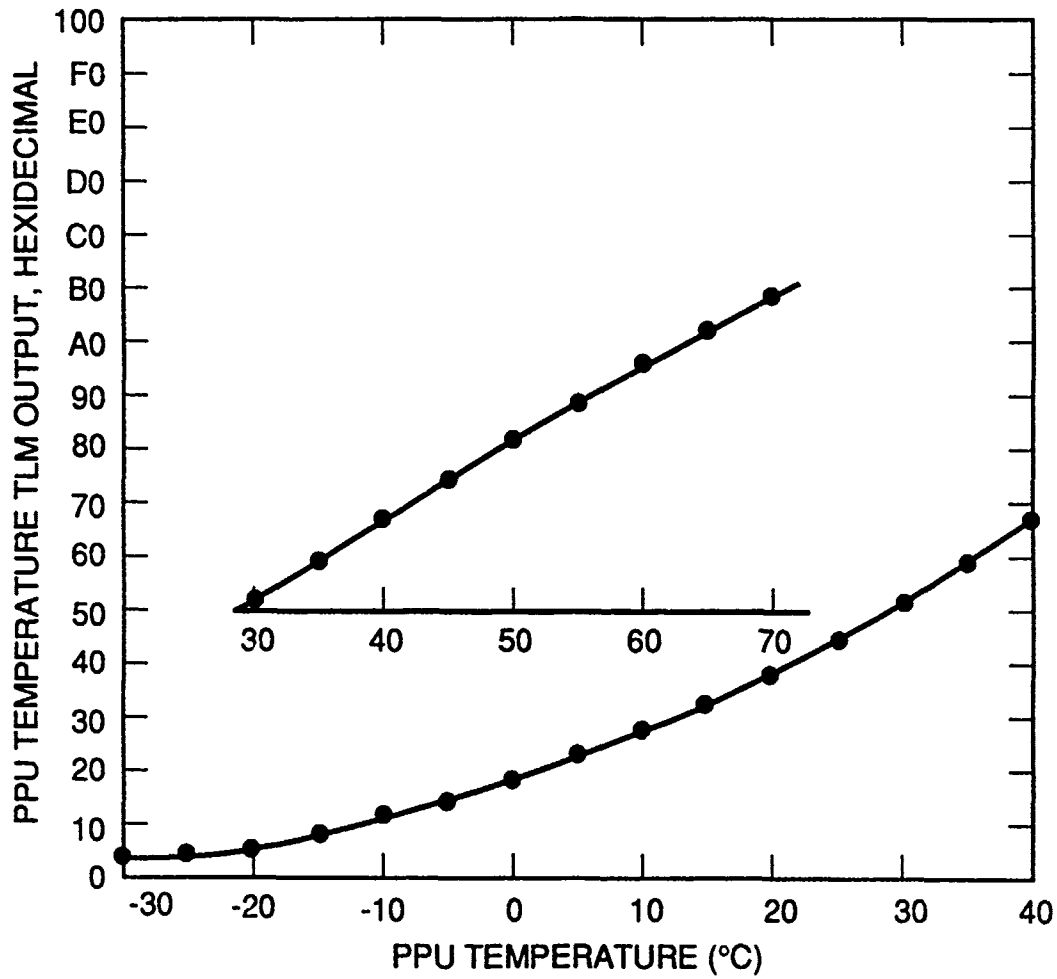
Figure 10-12. Calculated telemetry calibration curve for the plasma source electronics temperatures.
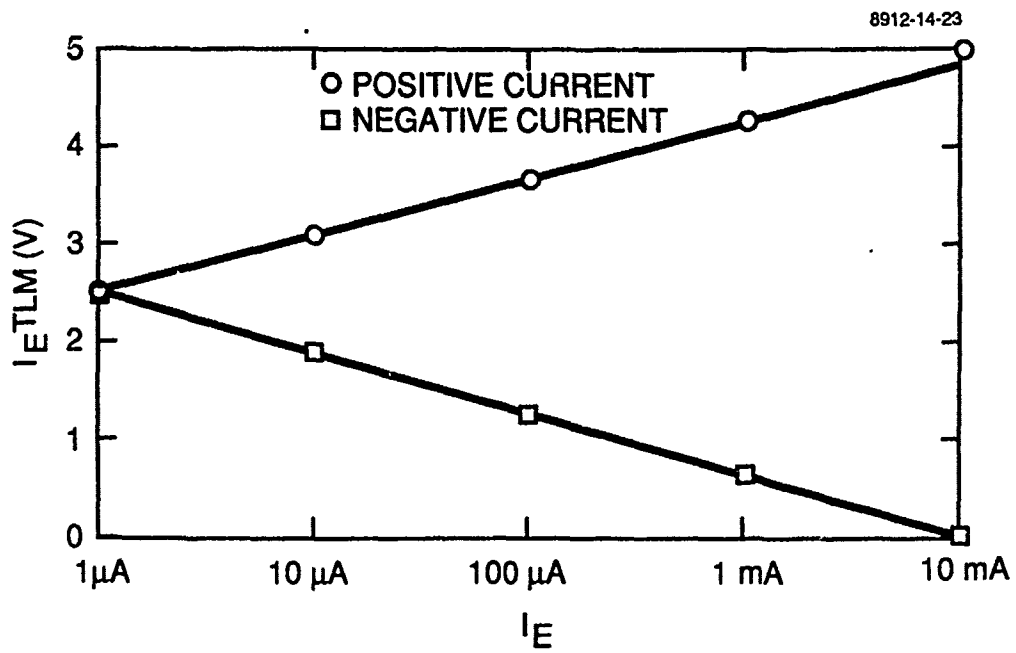
Figure 10-13. Telemetry calibration curve for the emission current.
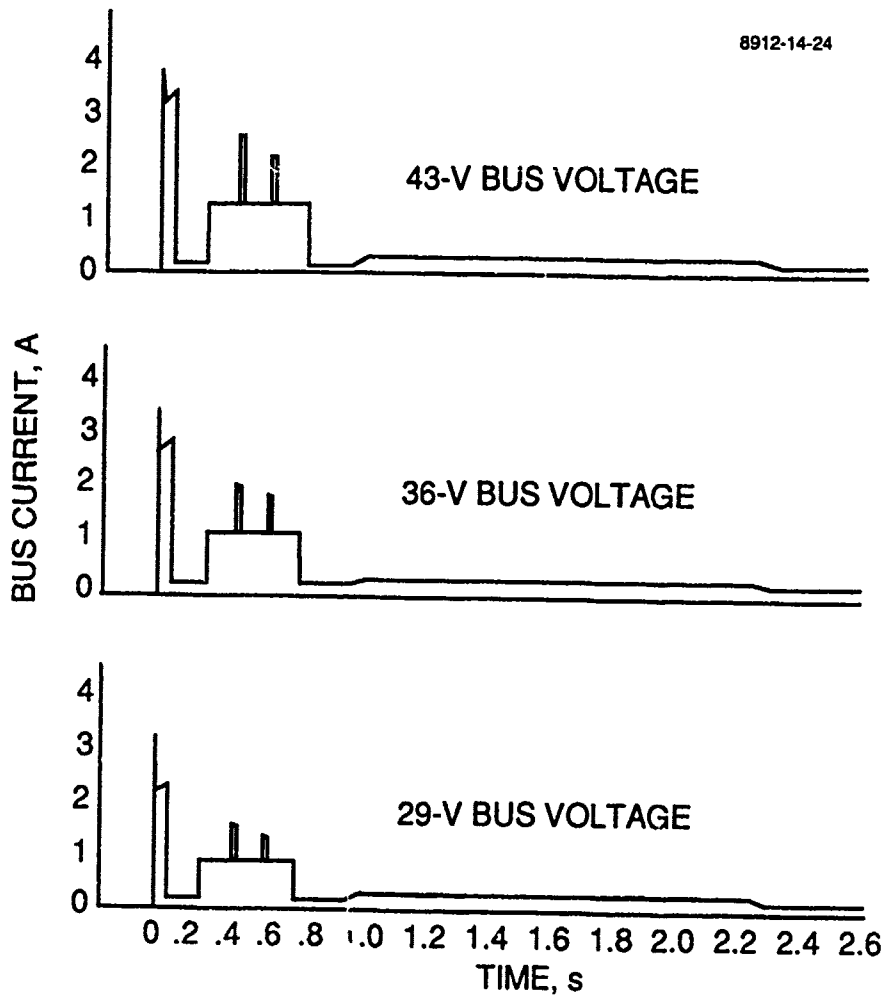
Figure 10-14. FMDS inrush current profile during application of bus power.
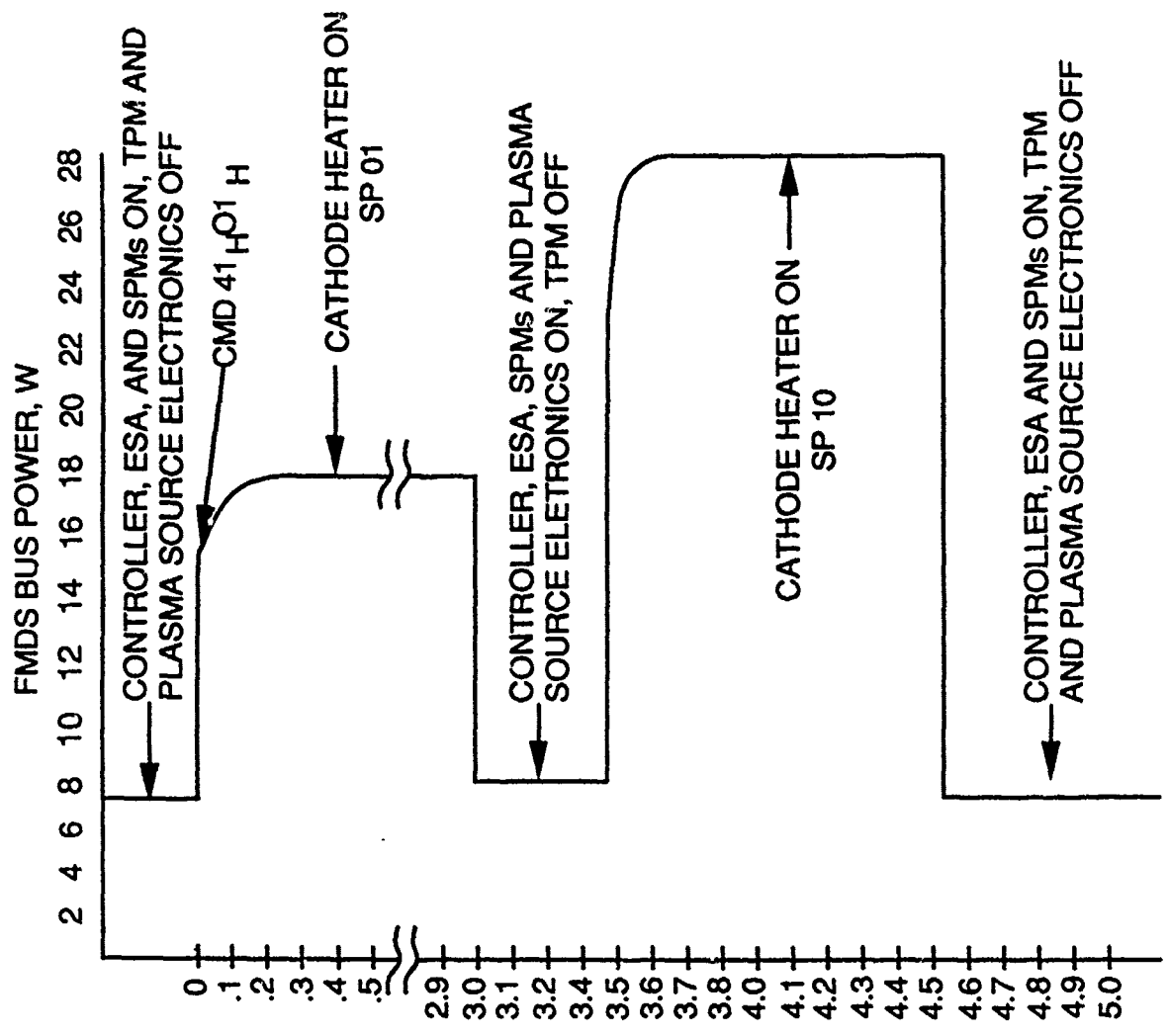
Figure 10-15. FMDS power profile during the automatic cathode conditioning mode (CMD 41_H 01_H).

8912-14-26
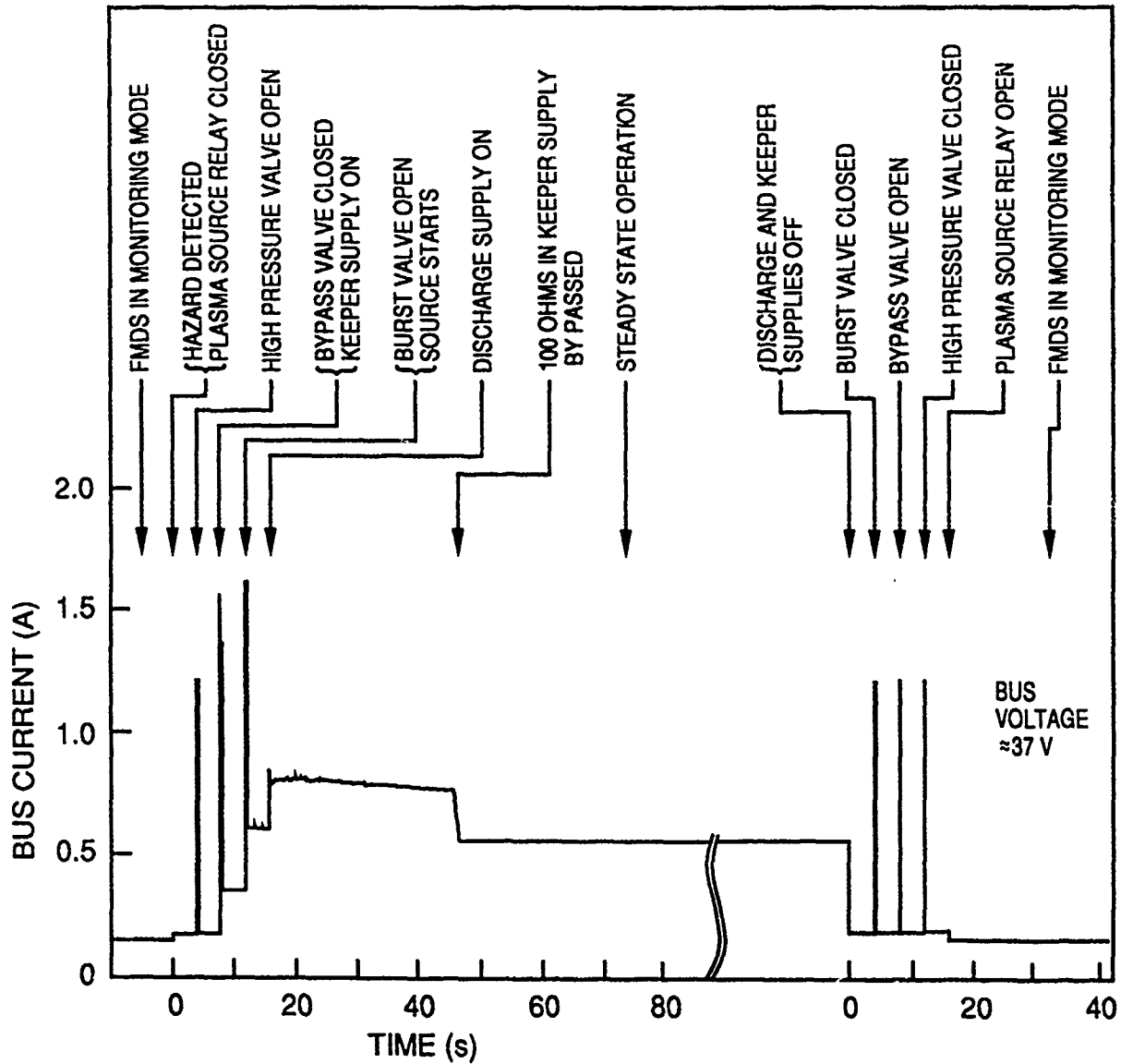
Figure 10-16. Bus current during startup and shutdown of the plasma source.

231

Current spikes 125-ms wide and up to 1.6-A in amplitude can be seen during actuation of the valves. Nominal power levels drawn from the input bus due to the various FMDS subsystems are listed in Table 10-1.

Table 10-1. FMDS Bus Power Due to the Various FMDS Subsystems.

FMDS SYBSYSTEM	NOMINAL BUS POWER W
CONTROLLER ONLY OPERATING	3.7
ESA	1.6
SPM 1	0.18
SPM 2	0.18
TPM	7.6*
PLASMA SOURCE RELAY CLOSED, SUPPLIES OFF	0.6
PLASMA SOURCE OPERATING SP 00	11.5
PLASMA SOURCE OPERATING SP 01	11.1
PLASMA SOURCE OPERATING SP 10	14.7
PLASMA SOURCE OPERATING SP 11	13.8

* Estimated

10.2.5 Plasma Source Operating Characteristics

The plasma source was operated at all of its setpoints during system testing. The measured emission current for a 30-V bias at each of the setpoints is listed in Table 10-2, and the nominal keeper and discharge currents for the four operating setpoints are listed in Table 10-3. Figure 10-17 shows the keeper voltage, discharge voltage, and emission current during startup of the plasma source. The emission current stays above 0.5 mA after the discharge supply turns ON at 4 s and reaches its final level of 1.13 mA in 15 to 20 minutes. The keeper and discharge voltages stabilize out at 15 and 20 V respectively in the same time frame.

232

Table 10-2. Measured Emission Current from the Plasma Source for a 30-V Bias.

OPERATING POINT	EMISSION CURRENT mA
SP 11	1.93 mA
SP 10	1.13 mA
SP 01	0.69 mA
SP 01, DISCHARGE SUPPLY OFF	0.66 mA
SP 00	0.74 mA
SP 00, DISCHARGE SUPPLY OFF	0.72 mA.

Table 10-3. Nominal Keeper and Discharge Currents for the Four Operating Setpoints.

SET POINT	KEEPER CURRENT mA	DISCHARGE CURRENT mA
SP 11	50	250
SP 10	250	200
SP 01	400	0
SP 00	420	0

The source did not operate in a stable manner when operated at SP 11. The discharge voltage had transients going down to ≈8 V and the discharge current had transients going to over 600 mA. With 30 ohms between the discharge power supply and the plasma source, the voltage on the power supply side of the resistor was stable while the voltage on the plasma source side of the resistor was still unstable. This proves that the instability is in the plasma source and not in the power supply. We do not believe that the oscillations observed are destructive; however, we do not have any lifetest data to prove this; therefore, we do not recommend operating at SP 11.

10.2.6   ESA Testing

The ability of the ESA to detect both protons and electrons was demonstrated under simulated geosynchronous environmental conditions. The electron channel entrance aperature was masked down a factor of ≈40 using three small holes in a plate over the normal entrance aperature. This was done to reduce the electron counting rate to a value consistent with a ten year lifetime for the channeltron. The arc length of the detection plates (only 28°) in the ESA

233
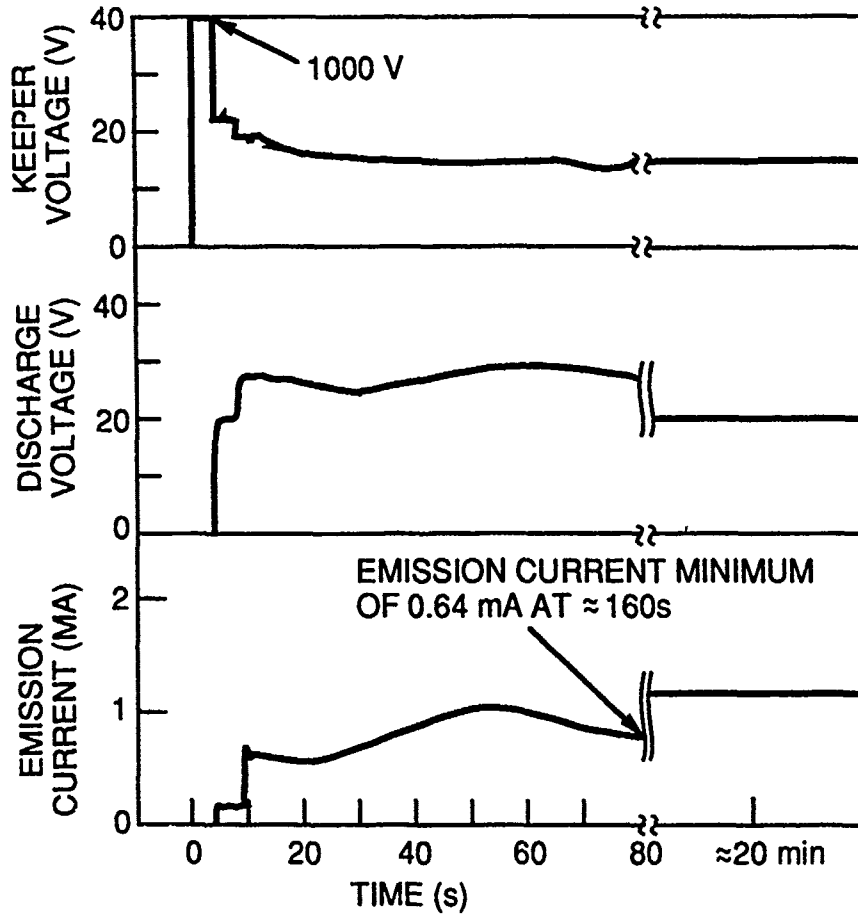
Figure 10-17. Keeper voltage, discharge voltage, and emission current during plasma source startup.

is not sufficient to prevent high energy electrons from being counted by the ion channel. Large counts were recorded by the ion channel when the ESA was exposed to only high energy electrons with no protons present. We understand that this result is consistent with data collected on orbit from similar type instruments. The only known fix is to rebuild the detection plates with a larger arc length.

10.2.7   Overall System Testing

The entire FMDS was biased negative with protons present in the vacuum chamber. When the potential of the FMDS exceeded the threshold level for the ion ESA, the algorithm in the controller detected a hazardous condition and the plasma source was automatically started. Similarly, when the SPMs were charged negative past their threshold level using the electron gun, the controller automatically started the plasma source. The functionality of the FMDS for all of its operating modes and capabilities was demonstrated during the system testing. All of the commands listed in Appendix A were sent to the FMDS and the proper response verified.

10.2.8   Thermal Testing

The thermal testing of the FMDS system was limited to one thermal cycle as follows:

- The plasma source was started and the FMDS was operated while transitioning from ambeient temperature to -14°C.

- The FMDS was turned OFF and cold soaked at -14°C for >4 hrs.

- The FMDS was turned ON and the plasma source started

- The FMDS was operated while transitioning to 60°C

- The FMDS was turned OFF and hot soaked for >5 hrs.

- The FMDS was turned ON and the plasma source started

- The FMDS was operated while transitioning back to ambient temperature.

No anomalies in the operation of the FMDS were observed during this thermal cycle.

SECTION 11
CONCLUSIONS AND RECOMMENDATIONS

A discharge system has been designed, fabricated, and functionally tested that can autonomously; detect that absolute and/or differential charging is occurring on a spacecraft; turn on its plasma source to negate that charging; operate its plasma source until the charging hazard has passed; and then return to its monitoring mode. The hardware and software demonstrated their ability to perform these functions under simulated charging conditions that exist at geosynchronous orbit. The system needs to be environmentally qualified (thermal testing, vibration testing, and EMI testing) before it can be flown.

The following upgrades to the system are also recommended before the system is flown:

1) Modify the ion ESA to have a larger arc length in its detection plates for improved discrimination against high-energy electrons.

2) Lower the number of sweeps required by the ESA algorithms to detect a hazardous condition in order to improve the system response time.

3) Replace the pressure transducers in the feed system with psig type units in order to prevent zero drift of these sensors on orbit.

4) Test the feed system for leaks to prevent the slow loss of expellant on orbit.

5) The system was delivered with the microprocessors and PROMS in the controller in sockets and without conformal coating on ≈75% of the electronics. The microprocessors and PROMS should be soldered directly into their PC boards, and all of the electronics should be conformally coated.

REFERENCES

1. D.J. McComas and S.J. Bame, "Channel Multiplier Compatible Materials and Lifetime Tests," Review of Scientific Instruments, Vol. 55, No. 4, pp 463-467, April 1984.

2. H. Rosenbauer, "Remarks on the Qualification of Continuous Channel Electron Multipliers (CEMs) for Use as Detectors in Long Term Space Flight Missions," (unpublished).

3. J.C. Sturman, "Development and Design of Three Monitoring Instruments for Spacecraft Charging," NASA Technical Paper 1800, 1981.

4. S.L. Spiegel and H.A. Cohen, "Real Time, Automatic Vehicle Potential Determination from ESA Measurements: The Distribution Function Algorithm," Journal of Spacecraft and Rockets 25, No. 3, p 234 (1988).

5. R.C. Olsen, "A Threshold Effect for Spacecraft Charging," Journal of Geophysics Research, Vol. 88, No. A1, pp 493-499, January 1, 1983.

6. E.R. Moog and M.B. Webb, "Xenon and krypton adsorbtion on palladium (100)," Surface Science 148, pp. 338-370, 1984.

7. Multiwire/West Division, Kollmorgan Corp.
    3901 East LaPalma Ave.
    Anaheim, CA 92807

APPENDIX A

FMDS COMMANDS AND TELEMETRY

TELEMETRY LIST
(updated   4/7/89)

ORDER IN OUTPUT TLM SEQUENCE DECIMAL	IDENTIFIER/CONVERSION EQUATION	ORDER IN INTERNAL TM1STACK DECIMAL
0 *	1st Frame-Identification byte (AA)	0
1 *	2nd Frame- Identification byte (55)	1
2 *	System Status Word:	2
	bit 0: 4-s Flag fault (failed to execute in 4 s)	
	bit 1: Analog Fault (failed to complete in 250 ms)	
	bit 2: TPM Fault (failed to complete in 250 ms)	
	bit 3: ESA Fault (failed to complete in 250 ms)	
	bit 4: Shorted instrument on powerup	
	bit 5: Plasma source went out 4 times	
	bit 6: Plasma source failed to ignite after 4 tries	
	bit 7: Command error (illegal command, or redundant pairs did not match)	
3	Telemetry Start Byte (4 to 179 dec)	3

-----------The   above   bytes   are   always   sent--------

4	Charging Flag:	156
	bit 0 = iESA	
	bit 1 = eESA	
	bit 2 = SPM1	
	bit 3 = SPM2	
	bit 4 = TPM	
	bit 5 = Electrometer	
5	Plasma-Source-ON flag	157
6 * †	Plasma-Source Mode:	158
	0 = OFF	
	1 = CATHCOND	
	2 = AUTO	
	3 = ON	
	4 = MANUAL	
7	iESA Vehicle Frame Potential (values correspond to iESA channel energies)	47
8	eESA Charging Flag	48

---

* When the master microprocessor is in its confined mode (operating in PROM only), only the data marked with asterisks are updated.

† The plasma-source mode is displayed as f0 when the master microprocessor is in confined mode. (The plasma source is actually OFF under this condition.)

239

9	SPM Ranges:	145

bit 0 = SPM1
bit 1 = SPM2
0 = LOW; 1 = HIGH range

10	SPM1 mantissa	15
11	SPM2 mantissa	16

SPM voltage:

$$V = -\left[2.5kV - \frac{5kV}{255} \bullet SPM\_mantissa\right] \bullet 10^{SPM\_rangebit}$$

12	SPM1 Sun sensor (8-bit ADC result)	30
13	SPM2 Sun sensor	31
14	TPM Positive counts	32
15	TPM Negative counts	33
16	Emission Current:	

Electrometer Characteristics
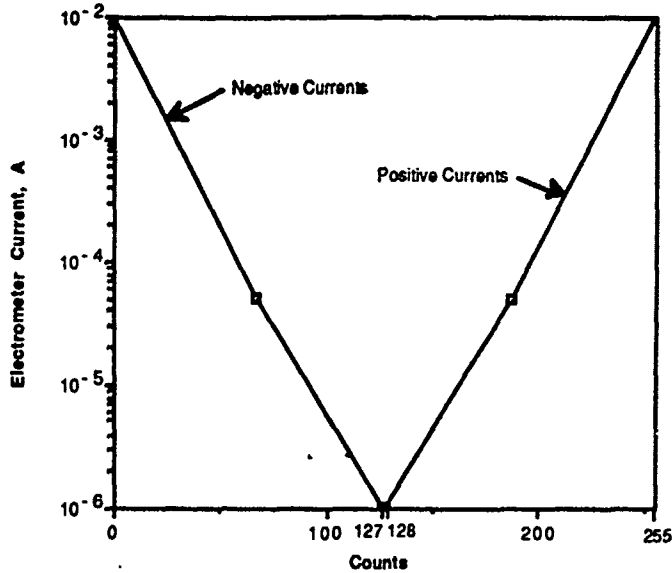
17*	Last Command Byte	171

Plasma-Source Data

18	Discharge Voltage	4
19	Discharge Current	5
20	Keeper Voltage	9
21	Keeper Current	10
22	Cathode-Heater Voltage	7
23	Cathode-Heater Current	8
24	Pressure upstream of burst valve	27
25	Tank Pressure	28

TPM Data (numbered 26 to 38):

26	Amplitude of highest external pos pulse	34
27	Amplitude of highest external neg pulse	35
28	Width of highest-ampl external pos pulse	36
29	Width of highest-ampl external neg pulse	37
30	Amplitude of widest external pos pulse	38
31	Amplitude of widest external neg pulse	39
32	Width of widest external pos pulse	40
33	Width of widest external neg pulse	41
34	Amplitude of internal pulse corresponding to the highest external pos· pulse	42
35	Amplitude of internal pulse corresponding to the highest external neg pulse	43
36	Amplitude of internal pulse corresponding to the widest external pos pulse	44
37	Amplitude of internal pulse corresponding to the widest external neg pulse	45

Engineering Data

38	TPM Relay status	46
39	+28-V Power input voltage	11
40	+5-V Housekeeping voltage	12
41	+12-V Housekeeping voltage	13
42	+28-V Power input current	14
43	PPU Temperature No. 1	17
44	PPU Temperature No. 2	18
45	TPM Temperature	29
46	ESA +5-V Housekeeping voltage	19
47	ESA +10-V reference voltage	20
48	ESA electron-CEM bias	21
49	ESA ion-CEM bias	22
50	ESA Temperature	23
51	ESA Sweep voltage	24
52	ESA High voltage (±50, ±300, ±500)	25
53	ESA +10-V housekeeping voltage	26

Cumulative Hazard-Algorithm and Ignition Data

54	Ion Hazard Count (low byte)	146
55	Ion Hazard Count (high byte)	147
56	Electron Hazard Count (low byte)	148
57	Electron Hazard Count (high byte)	149
58	SPM1 Hazard Count (low byte)	150
59	SPM1 Hazard Count (high byte)	151

241

60	SPM2 Hazard Count (low byte)	152
61	SPM2 Hazard Count (high byte)	153
62	TPM Hazard Count (low byte)	154
63	TPM Hazard Count (high byte)	155
64	Plasma Source Ignition Count (low byte)	169
65	Plasma Source Ignition Count (high byte)	170
66	Bit Flip Count (low byte)	172
67	Bit Flip Count (high byte)	173
68	Overtemperature Flag	174
69*	Power Relay Status	175
70	iESA-caused Ignition Count (low byte)	159
71	iESA-caused Ignition Count (high byte)	160
72	eESA-caused Ignition Count (low byte)	161
73	eESA-caused Ignition Count (high byte)	162
74	SPM1-Caused Ignition Count (low byte)	163
75	SPM1-Caused Ignition Count (high byte)	164
76	SPM2-Caused Ignition Count (low byte)	165
77	SPM2-Caused Ignition Count (high byte)	166
78	TPM-Caused Ignition Count (low byte)	167
79	TPM-Caused Ignition Count (high byte)	168

ESA Data

80	ESA Channel 0 Status Byte No. 1	49
81	ESA Channel 0 Status Byte No. 2	50
82	ESA Channel 0 Ion Count (high byte)	51
83	ESA Channel 0 Ion Count (low byte)	52
84	ESA Channel 0 Electron Count (high byte)	53
85	ESA Channel 0 Electron Count (low byte)	54

[The ESA data in No.s 86 to 175 are structured similarly to Channel 0, given in Nos. 80 to 85]

86-91	ESA Channel 1	55-60
92-97	ESA Channel 2	61-66
98-103	ESA Channel 3	67-72
104-109	ESA Channel 4	73-78
110-115	ESA Channel 5	79-84
116-121	ESA Channel 6	85-90
122-127	ESA Channel 7	91-96
128-133	ESA Channel 8	97-102
134-139	ESA Channel 9	103-108
140-145	ESA Channel 10	109-114
146-151	ESA Channel 11	115-120
152-157	ESA Channel 12	121-126
158-163	ESA Channel 13	127-132

164-169	ESA Channel 14	133-138
170-175	ESA Channel 15	139-144

Miscellaneous

176	Instrument-Shorted byte	176
177*	Memory Pointer (low byte)	177
178*	Memory Pointer (high byte)	178
179*	Memory Data (at pointer address)	179

COMMAND LIST
(updated 4/7/89)

The following list describes the commands that are available for execution by FMDS. The commands consist of a command byte, which identifies the action to be taken (and also tells FMDS how many bytes comprise the complete command), and up to three arguments. All commands to FMDS must be sent in matching byte pairs (for error-protection purposes). If a nonmatching byte pair is received (or any of several illegal commands), the most significant bit of the System Status Byte (SSB) is cleared, the partial command in memory is discarded, and all new commands are ignored until receipt of a clear-command-error command (see below). This process is intended to avoid inadvertent commands from being executed.

If FMDS undergoes a system reset during transmission of a command string, the system may be left with an odd number of command bytes, causing a command error when subsequent command strings are sent. To clear this condition, send a single byte that does not match the last byte sent (available in the telemetry stream), and then send the clear-command-error command. The first action eliminates the odd byte by causing a command error, and the second restores normal command functioning.

Command Listing

The commands are given in sequence by command number. The top three bits of each command tell the system how many total bytes (not counting the byte pairing described above) in the command. All numbers in the following list are in hexadecimal (unless otherwise noted), and bits are numbered from 0 to 7, bit 7 being the most significant bit. MSB and LSB denote most and least significant bytes, respectively, while MSb and LSb denote most and least significant bits, respectively.

Command 20: Clear Command Error. This command resets the FMDS command processor following a command error.

Command 41: Set Plasma-Source Mode. This command specifies the mode of operation of the plasma source. The specific commands are listed below.
41 00 **OFF mode.** The plasma source will remain OFF.

244

41 00 CATHODE CONDITIONING mode. The cathode will be automatically conditioned (the process takes 4.5 hours), and the system will be automatically placed in the AUTO mode. A bit is written to EEPROM so that the system will retain knowledge that the cathode has been conditioned after a system reset. Execution of cathode conditioning clears any prior ignition-fault counters.

41 02 AUTO mode. The plasma source remains OFF until the charging flag is set by an instrument that is not masked off. The plasma source remains ON as long as a charging environment is detected or until an adjustable timeout expires. The charging environment takes precedence.

41 03 ON mode. The plasma source is ignited and maintained in continuous operation in this mode.

41 04 MANUAL mode. When the system receives this command, it takes no actions concerning the plasma source. Manual adjustments may then be made by ground command to alter source operation. Note that if the initial mode is ON or CATHODE CONDITIONING, the timers associated with these modes continue to count down while the system is in MANUAL mode.

Sending any argument other than 0 to 4 will result in a command error.

Command 42: Set CEM Gains. The lower nybble of the single argument to this command sets the gain of the ion channel-electron multiplier (CEM), and the upper nybble sets the electron CEM gain. Sending 42 00 sets minimum gain for each instrument.

Command 43: Set ESA Sweep time. Bits 0 and 1 of the single argument determine the sweep time, and bit 2, when set, disables the ESA photodiode. Sending 43 03, for example, places the instrument in a 32-s sweep mode with the photodiode enabled. Bits 3 to 7 are don't cares. The following table gives the sweep times selected by the indicated bit pattern:

Bit 1	Bit 0	Sweep Time, s
0	0	4
0	1	8
1	0	16
1	1	32

Command 44: Set Overtemperature Mask/Clear Overheat Flag. The Executive routine will power down instruments whose temperatures exceed a predetermined value. Setting bit 7 of the single argument of this command clears the overheating flag, and setting each bit in the lower nybble will cause Executive to ignore overheating indications from the corresponding instrument. Bits 4 to 6 are don't cares.

Bit 1	Temperature Sensor
0	Plasma source electronics T1
1	Plasma source electronics T2
2	ESA
3	TPM

Command 45: Set Telemetry Start Byte. The telemetry stream consists of a5 (180 decimal) bytes, the first 4 of which are always sent. This command sets the starting point in the data set from which subsequent bytes are placed in the telemetry stream. (Command 46, below, specifies how many bytes are to be sent.) Sending 45 04 establishes the normal setting (i.e., no gap in the data set).

Command 46: Set Number of Telemetry Bytes to be Sent. Sending 46 b3 causes all bytes to be sent; an argument less than a5 will cause a telemetry stream of reduced length. An argument of greater than a5 will cause a command-error condition.

Command 67: Manually Operate Valves or Relays. The first argument specifies the valve or relay to be acted upon (only one at a time may be operated), and the second argument specifies ON (=01) or OFF (=00) for relays, OPEN (=01) or CLOSE (=00) for valves. N.B. — Avoid the semantic problem that CLOSEing a relay turns it ON, while CLOSEing a valves turns it OFF by adhering strictly to the foregoing defir. ·ons. The following table gives the identification numbers for each valve or re ·, ·

Valve/Relay Number	Identification
0	Plasma-source power relay
1	Low-pressure gas valve
2	Bypass valve
3	High-pressure valve
4	SPM1 power relay
5	ESA power relay
6	TPM power relay
7	SPM2 power relay

Removing the power to an instrument will cause the system to not consider data from that instrument; it will not attempt to power them again. Valves will similarly not be reset by the system until the next plasma source ignition attempt. The plasma-source ignition algorithm will not take into account manual valve alterations. Sending 67 02 00, for example, will close the bypass valve; an ignition attempt in this condition will fail the first time, but operate normally thereafter.

Any command (from any source) that would cause all three valves to be simultaneously open will produce a system reset.

Command 48: Manually Set Plasma-Source Setpoints. This command alters the plasma source setpoints. It will remain in effect until an ignition, cathode-conditioning, or shutdown process alters the setpoints. If the plasma source is ignited, the system will re-send the command every 4 s to protect against noise- or radiation-induced state changes. The following table indicates the bit pattern of the control byte. Multiple setpoint changes can be made simultaneously.

Bit	Function
0	Discharge ON/OFF
1	Cathode Heater ON/OFF
2	Cathode Heater setpoint LSb
3	Cathode Heater setpoint MSb
4	Discharge/Keeper setpoint LSb
5	Discharge/Keeper setpoint MSb
6	Keeper ON/OFF
7	Don't care

Command 49: Set Discharge-Current Run Setpoint. A short time after ignition, the plasma source is placed in a setpoint that will persist until the next ignition. This command selects this normal run-level setpoint from among the four alternatives. Sending 49 03, for example, places the plasma source in its maximum plasma-production mode, while 49 00 will produce minimum plasma production.

Command 6a: Set Memory Readout Address. The contents of the memory location in the Master microprocessor memory that is pointed to by the address specified in this command appears in the telemetry stream. The first argument is the LSB of the address, and the second argument is the MSB. Sending 6a 34 12, for example, will cause the contents of location 1234 to appear in the telemetry stream.

Command 4b: Set Cathode-Heater Levels. The plasma source is normally ignited and run without the use of the cathode heater. In case of degraded operation, however, the cathode heater may be turned ON before ignition and/or during running. Setting bit 7 causes the cathode heater to be turned ON 5 min prior to ignition (this will delay ignition by 5 min after a charging flag is encountered), and bits 4 (LSb) and 5 (MSb) specify the heater setpoint. Setting bit 3 enables cathode-heater operation after ignition (the cathode heater would otherwise be turned OFF), and bits 0 (LSb) and 1 (MSb) specify the run-time setpoint. The run-time and pre-ignition setpoints and operation are independent. Setting run-time cathode-heater operation will not delay ignition following detection of a charging event. [If a requirement for cathode-heater power occurs early in the plasma-source life, it is likely due to contamination; executing cathode conditioning may solve the problem by vaporizing contaminants.]

Command xc: Ground-Writable Command. This command presently does nothing, but 50 bytes (80 decimal) of space is provided to allow convenient ground writing of a new command. "x" will be either 2, 4, 6, or 8 depending on whether the command uses 0, 1, 2, or 3 arguments.

Command 4d: Set SPM Charging Threshold. Sending 0 through 3 will set the tolerance level of the system for detected spacecraft charging; if potentials are

detected above these levels by any instrument, the plasma source will be ignited. Sending 4d 02 sets the threshold to 1000 V.

Argument	Threshold
00	200 V
01	500 V
10	1000 V
11	2000 V

Sending any other argument will result in a command error.

Command 4f: Set Instrument Mask. This command causes the system to ignore data from a specified instrument (or instruments) in determining the presence of a charging event while still placing data from the instrument in the telemetry stream. It is an alternative to powering down an instrument that produces too many false alarms. The table below gives the instruments that are masked off when the corresponding bit is set.

Bit	Instrument masked off
0	ion ESA
1	electron ESA
2	TPM
3	SPM1
4	SPM2
	Electrometer
6 to 7	Don't care

Sending 4f 05, for example, will remove the ion-ESA and TPM data from consideration by the charging-hazard algorithm.

Command 50: Set Eclipse Limitation on eESA. If the single argument to this command is non-zero, a charging indication from the electron ESA (eESA) will cause plasma-source ignition only if the spacecraft is in eclipse (as detected by the ESA photodiode, whether enabled or not). Sending 50 00, for example, will cause the eESA to trigger plasma-source ignition in either darkness or sun.

Command 37: Warm Reboot. Sending this command causes the Controller to execute an 8085 HLT instruction; this causes a system reset similar to a power-up condition.

Command 58: Enable/Disable SPM Automatic Zeroing. This single-argument command enables the automatic zeroing algorithm for the SPMS. If the upper nybble or the argument is nonzero, then the routine looks for plasma-source-ON duration of two hours; it then stores the current value of the SPM telemetry-127 as the offset for SPM1. From then on, the SPM voltage is computed from the telemetry value-offset. The lower nybble of the argument affects SPM2. Sending 58 0f, for example, disables automatic zeroing for SPM1, and enables it for SPM2. The offsets generated by this command and the manual commands following do not affect the SPM voltage telemetry that is sent to the ground.

Command 59: Manually Set SPM1 Offset. This command sets up an offset (the single argument) which is subtracted from the telemetry value of the SPM1 potential output before computing the SPM potential. If automatic rezeroing is enabled, the offset will be overwritten when the plasma source is next on for two hours. Sending 59 02, for example, will correct the case in which SPM1 reads 81 (where 7f corresponds to zero charging) under conditions that are believed to be uncharged.

Command 5a: Manually Set SPM2 Offset. Same as command 59, except for SPM2.

Command 5b: Set iESA Threshold. This single-argument command specifies an iESA channel number 01 through 0f); if the iESA algorithm detects charging above a value corresponding to the channel center energy, then the charging flag will be set. Sending 5b 10, for example, sets channel 10 (2 kV) as the threshold (this is the default value).

Command 3c: Write Auto-Rebooting flag in RAM. If the byte eb is written at location 1002 in EEPROM FMDS will, on application of power, go through its automatic sequence of powering up the instruments. If not, the master processor will

be confined to executing code in PROM only (indicated by a plasma-source mode of f0 in the telemetry stream). The command string 93 ff ff xx must be sent to permit execution of code in EEPROM. If FMDS is reset, the above command would again have to be sent to bring FMDS to full operation. However, sending command 3c writes a flag to RAM (it puts fd28 at _Uend_+1) which will cause FMDS to power up normally after a reset.

Command 9d: Write Data to RAM. This command writes a byte to a specified address in RAM. It takes three arguments: (address low byte) (address high byte) (data). Sending 9d 3c 40 ab, for example, writes the byte ab at location 403c.